Forschungszentrum Jülich
in der Helmholtz-Gemeinschaft

Institut für Werkstoffe und Verfahren der Energietechnik
Institut 2: Werkstoffstruktur und -eigenschaften

Performance of metallic and carbon-based materials under the influence of intense transient energy deposition

Yoshie Koza

Jül-4137

Performance of metallic and carbon-based materials under the influence of intense transient energy deposition

Yoshie Koza

Berichte des Forschungszentrums Jülich ; 4137
ISSN 0944-2952
Institut für Werkstoffe und Verfahren der Energietechnik
Institut 2: Werkstoffstruktur und -eigenschaften Jül-4137
D 82 (Diss., Aachen, RWTH, 2004)

Zu beziehen durch: Forschungszentrum Jülich GmbH · Zentralbibliothek
D-52425 Jülich · Bundesrepublik Deutschland
☎ 02461 61-5220 · Telefax: 02461 61-6103 · e-mail: zb-publikation@fz-juelich.de

Abstract

Performance of metallic and carbon-based materials under the influence of intense transient energy deposition

Yoshie Koza

Intense energy is deposited on localized areas of the plasma facing materials under transient thermal loads such as edge localized modes (ELMs), plasma disruptions or vertical displacement events (VDEs) in a magnetic confined fusion reactor. Crack formation, thermal erosion and redeposition mainly take place under these conditions and may cause catastrophic damage in the materials. Dust formation associated with evaporation and liquid or solid particles emission are also serious issues to influence plasma contamination. In order to estimate the lifetime of the components during above mentioned events (ELMs, disruptions, VDEs), the thermal erosion mechanisms and performance of carbon-based and high Z materials have been investigated using energetic electron beam facilities. Moreover, a thorough calibration of an electron beam in the high heat flux facility JUDITH was done.

For the evaluation of erosion data obtained in different test facilities several factors have to be taken into account. Different material erosion processes at identical heat loads induced by different facilities take place due to different beam generation and beam modes (static/scanned beam). The different degradation processes were created by different surface tensions and vapor recoil pressures at local spots in the loaded area. Molten and re-solidified material remained within the loaded area by fast scanning of the electron beam in JUDITH, which leaded to a rippling surface.

Erosion scenarios have been elucidated on pure W and carbon-based materials. For W, the thermal erosion is initiated by convection of melt, strong evaporation or boiling processes. Moreover the formation of a vapor cloud was observed in the simulation experiments indicating vapor shielding on the surface. From screening tests on different high Z materials, pure W was found to show the highest resistance against thermal shock under plasma disruption conditions and are suitable for the components in Tokamak fusion reactors. A castellated structure was found to help reducing crack formation compared to monolithic structure.

For carbon-based materials (isotropic graphite, carbon fiber composites (CFCs), Si-doped CFC), material erosion in different particle emission regimes, and characterization of emitted particles have been studied. "Small" and "Big" particle emission regimes have been identified under brittle destruction, which represents the combined action of sublimation, crack formation and ejection of solid particles. These regimes were related to the ejected particle size and maximum erosion depth. The resulting erosion patterns on the test samples and the morphology of the ejected particles differ significantly for the three materials. For both carbon and tungsten, preheating of samples before loading enhances material damages such as weight loss and crater formation.

Kurzfassung

Verhalten von metallischen und Kohlenstoffbasis Werkstoffen unter dem Einfluss intensiver transienter Energiedeposition

Yoshie Koza

In zukünftigen Fusionsreaktoren des Tokamak-Typs werden die an das Plasma grenzenden Materialien unter transienten thermischen Belastungen wie Edge Localized Modes (ELMs), Plasma-Disruptionen und vertikalen Plasma-Instabilitäten (VDE), lokal mit hohen thermische Belastungen beaufschlagt. Unter diesen Bedingungen können Rissbildung, thermische Erosion, und Rekristallisation auftreten, welche katastrophale Schädigungen im Werkstoff zur Folge haben können. Die Bildung von Stäuben, hervorgerufen durch Verdampfung und die Emission flüssiger sowie fester Partikel und die damit verbundene Plasma-Verunreinigungen stellen ein weiteres Problem dar. Um die Lebensdauer der Komponenten abschätzen zu können, wurden an typischen Wandmaterialien mit Hilfe von Elektronenstrahlanlagen solche Belastungen simuliert. Aufgrund dieser Experimente konnten Aussagen bezüglich thermischer Erosionsmechanismen, Werkstoffverhalten und der Eignung von Refraktärmetallen bzw. Werkstoffen auf Kohlenstoffbasis getroffen werden. Des weiteren wurde eine Kalibrierung des Elektronenstrahls durchgeführt .

Bei der Bewertung des in verschiedenen Testanlagen gewonnenen Datenmaterials sind in Bezug auf die Erosion eine Vielzahl von Einflußfaktoren zu berücksichtigen. Dabei treten verschiedener Erosionsprozesse in unterschiedlichen Experimenten bei nominal identischer thermischer Belastung auf. Diese können auf die Differenz in den Strahlparametern zurückgeführt werden. Die Unterschiede in der Schädigung verschiedener Materialien können durch unterschiedliche Oberflächenspannungen und lokal auftretenden Dampfdrücke erklärt werden, die sich wiederum auf die Verdrängung der entstehenden Schmelzphase auswirken. Aufgrund der schnellen Abrasterung durch den Elektronenstrahl kommt es zu einer homogenen Werkstoffbelastung, bei der die Schmelze vorwiegend am Ort ihrer Entstehung erstarrt.

Erosionsszenarien wurden für reines Wolfram und Werkstoffe auf Kohlenstoff-Basis erstellt. Im Falle von Wolfram, wird die thermische Erosion durch die Konvektion der Schmelze und starke Verdampfung in Verbindung mit Siedeprozessen initiiert. Zusätzlich wurde in den Experimenten die Bildung einer Dampfwolke beobachtet, woraus auf eine Abschirmung der Oberfläche durch den Ablationsdampf gegen den Elektronenstrahl geschlossen wird. Anhand von Versuchen an verschiedenen hoch-Z Materialen wurde ermittelt, dass reines Wolfram unter fusionsrelevanten Bedingungen, die höchste Resistenz gegenüber Thermoschocks aufweist und daher für die Komponenten in Tokamak Fusionsreaktoren am besten geeignet ist. Weiterer Versuche ergaben, dass eine kastellierte Struktur im Vergleich zum massiven Werkstoff in der Lage ist, die Rissbildung weiter zu reduzieren.

Für Kohlenstoffe (Graphit, faserverstärkte Kohlenstoff-Werkstoffe (CFCs), und Si-dotiertes CFC) wurden die Erosionseffekte bei unterschiedlichen Belastungen und variierender Partikelemission untersucht. Die emittierten Partikel wurden mit unterschiedliche Verfahren charakterisiert. Für die hier verherrschende 'Brittle Destruction' die letztendlich eine Kombination von mehreren Prozessen wie Sublimation, Rissbildung und Emission fester Partikel darstellt, wurden Bereiche für die Emission "kleiner" und "großer" Partikel identifiziert. Für diese Bereiche konnte die Partikelgröße mit der maximalen Erosionstiefe korreliert werden. Die durch Erosion hervorgerufenen Oberflächenveränderungen auf den getesteten Proben und die Morphologie der emittierten Partikel sind für die drei Kohlenstoff-Werkstoffe unterschiedlich. Für die beiden Werkstoffgruppen Kohlenstoff und Wolfram gilt gemeinsam, dass ein Vorheizen der Proben zu einem Anstieg der Materialschädigung, wie z.B. Gewichtsverlust und/oder Kraterbildung führt.

Contents

1 Introduction

1.1 Nuclear fusion

Fusion is a physical process in which the nuclei of light atoms, like hydrogen, fuse together to create heavier atoms and to liberate enormous energy to force the nuclei to fuse. Hydrogen fusion produces the nuclear energy more than a million times higher than that can be generated from burning hydrogen. It takes extremely high temperatures and pressures. In the sun and stars, massive gravitational forces generate the conditions that fusion naturally occurs. On earth, sustainable and controllable fusion power is much harder to achieve in a sense that two nuclei of positive charge have to overcome the Coulomb repulsion [1].

If man-made fusion reactions ought to occur, the particles must be energetic enough, available in sufficient number of plasma particles (highly dense) and well confined. These simultaneous conditions can be achieved by a fourth state of matter known as plasma. In plasma, electrons are stripped off from their nuclei. Plasma, therefore, consists of charged particles, ions and electrons. Two principles are used, inertial and magnetic, to achieve the above-mentioned conditions. In inertial confinement powerful lasers or high energy particle beams compress the fusion fuel. In magnetic confinement strong magnetic fields, typically 100,000 times higher than the earth's magnetic field, prevent the charged particles from leakage (essentially a "magnetic bottle") and the hot plasma from contact with the wall structures. There are two main types of magnetic confinement: Stellarators and Tokamaks.

The expression "Tokamak" is derived from the Russian *toroid-kamera-magnit-katushka*, meaning "the toroidal (doughnut-shaped) magnetic chamber", which is shown schematically in Fig. 1A. Poloidal coils generate a toroidal field in the vacuum vessel and prevent the contact of plasma with surrounding material, so-called plasma facing materials (PFM). A transformer induces plasma current, and provides an additional poloidal magnetic field component and stabilization of the plasma. The induced plasma current makes pulsed operation and may initiate plasma disruptions. Another type is Stellarator, which is no induced plasma current. It can operate continuously and the disruptions caused by current-driven instabilities do not occur (Fig. 1B).

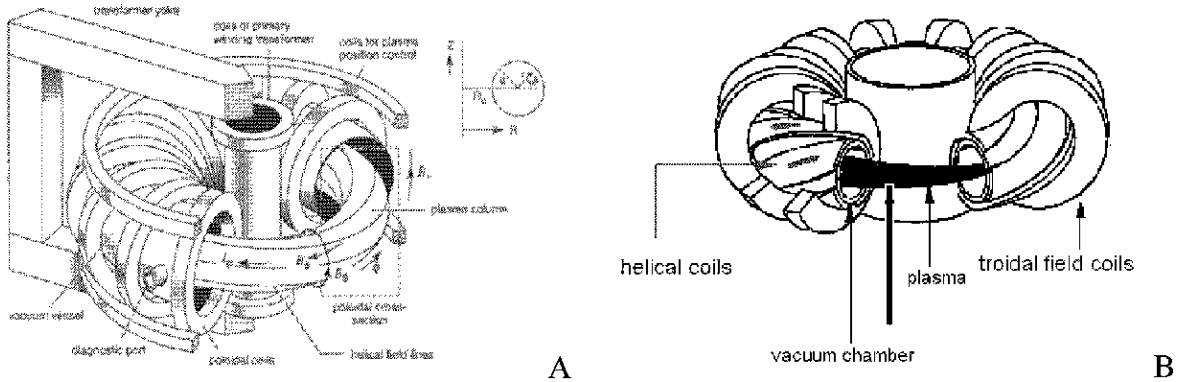

Fig. 1 Schematic view of the Tokamak (A) and Stellarator (B) reactor. [2]

The fuels are deuterium and tritium, which are isotopes of hydrogen and possess the lowest binding energy of all elements. Deuterium exists naturally in water. Tritium decays

with a half-life of 12.3 years and doesn't occur in nature except in the cosmetic rays and some life bodies. For technical applications, however, tritium can be produced via nuclear reaction from lithium, which is found in the earth's crust. The principle fusion reaction and the reaction of tritium breeding from Li are shown in the following [1, 2, 3]:

$$D+T \rightarrow {}^4He\ (3.5\ \text{MeV}) + n\ (14.1\ \text{MeV})$$
$${}^7Li + n \rightarrow {}^4He + T + n - 2.47\ \text{MeV}$$
$${}^6Li + n \rightarrow {}^4He\ (2.05\ \text{MeV}) + T\ (2.73\ \text{MeV})$$

The fusion reaction is associated with mass loss Δm equal to 0.01875 M_p. M_p denotes the mass of a proton. The energy released in the reaction is

$$E = \Delta m \cdot c^2 = 2.818 \cdot 10^{-12}\ \text{J} = 17.59\ \text{MeV}.$$

During operation of a fusion reactor, burning 1 mg of tritium will be sufficient to generate 500 MW of thermal fusion power [17]. Hydrogen will be heated up to extremely high temperature at least 50 million K measured in electron volts (eV), this temperature equals to 4500 eV and represents the temperature which is required to ignite the plasma. The fusion plasma will have a density of around $10^{20}\ m^{-3}$.

The main issues over years have been to avoid energy loss and to keep the high plasma temperature. The fusion plasma carries 80% of the energy; 20 % would be α particles and plasma heating. Neutrons will not be deflected by the magnetic field. The α particles are trapped in magnetic field. This contributes to the plasma heating.

Researchers refer to the overall mean time for heat to escape the plasma, as the energy confinement time. The product of the three quantities: confinement time (τ_E), plasma density (n), and temperature (T) ("fusion product" $n \cdot \tau_E \cdot T$) must be above a minimal value to ensure the thermonuclear power to be sufficiently high to compensate the loss. This self-ignition condition is known as "Lawson criterion" [4]:

$$n \cdot \tau_E \cdot T = \frac{12 \cdot k_B \cdot T^2}{\langle \sigma \cdot v \rangle \cdot E_\alpha - 4 \cdot c_1 \cdot Z_{eff} (k_B \cdot T)^2} \geq 3.0 \cdot 10^{21}\ s \cdot m^{-3} keV$$

τ_E:	Confinement time
n:	Plasma density
T:	Temperature
$\langle \sigma v \rangle$:	Probability of fusion
E_α:	Energy of ^4He particles
$4c_1 Z_{eff}(k_B T)^2$:	"Bremsstrahlung" for an effective Z- number Z_{eff}.

For example, the European Tokamak confinement experiment JET in the United Kingdom has achieved a fusion product of $1.0 \cdot 10^{21}\ s \cdot m^{-3}$ keV.

In order to build a fusion device which operates in the self-ignition regime, scientists and engineers from Canada, China, Europe, Japan, Russia, South Korea and USA have initiated a cooperative project named ITER (ITER means "the way" in Latin). ITER is an experimental fusion reactor design based on the "Tokamak" confinement principle to construct power plant in future. ITER would reach a fusion product of $1.0 \times 10^{22}\ s \cdot m^{-3}$ keV.

This donut-shaped configuration is characterized by a large current, up to several million amperes, which flows through the plasma. The main parameters for ITER are shown in Table 1.

Table 1 Main parameters for ITER [18, 25].

Fusion power	500 MW
Additional heating & current drive power	73 MW
Main radius	6.2 m
Minor radius	2 m
Plasma current	15 MA
Magnetic field	5.3 T
Plasma volume	837 m^3
Plasma surface	678 m^2
Neutron wall load	1 dpa
Operational mode	Pulsed (300-1000 s) $5 \cdot 10^4$ cycles

1.2 Plasma facing components

Because the magnetic confinement in Tokamaks is not perfect, energy and particles loss take place. For this reason, the investigation of the interaction of the plasma in future fusion devices with the reactor walls, so-called plasma facing components (PFCs) is important.

The PFCs for ITER mainly comprise first wall, limiters, and divertor systems. The main role of PFCs is briefly described below:

First wall: Protection of the breeding blanket modules
Blanket: Neutron shield and tritium breeding
Modular structure for the maintenance
Divertor: Exhaust of heat and He generated in the fusion reaction
Limitation of plasma impurities

For PFMs several candidate materials have been proposed at different parts; sintered or plasma sprayed beryllium will be used for the first wall, pure or Si-doped multi directional carbon fiber composites near the strike points of the divertor, and tungsten for the baffle and top part of the divertor [16, 17, 5, 6]. A cross section design of ITER is shown in Fig. 2. The first wall (Be) is shown in green color, the tungsten part of divertor in blue, and carbon part of divertor in orange color. The red lines show the magnetic field. The detail of the candidate PFMs is described in Chap. 2.2.

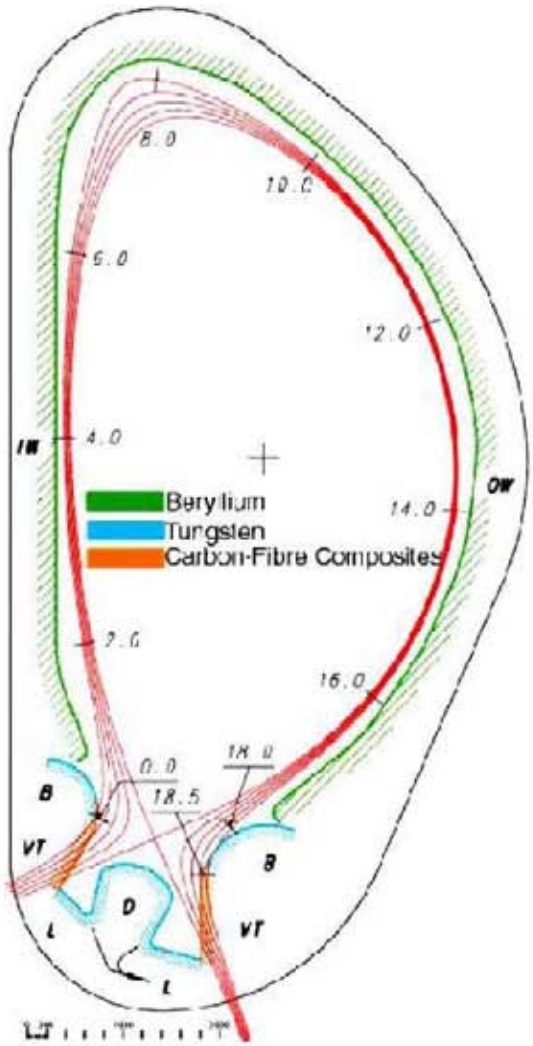

Fig. 2 Cross section design of ITER [7]

Behind the PFMs are heat sink parts. The interface between PFMs and the heat sink reduce the thermal and mechanical stresses [5, 8, 9, 10,32].

Heat sink / coolant tube: DS (dispersion strengthened)-Cu or CuCrZr alloy

Interface: OFHC (oxygen free high conductivity copper),
FGM (functionally graded material) or
several interlayer (Ni, Ni-Al-Si, CuAl, CuMnSnCe, Ti etc),

Joining technique: HIP (hot isostatic pressing), electron beam welding,
brazing with CuAl, CuMnSnCe or Ti (AMC® active metal cast)
etc.

A special active cooling system for PFCs has been developed to remove the heat. For the heat sink materials, a plate made of copper, or CuCrZr is attached by brazing, electron beam welding, or HIPing [11, 12,13]. The cooling tube cools down the reactor walls. Currently, the cooling fluid used in existing Tokamak devices is pressurized water. The development of cooling by helium at around 400 to 800 °C has been proposed as an alternative to pressurized water for future fusion reactors [14,15].

Structural materials with low neutron activation potential have been developed and optimized. Stainless steels are proposed as structural materials in ITER and vanadium alloy or silicon carbide is taken into consideration in future commercial reactors [16, 17,18].

1.3 Energy deposition on PFCs

During the discharge time, the PFCs absorb a certain heat flux and its surface temperature rises throughout the pulse time. The highest heat fluxes in ITER during normal operation are expected to be around 0.5 MWm^{-2} on the first wall and up to 10 MWm^{-2} on the limiter and divertor [18,8]. The heat flux during normal operation in fusion devices is in the range as in case of missiles, turbines, or other applications [19]. In addition, the material absorbs high neutron fluxes which is a byproduct of fusion reactions and degrade thermal and mechanical properties, and fluxes of ions and neutral particles that cause severe erosion. In ITER, neutron loads of 1 dpa for the first wall and up to 0.5 dpa for the divertor are expected [20].

During plasma operation, uncontrolled electromagnetic forces and fluctuations of the induced plasma current may lead to instabilities in the confinement of the plasma particles. These are classified as intense transient heat loads and have three main types: Edge-Localized Modes (ELMs), plasma disruptions and Vertical Displacement Events (VDEs) [21, 22]. The PFMs in divertor is subjected to heat fluxes of 2-5 GWm^{-2} for 0.2-0.5 ms (1-2 Hz) during ELMs, 1-10 GWm^{-2} within 1-5 ms during plasma disruptions, and 200-600 MWm^{-2} within 100 to 300 ms during VDEs [18, 6, 8]. The resulting high heat fluxes under these conditions are 1000 times higher than the max. heat flux during normal operation. Details about these events are described below.

ELMs are a common feature of H-mode discharge in steady state operation which leads to a periodic energy loss of the confined plasma. The ELMs are categorized into three kinds of instabilities that have been observed in Tokamaks. They are called "Type I giant ELMs", "Type 2 'grassy' ELMs", and "Type 3 ELMs" [23, 24]. The type I giant ELMs may cause the most significant damage in PFMs out of the three types. A typical type I ELM in ITER is expected to have energy density of 2-5 GWm^{-2} for pulse duration of 0.2 to 0.5 ms. A single ELM does not cause significant damage in PFCs. However, ELMs are expected to occur with a frequency of 1 to 2 Hz during normal operation and may amount to 1 million events in ITER (3000 pulses with each pulse taking 400 s) [25].

A plasma disruption is a sudden breakdown of the plasma current caused by instabilities in the spatial confinement of the plasma due to the large electromagnetic force. It is initiated by a fast thermal quench after which the plasma current rapidly drops to zero [26]. The basic phenomenon of a plasma disruption can be described in terms of the three classical phases: precursor phase, thermal quench and current quench. Plasma disruptions typically start with a *precursor phase* during which distortions of the shape of the plasma/magnetic field system in Tokamak are induced. These distortions result in the destruction of the internal magnetic surfaces, which leads to a rapid loss of the plasma thermal energy called thermal, *quench.* The thermal quench is followed by a *current quench*, i.e., a rapid decay of the plasma current. The plasma current is inductively coupled to the PFCs as a result of the breakdown. Erosion induced by a number of disruptions would depend on the efficiency of mitigation

effects due to vapor shielding, on the extent of erosion loss, and on the redeposition patterns [27, 28]. When plasma disruptions occur, a large amount of energy are deposited on relatively small sections of the PFCs, accommodating the plasma in extremely short time periods. The plasma disruption is expected to deposit energy density E_{abs} between 5 and 20 MJm^{-2} for pulse duration of 0.1 to 5 ms (P_{abs} = 1-10 GWm^{-2}) on the divertor surface and to occur in less than 10 % of operational cycles.

A vertical displacement event comprises an initially slow vertical drift phase of the plasma and releases a substantial fraction of their stored energy to the components. This is followed by the onset of a plasma disruption and the loss of vertical control. The heat flux of VDEs are expected to deposit E_{abs} of about 60 MJm^{-2} with pulse duration of 100-300 ms (P_{abs} = 200-600 MWm^{-2}) and to arise approximately 1% of operational cycles. The divertor materials may be in particular eroded during plasma disruptions and VDEs [8].

Furthermore, VDEs are lifetime limiting damage. It may result in the damage of coolant tubes. The vapor and particles produced by these events on the plasma facing surface due to erosion would contaminate the plasma and eventually terminate the fusion reaction. Therefore it is of prime interest to develop materials which can endure high thermal loads and neutron irradiation with the lowest damage as possible and overcome safety and economical requirements so that the reactor and the PFCs can be operated with a long lifetime.

1.4 Thermally induced material damage

The typical mechanisms which cause irreversible damage and shorten the lifetime of the components at high temperature applications, are creep, corrosion, thermal fatigue, and thermal shock [29]. For selection of PFCs in fusion reactors, thermal fatigue and thermal shock are the most critical issues that have to be taken into account.

Thermal fatigue is caused by continuous change of stresses due to the cyclic thermal loads. During operational cycles, the material absorbs a certain heat flux and its surface temperature rises until steady state conditions are achieved. The fatigue may cause crack growth even to the heat sink. Due to the high heat fluxes impinging onto the first wall and the divertor, and simultaneously cooling from the heat sink, large thermal gradients will occur. After the cyclic operation, the resultant thermal gradients give rise to pulsed stresses, which may lead to the above mentioned thermal fatigue damage of the components.

Thermal shock in PFCs happens during intense transient thermal loads such as ELMs, plasma disruptions and VDEs. Thermal shock generates thermal stresses and takes place in case of steep transient temperature gradients [29]. Ceramics and metals show different behavior under thermal shock conditions. In particular, the ductile metals show completely different response. Brittle materials like ceramics and metals below DBTT (ductile to brittle transition temperature) cannot endure high strain and experience significant damage under thermal shock. In contrast, metals above DBTT are ductile and withstand the high thermal strains and the damage under thermal shock loads.

Due to the intense energy deposition during these events, the PFMs will be heated up to several thousand °C. The combination of thermal fatigue and thermal shock may cause even stronger and critical erosion. Another concern is residual stresses in the joints between

PFMs and heat sink due to the difference of coefficients of thermal expansion (CTE) and other different thermo-physical properties.

1.5 Scope of the work

To guarantee the lifetime of PFCs, thermal erosion is a serious problem. Thermal erosion and redeposition mainly take place under intense transient thermal loads such as ELMs, plasma disruption, or VDEs. The heat fluxes under these thermal loads are up to 1000 times higher than during the normal operation and the PFMs are damaged irreversibly, especially divertor parts. The PFMs in the divertor are subjected to heat fluxes of 5-10 MWm^{-2} during operational cycles, 2-5 GWm^{-2} for 0.2-0.5 ms (1-2 Hz) during ELMs, 1-10 GWm^{-2} for 1-5 ms during plasma disruptions, and 200-600 MWm^{-2} for 100 to 300 ms during VDEs [18, 6, 8, see also Fig. 3]. Single off-normal event may result in an erosion of up to 100 μm depth after plasma disruption [30, 81], 0.2-1.5 mm after VDEs [31, 32]. Each individual ELM does not cause significant damage in PFCs. However, as ELMs are expected to occur at a repetition rate of 1-2 Hz, one million ELMs in ITER may provoke serious damage. In order to estimate and to improve the lifetime of PFCs, it is important to understand the mechanisms of thermally induced damage during intense transient thermal loads. A precise quantification of the erosion further allows to define the lifetime of the PFMs.

Several systems are available to simulate experimentally the different earlier introduced energy deposition modes. Simulation experiments have been performed in electron beam facilities under intense transient thermal loads, such as plasma disruptions, and VDEs. Other beam facilities are ion beams, IR (infrared) heaters, and plasma accelerators [33, 34]. Fig. 3 compares the relevant thermal loads during normal and off-normal operation to the operation regimes for different high heat flux test facilities. The plot assigns the assumed constant power deposition per square unit over the event duration. For the larger events, the product of power density and pulse duration, giving the total energy deposition, after determining the material degradation.

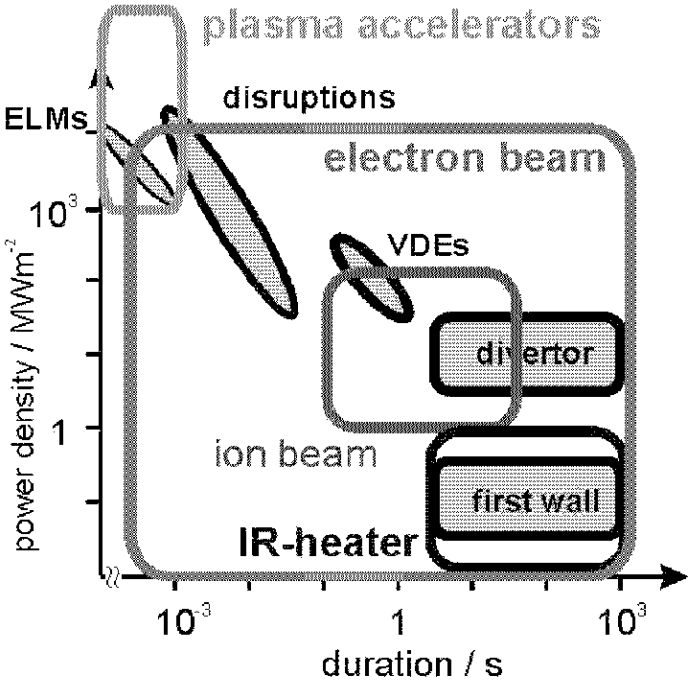

Fig. 3 Simulation of relevant thermal loads by different facilities [28,30, 81, 93].
-electron beam facilities : JEBIS, JUDITH
-ion beam facilities : Marion
-IR heater facilities : RITA
-plasma accelerators : VIKA, QSPA

Ion beam and IR heater facilities can simulate heat fluxes of normal operation. Power densities and pulse duration Δt required to simulate ELMs and plasma disruptions can not be realized. Plasma accelerators produce pulses in the range up to several hundred μs. Due to the loading with ions and the presence of a magnetic field, realistic simulation of ELMs and plasma disruptions can be performed.

The electron beam facilities cover these types of intense transient thermal loads with minimum pulse duration of 0.4 ms and up to maximum power density of 10 GWm^{-2}. Thus it is suitable for the assessment of material erosion under these conditions. These facilities further enable to conduct experiments on many specimens and allow quantitative analyses in single tests. In addition, it is possible to focus on the thermal effects of the materials. Also, small samples can be used because as thermal shock only affects the surface of the materials. Active cooling is not needed due to the extremely short pulse lengths. However, electron beam facilities cannot accurately simulate plasma-surface interactions because of a rather volumetric heating (penetration depth from several μm in high Z materials up to hundred μm in low Z materials for an acceleration voltage of 120 kV). Also the magnetic field in plasma has an influence on material degradation. Thus the plasma-surface interaction in a magnetized environment cannot be investigated by electron beam facilities. Furthermore, particle bombardment and chemical interactions can not be simulated by electron beams.

The aim of this work is to study the behavior of high Z and carbon based materials (CBMs) during intense transient heat loads using electron beam facilities as candidates for the divertor. Since there is almost no data of material behavior under ELMs conditions, it becomes very important to enable experimental simulation of ELMs. To do so, a careful calibration of the beam is necessary in order to control intense energy input during very short

pulses. Moreover, the effect of multiple events has to be studied because these events are expected to occur for a number of times.

Many experimental data were obtained from different test facilities in the past. However, these results showed discrepancies [35,36] at identical loading conditions. In order to find the reasons for the different results and to enable an evaluation of the data obtained from different test facilities, the comparison of material behavior by two electron beam facilities with different characteristics, JEBIS and JUDITH have to be carried out. Therefore, a calibration of the electron beam in the two facilities is necessary to determine the beam shape and widths. The conceivable factors from the different electron beam characteristics of the two facilities, which influence the erosion and crater formation, have to be analyzed at identical heat loads in terms of heat flux and pulse duration.

For refractory metals such as W, the melting, droplet formation, and the crack formation due to the brittleness (for T< DBTT) are the critical problems. W dust is a safety issue because W can be activated by neutrons. As the operation temperature in ITER will be 100-400 °C, the effect of preheating samples around DBTT (400-600 °C) has to be investigated especially with regard to crack formation. It should further help to optimize the material candidates.

Concerning CBMs, the combination of crack formation and the ejection of solid particles, so-called brittle destruction becomes critical issue in a sense that the ejected particles can react with tritium and form hydrocarbons. This is a serious safety issue because the redeposited hydrocarbons will increase the tritium inventory. Moreover, the particles contaminate the confined plasma and affect the fusion reaction due to radiation loss. In this study, the onset of brittle destruction, and the erosion mechanism of different carbon based materials will be investigated in combination with different particle emission scenario. Furthermore, the influence of preheating samples will be also investigated as the surface of carbon based PFM is supposed to operate at 100-1000 °C. Hence the effect of elevated surface temperatures has to be taken into account.

2 State of knowledge on plasma facing components (PFCs) and electron beam

2.1 Plasma-wall interaction

Interactions of hot fusion plasma with PFCs can cause irreversible damages and reduce the lifetime of the components. Ions and neutral particle loads on PFMs result in physical sputtering, chemical erosion, and radiation-enhanced sublimation. The most critical phenomena resulting from thermal and neutron loading are summarized below.

2.1.1 Surface damage

Physical sputtering

Physical sputtering is an atomization of materials by incident ions (deuterium, tritium, helium) [37, 38, 39,40]. Ejection of surface atoms arises if the atom energy is sufficiently high to overcome the surface binding energy. Self-sputtering is possible when the eroded ions return to the surface of the component. The yield of physical sputtering depends on the surface binding energy, incident ion energy, and the kinematical aspects of the momentum, such as incident angle of the ion particles. In addition, physical sputtering causes a roughening of the surface. The surface is modified in much smaller scale by hits of deuterium ions than by high energetic or heavy ion. The sputtering yield of W is lower compared to C.

Chemical erosion

Chemical erosion is a chemical reaction between incident ion particles and substrate atoms, producing binding volatile molecules [19,37]. In particular, hydrogen bombardment into CBMs, leads to the formation of hydrocarbons according to the following reaction;

$$nC + mH = C_n H_m$$

The chemical erosion mainly occurs in the temperature range from 300 to 700 °C. Volatile constituents are generated. Mostly the formation of methane (CH_4) leads to plasma impurities. Above 600 °C methane becomes instable and decomposition of methane may occur ($CH_4 = C + 2H_2$ or $4H$). At lower ion impact energy, the probability of C_2H_x, C_3H_x formation is higher than CH_4 [37]. The rate of chemical erosion depends on ion flux, and ion energy [41 - 47]. The maximum peak of methane yield is shifted from about 500 K for deuterium energy of 50 eV to 700 K for higher deuterium energy above 50 to 200 eV [37]. The chemical erosion yield of isotropic graphite increases linearly with the ion flux density and shows the peak at ion flux density of 10^{19} atom·m^{-2}s^{-1} [48].

Doping elements such as boron, silicon or titanium can reduce the chemical erosion by a factor of 5, due to the formation of a chemically and thermally stable carbide phases [49,50]. At temperatures above 1500 °C, the loss of the doping elements is increased, and the protection of the reaction is no longer effective for long operational cycles. However, the loss of the doping elements cannot be avoided during thermal shock, because the surface temperature can easily exceed the sublimation point of the dopants.

Radiation enhanced sublimation (RES)

Radiation enhanced sublimation (RES) is observed only in CBMs. RES involves a desorption of interstitial atoms through the displacement of carbon atoms caused by irradiation with energetic ion particles above 1200 K [50-53]. The resulting displaced interstitial atoms migrate to the surface with keeping their energy and momentum, and sublimate from the surface. Only monatomic C is emitted by RES, with energy distribution equivalent to the surface temperature, whereas in thermal sublimation, C_2 and C_3 are also emitted [52]. This effect represents the competing processes between sublimation of interstitial atoms from the surface and trapping in vacancies. At high vacancy densities, which accounts for highly irradiation material damage, RES is decreased in favor of thermal evaporation.

Doping with boron or silicon can help to reduce RES. However, at high temperatures, the dopants evaporate and leave the surface. A RES yield in the range from 10^{-2} to 10^{-1} carbon atoms per incident particle has been obtained at incident ion flux densities from 10^{19} to 10^{21} atoms·$m^{-2}s^{-1}$ with hydrogen ion energy (H^+, D^+) of 1 keV. The RES production yields increase exponentially with the reciprocal temperature. The activation energy of C atoms to leave the surface in the case of RES is 0.78 eV [53].

Evaporation

When a solid is heated up to high temperatures, some of the highly excited atoms will have enough energy to overcome the surface binding interaction. If these surface atoms have a momentum directed away from the surface, they will evaporate. The rate of evaporation can be estimated from the vapor pressure. For CBMs, the sublimation below 2700 K is negligible. For tungsten a noteworthy evaporation does not occur up to 3300 K. The evaporated material can form a vapor cloud close to the highly loaded PFMs and shields the components from further loading [83,134].

Redeposition

Metals may form droplets when they reach the melting and boiling points, and recrystallize as they cool down. For recrystallized surface materials thermal and mechanical properties depredate in most cases, which are not desirable for PFCs. CBMs do not melt but may sublimate or can be sputtered. Particles, might migrate into the plasma, react with hydrogen or other elements, and deposit again on the surface. Hydrocarbons layers on the surface entitled with hydrogen isotopes [54, 55]. If the hydrocarbon is produced from tritium, it would turn into a safety problem due to the tritium inventory. The retained tritium yield increases up to 850 °C. Redeposition is a very complicated phenomena due to the mitigation effect and reactions with different PFMs. Beneficial is that it increases the lifetime of the components. One detrimental effect is the increased tritium inventory.

2.1.2 Volumetric degradation

Influence after neutron irradiation

While ions of deuterium, tritium, and helium interact only with the surface of the material, neutrons penetrate into the bulk of the material. During irradiation by fast neutrons

($E \leq 14$ keV), the crystal structure of the materials accumulates defects. Through this impact process, atoms are hit from the lattice and cause interstitials [98, 56 - 62].

For CFCs, neutron irradiation induces mainly the degradation of thermal conductivity. It causes the displacement of carbon atoms from their initial position in the lattice to interstitial locations between two basal planes. Later the interstitials induce large dislocation loops or defect clusters, predominantly below 400 °C [98]. Above 1000 °C there is no degradation in thermal conductivity. After a neutron irradiation of 1 dpa (displacement per atom) at 200 °C the thermal conductivity decreases by a factor of 10 at room temperature and by a factor of about 4 at 800 °C compared to that of un-irradiated samples [63, 64].

Weight loss caused by thermal erosion under off-normal conditions of neutron irradiated CFC samples is about twice as high as the weight loss of un-irradiated samples [62]. The degradation of other properties such as Young's modulus, CTE (coefficient of thermal expansion), or dimensional changes is not significant, as long as the integrated neutron fluence do not exceed the above mentioned ITER specific valued of 1 dpa.

The main concern for metals like beryllium and tungsten is the brittleness, in particular after neutron irradiation. In combination with high heat fluxes, it might cause catastrophic damages such as crack formation and delamination [61]. For W and W-1% La_2O_3 , W-5% Re thermal conductivities decrease strongly below 800 °C after neutron irradiation [64]. The irradiation induced reduction of thermal conductivities is negligible over 800 °C.

Effect of helium bombardment (blistering, swelling)

The material can be damaged much more through mechanical damage processes than by physical and chemical processes at the conditions in a fusion reactor [65]. Helium also induces brittleness at high temperature as well as neutrons. The energetic particles invade into the material, and accumulate in the surface area. They interact with vacancies and clusters, and bubbles are formed. As a result, local swelling and degradation of mechanical properties occur.

2.2 Plasma facing materials (PFMs)

The main requirements for the PFMs with regard to plasma compatibility, thermal and mechanical properties, and neutron behaviors are listed in the table below.

Table 2 Main requirements for the PFMs.

plasma compatibility	low atomic number (to reduce radiation losses in the plasma) little out gassing good sputtering resistance low vapor pressure low tritium inventory
thermal and mechanical properties	high thermal conductivity high melting point high fracture toughness high thermal shock resistance
neutron irradiation behavior	low activation resistance against neutron induced degradation of material properties stability of joints
other properties	availability of materials low costs availability of joining techniques repairing possibilities

For the next step fusion device ITER two candidate materials have been chosen for the highly exposed areas within the divertor, namely carbon fiber composites and tungsten. Table 3 gives a summary of the pros and cons of the material properties.

Table 3 Pros and cons of candidate plasma facing materials; CFC and W.

	Material	
Pros	CFC	Good mechanical strength High thermal conductivity High thermal shock resistance Low Z number
	Tungsten	High melting point High thermal conductivity Low erosion rate Low swelling Low tritium retention Low vapor pressure
Cons	CFC	High erosion rate at elevated temperature Reduction of thermal conductivity after neutron irradiation Tritium retention Poor oxidation resistance Cleaning procedure necessary
	Tungsten	High Z number Poor machinability High volatility of the oxides. Neutron embrittlement High radioactivity High DBTT

2.2.1 Carbon based materials

Graphite materials have a low density, no melting point, a high sublimation point, and high heat of vaporization. Graphite crystals consist of sp^2 hybridized carbon layers stacked in an AB sequence and linked by van der Waals interaction [66 - 68] shown in Fig. 4.

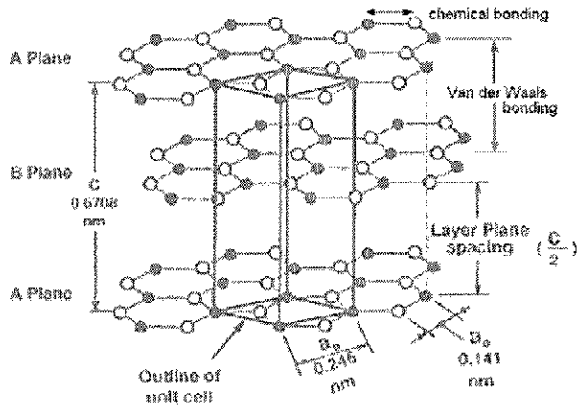

Fig. 4 Crystal structure of graphite.

Graphite is anisotropic due to its crystal structure and represents good electric and thermal conductivity within the layers which are connected by in-plane chemical bonding. But it has poor electrical and thermal conductivity between the layers. Due to its

characteristics and low cost, graphite is widely used in pencils, electrochemical electrodes, and wall parts in nuclear power plant. Other characteristics of graphite are its poor oxygen resistance, and chemically inert with acids, alkalis, and corrosive gas. Between 1000 and 1500 °C, graphite can react with hydrogen to form methane.

Most graphite products in industry are a mixture of carbon filler and organic binder. Petroleum coke is mainly used as carbon filler, and coal-tar pitch is used as organic binder [66]. Fig. 5 shows the manufacturing process of graphite.

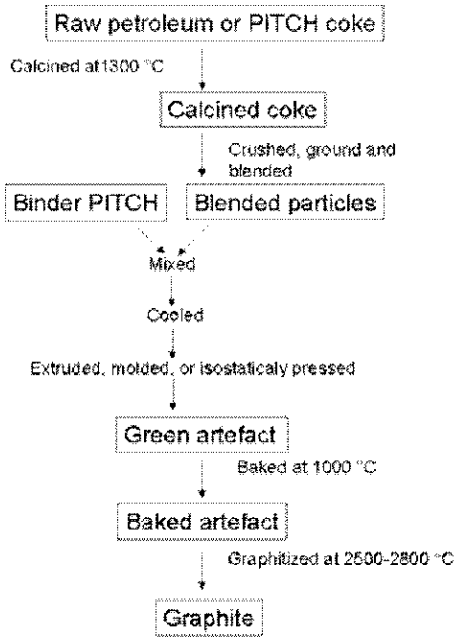

Fig. 5 Manufacturing process of graphite.

Coal tar pitch is hard, brittle and glassy. Filler and binder in optimized proportion with selected grain size by milling and sizing processes are blended with a large mixer. Each filler particle is coated with binder. Then isostatic molding is applied to get isotropic properties. The graphite is molded by pressure in every direction through a rubber membrane and acquires isotropic properties and uniformity. A wide range of graphite is available by choosing the size of the filler particles, the type of the filler and the binder, and the heat treatment.

Carbon fiber composites (CFCs) are composed of carbon fiber bundles embedded in a carbon matrix. These thermal and mechanical properties are better in fiber orientations, in particular when fiber bundles with high filament numbers are utilized. The manufacturing process of CFCs is shown in Fig. 6.

Carbon fibers are produced as a multifilament bundle, so-called tow with a number of hundreds to ten thousands of fibers. Each fiber is coated with carbon matrix. The liquid organic precursors of the carbon fiber bundles in CFCs are mostly PAN (poly acrylonitrile ($CH_2 = CHCN$)) and pitch fibers. PAN fibers have high tensile strength, and are produced through processes, spinning of the PAN co-polymer to form a fiber, stretching, oxidizing and stabilizing at approx. 220 °C under tension, carbonization in inert atmosphere at approx. 1600 °C, and graphitization at 3000°C. Pitch fiber is manufactured by the processes of polymerization, spinning, thermosetting, carbonization and graphitisation (heat treatment at

1200 to 1300 °C) to obtain fibers with high Young's modulus. The structure of pitch fibers can vary with spinning method and oxygen partial pressure. The crystallites can be changed by heat treatment. After the process of carbon fiber bundling, impregnation, carbonization, and graphitization is cycled for 5 times to manufacture the final products. Densification of the composites can be done after graphitisation by chemical infiltration.

CFCs have good mechanical properties at high temperatures. CFCs are available in 4 types of structure; discrete, linear (1D), laminar (2D) and integrated (3D). 3D CFC shows three directional weaving structures with three different fiber orientations [69]. The properties of CFCs are strongly related to the weaving structure (1D, 2D, 3D composites), machining procedure, and heat treatment [67]. CFCs have a high strength but are expensive to manufacture and type shapes are limited. Cracking of C-C fiber composites usually occurs in the direction parallel to the fibers. Cracks in the fibers might occasionally occur during the impregnation or in the manufacturing process [69]. Recrystallization can be also partially responsible for crack formation.

The needed quantity of CFCs for the ITER reactor is about 6300 kg. Today CFCs are mainly used in aerospace industry in brakes of space shuttles and airplanes. Therefore this required quantity for the ITER could be supplied by the present production capabilities in the world.

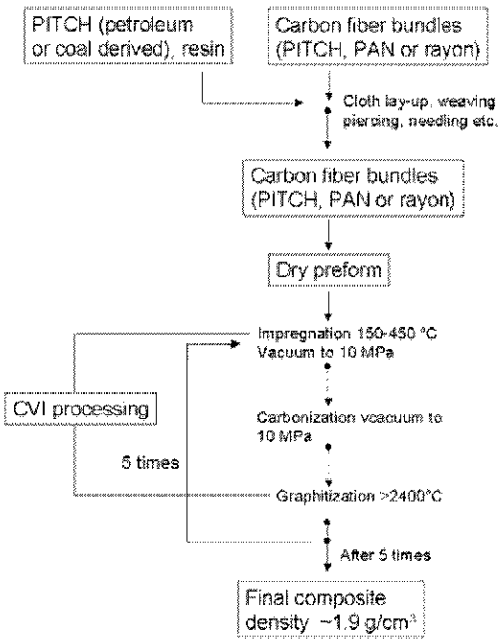

Fig. 6 Manufacturing process of CFC.

2.2.2 Tungsten

Tungsten (W) and tungsten alloys are manufactured by powder metallurgy (PM), casting, chemical vapor deposition, plasma spraying (PS), or sintering. The required amount of W for PFCs in ITER is ~ 85 t. This value stands for a small fraction of the world annual production. Consequently, sufficient W is available at industrial levels even if the additional W is necessary to exchange the reactor components [7].

W has good thermo-physical properties such as high melting point (the highest of all metals), good thermal conductivity, and low vapor pressure.

Disadvantages of tungsten are melting under intense transient thermal loads, poor machinability, high neutron activation, and high volatility of the oxides. Another point is that W is very brittle below DBTT (ductile to brittle transition temperature) with a relatively low CTE. Cracks might occur during thermal shock or thermal fatigue when W is utilized below DBTT in the range from 400 to 600 °C. The crack formation is critical, because as soon as the cracks propagate to the heat sink material, the whole component has to be replaced. To avoid the crack initiation, a macro-brush or lamella design is proposed [8, 32]. Moreover, the texture of tungsten alloys, i.e. the grains orientation and the anisotropy of the material have to be taken into consideration [70]. The DBTT varies with annealing temperature. Cracks do not form when the specimens are preheated above a DBTT of 600 °C. The DBTT increase after neutron irradiation.

It has been selected as material for the top part of the divertor and for the baffle. W is desirable because it has a lower sputtering yield compared to Be and CFC. This enables longer operation time. Another advantage is its low tritium retention.

2.3 *Interaction of electron beam with matter*

Intense transient thermal loads can be experimentally simulated by using various methods. Available facilities are electron beams [71, 72], ion beams [73], laser beams [74 - 76], neutral beams [77, 78], and plasma accelerators [79 - 83].

Plasma accelerators are good means to study surface and material interactions, but the possible loading pulse duration in the order of sub-microseconds are not sufficient. The laser beams are desirable to simulate plasma disruption-like conditions. For VDEs, they do not operate enough pulse duration and some improvements are required. Thus the following explanations concentrate on an electron beam.

When an acceleration voltage U_B is applied, electrons are accelerated in the electrostatic field of the beam source. They reach kinetic energy $E = eU_B$. At the point of beam impingement, interactions with the atoms of the matter convert the kinetic energy of the beam electrons into either heat, atomic or molecular excitation energy. A certain portion of the incident electrons will be backscattered (Fig. 7). In addition, secondary processes produce X-ray, secondary electron, and thermionic electron emission. The generated heat results in a rise of the surface temperature, heat conduction from the zone of energy conversion into the test sample, as well as heat radiation from the heated surface.

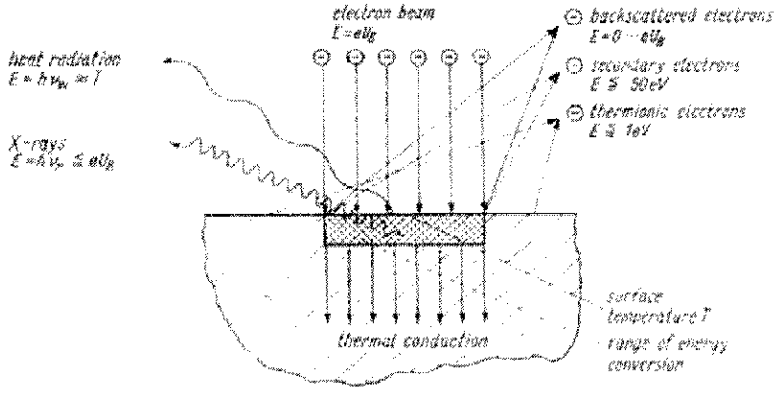

Fig. 7 Action upon electron beam impingement on matter [84].

The electron beam is suitable to simulate plasma disruptions and VDEs in terms of pulse duration and energy. Another advantage is the possibility to test small samples to perform screening test with relatively large number of different materials. It enables to multiple shot testing. Samples are easy to handle in electron beam facilities compared to ion beam facilities, plasma accelerators, and Tokamak reactors.

There are some drawbacks to use the electron beam for intense transient thermal load tests. On one hand, electron beam loading results in volumetric heating: the electron beam penetrates from several to 150 μm, whereas there is no remarkable penetration with the plasma accelerator. It may lead to underestimate the degree of erosion. On the other hand, the material reflects a certain fraction of incident electrons [84 - 86]. Both effects can result in overestimation of the thermal loads.

To reduce these drawbacks, scanning of the beam and measurements of the absorbed current, the acceleration voltage, and the pulse duration have been performed. Moreover, in the case that the absorbed currents are not monitored by oscilloscope, the reflection coefficients of the main candidate elements for PFCs have been taken from literature [84]. The data for acceleration voltage of 120 keV are shown in Fig. 8.

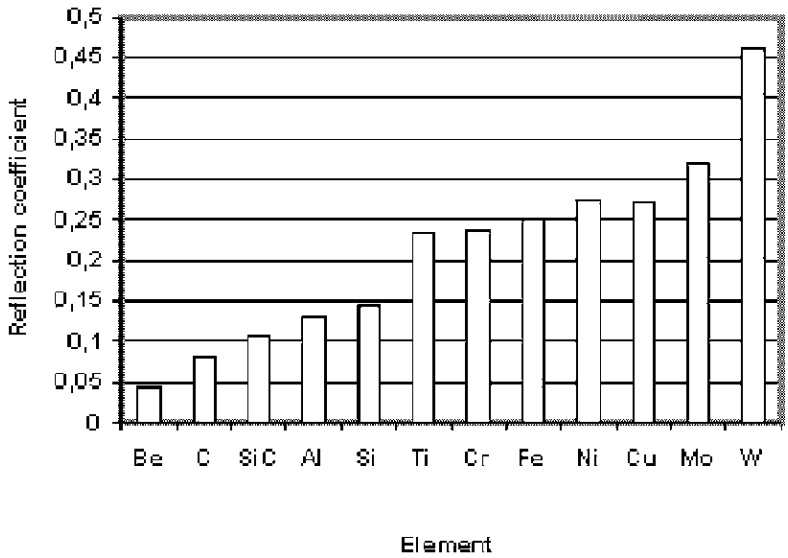

Fig. 8 Reflection coefficients of the main elements for plasma facing materials in JUDITH (Acceleration voltage = 120 keV) [84].

2.4 Modeling of material erosion by thermal load

Assuming no heat source in the bulk of the target material (q = 0), the case of a homogeneous material will be treated to determine the solution of a one-dimensional problem.

$$\frac{\partial}{\partial x}\frac{\partial T}{\partial x} - \frac{1}{a}\cdot\frac{\partial T}{\partial t} = 0 \qquad (1)$$

$$a = \frac{\lambda}{c_p \cdot \rho}$$

$$T(x,0) = 0$$
$$T(0,t) = f(t)$$
$$\lim_{x\to\infty} T(x,t) \to 0$$

a: isotropic thermal diffusivity [m^2s^{-1}]

The heat flux received from the surface is assumed to remain constant during the thermal loads and is taken as a boundary condition on this surface. The general heat equation that has been determined above is the initial point of this calculation.

$$j(x) = -\lambda \cdot \frac{dT}{dx} \qquad (2)$$

$j(x)$: heat flux at point x

$$\vec{\nabla}\lambda = 0$$

$$\frac{d^2 j}{dx^2} - \frac{1}{a}\cdot\frac{dj}{dt} = 0 \qquad (3)$$

With the boundary condition x = 0, t > 0 [87]

$$j(x,t) = erfc\left(\frac{1}{2}\frac{x}{\sqrt{at}}\right) \qquad (4)$$

$x = 0$: surface

a = thermal diffusivity [$m^2 \cdot s^{-1}$]

$$erf(x) = 1 - erfc(x) = \frac{2}{\sqrt{\pi}}\int_0^x e^{-\xi^2} d\xi$$

$$\xi = A \cdot \frac{x}{\sqrt{t}}$$

A = area [m^2]

The following equation provides the evolution of temperature in terms of pulse duration and depth of the material.

$$T(x,t) = -\frac{j(x,t)}{\lambda} = 2\frac{j(x)}{\lambda}\sqrt{\frac{at}{\pi}}\,e^{\frac{-x^2}{4at}} - \frac{j}{\lambda}\,x\,erfc\frac{x}{2\sqrt{at}} + T_0 \qquad (5)$$

For the surface, the evolution of the temperature follows a simple equation

$$T|_{x=0,t>0} = 2 * \frac{j_{surface}}{\lambda}\sqrt{\frac{at}{\pi}} + T_0 \qquad (6)$$

For two or three dimensional temperature distributions, a set of isothermal surfaces at a certain point in a cubic substrate can be written as the following equation [87].

$$Q_n = -\lambda\left(\frac{dT}{dx}\frac{dx}{dn}+\frac{dT}{dy}\frac{dy}{dn}+\frac{dT}{dz}\frac{dz}{dn}\right) \quad (7)$$

$\frac{d}{dn}$: differential along the normal to the isothermal surface

At the boundary, the temperature can be described as a function of space and time.

$$T(\vec{r},t)\Big|_{\vec{r}-\vec{r}_s} = T_s(\vec{r}_s,t) \quad (8)$$

When the heat flux comes to the surface, the boundary condition at a boundary surface $\vec{r} = \vec{r}_s$ and outward drawn normal vector $\hat{n}$ becomes

$$\lambda\left(\frac{dT}{dn}\right)_s = Q_n \quad (9)$$

For the numerical simulation of the material behavior during transient high heat fluxes induced by an electron beam facility, the following equations were applied with different phases (solid, liquid, vapor) and boundary conditions. Several parameters are taken into account, such as temperature dependent thermo-physical properties, volumetric heating, radiation, from the surface substrate.

3D transient (unsteady) time dependent heat conduction in solid state of carbon and metals [84,88] is described by the equation

$$\rho C_p \frac{dT}{dt} = \frac{d}{dx}\left(\lambda_x \frac{dT}{dx}\right)+\frac{d}{dy}\left(\lambda_y \frac{dT}{dy}\right)+\frac{d}{dz}\left(\lambda_z \frac{dT}{dz}\right)+Q(x,y,z) \quad (10)$$

$$Q(x,y,z) = P_v(z)\cdot dz \quad \text{for } (t \le t_{pulse}) \quad (11)$$

P_v : volumetric heat flux density [W·m^{-3}]
dz : depth step [m]
$z < R_m$, penetration depth [m]
V : acceleration voltage [V]
ε_{abs} : absorption coefficient

$$P_V(z) = P_{V,\max}\left\{1-\frac{9}{4}\cdot\left(\frac{z}{R_m}-\frac{1}{3}\right)^2\right\} \quad (12)$$

$$P_{V,\max} = \frac{4}{3}\cdot\frac{1}{R_m}\cdot\frac{V\cdot I_{inc}}{A}\cdot\varepsilon_{abs} \quad (13)$$

I_{inc} : incident current [A]
A : loaded area [m^2]

$$R_m = \frac{1}{\rho}\cdot 2.1\cdot 10^{-12}\cdot V^2 \quad (14)$$

V: (10 – 150 keV) [V]
ρ: density [kg·m^{-3}]

When the surface of the material reaches the melting and boiling points, the surface starts to melt and evaporate, and to sublimate in case of CBMs. For a better understanding of the thermal response of the materials, the different phases and interface conditions (solid-liquid, liquid-vapor, solid-vapor) have to be taken into account. These above mentioned boundary conditions are described below.

Solid-liquid interface of metals (Stefan boundary condition) [88,89]

$$\lambda(T_s)\frac{dT_s}{dn}\Big|_{\Gamma-0} - \lambda(T_l)\frac{dT_l}{dn}\Big|_{\Gamma+0} = \rho V_m \Delta H_m \quad (15)$$

$$\mu\frac{dv_x}{dz} = \frac{d\alpha}{dx} \quad (16)$$

n: outward drawn normal
ρ: density [kg·m^{-3}]
V_m: velocity of melt [m·s^{-1}]
μ: viscosity of melt [Pa·s]
ΔH_m : enthalpy of melting [J·kg^{-1}]
α: surface tension coefficient
Γ: position of the boundary surface

At the surface, solid-vapor interface for carbon and liquid-vapor interface for metals [88 - 91]

$x = x_L \quad T = T_0 \quad j = j(y,z,t)$

$x = x_s(y,z,t)$

$$-\lambda\frac{dT}{dx} = j(y,z,t) - \rho u_v \Delta H_v - j_{rad} \quad (17)$$

$$j_{rad} = -\varepsilon\cdot\sigma\left[(T_0)^4 - (T_k)^4\right]$$

$y = 0 \;\; T = T_0 \;, \;\; y = y_m \;\; T = T_k$

$z = 0 \;\; T = T_0 \;, \;\; z = z_n \;\; T = T_k$

u_v: velocity of the evaporated particles
ΔH_v : enthalpy of evaporation [J·kg^{-1}]
*for carbons ΔH_v of C_0 to C_5 clusters were taken into account [92]
σ: Stefan-Boltzmann constant
$5.67\cdot10^{-8}$ [W m^{-2} K^{-4}]
j (y,z,t) – heat flux at time (t) at position (y, z) [Wm^{-2}]

In the case of simulation experiments performed in the JUDITH facility, it's supposed to have some effects of electron beam scanning on the thermal behavior of the materials. The averaged heat flux during thermal loading with an electron beam sweeping are defined as following equations [88].

Definition of averaged heat flux

$$j_{av}(y,z) = \frac{1}{T}\int_0^T j(y,z,t)dt \quad (18)$$

T – pulse duration$j$ *(y,z,t)* – heat load at time (t) at position (y, z)

Definition of calorimetric heat flux:

$$j_c = \frac{1}{yz}\int_0^y\int_0^z j_{av}(y,z)dydz \quad (19)$$

irradiated area $(Y_1\text{-}Y_2)\times(Z_1\text{-}Z_2)$scanning frequency f_y =4 7 kHz, f_z = 43 kHzstarting position y = Y_1 = 0, z= Z_1 = 0

3 Experimental

In order to develop a better understanding of the material response under intense transient thermal loads, investigations have been carried out by electron beam facilities using various diagnostics. The detail of the test facilities and various diagnostics during (*in situ*) and after the thermal shock tests (*ex-situ*) are described below.

3.1 Test facilities

JUDITH

Electron beam facilities have been used for model experiments of intense transient thermal loads. They can experimentally simulate transient thermal loads such as plasma disruptions and VDEs in terms of power density and pulse duration. It also enables to conduct experiments on many specimens which allow quantitative analyses in single test. Most of the experiments described here were performed in the electron beam test facility JUDITH (Jülich Divertor Test Equipment in Hot Cells). A unique feature of JUDITH is the fact that it is located in hot cells. It enables to test neutron-irradiated specimens, which is essential to understand the neutron irradiation effects. A schematic view and a picture of JUDITH are shown in Fig. 9. JUDITH consists of the electron gun and applies magnetic coils to focus and deflect the beam. The electron beam is generated inside the electron gun. The electron generation is based on the emission of free electrons, their acceleration in an electrostatic field, and beam focusing, respectively, via magnetic and electric fields.

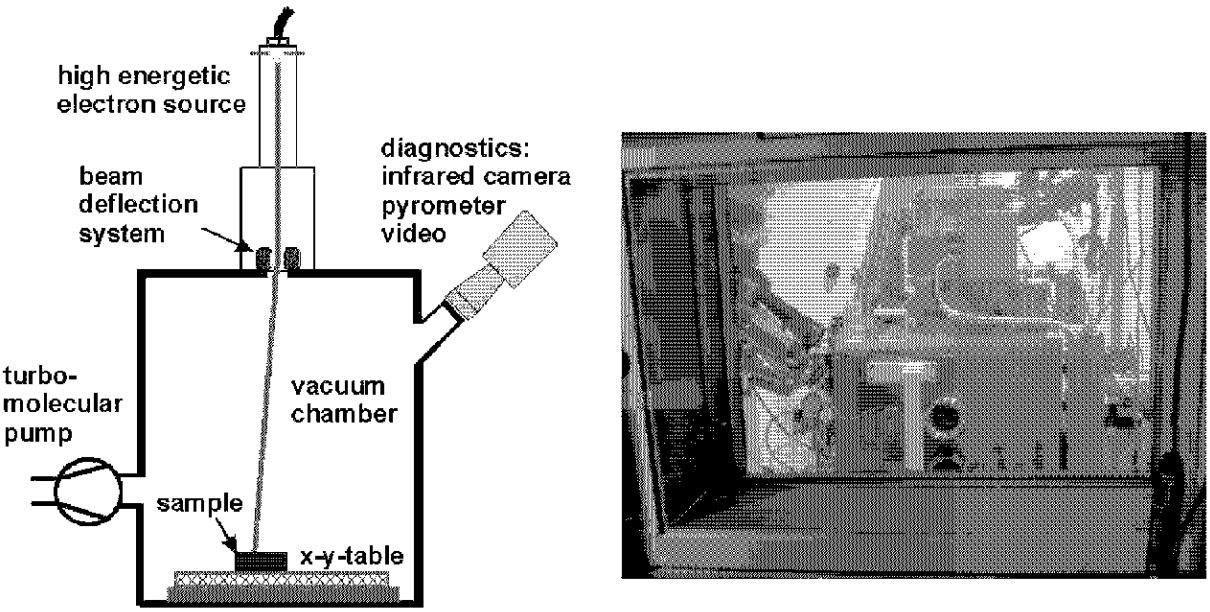

Fig. 9 Schematic view (left) and picture of the chamber (right) of JUDITH for transient heat load tests on non-actively cooled test samples.

The electron beam from a cathode type source is characterized by a relatively small beam diameter of ≥ 1 mm. The electron beam scans the specimen surface with the direction-dependent frequencies f_x = 47 kHz, and f_y = 43 kHz, respectively. It allows an almost homogeneous heating of the loaded area. The calculated electron beam tracks are shown in Fig. 10A. During transient heat load testing, the nominal acceleration voltage was set to 120 keV. A remarkable voltage drop occurs for pulse duration of several ten ms (Fig. 10B).

For VDE tests with 90 ms pulse duration, the mean voltage drop has been determined. The corrected acceleration voltage is 107 keV.

The generation and unrestricted propagation of the beam is only possible in high vacuum. Therefore it is necessary to evacuate the beam generator, the guidance systems, and the work chamber. The vacuum required in the beam-generating chamber is usually in the order of 10^{-2}–10^{-4} Pa. Generally it is around 2-4·10^{-2} Pa in the work chamber.

When the beam impinges on the matter to be investigated, the kinetic energy of the electrons is converted into various kinds of energy due to a series of elementary interaction processes. When the beam is utilized for melting, welding, evaporation, or thermal processing, only the released thermal energy is used. The main specification data of JUDITH are summarized in Table 4.

The holder on movable stage is composed of a brass or a pure copper plate. The samples are set on the holder and fixed with screws shown in Fig. 11. Between screws and the samples, a thin brass plate is applied to protect the samples by the force of screws from the side.

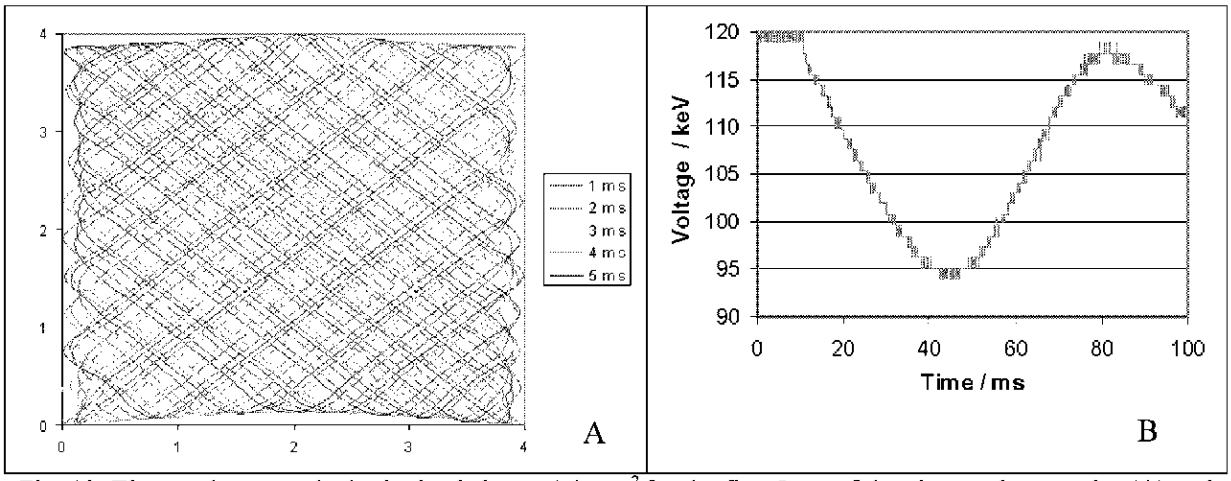

Fig. 10 Electron beam tracks in the loaded area 4·4 mm^2 for the first 5 ms of the electron beam pulse (A) and variation of acceleration voltage (nominal = 120 kV) with pulse duration from 1 to 90 ms (B).

Table 4 Main specification data of JUDITH facility for simulation of intense transient thermal loads.

Electron heat source	W cathode	
Vacuum chamber	800×600×900 mm^3 stainless steel	
System pressure in the chamber	≈2-4·10^{-2} Pa	
Beam deflection	±50 mm	
Beam power	≤60 kW	
Electron generator mode	capacitor	transformer
Pulse rise time	130 µs	> 0.5 s
Pulse duration	400 µs~90 ms	continuous
Scanning frequency (x,y directions)	0.1≤100 kHz	

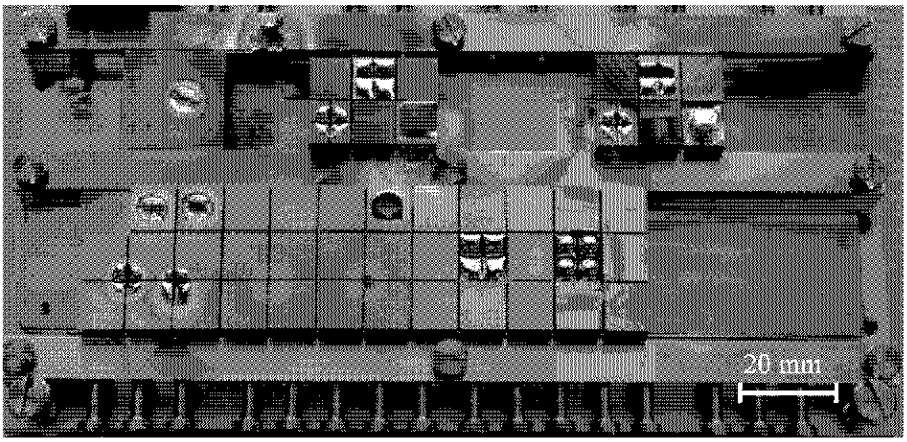

Fig. 11 W-1% La_2O_3 samples on a brass sample holder after VDE tests.

JEBIS

The second electron beam facility JEBIS (JAERI electron beam irradiation system, Japan) has been used to perform transient thermal load experiments and to compare JEBIS results with those obtained in JUDITH. A schematic view and a picture of the JEBIS facility are shown in Fig. 12. Here the electron beam is generated in a plasma discharge inside the electron gun. The electrons are extracted from the plasma using an extraction voltage ≤ 100 kV. The max. power in JEBIS is 400 kW, which is more than 6 times higher compared to JUDITH. The specifications of both electron beam facilities are listed in Table 5.

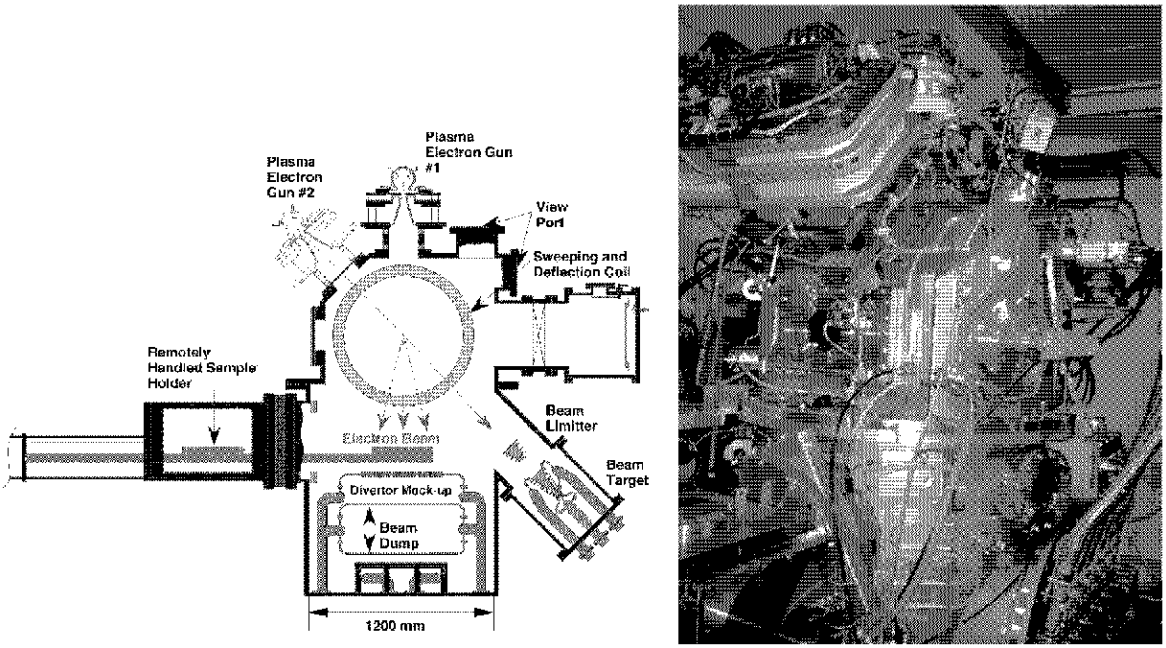

Fig. 12 Schematic view (left) and picture (right) of the electron beam facility JEBIS located at JAERI, Naka, Japan.

Table 5 Specifications of the two electron beam facilities.

	JUDITH	JEBIS
Max. voltage (kV)	150	100
Max. current (mA)	400	4000
Max. power (kW)	60	400
Max. loaded area (cm^2)	100	1800
Beam generation	thermal emission	plasma discharge
Beam spot	focused/ de-focussed	non-focused
Pulse duration (μs)	400 to continuous	500 to continuous

In JEBIS, the absorbed power density was measured by a calorimeter. The temperature and absorbed current were recorded before and after the shots. The calorimeter has a cylinder made of graphite or tungsten connected with a thermocouple and an aperture made of graphite with 5 mm in diameter. The mean absorbed energy density E_{abs} of the beam which passes through the aperture with a diameter of $d_{aperture}$ is given by the following equation:

$$E_{abs} = \frac{energy}{area} = \frac{m * C_p * \Delta T}{\pi * \left(d_{aperture} / 2\right)^2}$$

$[J \cdot m^{-2}]$

m: mass of calorimeter cylinder [kg]
C_p: specific heat of calorimeter cylinder [J/kg·K]
ΔT: temperature rise [K]
$d_{aperture}$: diameter of the aperture [m^2]

3.2 In-situ diagnostics

For diagnostics during transient heat loads in JUDITH (*in-situ* diagnostics), an oscilloscope, a fast pyrometer, and a digital camera have been utilized.

A resistor with 100 Ω applied to the specimen holder was used as grounding. With the oscilloscope, the absorbed current from the voltage drop was determined and the pulse duration during thermal loads were recorded. The principle is shown in Fig. 13

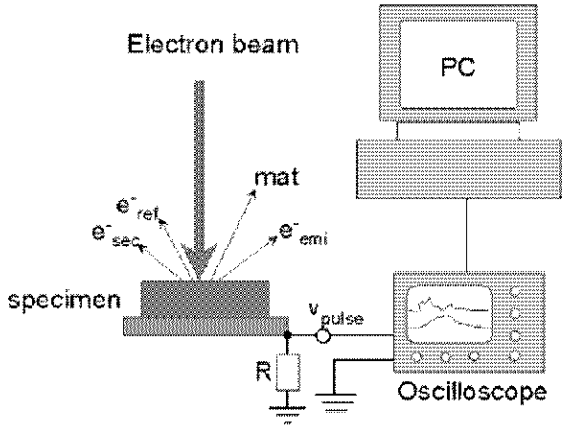

Fig. 13 Schematic diagram of current measurements.

The surface temperature after the shot has been measured by a fast pyrometer, or by a thermocouple connected to the samples [93]. A schematic presentation of the fast pyrometer is shown in Fig. 14 A. The optical sensor consists of a silicon photodiode with integrated

preamplifier to adjust the system; the laser target light is projected on the surface of the specimen using a beam splitter. The fast pyrometer is set in a 75-80 cm distance from the test samples; the focus point on the surface of the samples is about Ø 5 mm. The fast pyrometer has a time response of <15 μs and the surface temperature during transient heat loads can be measured precisely. It enables to determine surface temperatures above 1000 to 2500 °C according to the Stefan-Boltzmann equation:

$$j_{0,rad} = -\varepsilon_{rad} \cdot \sigma \cdot \left\{ (T_0)^4 - (T_{room})^4 \right\}$$

$j_{0,rad}$: radiated power density [Wm^{-2}]

ε_{rad} : emissivity

σ: Boltzmann constant; $5.6703 \cdot 10^{-8}$ [$W\ m^{-2}K^{-4}$]

T_0 : surface temperature [K]

T_{room} : ambient temperature [K].

For the calculation, it is necessary to have data on the thermal emissivity of the material, and the calibration of the temperature measurement for each material. A calibration of the fast pyrometer has been only done for graphite.

The digital camera Minolta Dimage R 3000 was used to detect emission of particles from the surface of the samples. The exposure time of the camera t_{exp} was longer than Δt; i.e. all particles emitted during the electron beam exposure were detected.

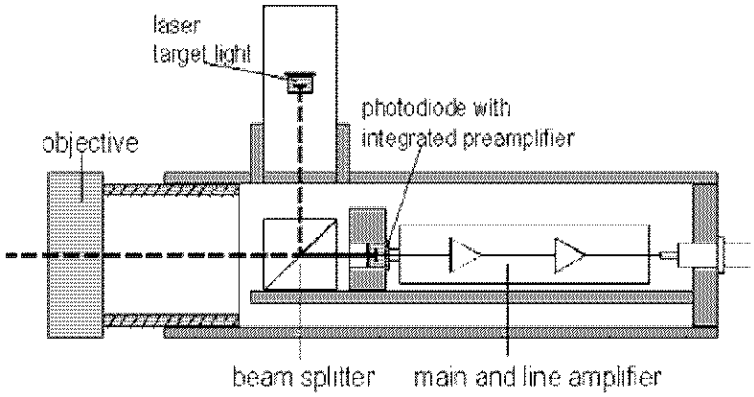

Fig. 14 Schematic presentation of the fast pyrometer [93].

3.3 Ex-situ diagnostics

Ex-situ diagnostics for characterization of the materials were applied using weight loss measurements, profilometry, scanning and transmission electron microscopy (SEM, TEM), ceramography, and metallography. Using these methods the eroded area, droplets, crack formation, crater depth, size of the recrystallized area, and adhesion can be determined.

Weight loss has been measured by a microbalance, Satorius MC210P. With weight loss data of the samples, it is possible to assess how much evaporation and sublimation occurs during the experiments quantitatively. The detection limit is 10^{-5} g.

Laser profilometry is produced by UBM GmbH. The measurement provides information about surface roughness of the samples such as pores and craters from 0.01 to 1000 μm in depth within an area of 50×50 mm^2. This method uses laser reflection on the sample. It enables to do very fine measurements, up to 2000 points / mm, 1-12 mm/s in scanning speed. A software package "SURFACEVIEW" evaluates the surface profile

according to the distance from a base line. It is very helpful to examine micrometer range of erosion or roughness of the surface. Examples of surface profiles are shown in Fig. 15.

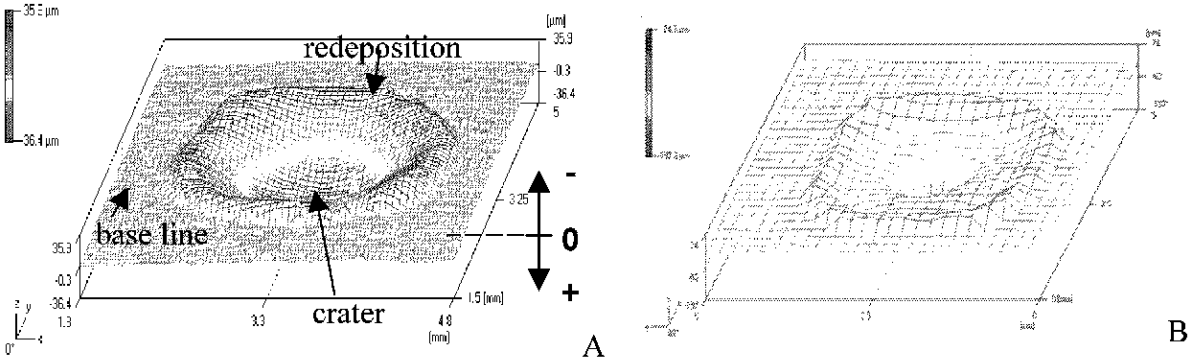

Fig. 15 Surface profiles of W sample (M168_8 at P_{abs} = 1.4 GWm^{-2}, A) and Ta sample (M27_27 at P_{abs} = 1.2 GWm^{-2}, B). I_{inc} = 160 mA, Δt = 4.4 ms

The SEM (secondary electron microscopy) images have been taken by Oxford instruments LEO 440, which is combined with an energy dispersive X-ray spectrometer ISIS 300 operating. The SEM has been used to perform observations of the surface and to determine characteristic modifications such as craters and crack formation, and recrystallization. The backscattered images enable to determine element distributions; heavier elements appear brighter than the lighter elements. The chemical composition is obtained by EDX (Energy Dispersive X-ray spectrometer) with a detection limit of 1 mass%.

The cross section images obtained by ceramography or metallography give information about texture and grain size of the specimens. Ceramography and metallography require several steps for sample preparation: cutting, mounting, grinding, polishing, and etching. After mounting of the sample, the specimens are grinded by SiC paper (80 or 120 up to 1200). The surface of the specimens is polished with diamond paste (1~6 μm). Finally the samples are etched by an acid solution, which contains 10 ml of nitric acid with 25 % concentration, 20 ml of peroxide with 30 % concentration, and 70 ml of pure water. After this preparation, the cross sections have been observed by microscope, and digital images were taken.

3.4 Materials

The materials used for the intense transient thermal load tests were carbon based materials, refractory metals (W, Mo, Ta), W-alloys, and reference metals (Al, Cu, stainless steel). Further details concerning producer and a brief description of these characteristics are given below. Typical material properties of these materials are listed in Table 8 [94 - 97].

3.4.1 Carbon based materials (CBMs)

CBMs used in the experimental campaigns are three different types; fine grain graphite, 3 directional (3D) carbon fiber composites (CFCs), and Si-doped 3D-CFC.

Table 6 Overview of carbon based materials tested in experiments

Material	Material No.	Producer
EK 98, isotropic fine grain graphite	11	Ringsdorffwerk: SGL Carbon group, Bonn
R6650, isotropic fine grain graphite	221	Ringsdorffwerk: SGL Carbon group, Bonn
NB31, 3D-CFC	219	SNECMA Propulsion Solide, Bordeaux, France
NS31, Si-doped 3D-CFC	220	SNECMA Propulsion Solide, Bordeaux, France

The isotropic fine grain **graphite** (EK98, R6650) exhibits a mean grain size of 7-10 μm. Within this grain size range, graphite products have superior properties such as high density, high thermal expansion, high strength, and low permeability compared to the graphite with larger grain size. In the experiments, isotropic fine grain graphite was used to reduce the deflection due to the anisotropy of graphite.

NB31 (3D CFC): This 3D CFC consists of ex-pitch fibers in x direction and ex-PAN fibers in y direction, and needling with ex-PAN fibers in z direction [97]. The volumetric fraction of the fibers is 35 % (27 % in x direction, 4 % in y and 4 % in z directions). The ex-pitch fibers have very good thermal conductivity and rather high Young's modulus. The thermal conductivity of x direction is 323 [W/m·K] at RT, which is 3 times higher than the other directions. This x direction is parallel to the heat flux. This 3D structure is densified with pyrocarbon through a CVI (Carbon Vapor Infiltration) process. The densified material is heat treated at high temperatures to enhance the thermal conductivity. The final treatment is densification with pitch coke. The total amount of impurities is less than 100 ppm.

NS31 (Si-doped 3D CFC): The fiber structure is the same as NB31. Si is one of the possible elements to dope graphite materials. In addition to carbon impregnation and heat treatment at a temperature beyond 2500 °C, NS 31 is densified by chemical infiltration with Si. Afterwards, liquid silicon is reacting with graphite under pressure leading partly to the formation of silicon carbide (SiC). NS31 contains about 8 % of silicon and its porosity is about 3-5 % [97]. The resulting material consists of a mixture of carbon, Si, and SiC. It reduces chemical erosion by hydrogen ions or atomic hydrogen. Chemical sputtering yield of Si-doped CFC (NS31) is two times lower than that of un-doped CFC [98].

3.4.2 Metals

Table 7 gives an overview of the tested metals; the specification number used in this thesis and the producer for each product. Further information is given below.

Table 7 Overview of metals tested in the experiments.

Material	Material No.	Producer
Al	M57	
Cu	M16	
Stainless steel (1.4571)	M139	
W	M168	Plansee AG, Reutte, Austria
Mo	M20	Plansee AG, Reutte, Austria
Ta	M27	Plansee AG, Reutte, Austria
W <111>- 0.02% Re (single crystal)	M 133	Efremov Institute in Russia
W-5%Re	M103	Plansee AG, Reutte, Austria
W-26%Re	M39	Plansee AG, Reutte, Austria
W-1%La_2O_3	M104	Plansee AG, Reutte, Austria
W1%La_2O_3	M 129	Plansee AG, Reutte, Austria
W 0.2 mm lamellae-Monoblock Mock-up	FT84	Plansee AG, Reutte, Austria
W-1%La_2O_3 4 mm lamellae-Monoblock	FT89	Plansee AG, Reutte, Austria
W-carbide	M45	Plansee AG, Reutte, Austria
PS (plasma sprayed) W coating (1 mm) on Cu	M105	Dr. Mallener, FZJ
PS W coating (5 mm) on Cu	M105	Plansee AG, Reutte, Austria
PS W coating (500 μm) on C (graphite, EK98)		Plansee AG, Reutte, Austria

Al, Cu and stainless steel have been used as reference material (Ref. Table 8).

W has good thermo-physical properties such as high melting point (highest in all metals), good thermal conductivity, and the lowest vapor pressure. Disadvantages are poor manufacturing, high neutron activation, and high volatility of the oxides. Moreover it is very brittle under DBTT (400-600 °C) and low CTE.

W-1% La_2O_3 is a dispersion-strengthened alloy, prepared by powder metallurgy. DBTT is similar to pure W. But it has smaller grain size, higher recrystallization temperature, higher strength after recrystallization, and easier to manufacture at room temperature. La_2O_3 particles play an important role in controlling recrystallization and the recrystallized grains [12, 17]. These particles prevent the growth of secondary grains (grain boundary migration) during the recrystallization and strengthen the grain boundaries [17]. After recrystallization, W-1% La_2O_3 was superior mechanical properties compared to sintered W at low temperature. However, the erosion resistance is reduced due to oxygen in alloy. The melting point of La_2O_3 is 2300 °C, and the boiling point is 4200 °C (Ref. Tables 7-8).

W-Re alloy is considered in terms of a lower DBTT. W-5% Re has a high strength and an excellent recrystallization resistance, a good machinability, and a low DBTT (286 °C) [17, 99]. In fact, the DBTT becomes lower with increasing Re content. The DBTT is about room temperature for W-26%Re. Another interesting characteristic for W-Re alloy is the fact that the swelling of W at high dose rates is strongly reduced for all irradiation temperatures.

However the addition of Re reduces thermal conductivity and increases the activation due to neutron irradiation. Moreover, Re is expensive and the industrial availability is not sufficient.

Plasma sprayed tungsten is an attractive technique because of the high deposition rate, and coating thickness up to several mm. However, it is inferior in thermal shock behavior and other thermal and mechanical properties compared to sintered W. For example, the thermal conductivity of vacuum plasma sprayed (VPS) W coating is approximately 60 % of high purity sintered W [100]. The Young's modulus of plasma sprayed W decrease by a factor of 3 (VPS) to 7 (atmosphere plasma sprayed, APS) compared with the sintered W [101]. Furthermore, these properties differ drastically when different spraying processes and conditions have been used; nature of the spraying atmosphere, the thickness of the coating, the plasma arc gas, the size and velocity of the coating powder, the spraying distance, and the substrate surface preparation before coating deposition. The thermal shock resistance is affected by several factors; presence of microcracks, porosity, thickness of the coating, and the difference in CTE between the substrate and the coatings [100]. The other difficulty is an increase of thermal and mechanical stresses at the interlayer between W and Cu to cause delamination due to the different CTE values. In order to achieve a high quality of the plasma spraying samples, the optimization of the spraying parameters for a reduced porosity, a low level of oxygen and impurity contents, and reduction of stresses at the interlayer is required.

Single W crystals have a lower DBTT (~RT) compared to pure W, lower neutron embritterment, high thermal conductivity, is stronger against thermal fatigue damage, and has a more stable microstructure at elevated temperature. The disadvantages are the high cost of fabrication and a low industrial availability.

Mo is characterized as a high Z material, with a high melting point, high thermal conductivity, hardness and toughness [102].

Ta is also a high Z material, and possesses a high melting point. It is ductile up to approx. –200 °C despite its body centered cubic (b.c.c) lattice, and can be machined easily compared to the other b.c.c. metals (Mo, W etc.). It is inert with water and air at room temperature. At high temperatures, it can react with halogens (F, Cl. Br, I) or hydrogen to form tantalum halides and tantalum hydrides (Ta_2H).

WC is very hard with a high Young's modulus; 707 GPa. When it is mixed with Co, and calcined at 1400 °C, the hardness increases tremendously and it becomes one of the hardest compounds.

Table 8 Typical material properties of the different materials [94 -97].

Material	m.p./ °C	v.p./ °C	ρ g/cm^3	E / GPa	CTE K^{-1}	*C_p J/(kg*K)	λ W/m*K	ΔH_m kJ/kg	ΔH_v kJ/kg	ε	Remarks
Al	660.4	2494	2.70	70	27.4	900	247	397	10780	0.047	F.C.C
Cu	1085	2595	8.93	130	49.5	386	398	205	4729	0.022	F.C.C
Steel	1447		8.00	207		510	13				
Mo	2610	5560	10.22	329	2.1	276	142	270	5123	0.25	B.C.C, 900°C:recrystallization temp.
Ta	2996	5427	16.6	186	6.5	139.1	54.4	145-174	4160-4270	0.26	B.C.C, low DBTT
W	3410	5700	19.3	411	4.4	134	144	220	4680	0.34	B.C.C
W-1%La_2O_3			19.3	478	408	126	126				
W-5%Re			19.4	435	400	133	88.5 at 200 °C				low DBTT
WC			15.7	707	2.25	15.9					
Graphite*			1.85		5		90		23000	0.8	Grain size 7 μm, isotropic
CFC (NB31)			1.9	107 (pitch) 15 (PAN)	0.5 1.2 2.7	721	328.7(pitch) 144 (PAN)) 111 (needling)				3 directional CFC
Si-CFC (NS31)			2.0	120 (pitch) 55 (PAN) 40 (needling)	0.5 1.2 4.2	679.9	320 (pitch) 160 (PAN)) 116 (needling)				Si-doped 3 directional CFC
SiC	2830		3.2		2.9	690	67				β :low temperature, cubic

*Graphite: data from fine grain graphite R6650
*m.p.: melting point
* v.p.: boiling point
*ρ: density at room temperature
*CTE:coefficient of thermal expansion, at RT (20 °C) to m.p.
*C_p : specific heat
*λ: thermal conductivity at RT
*ΔH_m: enthalpy of melting
*ΔH_v. : enthalpy of vaporization
*ε: emissivity

Table 9 List of melting and boiling points (m.p., v.p., respectively) for the elements contained in stainless steel and W-alloys.

	Si	Cr	Mn	Fe	Ni	Re	La_2O_3
m.p. / °C	1414	1907	1246	1538	1455	3186	2300
v.p. / °C	2900	2671	2061	2861	2913		4200

3.5 Beam calibration in JUDITH and JEBIS

3.5.1 Introduction

The electron beam parameters such as profile, width, and spatial distribution of current are important for welding, material processing, and surface analysis.

The calibration of the beam in JUDITH and JEBIS was conducted to comprehend the characteristics of the beam facility. As the electron beam profiles depend on the applied power, it is important to calibrate electron beam under the prevailing loading conditions.

The beam parameters also play an important role to predict interaction of plasma with material during transient thermal loads. In particular, this is the case for the very short pulses. For example, under disruption simulation tests using electron beam facilities, beam parameters such as beam shape, pulse duration, power, and scanning frequencies, will have a significant influence on the resulting material damage. Therefore, a precise knowledge of the heat load parameters such as heat flux and energy density is necessary. This is also important for a comparison of the data from JUDITH and JEBIS with the different beam characteristics. The calibration of the beam to acquire the beam profile and the spatial distribution of the current density has been performed using several methods. [103 - 105].

In experiments, three methods; (1) a W-Cu sandwich sample, (2) a calorimeter, and (3) stainless foil packages were applied to find the beam shape and diameter at different power, and different focus modes in JUDITH. Moreover, a static beam focus for simulation of ELMs in JUDITH has been optimized. In JEBIS the method (2) has been applied.

3.5.2 Experimental procedure

The specifications of the electron beam facilities JUDITH and JEBIS are described in the experimental part (Chap. 3.1). For the calibration of the electron beam in JUDITH, three methods, a W-Cu sandwich sample, a calorimeter, and stainless foil package, are applied as described below (Fig. 16 - Fig. 17).

First method: Scanning W-Cu-W-Cu-W sandwich sample with the electron beam, the transition of scanning on the surface of W to Cu, or Cu to W. The absorbed current gradually changes higher, or lower due to the different reflection coefficients of W (46 %) and Cu (27 %). The W-Cu-W-Cu-W sample had a total length of 25 mm with a length of 5 mm for each element as shown in Fig. 16. The scanning of the sandwich sample was performed at the incident current in the range of 10 to 320 mA and at acceleration voltage of 120 kV. The resulting absorbed current profiles were compared with a fitting curve (Fig. 21). This method allows the measurement of one-dimensional profiles using our electron beam, which is scanned with frequencies of $f_x = 1.1$ kHz, $f_y = 0.9$ kHz. The fast beam scanning in x-, and y – direction, has been used to distinguish the incident energy over a longer surface area of the sandwich sample to avoid surface melting. This method is the only one which is able to calibrate at high current up to 320 mA, because any melting of the measuring device can be excluded. For high currents of 160 and 320 mA, different scanning frequencies were applied at $f_x = 6.8$ kHz, $f_y = 1.1$ kHz in order to avoid critical power densities.

The second method: A holder with a measuring device for calibration of the beam was set up into the chamber in JUDITH, which is shown in Fig. 17. A schematic view is shown in

Fig. 18. A cylinder of W is fixed below Cu or W aperture of 0.5 mm or 1.0 mm in diameter. The Cu aperture is mainly used from 10 to 80 mA, and the W is used at higher currents, at 80 and 100 mA. A thermocouple is inserted into the cylinder fixed by graphite glue to keep good contact. The cylinder is grounded via a resistor of 100 Ω. The voltage drop along this resistor is measured by oscilloscope. The stainless steel cladding of the thermocouple is electrically isolated from the plate by ceramic plates. The thermocouple and oscilloscope with a resistor connected to the cylinder enable to measure both the thermal and the electric energy from temperature increase and absorbed current in the cylinder, respectively. It is a direct method to calibrate the beam profile by plotting the absorbed current as a function of scanning position. The position (x and y directions) where the electron beam was scanning was recorded simultaneously with the oscilloscope. This allows us the generation of 3D current distribution profiles. A 10 nF capacitor was set parallel to the resistor to maximize the S/N (signal to noise) ratio of the absorbed current. The very low frequency in one direction has been applied to cover a sufficient number of data points where the electron beam is scanning. The scanning frequencies are f_x = 0.63 kHz, f_y = 7.8 kHz or f_x = 6.8 kHz, f_y = 0.55 kHz. The loading area is 65 mm^2 for pulse duration of 20 ms and incident current up to 100 mA.

The third method: The stainless steel foil package was prepared with stainless foils of 0.1 mm thickness and spacer plates with a Ø 5 mm aperture and a thickness of 1.0 mm inserted between the foils and packed and fixed on the holder shown on the right side of Fig. 17. The power density distribution of the electron beam can directly be recognized from melting or break of the stainless steel foils. Two-focus modes were applied. One is standard focused mode (focus 1 = 290 mA, and focus 2 = 613 mA) and another one is defocused mode.

The experimental conditions to optimise the beam focus for the simulation of ELMs in JUDITH were incident current I_{inc} 50 to 80 mA for pulse duration of 20 ms with loaded area of 65 mm^2. The scanning frequencies were f_x = 6.8, f_y = 0.55 kHz and f_x = 0.63, f_y = 7.8 kHz. The (x, y) positions of the beam scanning were recorded together with the absorbed current and temperature. The FWHM (full width at half maximum) was taken from the 2D or 3D diagrams.

In JEBIS, a calorimeter array with 15 individual calorimeters has been used to determine the beam diameter. An oscilloscope with a 1 Ω resistor connected to earth was also installed to measure a voltage of absorbed current to the thermocouple. Over the holes of this plate W Ø 1 mm apertures were set to measure the spatial absorbed energy at the different positions. This method is the same principle as "the second method" as mentioned above.

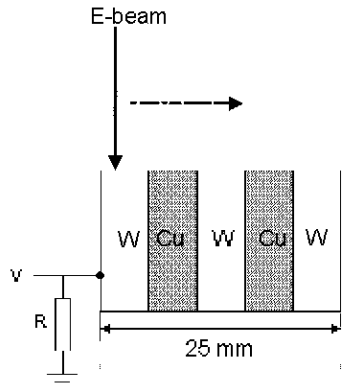

Fig. 16 Schematic view of a W-Cu sandwich sample (first method).

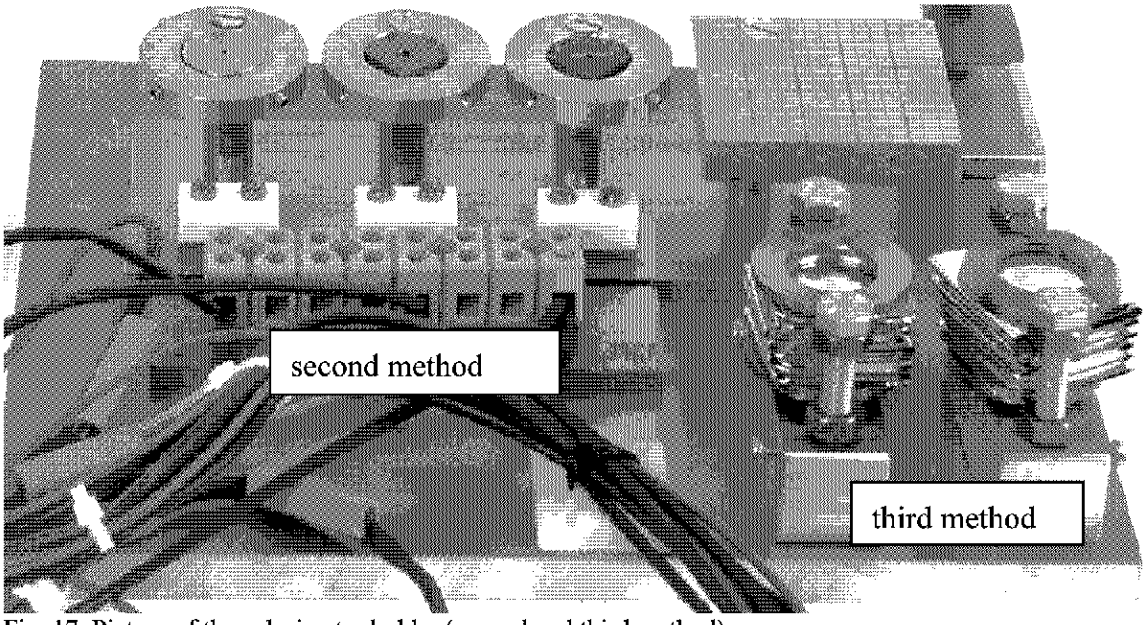

Fig. 17 Picture of the calorimeter holder (second and third method).

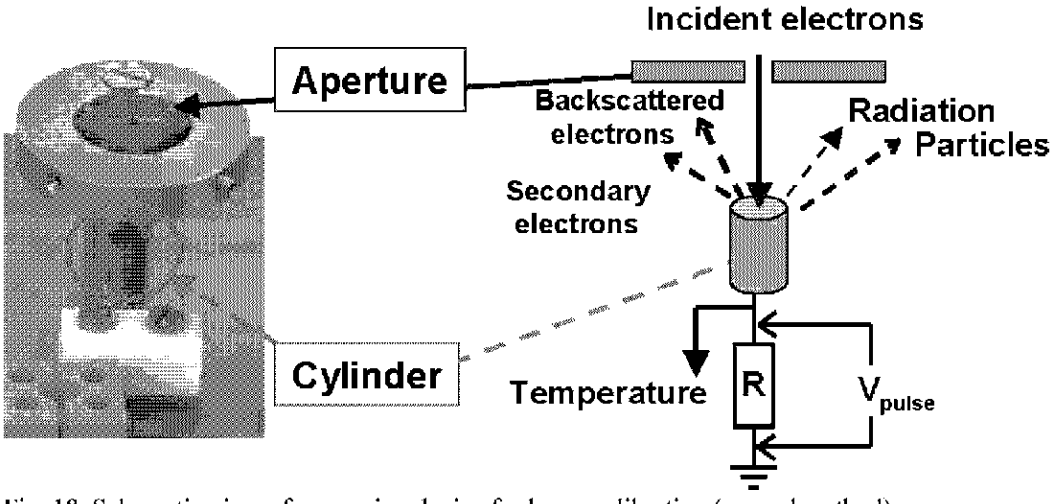

Fig. 18 Schematic view of measuring device for beam calibration (second method).

3.5.3 Beam profile of JUDITH

Full width at half maximum (FWHM)

"First method - W-Cu sandwich sample"

The higher absorbed current is from scanning of Cu part compared to W part due to different reflection coefficients (R) of Cu and W. Fig. 20 shows the absorbed current distributions as a function of the beam position for different incident currents. The reflection coefficients of Cu and W changed with different incident current, resulting in the different relative absorbed currents ($I_{abs}/I_{inc}\times 10$).

The integration of the Gaussian profile (Fig. 19) multiplying with (1-R) was used as a fitting of the observed curves (Ref. Fig. 8). The electron beam profile assumes to be Gaussian on the analogy of the electron microscope. A 75 % fraction of the incident current was absorbed onto copper and ca. 50 % onto tungsten making a trapezoid-shaped curve. For the calculation, a simpler Gaussian formula was applied as described in the following:

$$f(x) = \exp\left(\frac{-r^2}{2\sigma^2}\right)$$

r: radius
σ: sigma

For full width at half maximum (FWHM = F),

$$0.5 = \exp\left(\frac{-r^2}{2\sigma^2}\right)$$

$$2\ln(0.5) = \frac{-r^2}{\sigma^2}$$

$$r = \frac{F}{2}$$

$$F = 2\sigma \cdot (2\ln 2)^{0.5} \cong 2.35\,\sigma$$

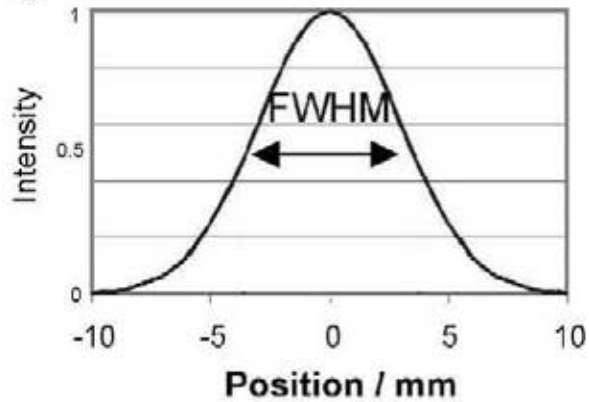

Fig. 19 Schematic view of Gaussian distribution

The resultant absorbed current profiles were compared with a fitting curve shown in Fig. 21. The measured curve of 20 mA in Fig. 21 corresponds to the fitting curve with FWHM between 1.75 and 2 mm. The precision of W-Cu method is ± 0.25 mm.

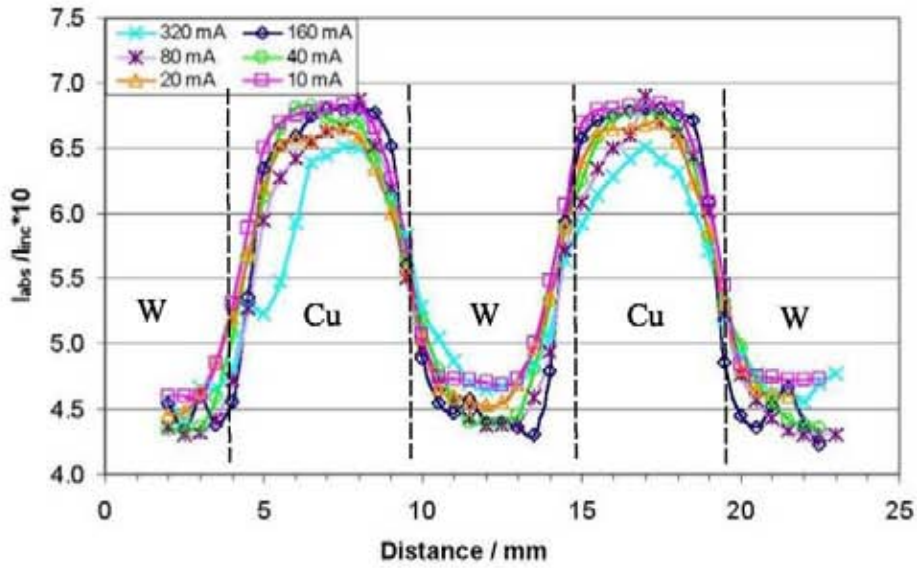

Fig. 20 Current absorbed by the sandwich sample for different incident currents in the range from 10 to 320 mA. The beam was scanned in a range from 2 to 23 mm..

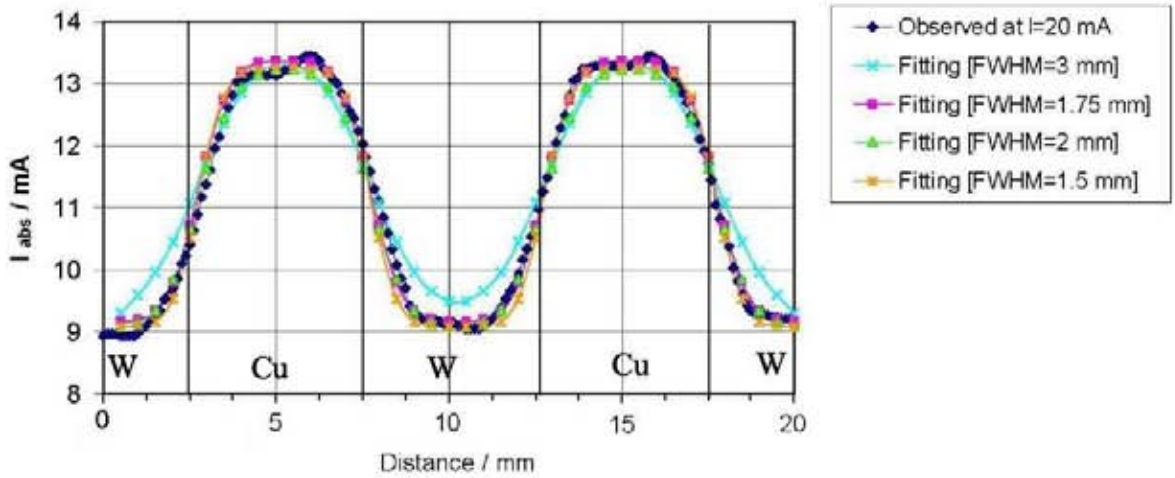

Fig. 21 Fitting of an observed curves loaded at an incident current of 20 mA with calculations applying different widths from 1 mm to 3 mm in FWHM.

"Second method - Measuring device with a cylinder and an aperture"

A current distribution of the electron beam was measured with an incident current I_{inc} in the range from 10 mA to 100 mA. The focuses of magnetic coils were applied with 290 mA for focus 1 and 613 mA for focus 2.

The beam diameter of electron beam shots using Ø 0.5 and 1.0 mm Cu aperture did not affect the result of the measured beam widths at 80 mA. For example, the FWHM of the beam profile loaded at 80 mA with scanning frequencies of f_x = 0.63 kHz, f_y = 7.8 kHz, the beam widths (FWHM) resulted in x = 0.50 mm, y = 0.90 mm for Ø 0.5 mm (Fig. 22) and x = 0.71 mm, y = 0.84 mm for Ø 1.0 mm Cu aperture. The differences of FWHM between these two apertures are acceptable for the calibration; ± 0.1 mm. This "second method" is more

precise compared to the "first method". Fig. 21 shows the spatial absorbed current distribution both in x, and y directions.

Fig. 23 shows the beam widths as a function of incident current, the observed beam profile is rather broad at low currents and the beam width becomes focused with increasing currents. The beam width for x direction at 10 mA is about 2 mm and decreases to 0.8 mm at 80 mA and 100 mA. The beam width for y direction is 2.7 mm at 10 mA and decreases to 1.1 mm at 100 mA. As a result, FWHM in y direction was slightly larger than in x direction. It indicates that the electron beam is not circular.

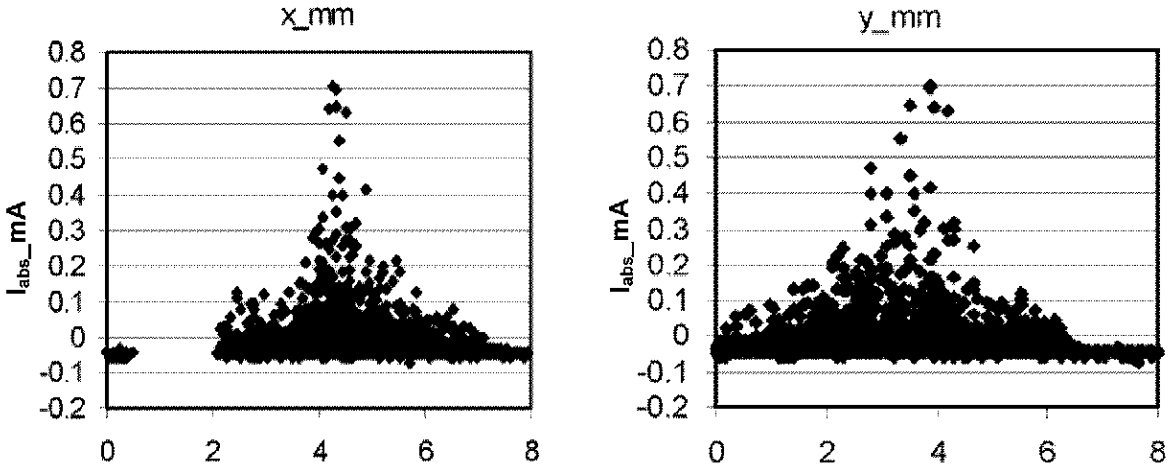

Fig. 22 Beam profiles of x (left) and y (right) axis at an incident current of 80 mA, and with scanning frequencies of fx = 0.63, fy = 7.8 kHz with a Ø 0.5 mm Cu aperture.
(focus 1 = 290 mA, focus 2 = 613 mA)

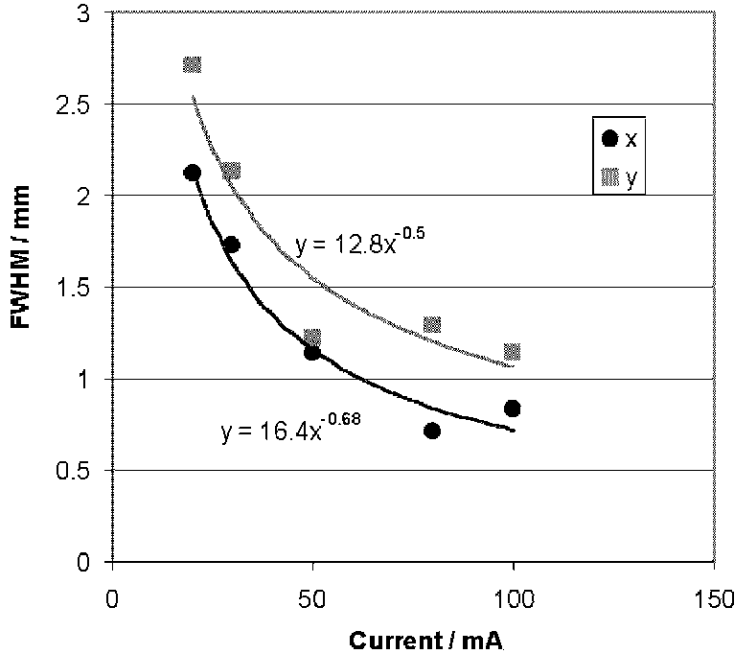

Fig. 23 FWHM as a function of incident current. Focus 1 = 290 mA, Focus 2 = 613 mA

Focus change

"Second method"

A standard focus mode of 290 mA for focus 1 and 613 mA for focus 2 has been applied for the fast scanning during intense transient thermal loads. To confirm whether the standard mode is well focused, the electron beam shot on the cylinder with an aperture have been applied with changing focuses. The absorbed energy and the beam profiles were compared with those for the standard focus mode. One focus of two magnetic coils was kept as the standard focus value and the other focus was gradually changed; in the range of 180 to 320 mA for Focus 1 in the first experiment and 360 to 913 mA for Focus 2 for the second experiment. Then the spatial current distribution in x and y directions was measured at incident current I_{inc} = 80 mA for pulse duration of 20 ms. The temperature increase and the current absorbed in the cylinder during the loading were also measured in the cylinder using a thermocouple and an oscilloscope, respectively.

Fig. 24 presents the variation of thermal and electric energy for different currents in the coils. The absorbed thermal energy and the absorbed electric energy are strongly correlated. The ratio of thermal to electric energy is in the range from 0.86 to 1.2. On the left side of Fig. 24, thermal and electric energy reach a maximum for focus 1 at 260 mA. Between 260 and 290 mA the thermal energy curve stays constant and decreases significantly above 290 mA (Fig. 24).

With focus 1 at 280 mA and 290 mA and focus 2 at 613 mA, the profile is better focused than the profiles with other focuses. Above 290 mA, two side peaks appear in x- and y-directions and over 320 mA the profile became defocused. In Fig. 25, three peaks are present in the beam profile with focus 1 at 320 mA and with focus 2 at 613 mA. This one big peak with two small peaks was also observed in the other electron beam facility, when it is not defocused in Fig. 26 [104].

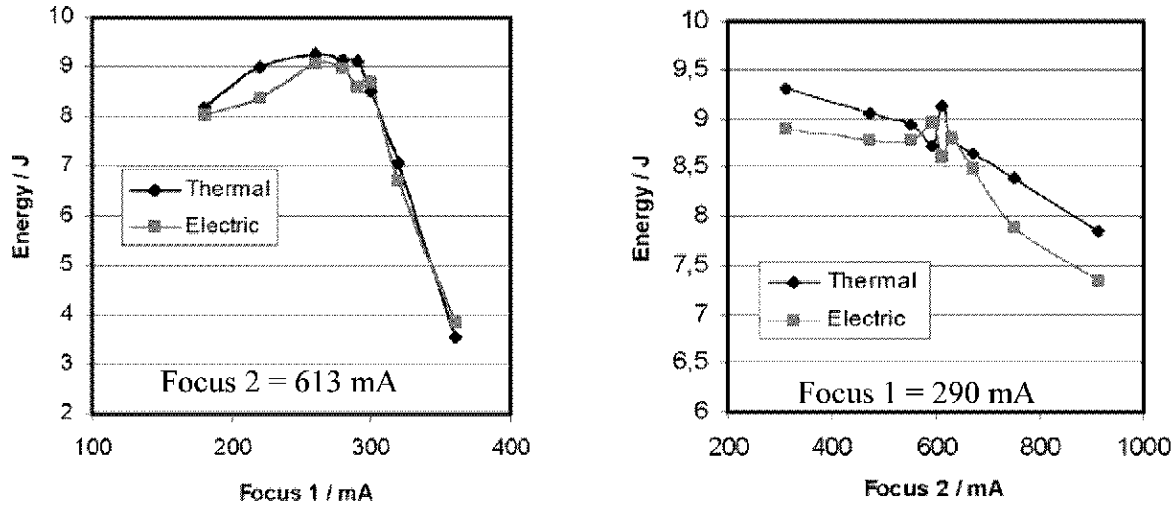

Fig. 24 Absorbed thermal energy and electric energy onto W cylinder at different focuses. (f_x = 5.5 kHz, f_y = 5.0 kHz, 2.0 mm W aperture, I_{inc} = 200 mA, V = 110 keV, Δt = 20 ms)

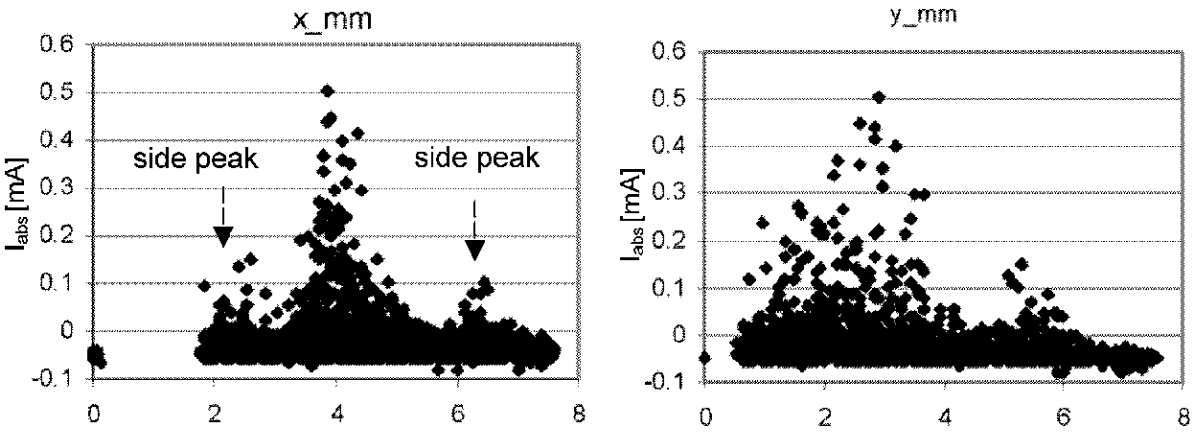

Fig. 25 Beam profile at an incident current of 80 mA, and fx = 0.63, fy = 7.8 kHz with a Cu aperture with Ø 0.5 mm. Focus 1 = 320 mA Focus 2 = 613 mA (JUDITH)

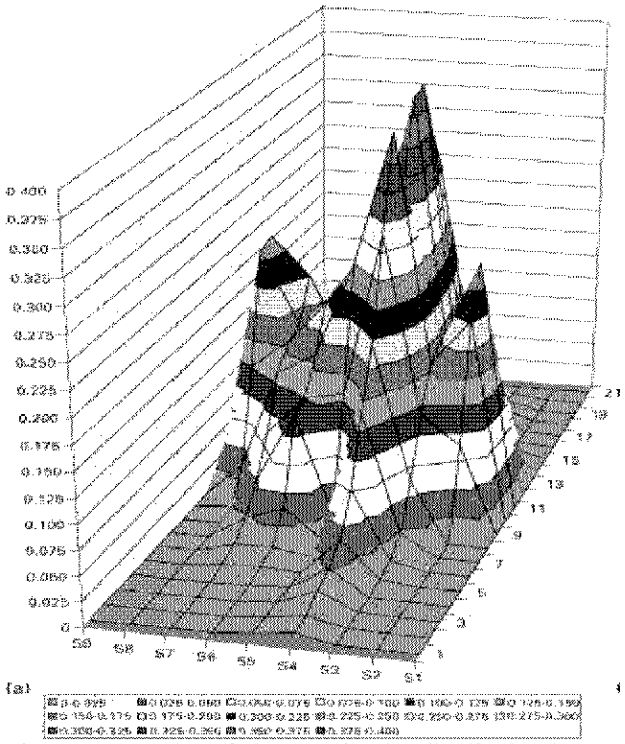

Fig. 26 Examples of electron density distribution in "non-symmetrical" electron beam: 3D profile with one big and two small peaks in electron beam at P_{inc} = 60 kV·30 mA = 1.8 kW and average power density ≈3.6 kWm^{-2} [Ref. S. Wojcicki and G. Mladenov 104].

"Third method"

Stainless steel foil experiments show the traces of the electron beam clearly with different focuses of the magnetic coils. Stereo microscope images are shown in Fig. 27. The pictures were taken from the top. This view allos to recognize how many foils were directly destroyed by the beam. The shape of the remaining edges at each layer reflects the shape of the electron beam. Loading conditions were chosen for the beam to penetrate the foil but not to destroy it completely. One test was 290 mA for focus 1 and 613 mA for focus 2 at I_{inc} = 20 mA for a standard focus mode, and another test was 360 mA for focus 1 and 613 mA for focus 2 at I_{inc} = 80 mA for a defocused mode. The shots were performed at static mode without scanning. For both focused and defocused modes, the electron beam penetrated four

foils. The diameters of the penetrated foils for focused mode are twice as large as those for defocused mode. The foil loaded with standard mode shows a "semi-triangle" shape and another foil loaded with defocused mode shows a "square" shape with smoothed corners. These images confirmed that the electron beam with standard focus mode is well focused in contrast to the defocused mode.

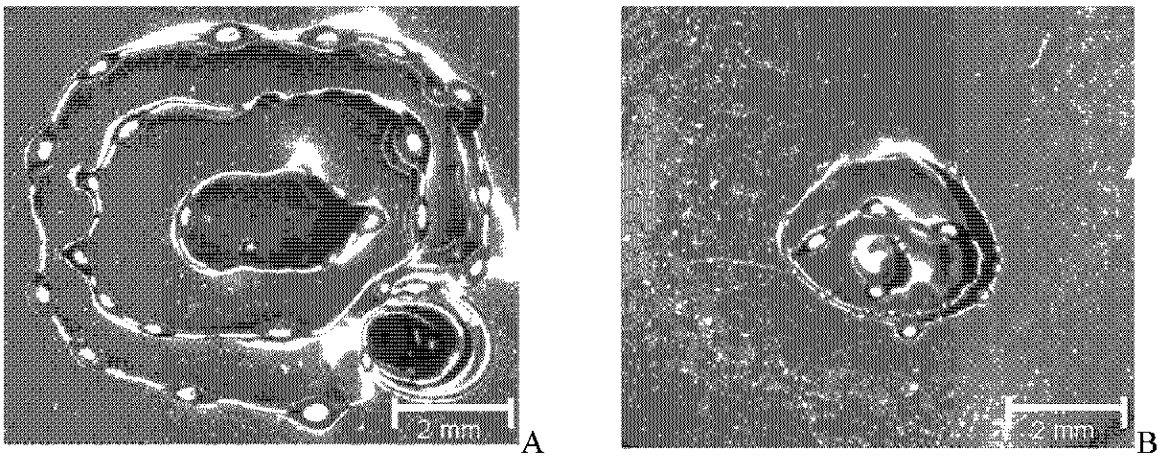

Fig. 27 Stereo microscope images of defocused (A) and focused (B) electron beam.
A: I_{inc} = 80 mA for Δt = 4 ms, focus 1 = 360 mA, focus 2 = 613 mA
B: I_{inc} = 20 mA for Δt = 4 ms, focus 1 = 290 mA, focus 2 = 613 mA

In the range of 260 and 290 mA for focus 1 and 613 mA for focus 2, the beam profile is focused and the absorbed energy is higher compared to the other focuses. With focus 1 at 290 mA and focus 2 at 313 mA the beam shows the highest thermal energy (Fig. 24 in the right) but the shape in y direction was defocused. The conditions with 290 mA for focus 1 and between 473 and 613 mA for focus 2 show focused profiles and have higher absorbed energy compared to the conditions with 290 mA for focus 1 and above 613 mA for focus 2 with the defocused profile in y direction. It is confirmed that the standard mode, that is 290 mA for focus 1 and 613 mA for focus 2, shows a focused beam profile and high-absorbed energy compared to the other focuses. It is no problem to keep this condition.

Optimization of static beam focuses for ELMs simulation

A measuring device with a Cu aperture of 1 mm in diameter (second method) was applied to optimize the defocused mode for ELMs conditions which is not focused as the standard mode, but does not show the side peaks. Because the thermal load under ELMs conditions with scanning electron beam in JUDITH is not homogeneously distributed over the loaded area for pulse duration of 0.5 ms (Ref. B. Bazylev 106). Spatial distribution of energy deposition at P_{abs} 1.0 GWm^{-2} for 0 - 0.2 and 0.2 - 0.4 ms by numerical simulation is shown in Fig. 28 (Ref. B. Bazylev 106). Some parts were locally more heated than other parts.

Fig. 29 shows the different surface morphologies of stainless steel samples loaded with different focus modes. The two focus modes; focus 1 = 320 mA, focus 2 = 633 mA, and focus 1 = 260 mA, focus 2 = 630 mA were chosen for defocused beams. The surface shapes are circular loaded at I_{inc} = 100 mA with focus 1 = 320 mA and focus 2 = 633 mA, square loaded at I_{inc} = 100 mA with focus 1 = 260 mA and focus 2 = 630 mA, and "quasi-triangle" loaded at I_{inc} = 50 mA focus 1 = 290 mA and focus 2 = 613 mA. The measured FWHM for defocused modes are listed in Table 10. The FWHMs turn out to be the smallest at standard

mode (Fig. 23) and the widest with focus 1 = 320 mA, focus 2 = 633 mA out of the three beam focuses.

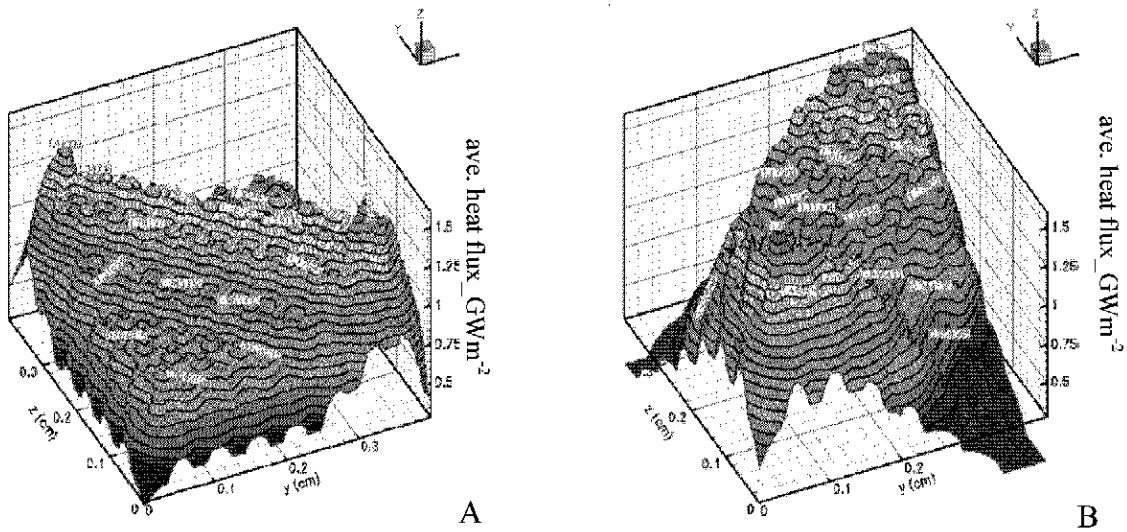

Fig. 28 Spatial distribution of energy deposition at P_{abs} 1.0 GWm^{-2} for 0 – 0.2 ms (A) and 0.2-0.4 ms (B) [Ref. B. Bazylev 106].

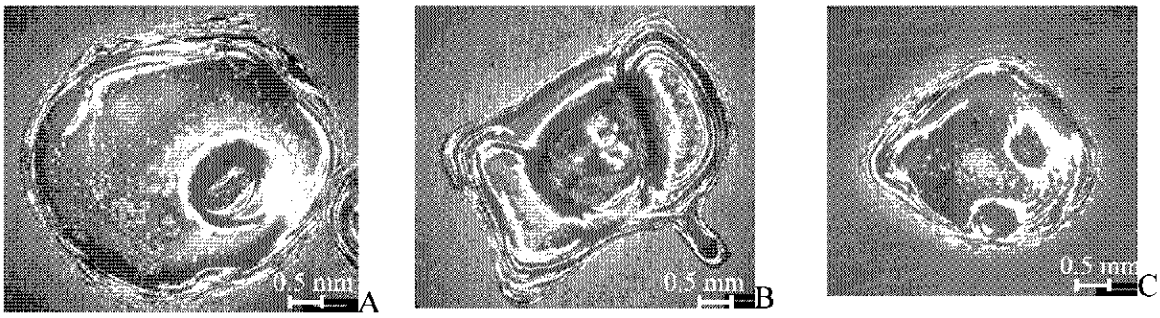

Fig. 29 Surface morphologies of stainless steel samples loaded with different focus modes in JUDITH.
A: I_{inc} = 100 mA with focus1 = 320 mA, focus 2 = 633 mA
B: I_{inc} = 100 mA with focus1 = 260 mA, focus 2 = 630 mA
C: I_{inc} = 50 mA with focus1 = 290 mA, focus 2 = 613 mA

Table 10 Measured beam widths, FWHM at 80 mA.

Focus 1 mA	Focus 2 mA	I_{beam} mA	FWHM_x mm	FWHM_y mm
260	630	80	1.27	1.49
320	633	80	1.72	1.96

Under the condition of focus 1 = 320 mA, focus 2 = 633 mA in electron beam is defocused, but the two additional peaks did not appear in the electron beam profile in Fig. 30. If it is more defocused, the two additional peaks arise (see Fig. 25). Thus it is possible to perform thermal load tests under ELMs condition using static mode with focus 1 = 320 mA, focus 2 = 633 mA of magnetic coils.

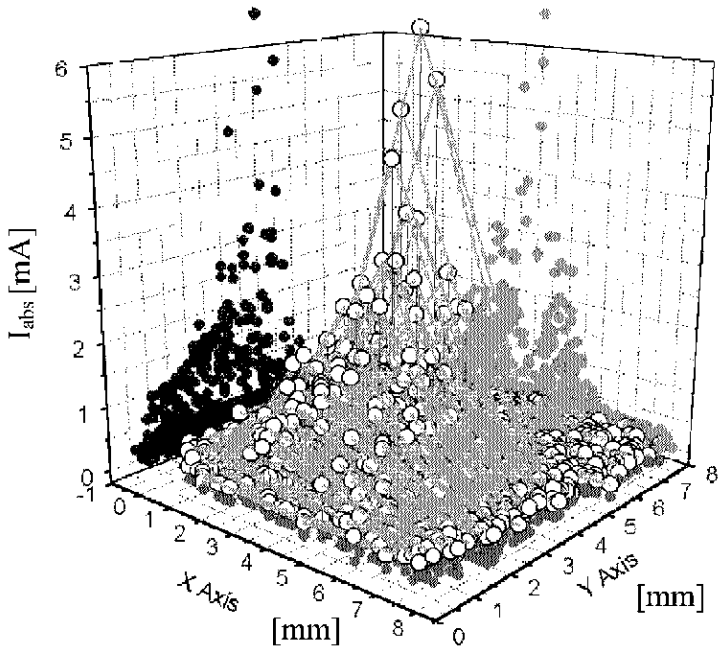

Fig. 30 3D profile of the beam absorbed on the measuring equipment with a cylinder and a Ø 1 mm Cu aperture at focus1 = 320 mA, focus 2 = 633 mA of magnetic coils.

3.5.4 Beam profile of JEBIS

The beam profiles were calibrated at 52 and 65 keV with pulse duration of 0.5 to 2.0 ms by measuring absorbed currents at different spots in both x and y directions with a distance between 0 and 7 mm from the center of the beam. The FWHM of the measured plots were determined by fitting with the Gaussian distribution. Examples of observed and fitting plots, which were loaded at 52 kV for 0.5 ms and 65 kV for 2 ms, respectively, are shown in Fig. 31. The FWHM of the beam is relatively wide for short pulses (0.5 ms) 4.5 mm at 52 keV and 2.8 mm at 65 keV, and becomes narrower into 2 mm for 2 ms at both 65 and 52 keV (see Fig. 32). At high voltages, the beam becomes more focused due to the Lorentzian force. It takes about 2 ms to reach a well-focused stage.

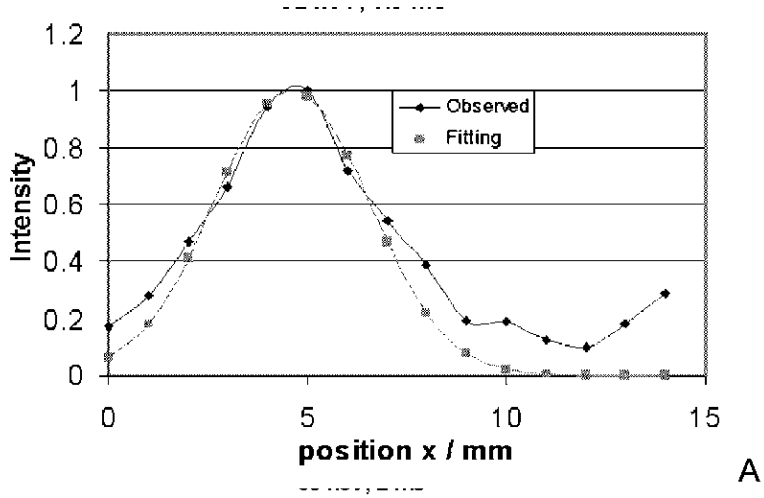

A

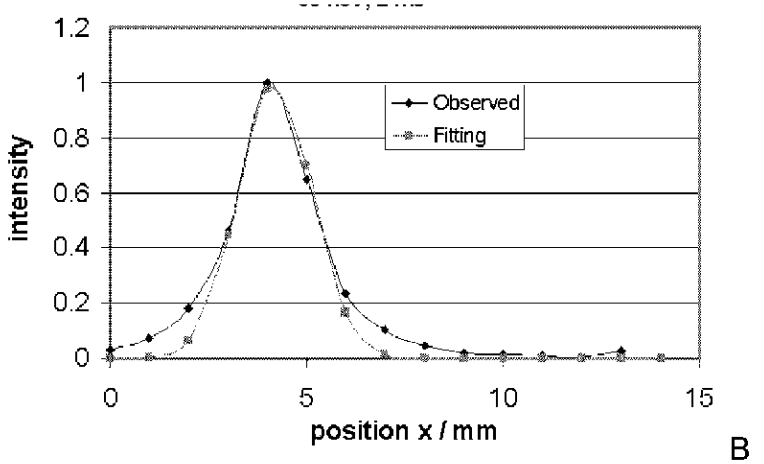

B

Fig. 31 Observed beam profiles and the Gaussian fitting curve in JEBIS at 52 keV for 0.5 ms (A) 65 keV for 2 ms (B) The fitting curve has been used to determine the beam width.

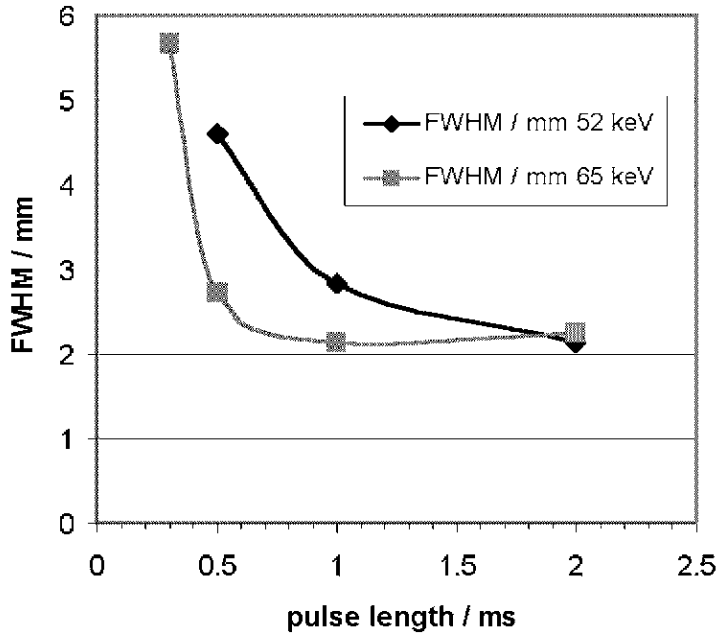

Fig. 32 Variation of FWHM as a function of pulse duration.

3.5.5 Conclusion

Calibration tests in the JUDITH facility show a strong dependence of the different beam profiles on the incident power. The beam width in x direction at incident current I_{inc} = 10 mA is 2 mm and decreases to 0.8 mm at I_{inc} = 80 mA. The beam shape turned out to be asymmetric; the beam width in y direction was slightly larger than in x direction. To maintain constant beam width, it is preferable to give electron beam shot with I_{inc} over 80 mA.

To enable simulation experiments of ELMs conditions, the defocused beam profiles in JUDITH were determined. In order to get high energy density and focused shape, 260 to 290 mA for focus 1 and 553 and 613 mA for focus 2 are favorable. For ELMs simulation experiments, 320 mA for focus 1 and 633 mA for focus 2 are selected.

The beam profiles were calibrated at 52 and 65 keV with pulse duration of 0.5 to 2.0 ms in JEBIS facility. At high voltages, the beam becomes more focused due to the Lorentzian force. It takes about 2 ms to reach a well-focused stage.

4 Results and discussion

4.1 Material degradation by intense transient heat loads

4.1.1 Introduction

For the assessment of the thermal behavior and for the estimation of the lifetime of PFMs, it is important to comprehend the mechanisms of material erosion. Typical material damage by thermal heat loads in metals is melting, crack and droplet formations [70, 80, 107, 108]. For carbon materials chemical sputtering [42, 109 - 111], sublimation, or solid particle emission [109, 111, 112] are the critical issues. However, the erosion mechanisms have not been fully clarified yet.

In order to evaluate the degradation of PFMs under off-normal events such as plasma disruptions and vertical displacement events (VDEs), model experiments have been conducted by electron [31, 113 - 115], laser [74 – 76], or plasma beam facilities [81, 82, 116]. However, the results from these different facilities are difficult to be compared due to different beam characteristics , especially under transient thermal loads [36, 115]. Model experiments for material erosion analyses under transient heat loads have been performed using the electron beam facilities JEBIS and JUDITH with identical heat loads.

The objectives of this campaign are described as follows; (1) comparison of material damage from JUDITH samples with that from JEBIS samples exposed to identical heat loads: absorbed power density and pulse duration, (2) analysis of mechanisms of molten flow of metals, (3) observation of particle emission or vapor cloud formation in JUDITH using digital imaging techniques, (4) investigation of the effect of surface polishing.

4.1.2 Experimental

The electron beam facilities JEBIS and JUDITH were used for transient thermal load tests. These electron beam facilities have a different power range, beam profile, and use a different beam-loading pattern (Table 5). The material erosion from these facilities was compared for identical absorbed power density and pulse duration. The loading conditions were typical disruption tests with absorbed power densities P_{abs} of 1.0 to 2.5 GWm^{-2} and pulse duration of 1.5 to 5 ms. The loading conditions are listed in Table 11 for JEBIS and Table 12 for JUDITH. The main difference between JEBIS and JUDITH is given by the application of the thermal loads. The loaded area in JUDITH is in the range of 14 to 37 mm^2 using scanning of the beam on the specimen's surface with frequencies f_X = 47 kHz, f_Y = 43 kHz to get a homogeneously loaded area. In JEBIS the thermal load was applied using a static beam with a FWHM of 2 to 6 mm (Ref. Chap. 3.5). The determination of the absorbed energy density for JUDITH is described in Chap. 3.2. The loading with and without an aperture on stainless steel samples was also performed in JUDITH. A static beam without scanning was applied for which the focuses were optimized by the calibration test (Ref. Calibration part). The two different apertures Ø 3, and Ø 5 mm were used. The apertures with Ø 3 and Ø 5 mm were made of brass, fixed with a pole to the sample holder was set 20 mm above the specimen (Fig. 43). The loading conditions are listed in appendix.

During the experiments, the pulse duration and the absorbed current were recorded using an oscilloscope connected with a resistor (100 Ω for JUDITH and 1 Ω for JEBIS). In JEBIS, the absorbed power density was mostly measured by a calorimeter. A fast pyrometer and a CCD camera were applied in JUDITH to measure the surface temperatures and to detect the emission of particles during thermal loads, respectively [Ref. Chap. 3.2].
The materials used for the experiments were pure aluminum, pure copper, stainless steel, pure tungsten, graphite (EK98), 3-D CFC (NB31), and Si-doped 3-D CFC (NS31). Dimensions are 12×12×5 mm^3 for JUDITH and 25×25×10 mm^3 for JEBIS samples.

Table 11 Loading conditions and results of thermal shock tests and results in JEBIS:

Sample ID	Materials.(1)	V kV	I_{beam} A	Δt ms	n(2)	Aperture	P_{abs} GW/m^2	E_{abs}(3) MJ/m^2	P_{abs}·sqrt(t) MJ/$m^2s^{-1/2}$	Δm mg	Δm / area(4) kg / m^2	Erosion(5) μm
11_375	EK98	65	2.36	1.5	1		1.69	2.5	65.4	1.70	0.150	122.85
11_376	EK98	65	2.44	1.5	1		1.57	2.4	60.7	1.68	0.148	116.77
11_377	EK98	52	1.72	2.63	1		0.97	2.5	49.7	0.74	0.073	63.91
11_378	EK98	52	1.70	2.76	1		0.97	2.7	50.9	0.74	0.073	68.08
11_380	EK98	65	2.26	1.51	1	W: 5mm	2.37	3.6	92.1	2.43	0.214	114.1
11_381	EK98 pol.	65	2.22	1.51	1	C: 5mm	2.37	3.6	92.1	1.53	0.134	
11_382	EK98 pol.	65	2.18	1.65	1		2.36	3.9	95.8	1.39	0.123	116.5
219_1	NB31	52	1.68	2.96	1		0.879	2.6	47.8	0.56	0.056	50.15
219_2	NB31	65	2.22	1.49	1	C: 5mm	2.37	3.5	91.5	0.98	0.086	40.17
219_4	NB31 pol.	65	2.20	1.7	1		2.07	3.5	85.5	1.35	0.119	54.64
219_5	NB31 pol.	65	2.12	1.48	1	C: 5mm	2.02	3.0	77.7	1.22	0.107	77.43
220_1	NS31	52	1.68	3.21	1		0.853	2.7	48.3	1.07	0.105	75.81
220_2	NS31	65	2.14	1.89	1	C: 5mm	2.32	4.4	100.9	1.19	0.105	96.75
220_4	NS31 pol.	65	2.10	1.65	1		2.31	3.8	93.7			123
M57_27	Al	65	2.14	5	1		1.65	8.3	116.9	71.09	6.269	
M57_28	Al	65	2.08	5	1	W: 4mm	1.93	9.7	136.5	39.99	3.526	
M57_25	Al	65	2.36	2	1		2.21	4.4	98.9	8.49	0.748	
M57_26	Al	65	2.36	5	1		2.00	10.0	141.4	38.82	3.423	
M16_76	Cu	65	2.32	5	1		1.68	8.4	118.8	5.60	0.494	
M139_1	1.4571	65	2.32	2	1		2.06	4.1	92.2	3.95	0.349	375
M139_2	1.4571	65	2.36	5	1		1.73	8.6	122.1	12.37	1.091	
M139_3	1.4571	65	2.20	5	1		1.65	8.3	117.0	11.14	0.982	530
M139_4	1.4571	65	2.14	5	1	W: 5mm	1.61	8.1	113.9	14.25	1.257	1168
M139_6	1.4571	65	2.24	5	1							
M168_1	W	65	2.36	5	1		1.24	6.2	87.4	3.15	0.278	478.4
M168_2	W	65	2.36	2	1		1.36	2.7	60.6	0.70	0.062	
M168_4	W	65	2.02	5	1	W: 5mm	1.19	6.0	84.4	10.85	0.957	

1. pol. = surface of the sample is polished, 2. n = number of shots,
3. $E_{abs} = \Delta m \cdot C_p \cdot \Delta T/\pi\ (d_{aperture}/2)^2$, Δm: weight loss, C_p: specific heat, ΔT: temperature rise, $d_{aperture}$:diameter of aperture
4. Erosion = crater or erosion depth
5. Δm /area = weight loss/$[\pi \cdot (2\pi)^2]$ (2π is obtained from FWHM values in Chap. 3.5.4 assuming that the JEBIS beam has Gaussian distribution)

Table 12 Loading condition and results of thermal shock tests and results in JUDITH.

Sample ID	Material	V kV	I_{abs} mA	Δt ms	n(1)	Area mm^2	P_{abs} GW/m^2	E_{abs} MJ/m^2	P_{abs}·sqrt(t) $MJ/m^2s^{-1/2}$	Δm g	Δm / area kg / m^2	Erosion(2) µm
11_392	EK98	120	313	1.7	1	15.20	2.5	4.2	101.8	-1.00E-05	-6.58E-04	0
11_393	EK98	120	299	1.76	1	15.20	2.4	4.2	99.0	-5.00E-06	-3.29E-04	0
11_395	EK98	120	297	2.71	1	36.60	1.0	2.6	50.7	-2.00E-05	-5.46E-04	0
11_396	EK98	120	306	3	1	15.20	2.4	7.2	132.3	4.00E-05	2.63E-03	0
219_74	NB31	120	329	1.70	1	17.37	2.3	3.9	93.8	-1.00E-05	-5.76E-04	0
219_75	NB31	120	298	3.00	1	41.64	0.9	2.6	47.1	2.50E-05	6.00E-04	0
219_76	NB31	120	306	3.03	1	17.37	2.1	6.4	116.3	-5.00E-06	-2.88E-04	107.67
219_77	NB31	120	302	1.70	5	17.37	2.1	3.5	86.0	3.50E-05	2.02E-03	0
220_74	NS31	120	328	1.74	1	15.20	2.6	4.5	108.1	1.50E-05	9.87E-04	0
220_75	NS31	120	298	3.06	1	28.92	1.2	3.8	68.4	-4.00E-05	-1.38E-03	0
220_76	NS31	120	302	2.94	1	15.20	2.4	7.0	129.2	1.30E-04	8.55E-03	0
220_77	NS31	120	302	1.68	5	15.20	2.4	4.0	97.5	5.50E-05	3.62E-03	0
M57_39	Al	120	272	5.00	1	19.68	1.7	8.3	117.4	1.01E-03	5.11E-02	671.25
M57_40	Al	120	273	1.88	1	14.17	2.3	4.3	100.2	5.25E-03	3.70E-01	403.05
M16_87	Cu	120	234	4.91	1	16.27	1.7	8.5	121.0	3.00E-05	1.84E-03	40.31
M16_88	Cu	120	235	5.00	1	14.17	2.0	10.0	140.9	3.50E-05	2.47E-03	29.15
M139_75	SS	120	235	5.00	1	17.37	1.6	8.1	114.9	8.45E-04	4.86E-02	238.42
M139_76	SS	120	237	2.00	1	13.18	2.2	4.3	96.6	2.55E-04	1.94E-02	162.55
M168_38	W	120	177	5.00	1	16.27	1.3	6.5	92.4	0.00E+00	0.00E+00	0
M168_39	W	120	179	1.88	1	14.17	1.5	2.9	65.9	0.00E+00	0.00E+00	0
M168_40	W	120	175	4.94	1	14.17	1.5	7.3	104.3	2.00E-05	1.41E-03	0
M168_41	W	120	150	5.00	1	11.30	1.6	8.0	112.7	-7.00E-05	-6.20E-03	-6

1. n = number of shots
2. Erosion = crater or erosion depth

4.1.3 Material erosion of samples loaded in JUDITH and JEBIS

After the thermal shock loads in JEBIS and JUDITH the material erosion has been quantified by two independent methods: weight loss measurements and erosion depths determined by laser profilometry. Variations of specific weight loss and erosion depth with $P_{abs}\sqrt{t}$ [see page 22, ref., 117] are shown in Fig. 33 and Fig. 34. The heat flux parameter $P_{abs}\sqrt{t}$ was used because the pulse lengths were different (Ref. Table 11, Table 12). The loaded areas of the JEBIS samples are $\pi\cdot(2\sigma)^2$ assuming that the electron beam in the JEBIS facility is circular and Gaussian. The "2σ" is calculated from FWHM (Ref. Chap. 3.5.4).

Weight loss and surface erosion were significant for the JEBIS samples, whereas the samples in JUDITH showed only negligible erosion under similar thermal loads (see Fig. 33, Table 11, Table 12). For example, the specimens loaded in JEBIS had a specific weight loss of 0.28 kgm^{-2} at $P_{abs}\sqrt{t}$ = 87 $MJm^{-2}s^{-1/2}$ for W, 0.98 kgm^{-2} at $P_{abs}\sqrt{t}$ = 117 $MJm^{-2}s^{-1/2}$ for stainless steel, 0.49 kgm^{-2} at $P_{abs}\sqrt{t}$ = 119 $MJm^{-2}s^{-1/2}$ for Cu, and 6.27 kgm^{-2} at $P_{abs}\sqrt{t}$ = 117 $MJm^{-2}s^{-1/2}$ for Al. In contrast, the JUDITH samples showed at identical thermal load less than half erosion as JEBIS samples. W, stainless steel, and Cu samples results were below the detection limit at identical heat loads, and for Al, the specific weight loss was 0.37 kgm^{-2} at $P_{abs}\sqrt{t}$ = 100 $MJm^{-2}s^{-1/2}$. Carbon based materials also showed similar characteristics. The specific weight loss of Si-doped CFC was $9.9\cdot10^{-4}$ kgm^{-2} at $P_{abs}\sqrt{t}$ = 108 $MJm^{-2}s^{-1/2}$ in a JUDITH sample and 0.1 kgm^{-2} at $P_{abs}\sqrt{t}$ = 101 $MJm^{-2}s^{-1/2}$ in a JEBIS sample.

With respect to the crater depth, stainless steel sample loaded in JEBIS had twice as deep craters as the sample loaded in JUDITH at an identical pulse length of 5 ms; 530 µm at an $P_{abs}\sqrt{t}$ = 117 $MJm^{-2}s^{-1/2}$ (Ref. Fig. 34) for JEBIS sample and 238 µm at $P_{abs}\sqrt{t}$ = 115 $MJm^{-2}s^{-1/2}$ for JUDITH sample. In JEBIS samples, the carbon materials had crater depths in the order of 40~120 µm for $P_{abs}\sqrt{t}$ = 50~117 $MJm^{-2}s^{-1/2}$. The CBMs loaded in JUDITH showed no visible crater determined by laser profilometry. The degradation of the CFC samples was mainly given in the PAN fiber bundles. No significant damage was found in the pitch fiber bundles for both JEBIS and JUDITH loaded samples.

Tungsten materials loaded at identical conditions with JEBIS showed mostly no crater in the samples loaded in JUDITH. The results showed different erosion at identical heat flux. A W sample loaded in JUDITH with $P_{abs}\sqrt{t}$ = 94 $MJm^{-2}s^{-1/2}$ for 4.5 ms showed a 48 µm deep crater (P_{abs}=1.4 GWm^{-2}, loaded area = 2.7·2.7 mm^2 (M168_8, Fig. 55), while another W sample showed no crater at an $P_{abs}\sqrt{t}$ = 92 $MJm^{-2}s^{-1/2}$ for 5 ms (P_{abs} = 1.3 GWm^{-2}, loaded area = 4.0·4.0 mm^2, in Fig. 49). The differences in the loading conditions are the incident power and the loaded area, but identical heat flux parameter $P_{abs}\sqrt{t}$. These inconsistent results might be attributed to the different loaded area that the threshold heat flux for melting leading to crater formation is lower for the sample loaded on a smaller area than the other on a larger area. This effect will be discussed in Chap.4.2.3.4.

One conceivable explanation for the fact that there is a difference in material degradation between JEBIS and JUDITH samples is the difference in vapor recoil pressure and surface tension due to the high thermal gradients in the loaded area (Ref. Chap. 4.1.4); JEBIS applies a static mode while JUDITH applies a scanning mode. The JEBIS sample has a quasi-Gaussian distribution. Thus the center always absorbs the highest heat flux, whereas the surrounding areas absorb a lower flux. This causes high thermal gradients in the loaded

area and melt layer motion occurs due to the high surface tension (Fig. 38 for stainless steel, Fig. 46 for W).

Moreover, the density of evaporation in JEBIS is the highest at the center and the vapor recoil pressure becomes high to cause melt layer ejection. In contrast, the JUDITH has a homogeneous loaded area by fast scanning of the electron beam and the evaporation density is rather homogeneously distributed in the whole loaded area. The resulting surface tension and vapor recoil pressure is much smaller in JUDITH and the ejection of the melting outside the loaded area does not proceed, resulting in less material erosion for the samples loaded in JUDITH compared to JEBIS samples. The details about this mechanisms are described in Chap. 4.1.4.

Another explanation for the low material erosion in JUDITH could be surface rippling [118, 120] induced by the beam scanning. An illustration of the different erosion mechanisms is shown in Fig. 35. When the surface of metal samples absorbs a certain high heat flux, the surface starts to melt, and a hole is created on the specimen [119]. When the electron beam sweeps at certain velocity, the beam pushes the melt layer to the opposite direction of beam scanning. This melt layer re-solidifies as it cools down. In the case of scanning only in one direction, the melt layer will deposit on the rim. Because the electron beam in JUDITH scans in both x and y direction, start of melting and melt layer movement continuously occur until the beam terminates and finally the melt layer re-solidifies within the loaded area. This results in the roughness and rippling of the surface. Sometimes a "deep" hole is seen in the samples, which indicates the end of the beam scanning. Tantalum and stainless steel samples in Fig. 15 and Fig. 44 show examples of "deep" hole. When the beam is turned off, in the last moment of the beam scanning, a hole is created. In contrast, the electron beam in JEBIS has always the highest heat flux in the center during thermal loading. When the center reaches the melting point and boiling point, the melt ejection continues due to the above mentioned forces of surface tension, vapor recoil pressure and high thermal gradient in the loaded area (Fig. 38, Fig. 46).

Finally also the difference in penetration depth of the electron beam in JEBIS and JUDITH has an influence on the different material erosion. The penetration depth of the two facilities especially for W is significant; 16 μm in JUDITH (120 keV) and 5 μm in JEBIS (65 keV). However, the degree of erosion in JEBIS is about five times larger than that in plasma accelerator [36, 79], although the erosion by plasma accelerators is only affected by surface heating. Numerical modeling [89] also showed different result from experimental one in JEBIS. Numerical results showed no melt with E_{abs} = 2.3 MJ m^{-2} for 1.8 ms (P_{abs} = 1.27 GWm^{-2}), whereas the W sample loaded in JEBIS formed a crater with 27 μm depth and a melt layer thickness with 110 μm.

Nevertheless, it is difficult to compare the results from JEBIS and JUDITH. Because the heat flux profile in JEBIS is not constant during the thermal loading. During the static beam, the distance is large up to 6 mm and it focuses down to 2 mm. In JUDITH the heat flux is distributed homogeneously in the scanned area. This results in a relatively flat heat flux distribution.

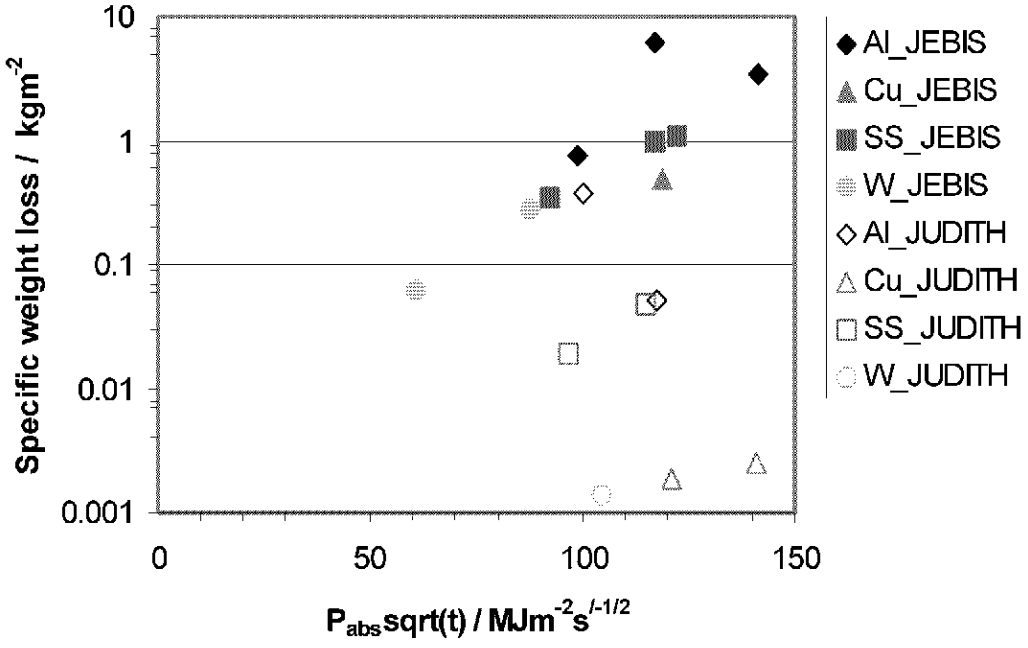

A

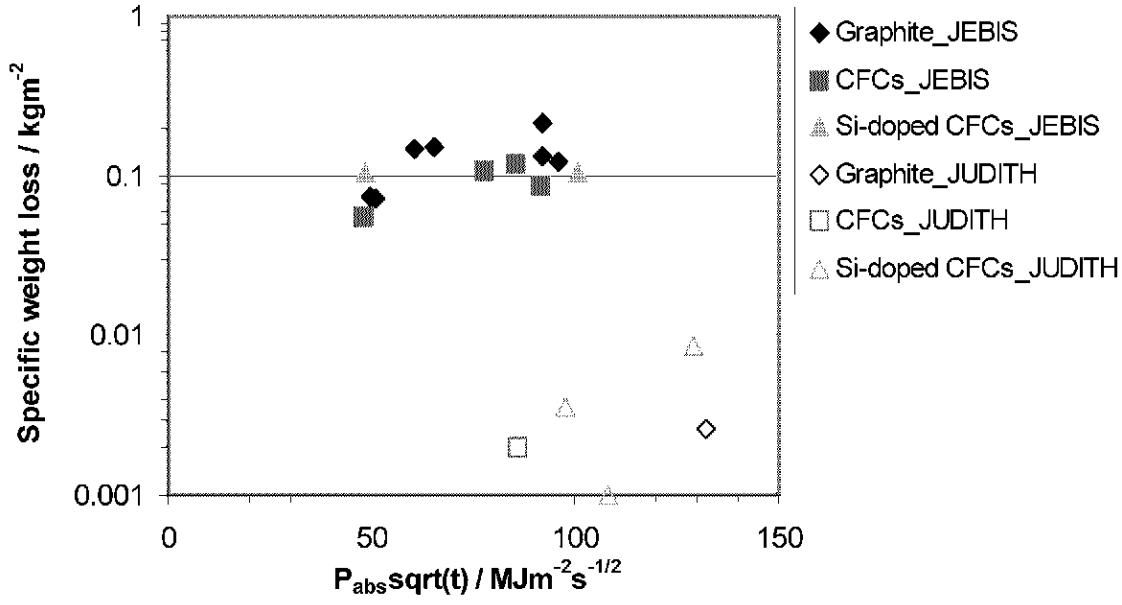

B

Fig. 33 Variation of specific weight loss with $P_{abs} \cdot t^{1/2}$ for metal samples (A) and carbon based materials (B) loaded in JEBIS and JUDITH.
*Specific weight loss = Δm (weight loss) /loaded area
*Area in JEBIS = $\pi \cdot (2\sigma)^2$ (2σ = ca. 0.85·FWHM assuming that the JEBIS beam is the Gaussian distribution, Ref. Chap. 3.5.4)

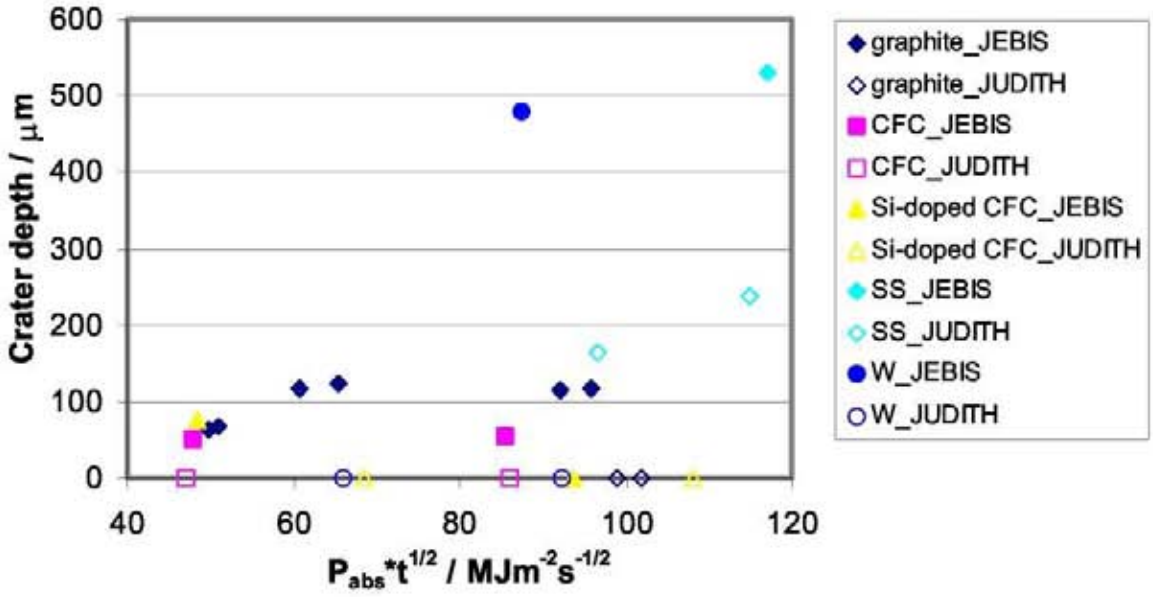

Fig. 34 Variation of crater depth with $P_{abs} \cdot t^{1/2}$ for carbon based materials and metal samples loaded in JEBIS and in JUDITH .

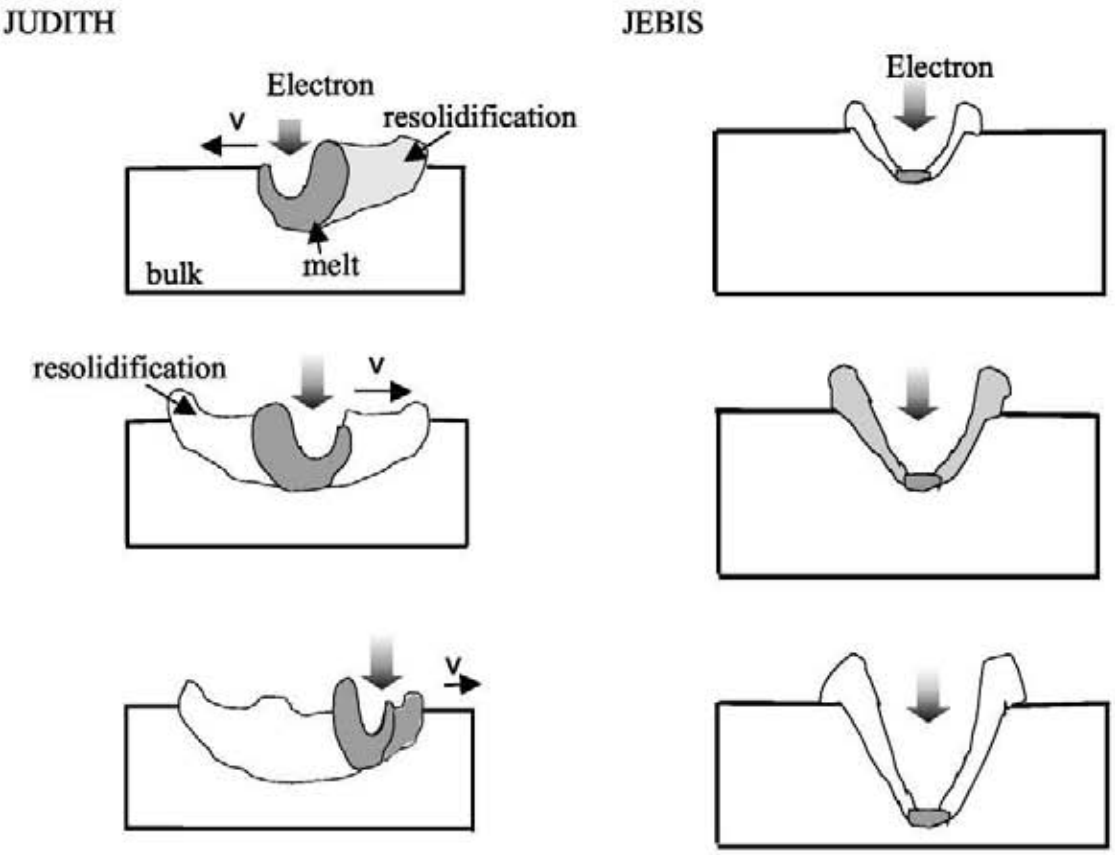

Fig. 35 Illustration of melting and resolidification by scanning in x and y direction (JUDITH), and static beam (JEBIS).

4.1.4 Melt layer motion

In order to study the melt layer motion under transient heat loads, the electron beam shots in JEBIS were conducted in two ways, with and without a graphite or tungsten cover having a Ø 5 mm aperture above the specimens (Fig. 36). Schematic view of the thermal loading with and without an aperture in JEBIS is shown in Fig. 37. It is assumed that the beam in JEBIS has a Gaussian distribution with FWHM of 2 mm (Ref. calibration), and the aperture shields only a few percent of the beam power. The diameter of the crater with rim loaded with an aperture is 20 mm, which is the same for the sample loaded without an aperture (Fig. 36). The difference between loading with and without an aperture was observed in the outer shape of the crater. The outer area for the sample loaded without an aperture shows a smooth circle on the rim and heat affected zone around (Fig. 36A). In contrast, the sample loaded with aperture shows a sharp-pointed circle around the rim (Fig. 36B).

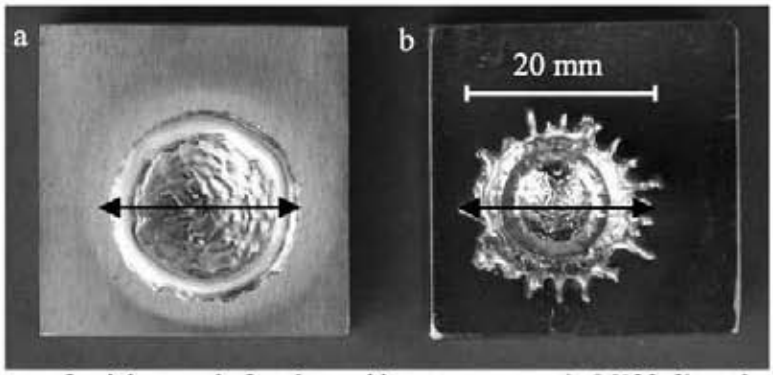

Fig. 36 Pictures of stainless steel after shots without an aperture (a, M139_3) on the left and with an aperture (b, M139_4) on the right at identical heat loads loaded in JEBIS. P_{abs}: 1.65 GWm^{-2}, $\Delta t = 2.20$ ms on the left and 1.61 GWm^{-2}, $\Delta t = 2.14$ ms

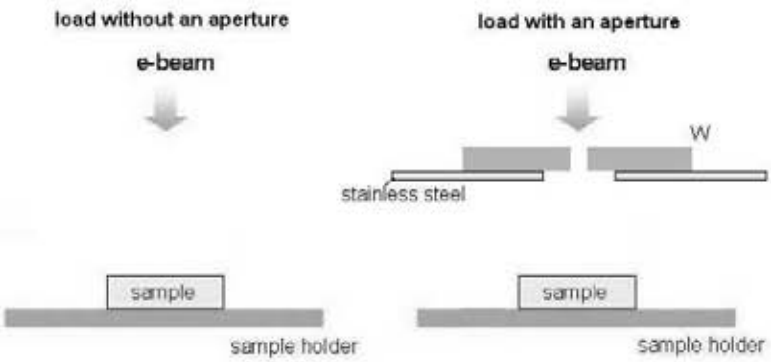

Fig. 37 Schematic view of thermal loading with and without an aperture in JEBIS.

The crater of the sample loaded without an aperture looks similar to most of the specimens (Fig. 36a, Fig. 38). Both the microstructure of the surface in the center of the crater and the rim consist of recrystallized grains (Fig. 38). In contrast, the secondary electron and metallographic images of a stainless steel sample loaded with an aperture in Fig. 39 and Fig. 40 show the different structures inside and outside the crater. The shape of the crater loaded with an aperture splashing of the melt layer out of the crater (Fig. 39A). Part of the resolidified material around the crater was detached from the specimen (Fig. 36b, Fig. 40).

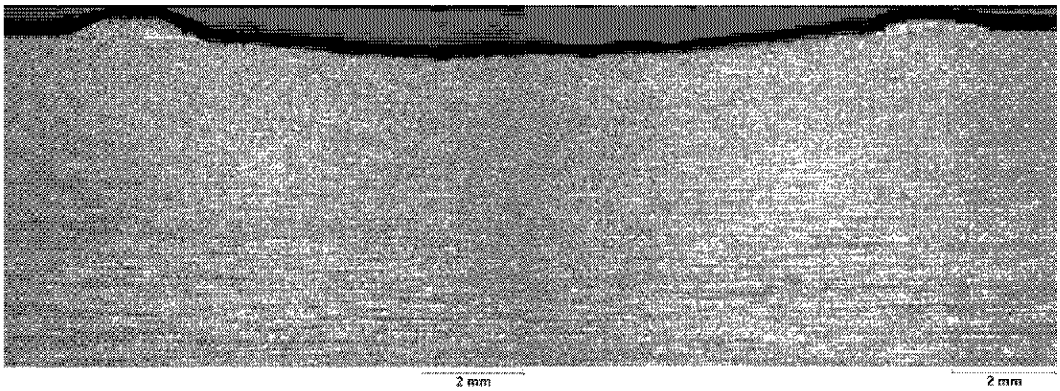

Fig. 38 Cross section of stainless steel (M139_3) loaded in JEBIS without aperture.
P_{abs} = 1.7 GWm^{-2}, Δt = 5 ms (Fig. 36a)

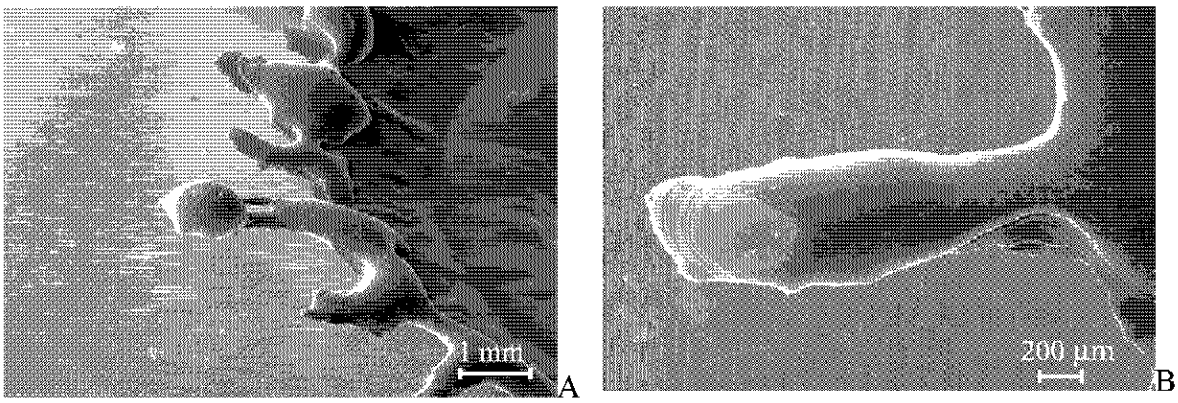

Fig. 39 SEM images of stainless steel (M139_4) loaded in JEBIS with aperture Ø 5 mm W.
P_{abs} = 1.6 GWm^{-2} Δt = 5 ms (Fig. 36b)
A: overview, B: higher magnification of the droplet

The cross section also indicates different crystal structures mainly grain size and columnar structure. Fig. 40 A shows a wavy structure inside the crater. It indicates the convection of the melt. The wavy structure of the molten part is also seen at the splashed rim shown in Fig. 40 C, D. The columnar structures appear in the molten layers in the craters of both samples. Small grains, which are different from substrate grains, can be seen on the surface over the columnar structure in both samples indicating a fast recrystallization process. Moreover, the bottom of the splashed molten part of the sample with an aperture (Fig. 40 D) shows small recrystallized grains. The grain size increases at the top of the splashed molten parts. In contrast, the periphery of the sample without an aperture appeared to have a columnar structures adherent to the substrate (Fig. 38).

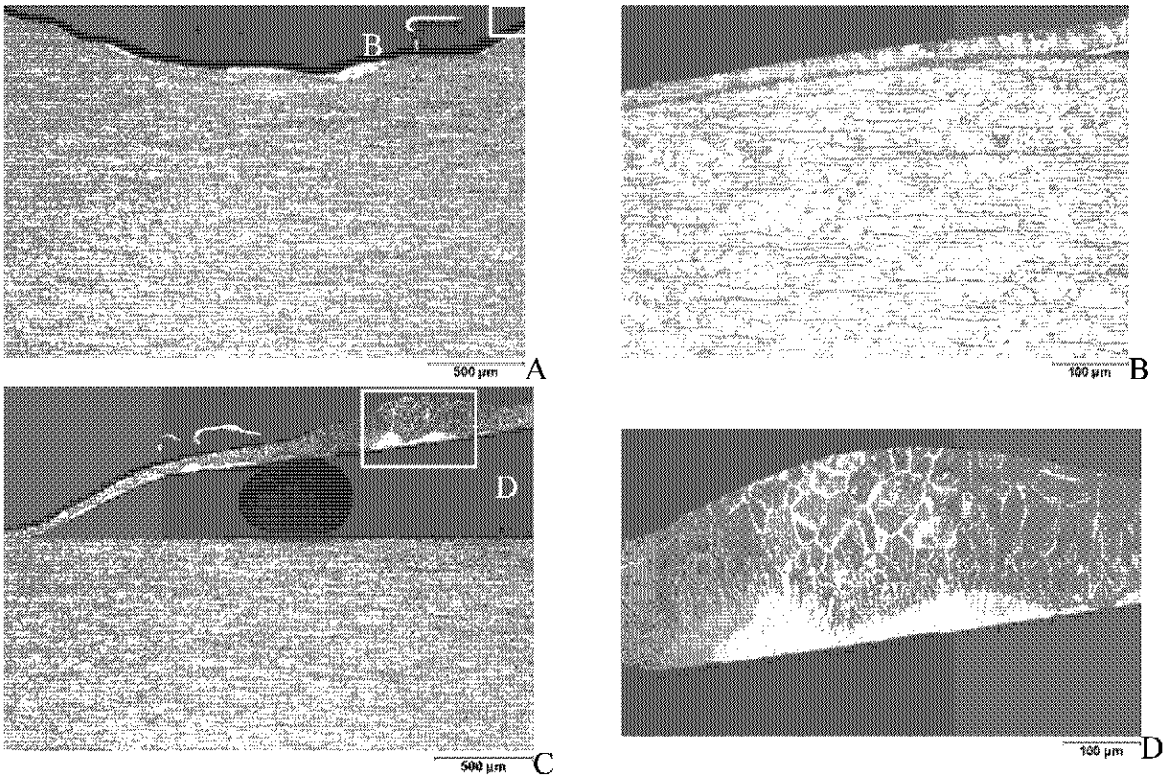

Fig. 40 Cross section of stainless steel (M139_4) loaded in JEBIS with aperture Ø 5 mm W.
P_{abs} = 1.6 GWm^{-2} Δt = 5 ms (Fig. 36b)
A: crater, B: center of the loaded area, C: right side of the molten rim,
D: higher magnification of the molten part in B

The sample loaded with an aperture shows a deeper crater and higher redeposition at the periphery compared to the sample loaded without an aperture. The crater depth was 1.1 mm for the stainless steel sample with an aperture and approximately half of this depth (530 µm) for the sample without an aperture at identical heat flux. However, the residual melt layer was approx. 62 µm, which was thicker for the sample loaded without an aperture than that for the one with an aperture (approx. 46 µm). The same trend can be seen in W samples. The crater depth also showed half of the depth and longer thickness of melt layer for the sample loaded without an aperture compared with the one loaded with an aperture at identical heat fluxes.

The splashing at the periphery of the melt layer and the crater formation may be caused by convection, surface tension, and high vapor recoil pressure [120]. If high heat flux is applied to localized surface fractions of the specimen while other parts keep around RT, the beam creates a deep hole in the specimen [121] due to the high surface temperature in the heat affected zone and high thermal gradients in the loaded area. A schematic diagram of melt movement is shown in Fig. 41.

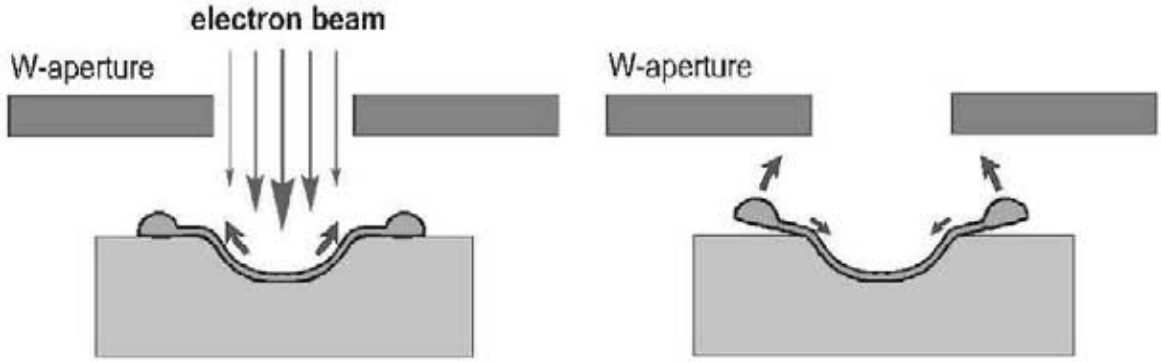

Fig. 41 Schematic diagram of melt layer motion during (left) and after (right) the heat load.

The vapor recoil force of the surface generated by the evaporation pushes the melted zone outwards [120, 122, 123, 124]. At the center of the crater, there is strong surface tension which causes rapid melt ejection. At the end of the electron beam pulse, the molten parts cool down immediately and the rim becomes detached from the sample. This detachment of the sample loaded with an aperture is induced by a higher contraction of solidified molten layer after thermal loading because the area outside the loaded area remained at room temperature.

The loading with and without an aperture on stainless steel samples was also performed in JUDITH. The crater depths as a function of absorbed power density P_{abs} is presented in Fig. 42. The schematic view of thermal loading with aperture is shown in Fig. 43. The crater depths of the sample with static and scanning mode increased with the power density. The crater depths of the sample loaded with shielding the Ø 5 mm aperture was in agreement with the extrapolated line, but the crater depths of the sample loaded with Ø 3 mm aperture was far below the line. The crater depth of the sample with and without an aperture (Ø 5 mm) did not show the differences like the JEBIS samples. The question for the discrepancy is still open.

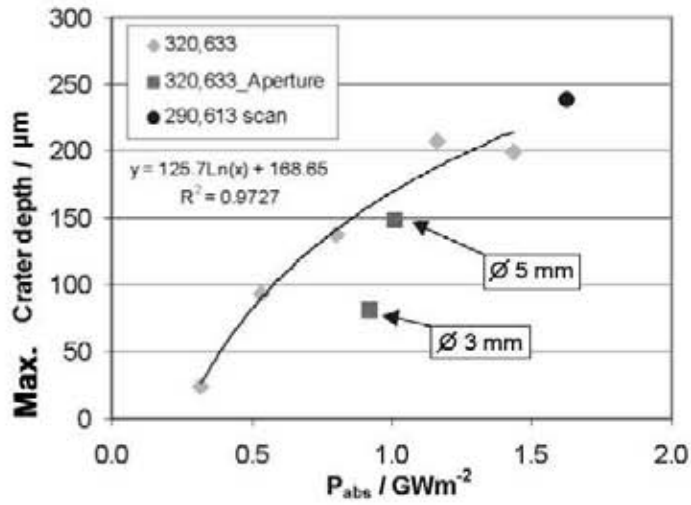

Fig. 42 Crater depths of stainless steel as a function of power density P_{abs} with pulse duration of 5 ms loaded with scanning (focus 1 = 290 mA, focus 2 = 613 mA) and static mode (focus 1 = 320 mA, focus 2 = 633mA) with and without apertures Ø 3, 5 mm (loaded in JUDITH). Loaded areas in P_{abs} for static mode are $\pi\times(2\sigma/2)^2$

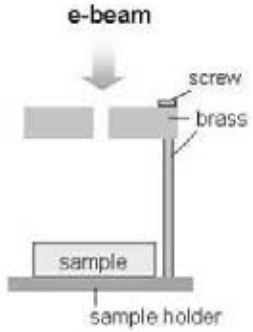

Fig. 43 Schematic view of thermal loading with an aperture in JUDITH.

Digital camera images proved the formation of a vapor cloud of stainless steel sample loaded in JUDITH (Fig. 44). It is presumed to be vapor formation generated from the surface of the material. The loading condition was in the same heat flux and pulse duration as the JEBIS sample (Fig. 36 on the left, Fig. 38). The absorbed current decreased after 0.7 ms to about 20 % of the initially absorbed current and is kept at this value until the end of the thermal load. The deposited layer on the brass plate with aperture, set above the stainless steel sample, found to be composed of Cr and Fe by EDX. It indicates that the vapor cloud observed in digital image was composed of Cr and Fe [125]. The vapor shield effect is discussed in detail in chapter 4.2.3.5.

The stainless sample loaded in JUDITH showed a wavy surface morphology (Fig. 44) similar to the samples loaded in JEBIS (Fig. 38), but a square shaped load pattern due to the beam scanning (Fig. 45). The crater depth was 238 µm, which is about half compared to the JEBIS samples with identical heat fluxes. On the contrary, the melt layer was 82 µm, which was thicker than the JEBIS sample (62 µm). The reasons for this surface roughness, the lower crater depth and the thicker melt layer were high surface tension and thermal gradient in the loaded area, vapor recoil pressure, and rippling. The details of these phenomena are described in Chap.4.1.3.

Fig. 44 Surface morphology, digital camera, absorbed current of stainless steel (M139_75) P_{abs} = 1.6 GWm^{-2} Δt = 5 ms (loaded in JUDITH)

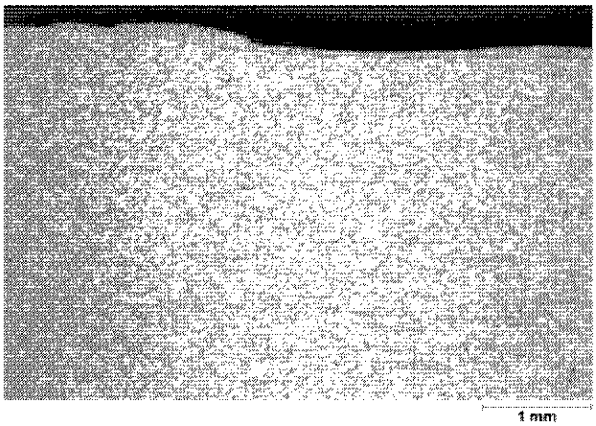

Fig. 45 Cross section of stainless steel sample (M139_75) loaded in JUDITH at P_{abs} = 1.6 GWm^{-2}, Δt = 5 ms.

For W, the differences of samples loaded with and without an aperture in JEBIS can be clearly seen (Fig. 46, Fig. 47). The SEM images in Fig. 46 and Fig. 47, both showed melting and crater formation with a molten rim and cracks passing the crater with diagonal orientations. However, the sample loaded with an aperture is characterized by a large number of droplets, whereas there is no droplet formation for the sample loaded without an aperture. Moreover, bubbles are presented between substrate and molten parts, or over the columnar structure in molten parts at the periphery for the sample loaded without an aperture. The bubbles do not appear in W loaded with an aperture (Fig. 47C). The negative absorbed current of the W sample in Fig. 47A implies the thermoionic emission or ejection of W droplet or evaporation.

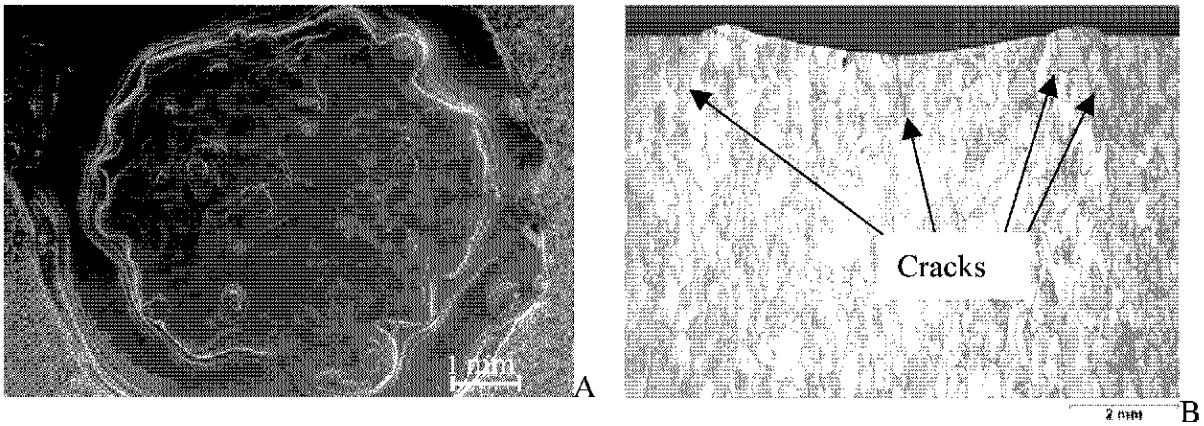

Fig. 46 SEM images of tungsten (M168_1) loaded in JEBIS at P_{abs} = 1.2 GWm^{-2} Δt =5 ms without an aperture. A: overview, B: higher magnification of the loaded area

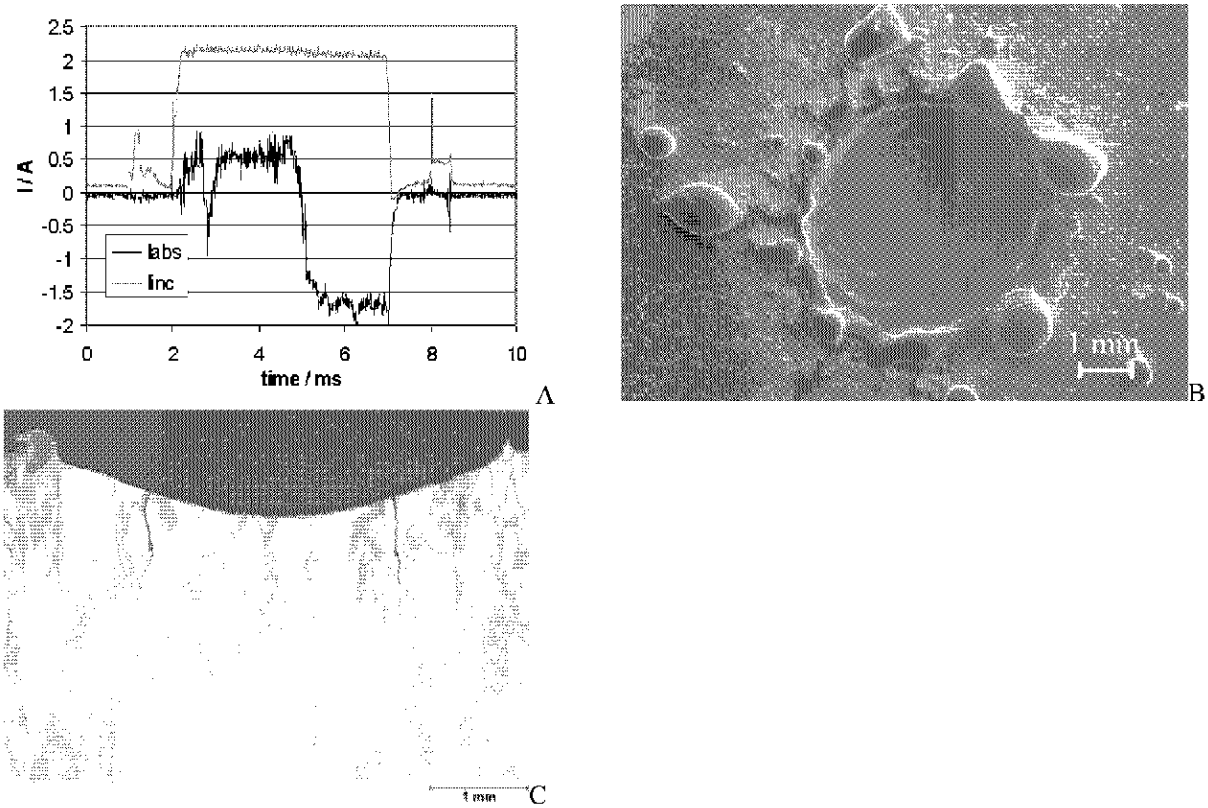

Fig. 47 Current plot (A), surface (B), and cross section (C) images of tungsten (M168_4) loaded in JEBIS at P_{abs} = 1.2 GWm^{-2} Δt = 5 ms with aperture Ø 5 mm W.

Because of its low melting point, aluminum samples help to understand the mechanism of melting and crack formation. In addition, Al has properties, which can simulate the performance of Be much better than other metals. Beryllium cannot be used in electron beam tests without special safety measures. For Al, melting and cracks in the molten parts are clearly seen in SEM images (Fig. 48 A). In the cross section images, the cracks were formed inside and outside the crater; these cracks pass through the recrystallized melt layer down to the substrate (Fig. 48 B). These images indicate that the crack formation occurred in the cooling phase, after the loading is terminated. The melt formation starts when the surface reaches temperatures above the melting point. The molten layer is ejected outwards from the center due to the vapor recoil pressure and surface tension in the molten layer. When the surface cools down, resulting in high tensile stresses parallel to the surface, cracks perpendicular to the surface are formed.

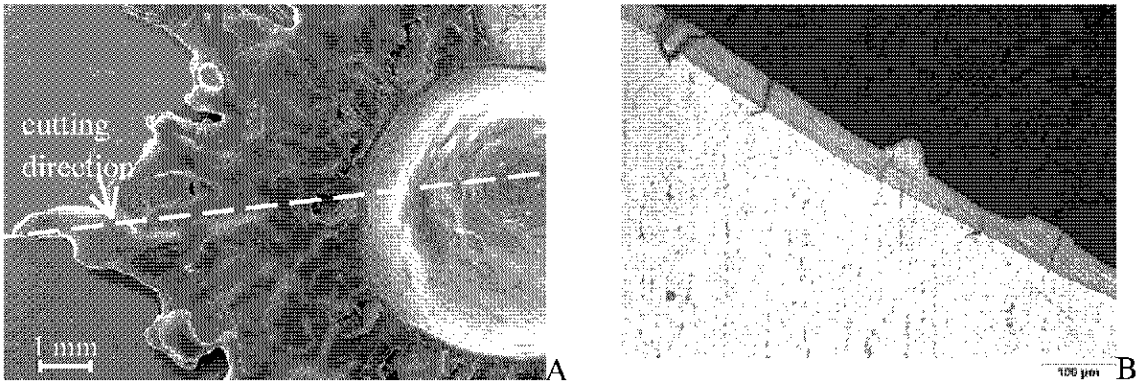

Fig. 48 SEM image (A) and Cross section images (B) of aluminium (M57_28) loaded in JEBIS with a W aperture Ø 4 mm at P_{abs} = 1.9 GWm^{-2} Δt = 5 ms
A: surface overview, B: left corner of the loaded area

4.1.5 Particle emission

In order to detect *in-situ* particle emission, digital images were taken using a CCD camera in JUDITH. It was found that not only carbon samples but also the metals emitted particles. Fig. 49B shows particle trajectories from a W sample in the digital images, although the W sample does not show any macroscopic erosion. Some spikes appear in the current graph (Fig. 49 C). These spikes may be associated with particle emission. The decrease of absorbed current did not appear for W loaded in JUDITH, whereas the absorbed current of the sample loaded in JEBIS changes into negative value after 3 ms (Fig. 47).

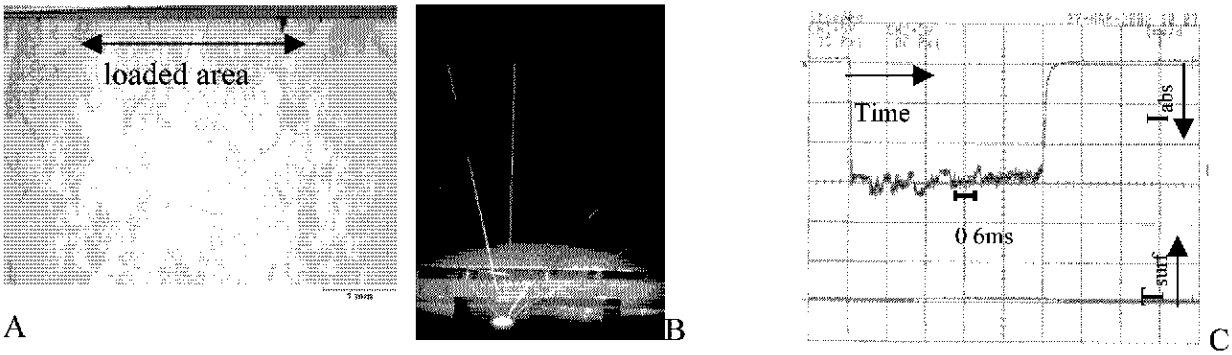

Fig. 49 Surface morphology (A), emission of particles (B), absorbed current (C) of W (M168_38)
P_{abs} = 1.3 GWm^{-2} Δt = 5 ms (loaded in JUDITH)

Spikes of the current plot and particle emission were also observed in carbon specimens loaded in JUDITH facility. However the decrease of absorbed current showed to be different. In Fig. 50, the absorbed current recorded during loading Si-doped CFC is shown. It started to decrease at approximately 0.9 ms and reached 25 % of initial absorbed current at the end of the pulse. Weight loss of the Si-doped CFC sample was zero (Table 11). Nevertheless, the erosion along the PAN fiber area of the surface was observed (Fig. 51). Increasing the pulse duration from 1.7 to 3.0 ms at almost the same power density (Fig. 52), fine particles were emitted and the absorbed current started to decrease after 1 ms and kept at 17 % of initial absorbed current after 2 ms until the end of the pulse.

The redeposition of molten Si in Si-doped CFCs in Fig. 50 is composed of Si and trace amounts of Ca, Fe, Ti, Cr which were determined by EDX. The material (NS31) without

thermal loading contains these elements except Ca analyzed by ICP-MS (Ref. appendix). The elements might come from the manufacturing process of doping with silicon (CVI process). For un-doped CFCs, these elements were not detected by EDX.

The Si-doped CFC sample was also loaded at P_{abs} = 2.3 GWm^{-2} for 1.7 ms in JEBIS (Fig. 53), the thermal load was identical to the sample shown in Fig. 43. However, pulse duration was not possible to extend the pulse duration over 1.7 ms in JEBIS because the electron beam abruptly terminated.

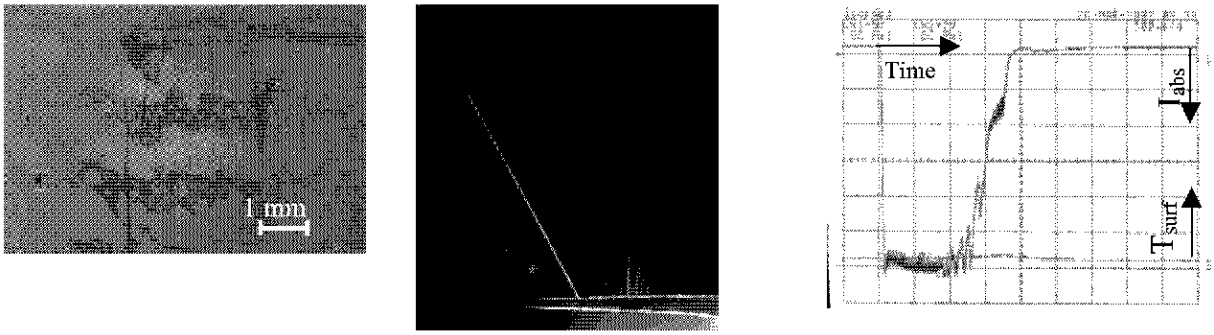

Fig. 50 Surface morphology, emission of particles, absorbed current and surface temperature of Si-doped CFC (NS31, 220_74) loaded in JUDITH
(P_{abs} = 2.6 GWm^{-2} Δt = 1.7 ms)

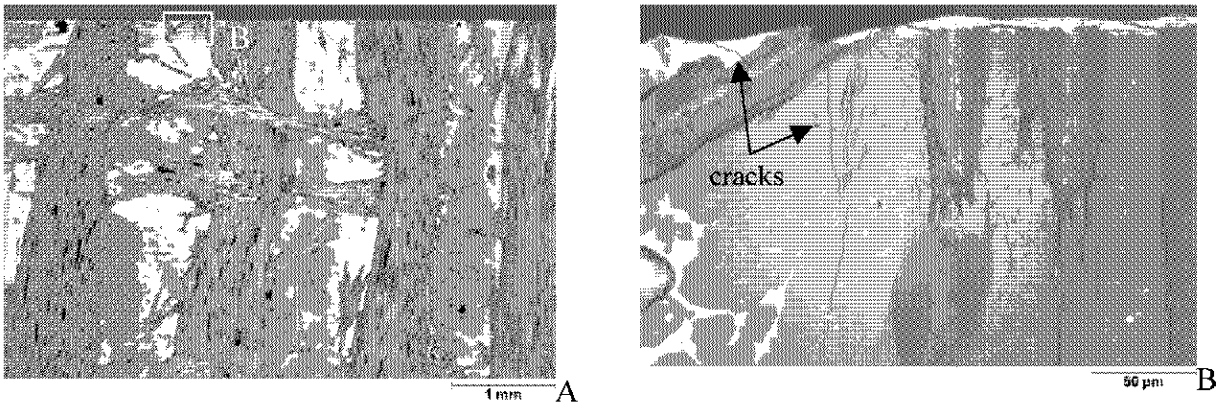

Fig. 51 Cross section images of Si-doped CFC (220_74) loaded in JUDITH at P_{abs} = 2.6 GWm^{-2} Δt = 1.7 ms. A: overview, B: crack formation in Si and SiC phase

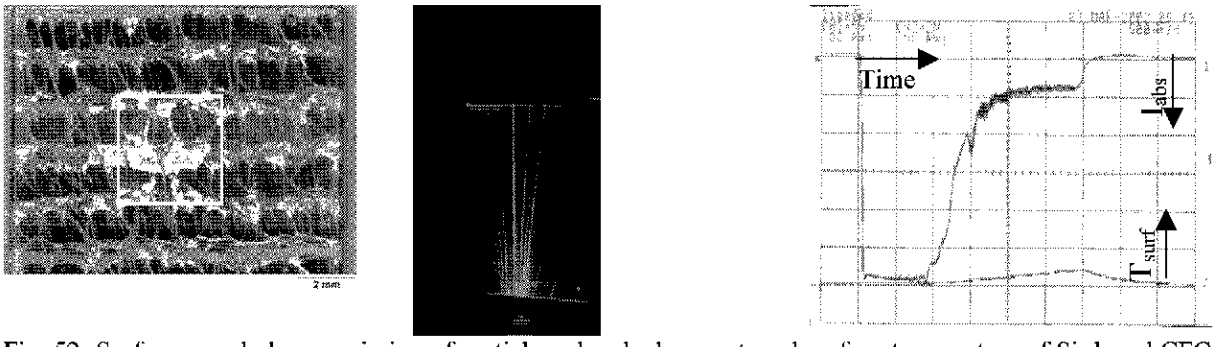

Fig. 52 Surface morphology, emission of particles, absorbed current, and surface temperature of Si-doped CFC (NS31, 220_76) P_{abs} = 2.4 GWm^{-2} Δt = 2.9 ms (loaded in JUDITH)

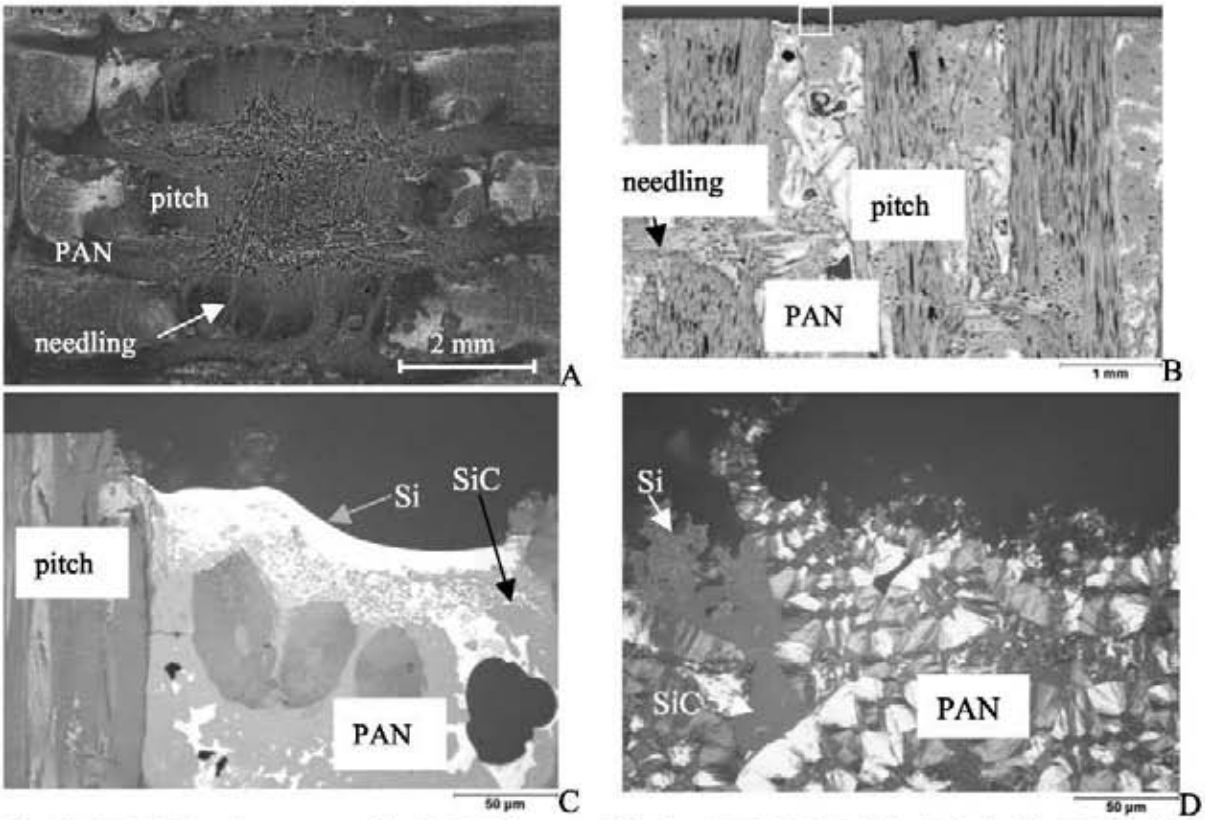

Fig. 53 SEM (A) and ceramographic (B,C,D) images of Si-doped CFC (NS31, 220_4) loaded in JEBIS without an aperture at $P_{abs} = 2.3\ GWm^{-2}$ $\Delta t = 1.7$ ms.
A: overview of the cross section, B-D : higher magnification of the cross section images

The reason for the termination of heat loads after 1.7 ms is probably due to an increase of the ejected particles. The particle emission started after approx. 1ms (Fig. 50) and the emitted particles are supposed to reach the plasma source at 1.7 ms due to the arching. This beam termination did not occur in JUDITH because the electrons were generated from a W cathode. The beam generation is less sensitive to particles which penetrate in to the electron beam gun. Moreover, this effect was only observed on carbon based materials, although the weight loss of CBMs was much smaller compared to metal samples (Fig. 33, Table 12). It indicates the velocity of ejected particles or droplets of CBMs to be much faster than the velocity of ejected particles from metal samples [157].

4.1.6 Polished and non-polished samples

In JEBIS graphite and CFC samples have been tested with polished and non-polished surfaces. The damage of non-polished samples was more severe for graphite in comparison with the damage of polished samples. For graphite, the polished sample (11_382) showed the same crater depth but smaller weight loss compared to the unpolished ones at almost the same thermal loads (11_380) (see Table 11). But the results for CFCs were the opposite of graphite; the damage of non-polished samples was less severe. The material erosion of 3-D CFC of non-polished samples and polished ones are shown in Fig. 54.

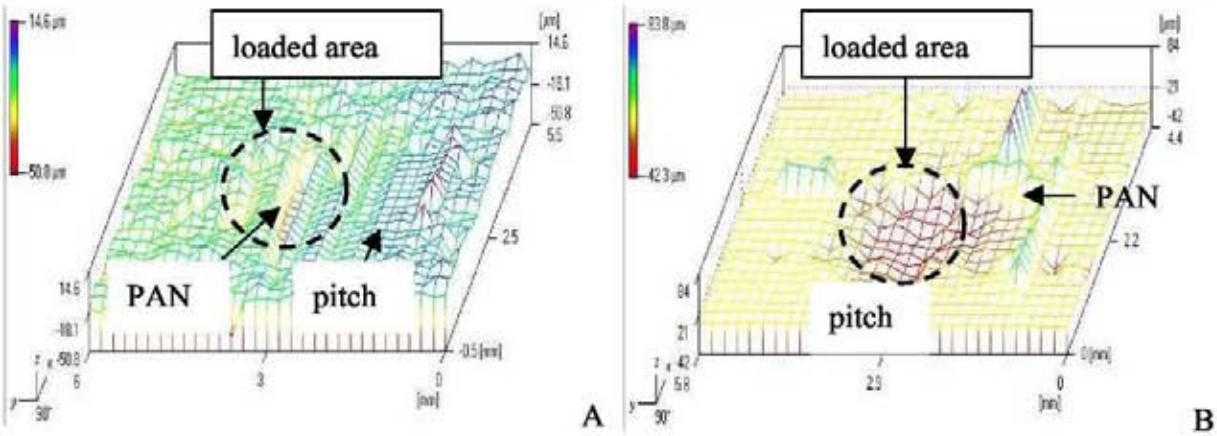

Fig. 54 Surface profiles of 3-D CFC (NB31) for non-polished (219_2, A) and for polished (219_4, B) samples. A: P_{abs} of 2.37 GWm^{2} , Δt = 1.49 ms, $P_{abs}\sqrt{t}$ = 91.5 $MJm^{-2}s^{-1/2}$, B :P_{abs} of 2.07 GWm^{-2} , Δt = 1.7 ms, $P_{abs}\sqrt{t}$ = 85.5 $MJm^{-2}s^{-1/2}$

The crater depth and the weight loss of CFCs were higher in polished samples (219_2, 4, 5) (See Table 11). The non-polished CFC sample in Fig. 54A shows the erosion only in the PAN fiber area, whereas the polished CFC sample in Fig. 54B shows the erosion both in the PAN and pitch fiber area. Due to the thin beam diameter in JEBIS (FWHM = 2 mm after 1 ms), the beam might affect different parts of the inhomogeneous materials. The purpose of the polishing was to see material damage clearly. But because the surface profiles of non-polished samples measured by laser profilometry could also show the material damage clearly, any additional polishing is not necessary.

4.1.7 Conclusion

In order to assess the thermal behavior of PFMs under transient thermal loads, the mechanisms of melt layer flow of metals, particle emission of carbon materials, and material erosion has been investigated experimentally in two electron beam facilities JEBIS and JUDITH.

The samples loaded in JEBIS showed higher erosion than the samples loaded in JUDITH. The specific weight loss in JEBIS was more than 10 times higher. With respect to the crater depth, the stainless steel samples loaded in JEBIS, for example, had twice as deep craters as the samples loaded in JUDITH at energy density of 8 MJm^{-2} (Ref. Fig. 55). It seems to be caused by the following effects; surface tension in the loaded area, vapor recoil pressure and surface rippling due to the different beam mode. JEBIS applies a static beam with Gaussian heat distribution. The center of the loaded area receives the highest heat flux and starts to melt. Then ejection of the liquid or solid particles continuously occurs, resulting in higher material erosion. When the surface reaches the boiling point, the center of the loaded area has the highest vapor density with strong vapor pressure gradient in the loaded area. The JUDITH samples have a homogeneous loaded area and a low gradient in vapor recoil pressure. The second explanation of the low material erosion in JUDITH is surface rippling induced by the beam scanning. When the electron beam provides heat flux and the spot reaches a temperature above the melting point, a "deep" hole is created on the specimen. When the electron beam sweeps at certain velocity, the melt layer moves and deposits just behind the beam scanning, and re-solidifies. This process; melting, melt layer movement and re-deposition behind the beam scanning, continues until the beam terminates. The third assumption is the difference in penetration depth of the electron beam in JEBIS and JUDITH. The penetration of the electron beam in JUDITH is more than twice as deep as the beam in JEBIS. The effect of volumetric heating becomes higher for JUDITH samples, resulting in lower degradation of the materials.

Melt layer flow of metals was characterized by loading the specimens with an aperture. The cross section of stainless steel shows a wavy morphology in the crater, and the same microstructure in the resolidified layer inside the crater as the periphery of the crater. It indicates convection of the melt during the thermal load and outward directed melt flow. The crater of the sample loaded with an aperture was only half as deep as the sample loaded without an aperture. Moreover, the sample loaded with an aperture was no adhesion between resolidified melt layer and cold substrate. It might be due to the high contraction directed to the center of the loaded area.

Particle emission has successfully been detected by CCD camera under the condition of plasma disruption in JUDITH. It was found that besides CBMs, also metals like aluminum, copper, stainless steel, and tungsten showed particle or vapor emission from the surface. The stainless steel formed a visible vapor cloud above the surface which consists mainly of chromium and iron. The decrease of absorbed current was recorded in graphite and CFC samples as well as in stainless steel samples. The oscillation or decrease of the current plots might be associated with particle emission.

It was not possible to extend the pulse duration beyond 1.7 ms for CBMs in JEBIS maybe because of an electric arc to the plasma source. The emission for metals did not

obstruct the performance of thermal loads up to 5 ms, although the weight losses of metals were higher than that of CBMs at identical loading conditions. It indicates that the velocity of ejected particles or droplets of CBMs is much faster than that from metal samples. The emission of W and stainless steel particles was below the threshold to terminate the operation of the plasma source. The ejection of solid particles for CBMs might be a serious concern in fusion reactors.

Several graphite and CFC samples have been polished to see the material damage visible. It was found that any additional polishing is not necessary. Because the surface profiles of non-polished samples measured by laser profilometry could show clearly the material damage.

4.2 *Investigation of high Z materials under intense transient thermal loads*

4.2.1 Introduction

Tungsten is a prime candidate for the divertor and the lower part of the baffle in Tokamak fusion reactors. Mo and Ta are taken into consideration as an alternative to the W armor [126]. The fusion plasma under off-normal events such as plasma disruptions and VDEs will interact with these components, and lead to thermal erosion from these high Z materials. This ablation, crack formation, and melt layer formation result in reduction of the lifetime of the components [114]. ELMs were observed in the present Tokamaks and its also expected to occur in next step maxchines such as ITER. The influence of ELMs on PFMs has been estimated by numerical simulations [127, 128]. There are only a few experiments on using plasma accelerator, but there has not been much data available so far. During operational cycles in ITER, the divertor surface will be exposed to quasi-stationary heat flux and thus be heated up to 300 - 500 °C [129]. K. Nakamura et.al [113] reported that for samples with initially elevated temperature above DBTT, the weight loss increases but cracks do not occur. In contrast, for samples preheated around DBTT (200 and 600 °C) there was no significant change in the material response compared to samples without preheating [30].

The evaporated atoms, clusters, and droplets from high Z materials would interact with plasma and redeposit on the other parts of PFCs such as first wall (Be) or on adjacent divertor region [130, 131, 132]. The interaction of the plasma with vapor cloud formed by evaporation of the materials is known as shielding effect [83, 134]. The produced cloud insulates the surface from incoming energy and less erosion occurs with the full energy deposition. The vapor shield effect occurred only in Tokamak or plasma accelerator devices [80, 83, 133]. However, in the previous chapter 4.1.4, the vapor cloud formation was observed from the stainless steel sample (Fig. 44), which might shield the incoming energy and reduce the subsequent material erosion. There is also the presumption that it is the droplet formation during plasma disruption conditions [134, 135]. The dust formation of W associated with evaporation and droplet formation is a radiological safety issue because neutron irradiated tungsten is highly radioactive.

In order to acquire longer operation, different W-alloys with different designs of the components have been developed. [70, 108, 136, 138] Thin tungsten lamellae or castellation also represent a candidate design for the ITER divertor to reduce the thermal and mechanical damage. Thermal fatigue testing [11, 115], transient heat load tests [70 - 83, 105 - 114], neutron irradiation effects [71, 126, 139], sputtering effects [137, 138] using electron beam facilities and plasma accelerators have been investigated.

In this study, transient heat flux tests were conducted in an electron beam facility JUDITH on different refractory materials to evaluate and optimize their thermal response for a careful selection of the PFMs. Different high Z materials (W, Mo, Ta, WC), W-alloys (W-La_2O_3, W-Re), single crystal and plasma sprayed W were tested under plasma disruption and VDE conditions. Moreover, the influence of samples preheating up to 200-460 °C, the influence of the loaded area, and vapor shielding effects have been also investigated on pure W or W-1%La_2O_3 samples.

4.2.2 Experimental

4.2.2.1 Materials

Materials used for the experimental campaign under plasma disruption conditions are, W, Mo, Ta, WC, plasma sprayed W on Cu, plasma sprayed W on graphite (EK98), W alloys such as W-1 % La_2O_3, W-5 %Re, W-26 % Re, and single crystal W<111>-0.02 %Re (Ref. Table 7 pp29). The VDE tests were performed at; pure W, Mo, W-La, W-Re alloy, WC, and lamellae module, loaded at power densities E_{abs} 55 MJm^{-2} for pulse duration of 90 ms or 300 ms. The details of these materials have been described in Chap. 3.4.2. The typical sample dimensions are 12×12×5 mm^3 for disruption and 25×25×10 mm^3 for VDE tests. Disruptions with heat fluxes in the GWm^{-2} –range mainly influence the surfaces, whereas VDEs conditions are characterized by lower heat fluxes of about 750 MWm^{-2} but longer pulse duration and thus more volumetric damage.

The 5 mm thickness plasma sprayed W was coated on flat CuCrZr heat sinks with a Ni-Al-Si interlayer to improve adhesion strength. This coating has 90 % density and 70 % thermal conductivity compared to bulk W [62]. This sample was previously tested in a thermal fatigue test at a heat flux of 7.6 MWm^{-2} for 42 cycles. After thermal fatigue testing, a test coupon for the plasma disruption test was cut from the module [139].

The plasma sprayed coating of W on fine grain graphite (EK98) was produced in vacuum with a thickness of 550 μm [140, 141]. There is a 10 to 20 μm thickness of Re between W and graphite to improve adhesion strength and to avoid formation of brittle WC. After spraying, a heat treatment was carried out at 1400 °C for one hour in order to obtain homogeneous grains and to reduce the porosity.

To include more stress resistant sample geometries, W or W-1 % La_2O_3 samples with a 5-10 mm castellation and modules with 0.2 mm and 4 mm lamellae were tested. The lamellae samples were cut from W-1 % La_2O_3 mock up which were previously used in thermal fatigue tests [139]. FT 89_3 consists of lamellae module with a thickness of 4 mm in each W 1 % La_2O_3 lamella, casted with OFHC-Cu and joined to a heat sink material CuCrZr by HIPing. FT84_1 is W lamellae module with 0.2 mm thickness of each lamella hiped to CuCrZr.

4.2.2.2 Experimental procedure

The loading conditions of plasma disruption and VDE conditions in JUDITH were P_{abs} of 1.2~1.6 GWm^{-2} for Δt = 4 ~ 4.5 ms (incident current I_{inc} = 160 mA), 5~7 MJm^{-2} with a loaded area of 7.3 mm^2 for disruption tests and 60~70 MJm^{-2} for 90~300 ms with a loaded area of 64 mm^2 for VDE tests (Table 13, Table 14). All tests were performed at nominal beam voltage of 120 kV. For short pulses <100 ms, the test facility was operated in the capacitor mode. For 300 ms pulses, a starter block was used during the ramping up phase in the transformer mode of the electron beam generation. When the nominal beam current was achieved, the electron beam was moved to the target samples. To terminate the electron beam pulse, the beam was ramped down on the starter block. In order to examine the effect of initial elevated temperature on pure W, the samples were preheated before the thermal loading under plasma disruption and VDE conditions (Table 15). In order to see if the size of the loaded area affects the surface behavior of the materials, thermal shock tests at different loaded areas were conducted on pure W samples with max. E_{abs} of 5 ~ 11 MJm^{-2} for 5 ms (Table 16). To

investigate the effect of vapor shielding on refractory metals under disruption, specific thermal loads systematic experiments were performed on test specimens made from sintered tungsten (Table 17). In these tests the incident current I_{inc} was increased from 40 to 320 mA (increment I_{inc} = 40 mA, V = 120 kV) for pulse duration T_{inc} of 5 ms. Simulation experiments of ELMs were performed on pure W for low cycle numbers (n = 100) in JUDITH with static beam. The loading conditions were maximum energy density E_{abs} = 1.2 MJm^{-2} for pulse duration of 0.52 ms (I_{inc} = 150 mA, V = 120 kV) and E_{abs} = 2.7 MJm^{-2} for pulse duration of 0.6 ms (I_{inc} = 300 mA, V = 120 kV). The beam diameter was FWHM = 1.84 mm [Ref. Chapter 3.5], assuming a Gaussian distribution of the beam. The focuses of the electron beam controlled by magnetic coils were, focus 1 = 320 mA and focus 2 = 633 mA (Ref.3.5.3).

For plasma disruption and VDE tests the electron beam was scanned in a triangular mode on the specimen's surface with frequencies f_x = 47 kHz, f_y = 43 kHz. The applied pulse duration and the absorbed current were monitored by oscilloscope. The surface temperatures were recorded by fast pyrometer.

After the thermal load testing, characterization of the materials was carried out using weight loss measurements, laser profilometry (e.g. Fig. 15), and optical and scanning electron microscopy (SEM). Maximum crack depths of all samples have been also determined in the cross section images. The melt layer thickness of all samples after VDE tests was determined from the cross section images.

Table 13 Loading conditions and results of different high Z materials for disruption tests.

Material	Sample ID	Sample dimension mm^3	Δt ms	P_{abs} [1] GW/m^2	E_{abs} [1] MJ/m^2	Weight loss mg	Crater depth μm
W	M168/8	12×12×5	4.45	1.40	6.21	0	48.7
Mo	M20/121	12×12×5	4.44	1.62	7.21	0.11	53.9
Ta	M27/27	Ø 25×10	4.35	1.23	5.34	0	195.1
WC	M45/21	20×20×5	4.41	1.30	5.74	3.92	108.1
PS W on Cu	M105/1	10×10×5	4.29	1.21	5.18	5.79	257.8
PS W on Cu	FT76/1	15×10×8	4.35	1.19	5.17	10.66	236.4
PS W on grpahite		25×25×25	4.5	1.3	5.60	n.m [2]	141.8
W La_2O_3	M104/1	10×10×5	4.38	1.26	5.54	0	101.0
W26Re	M39/46	Ø 25×10	4.35	1.25	5.42	0.02	61.5
W<111>) – 0.02% Re	M133/7	10×10×5	4.38	1.25	5.46	0.06	69.4

1) Loaded area = 2.7×2.7 mm^2

1) V: acceleration voltage = 120 keV, number of shots n = 1

2) n.m = not measured

Table 14 Loading conditions and results of different high Z materials for VDE tests.

Material	Sample ID	Sample dimension mm^3	Δt ms	P_{abs} [2] MW/m^2	E_{abs} [2] MJ/m^2	d_{melt} [3] mm	Max. crack depth mm
W	M168/6	25×25×10	88.9	593.6	52.8	1,25	4.35
Mo	20/123	Ø 25×10	88.2	735.7	64.9	2.5	2.6
WC	45/25	20×20×5	88.9	604.4	53.8		
W-1%La_2O_3	129/2	25×25×10	89.4	582.8	52.1	1.2	10
W5Re	103/1	1/2 module	89.4	625.9	56.0	1.25	10
W26Re	39/50	Ø 25×10	89.4	608.7	54.4	1.26	4.5
0.2 mm W lamellae[1]	FT84/1a	Module[1]	89.4	658.3	58.9	1.5	0.175
4 mm W lamellae[1]	FT89/3	Module[1]	88.2	723.1	63.8	1.38	0.96
W-1%La_2O_3 castellated	M171/4d	11×10×10	90	622.1	56.0	1.6	0.3
W-1%La_2O_3 castellated	M171/5d	11×10×10	300	205.9	61.8	0.24	

number of shots n = 1

1) W lamellae module: The central parts were cut from the complete module after thermal fatigue tests.

2) absorbed current in the samples M171_4d, M171_5d = I_{inc}× (1-0.47) 0.47 = reflection coefficient

2) loaded area = 5.4×5.4 mm^2

3) d_{melt} = the sum of residual melt layer thickness and a crater depth

Table 15 Loading conditions and results of pure W for effect of preheating samples under plasma disruptions and VDEs (Chap. Effect of preheating samples).

	Sample ID	Preheating	I_{inc} mA	I_{abs} mA	Δt ms	area mm^2	P_{abs} GW/m^2	E_{abs} MJ/m^2	Crater depth µm
plasma disruptions	M168_67_2	RT	40	18.33	3.82	$(2.7)^2$	0.30	1.16	0
	M168_67_3		160	74.17	4.39	$(2.7)^2$	1.23	5.40	60.24
	M168_67_4		280	143.85	4.54	$(2.7)^2$	2.39	10.8	45.11
	M168_64_2	300 °C	40	18.7	3.81	$(2.7)^2$	0.31	1.2	0
	M168_64_5		160	76.67	4.37	$(2.7)^2$	1.27	5.6	63.27
	M168_64_7		200	93.75	4.41	$(2.7)^2$	1.56	6.9	54.95
	M168_64_8		240	125	4.50	$(2.7)^2$	2.07	9.3	13.19
	M168_64_6		270	135.4	4.54	$(2.7)^2$	2.25	10.2	1.71
	M168_64_4		280	150	4.54	$(2.7)^2$	2.49	11.3	7.39
	M168_65_1		40	18.54	3.79	$(2.7)^2$	0.31	1.2	0
	M168_65_2	400 °C	160	77.5	4.47	$(2.7)^2$	1.29	5.8	55.21
	M168_65_5		200	93.75	4.41	$(2.7)^2$	1.56	6.9	10.13
	M168_65_4		240	116.7	4.54	$(2.7)^2$	1.94	8.8	20.42
	M168_65_6		260	125	4.47	$(2.7)^2$	2.07	9.3	28.66
	M168_65_7		270	133.3	4.50	$(2.7)^2$	2.21	10.0	20.39
	M168_65_8		290	145.8	4.63	$(2.7)^2$	2.42	11.2	24.18
	M168_66_1		40	18.8	3.82	$(2.7)^2$	0.31	1.2	0
	M168_66_6		140	65	4.34	$(2.7)^2$	1.08	4.7	57.56
	M168_66_2	500 °C	160	75.83	4.47	$(2.7)^2$	1.26	5.6	61.74
	M168_66_5		180	87.5	4.34	$(2.7)^2$	1.45	6.3	38.33
	M168_66_4		200	95.8	4.41	$(2.7)^2$	1.59	7.0	10.1
	M168_66_3		270	133.3	4.54	$(2.7)^2$	2.21	10.0	24.63
VDEs	M168_67_1	RT	40	n.m.	n.m.	$(5.4)^2$	-	-	
	M168_61	300 °C	320	n.m.	n.m.	$(5.4)^2$	-	-	413.7
	M168_62	400 °C	320	147.9	88.77	$(5.4)^2$	0.66	58.6	329.2
	M168_63	500 °C	320	145.8	90	$(5.4)^2$	0.66	59.4	260.8

number of shots n = 1, I_{inc} : incident current, I_{abs} = absorbed current, Δt = pulse duration, crater depth = deepest point of the crater

Table 16 Loading conditions and results of pure W for disruption tests with different loaded areas (Chap. Influence of loaded area).

Shot #	Sample	Loaded area mm^2	Δt ms	I_{inc} mA	I_{abs} mA	P_{abs} GW/m^2	E_{abs} MJ/m^2	Erosion μm
1	1C	$(3.5)^2$	5	200	107.6	1.1	5.3	-10.0
2	1C	$(3.5)^2$	5	300	161.4	1.6	8.0	-9.2
3	1C	$(3.5)^2$	5	350	188.3	1.9	9.3	-6.4
4	1C	$(3.5)^2$	5	350	188.3	1.9	9.3	10.1
5	1C	$(2.7)^2$	5	200	107.6	1.8	9.0	31.0
6	1C	$(2.7)^2$	5	300	161.4	2.7	13.5	38.2
7	1C	$(2.7)^2$	5	350	188.3	3.1	15.7	38.6
8	1C	$(2.7)^2$	5	350	188.3	3.1	15.7	32.9

V: acceleration voltage = 120 keV, number of shots n = 1
I_{inc} : incident current, I_{abs} = absorbed current, Δt = pulse duration
*Erosion = the deepest point of the crater. Negative values in crater depths mean the top of convex shapes

Table 17 Loading conditions and results of pure W (M168_43) for disruption tests with different loaded areas (vapor shielding effect).

Sample ID	I_{inc} mA	I_{abs} mA	Δt ms	area mm^2	P_{abs} GW/m^2	E_{abs} MJ/m^2	Erosion μm
M168_43_1	40	19.17	3.83	$(2.69)^2$	0.3	1.59	
M168_43_2	80	38.75	4.14	$(2.69)^2$	0.6	3.22	-6.93
M168_43_3	120	55	4.33	$(2.69)^2$	0.9	4.56	25.27
M168_43_4	160	74.17	4.36	$(2.69)^2$	1.2	6.16	40.26
M168_43_6	200	95.83	4.4	$(2.69)^2$	1.6	7.95	28.66
M168_43_8	240	114.996	4.4	$(2.69)^2$	1.9	9.54	53.17
M168_43_9	280	125	4.47	$(2.69)^2$	2.1	10.37	43.43
M168_43_10	320	152.1	4.55	$(2.69)^2$	2.5	12.62	

V: acceleration voltage = 120 keV, number of shots n = 1
I_{inc} : incident current, I_{abs} = absorbed current, Δt = pulse duration
Erosion : the deepest point of the erosion.
Negative values in crater depths mean a formation of convex shapes

4.2.3 Results

4.2.3.1 Disruption tests

The surface (observed by SEM) and cross section images of the different materials after the plasma disruption simulations are presented in Fig. 55 - Fig. 67.

Variation of crater depths and weight loss and crack length in different high Z materials are shown in Fig. 68 and Fig. 69.

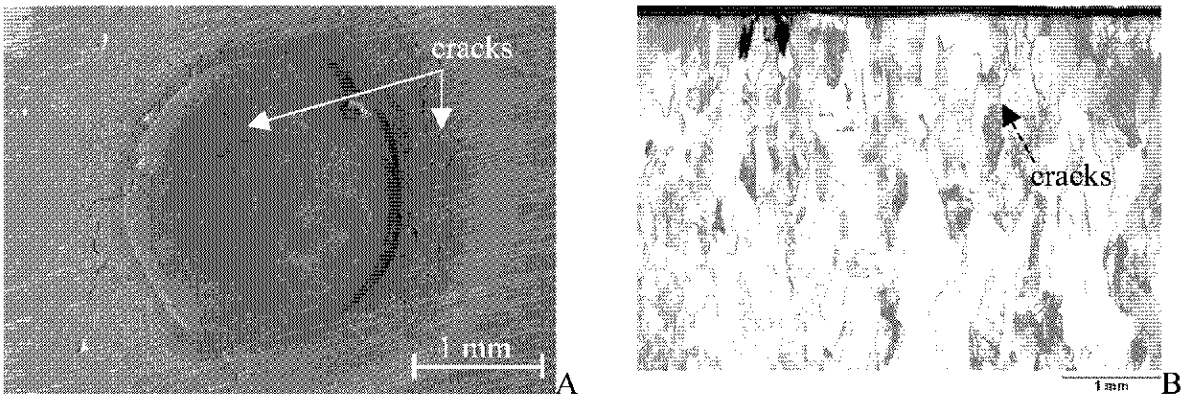

Fig. 55 SEM (A) and cross section (B) images of pure W.
(M168_8, I_{inc} = 160 mA, P_{abs} = 1.4 GWm^{-2}, Δt = 4.4 ms)

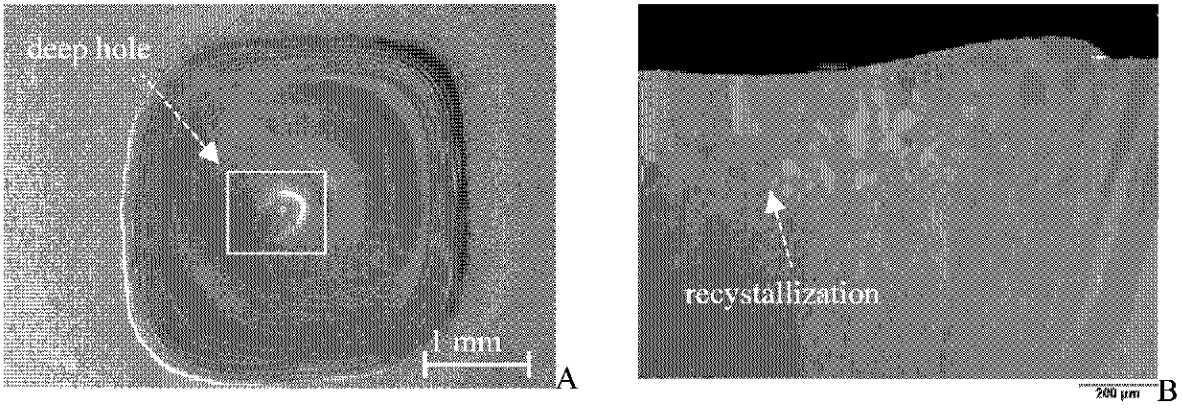

Fig. 56 SEM (A) and cross section (B) images of pure Ta.
(M27_27, I_{inc} = 160 mA, P_{abs} = 1.2 GWm^{-2}, Δt = 4.4 ms)

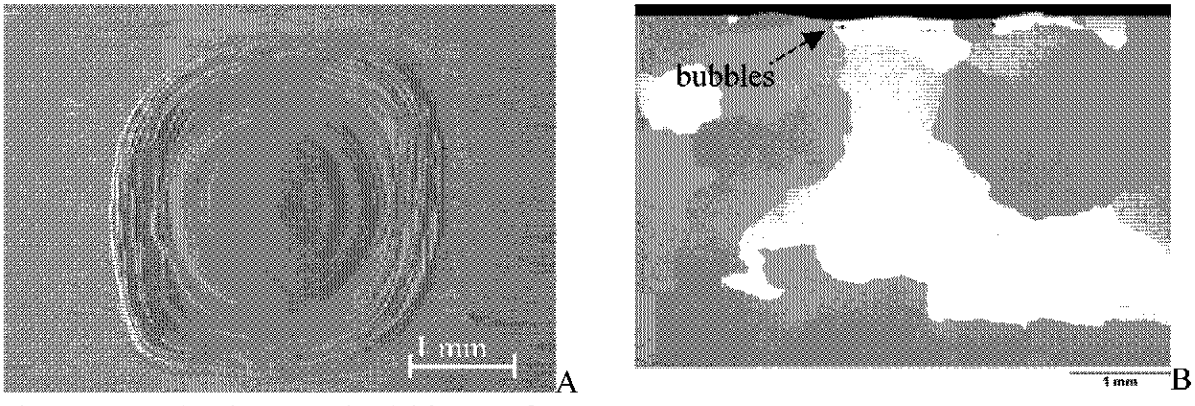

Fig. 57 SEM (A) and cross section (B) images of pure Mo.
(M20_121 at P_{abs} = 1.6 GWm^{-2}, Δt = 4.4 ms)

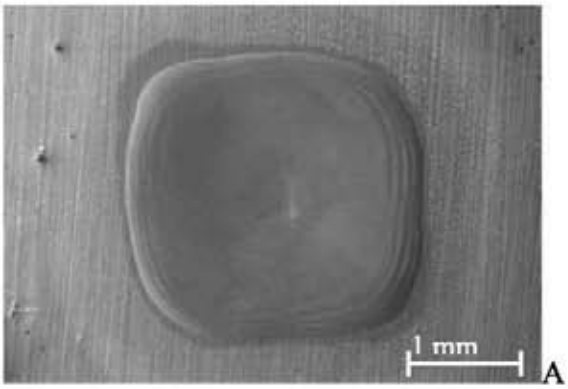

Fig. 58 SEM (A) image of W<111> 0.02%-Re.
(M133_7 at I_{inc} = 160 mA P_{abs} = 1.2 GWm^{-2}, Δt = 4.4 ms)

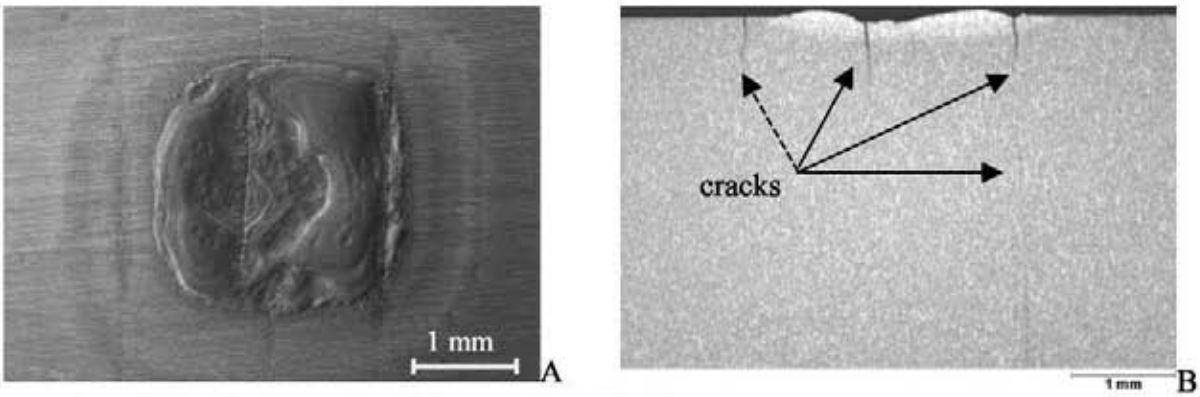

Fig. 59 SEM (A) and cross section (B) images of W-1% La_2O_3.
(M104_1, I_{inc} = 160 mA, P_{abs} = 1.3 GWm^{-2}, Δt = 4.4 ms)

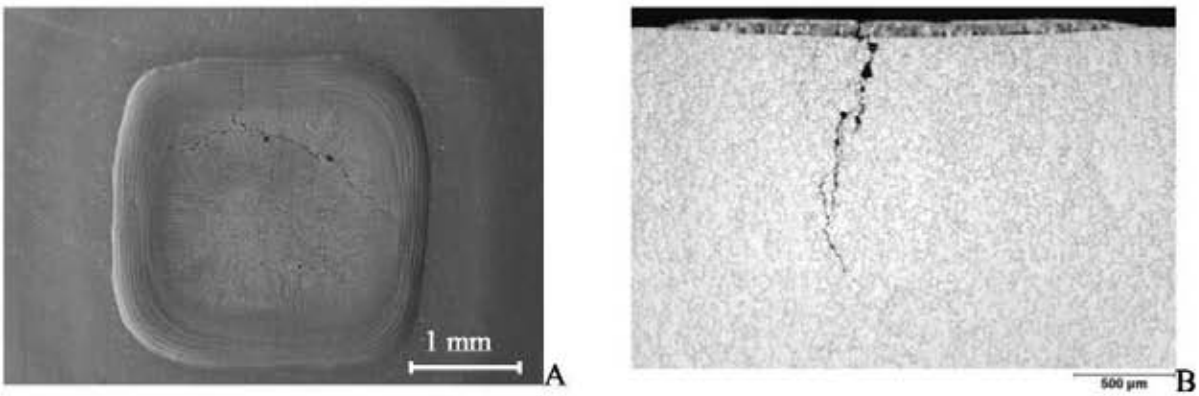

Fig. 60 SEM (A) and cross section (B) images of W-26% Re.
(M39_46, I_{inc} = 160 mA, P_{abs} = 1.2 GWm^{-2}, Δt = 4.4 ms)

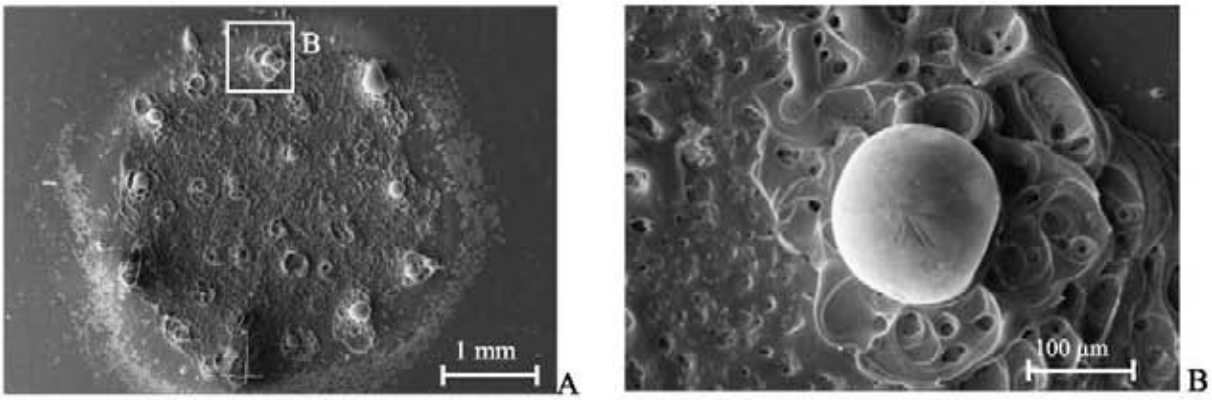

Fig. 61 SEM images of WC (M45_21). A: overview, B: high resolution image of a droplet.
I_{inc} = 160 mA, P_{abs}=1.3 GWm^{-2}, Δt = 4.4 ms

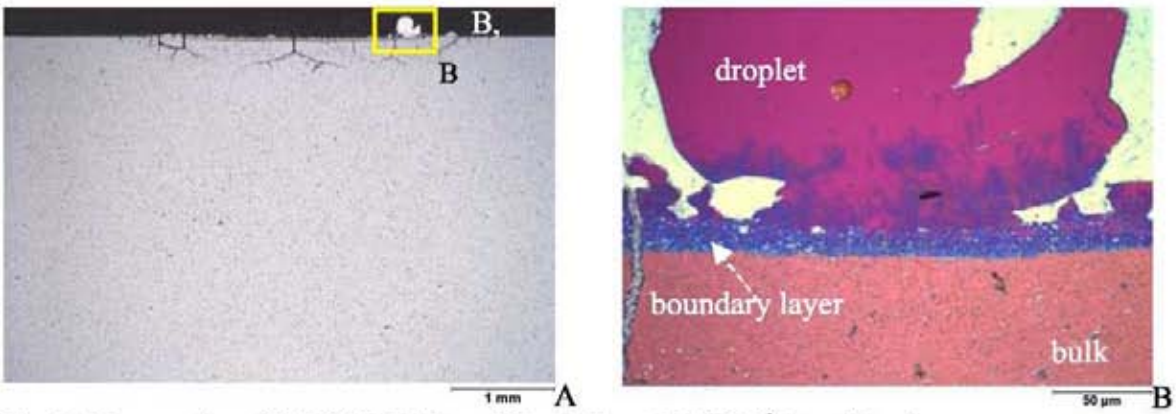

Fig. 62 Cross section of WC (M45_21, I_{inc} = 160 mA, P_{abs} = 1.3 GWm^{-2}, Δt = 4.4 ms).
A: overview, B: the droplet on the right side of the crate; different colors indicate different phases

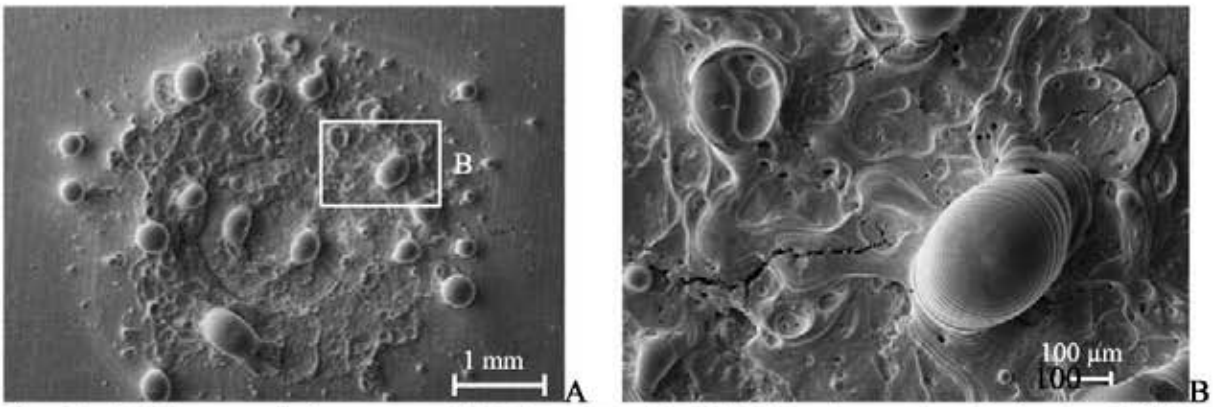

Fig. 63 SEM images of plasma sprayed W (1 mm) on Cu (M105_1). A: overview, B: droplet, C: higher magnification from the part of B. I_{inc} = 160 mA, P_{abs} = 1.2 GWm^{-2}, Δt = 4.3 ms

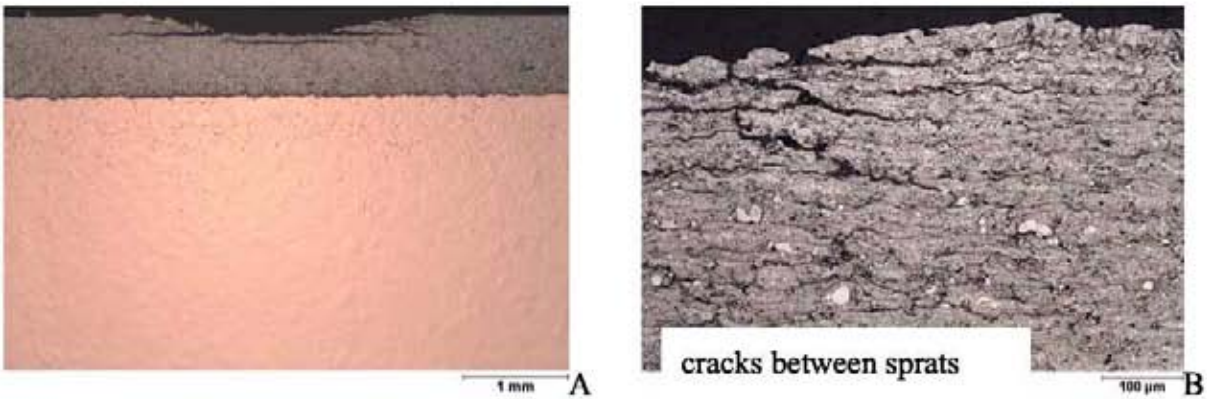

Fig. 64 Cross section of PS-W (1 mm, M105_1, I_{inc} = 160 mA, P_{abs} = 1.2 GWm^{-2}, Δt = 4.3 ms).
A: left side of the crater, B: right side of the crater,

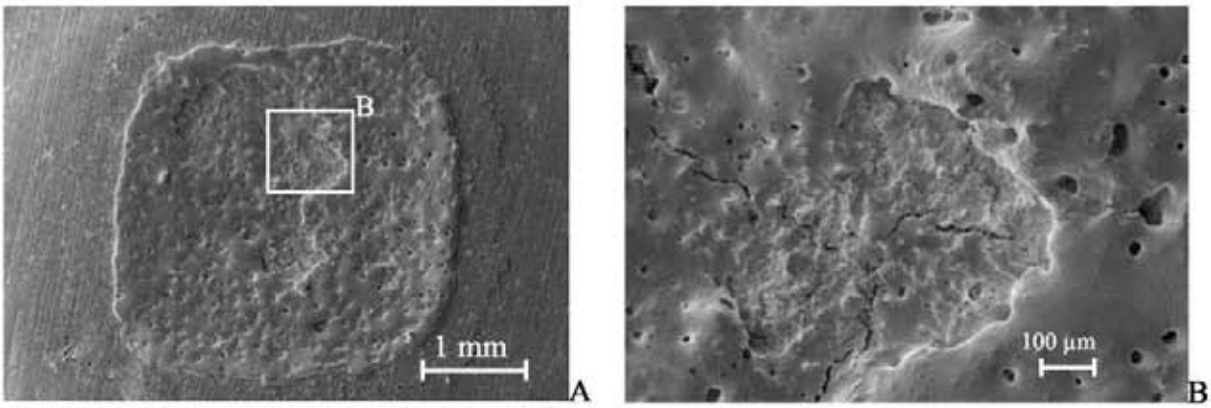

Fig. 65 SEM images of PS-W (5 mm) on Cu (FT76_1).
A: overview, B: center of the crater. I_{inc} = 160 mA, P_{abs} = 1.2 GWm^{-2}, Δt = 4.4 ms

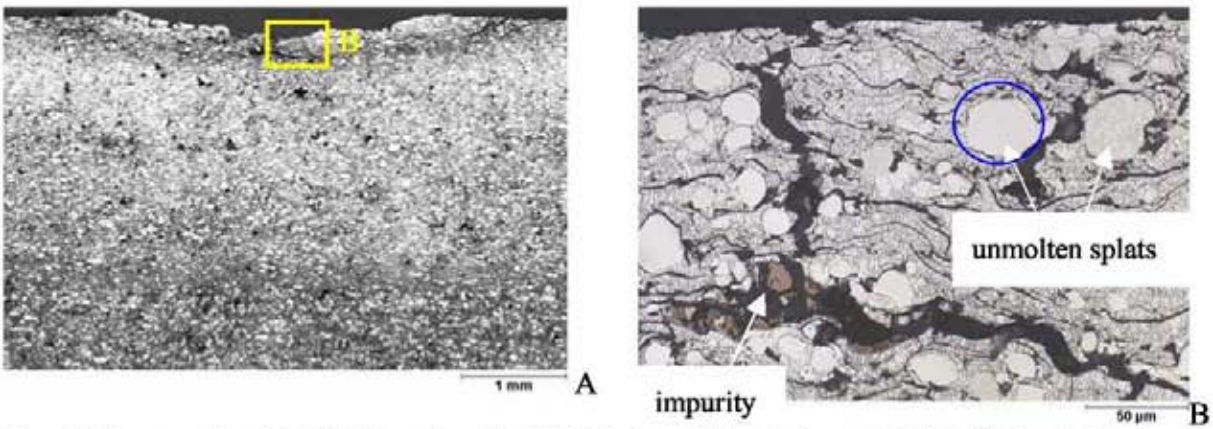

Fig. 66 Cross section of PS-W (5 mm) on Cu (FT76_1, I_{inc} = 160 mA, P_{abs} = 1.2 GWm^{-2}, Δt = 4.4 ms). A: overview, B: crack formation in the center of the crater.

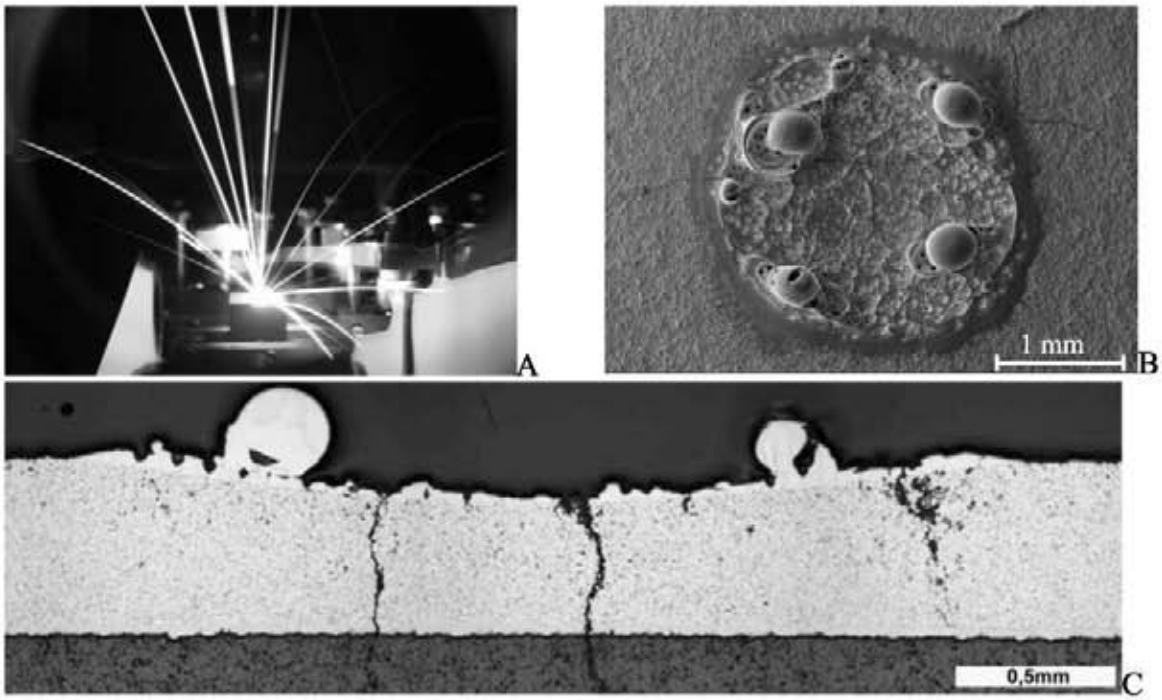

Fig. 67 Digital camera (A), SEM (B), and cross section (C) images of PS-W on graphite at P_{abs} = 1.3 GWm^{-2} Δt =4.5 ms

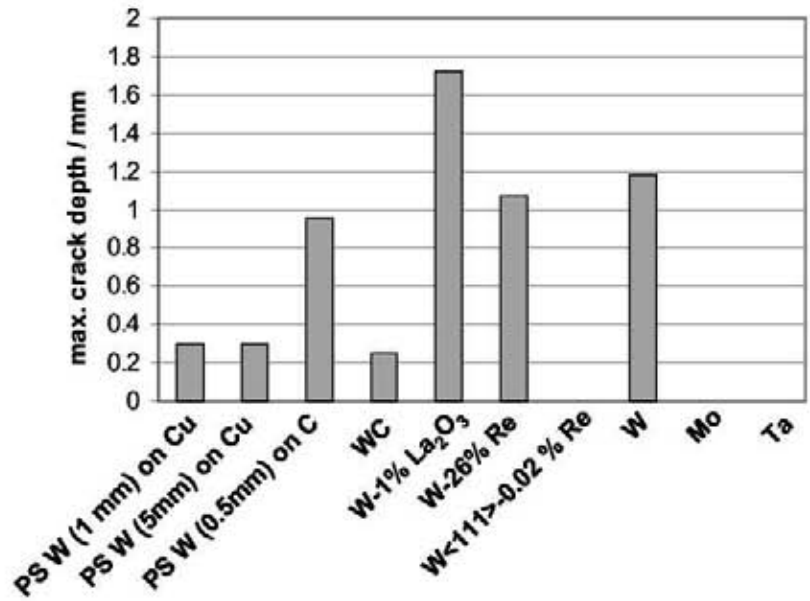

Fig. 68 Maximum crack depths in different high Z materials after plasma disruption tests.
I_{inc} = 160 mA, P_{abs} = 1.2-1.6 GWm^{-2} Δt = 4.3-4.5 ms
*Maximum crack depths in the graph were chosen from inside or outside of the crater in cross section images. Ta, W(111)-0.02%Re, and Mo formed no crack.

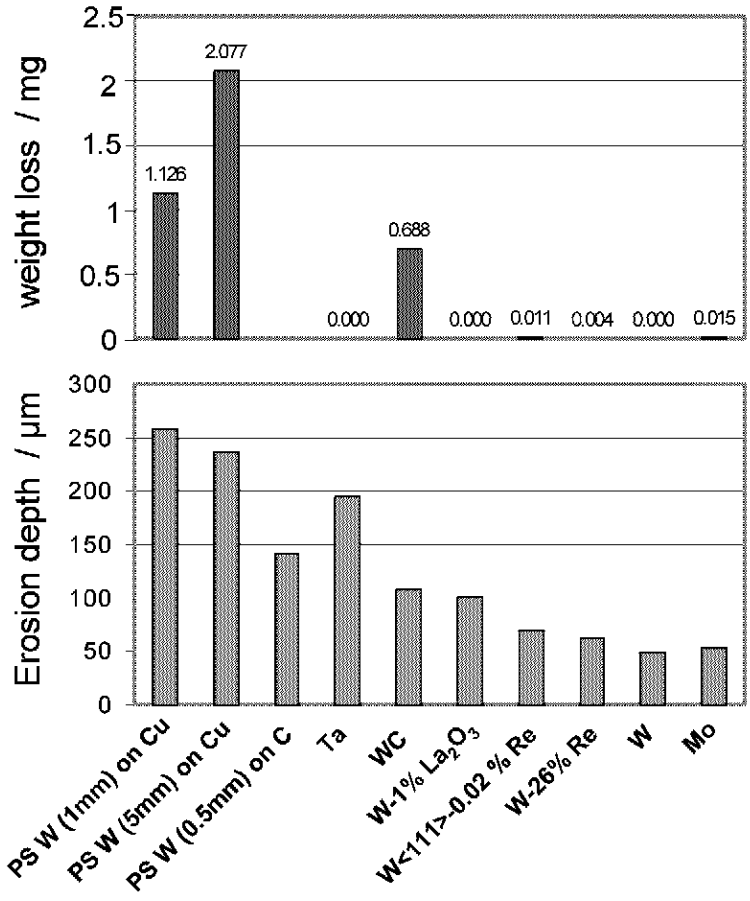

Fig. 69 Variation of weight losses (top) and crater depths (bottom) after disruption tests.
I_{inc} = 160 mA, P_{abs} = 1.2-1.6 GWm^{-2} Δt = 4.3-4.5 ms
*Weight losses of Ta, W-1%La_2O_3, and W were below the detection limit of the microbalance. Weight loss of PSW (0.5 mm) was not measured

Pure sintered W showed clear melting but no detectable weight loss ($\Delta m < 10^{-5}$ g). There was neither droplet formation nor splashing of the melt; all melt layer material recrystallized. Since tungsten is rather brittle below DBTT, a significant crack formation has been observed at the periphery of the melt crater. The resulting crater shows a slight displacement of the melt layer caused by the arising vapor pressure. The resulting crater depth was about 50 µm, and four cracks with the max. depth of about 1.2 mm developed vertical to the surface after the disruption tests (Fig. 55, Fig. 68).

Similar to the pure sintered W, Ta also showed a good resistance against thermal shock. Neither weight loss nor crack formation was noticed after the tests (Fig. 56, Fig. 68, Fig. 69). The sample showed a rather high max. crater depth. The deep hole was probably produced at the end of the thermal loading pulse (Fig. 15B). That is why the Ta showed high crater depth.

Mo showed no crack formation and a low crater depth. The fact that there is no crack in the Mo sample might be attributed to the large grain size and the resulting ductility. The average grain size of the Mo sample for the disruption test was about 0.4 mm in diameter. However, bubbles formed inside the sample just below the surface during disruption tests (Fig. 57B). The reason for the bubble formation in Mo might be the lower melting point compared

to W. Another possible explanation could be the residual gas impurities. If it's used as a PFM in Tokamak reactors, droplets of Mo might enter the vacuum chamber and contaminate the plasma or interact with other plasma facing materials. From these results Mo is less favorable as plasma facing candidate.

Differences between W and single crystal W were investigated. Single crystal W<111> 0.02%-Re showed no cracks (see Fig. 58), however a slightly higher damage than pure W, in particular a higher weight loss and a higher crater depth (Fig. 69). The cross section image was not taken. There is no remarkable improvement in thermal response compared with pure sintered W. This single crystal has higher cost than the pure W and thus is not desirable for PFM in ITER.

Deep cracks were formed in the W 1 %-La_2O_3 alloy, penetrating almost the half thickness of the sample after single disruption test (Fig. 59, Fig. 68). Secondary cracks were observed along the rolling direction. The cracks tend to form in the direction of the elongated grains due to the weak binding forces between the grains. These cracks entered several millimeters into the bulk material. However, these cracks are less critical because they are oriented perpendicular to the surface; they do not form a thermal barrier or ablate the substrate. Obviously La_2O_3 started to evaporate after 1 ms of loading according to a sudden drop of the absorbed current which was not observed in pure W samples. This vapor and the convection of the melt layer deform the molten, which finally results in the formation of a rough resolidified surface. The weight loss was under the detection limit. Only a little amount of vapor seems to have been produced from 1 %-La_2O_3 of the material.

W-Re alloys formed cracks right in the center of the loaded area (Fig. 60). In the cross section, cracks going from the melted layer into the substrate were observed (Fig. 60B). In contrast to pure W, there was no crack formation outside the loaded area for the W-Re alloy. It indicates that the part outside the loaded area was ductile due to the fact that W-Re has a low DBTT (DBTT≈ RT).

Tungsten carbide (WC) showed many 'flower-shaped' droplets after the disruption tests (Fig. 61, Fig. 62). Obviously new phases different from the bulk and from the boundary layer were formed (Fig. 62B). In the loaded area C, WC, WC_{1-x} and α-W_2C were detected by XRD. The tungsten carbide before loading consisted only of WC and small amounts of C. It infers that the phase transition occurred when the surface of WC melted as indicated by the following reactions which may be the phase diagram of tungsten carbide. [94 phase diagram]

$WC\ (l) \rightarrow W_2C\ (\gamma) + \alpha WC_{1-x}$	at approx. 2735 °C and 36.5 at. % of C
$W_2C\ (\gamma) \rightarrow W_2C\ (\beta)$	at approx. 2490 °C and 32.6 % of C
$W_2C\ (\beta) \rightarrow W_2C\ (\alpha)$	at approx. 2190 °C and 32.5 % of C

When the surface of tungsten carbide melts, the molten parts tend to transform into α-WC_{1-x} and α-W_2C because some carbon evaporates. WC is changed into α-W_2C up to 2100 °C and α -WC_{1-x} is formed at about 2700 °C. The concentration of carbon is about 38 % for α -WC_{1-x}. It is assumed that the α -W_2C phase is formed from γ- and β- W_2C during cooling of the surface after thermal loading. In back-scattered electron image, the top of the droplet presented lighter than the bulk material. The light color implies heavy elements. Therefore the top of the droplet is supposed to be α -W_2C (32.5 % of C), the bulk is WC (50 % of C), and the intermediate phase is α -WC_{1-x} (38 %). The cracks formed in tungsten carbide resulted in a

catastrophic failure of the test sample. This intense crack propagation is not favorable for plasma facing materials.

Similar to tungsten carbide, plasma sprayed W coatings on Cu showed severe damages after plasma disruption tests, in particular the highest weight losses and crater depths. Two types of plasma sprayed W on Cu were tested; one with a thickness of 5 mm, and another one with a thickness of 1 mm.

After the disruption tests, the two plasma sprayed W coatings on Cu showed a different surface morphology. The thermal shock resistance of the coated materials is affected by several factors; presence of micro cracks, porosity, thickness of the coating, and the difference in CTE between the substrate and the coatings [100]. The behavior of the 1 mm thick W coating was characterized by a large number of droplets, and cracks (Fig. 63, Fig. 64). The porosity of these coatings and the microstructure with elongated splats are the main reasons for a reduced thermal conductivity. Hence overheating of the melt layer and boiling effects become essential at lower incident energy density in comparison with monolithic sintered tungsten. The crack growth between the individual splats (Fig. 64C) and the subsequent detachment from adjacent layers may be another possible source for the generation of tungsten dust particles.

On the other hand, the 5 mm thickness PS W coating had no droplets, however, bubbles, voids after boiling, and cracks have been detected in the loaded area (Fig. 65, Fig. 66). This 5 mm coating has a higher porosity than a 1 mm W coating. These pores in the 5 mm coating sample can degas, resulting formation of bubbles and no droplets of the surface. Looking at the microstructure in the cross section, there are some big globular grains distributed in small grains (Fig. 66 B). These globular objects are supposed to be non-molten powder particles during plasma spraying. A detailed analysis of the cross sections of these samples showed a brown phase inside the cracks (Fig. 66 B), which seems to be impurities during the plasma spraying process.

During testing of plasma sprayed W coating on graphite, trajectories from emitted particles originating from PS-tungsten coatings were characterized by bright curved traces, suggesting the creation of heavy droplets, which are moving at a relatively low speed (Fig. 67A). The crack growth between the individual splats and the subsequent detachment from adjacent layers may be another possible source for the generation of tungsten dust particles. The cross section image showed that cracks penetrate the whole W layer and pass through the graphite substrate with a depth of 0.9 mm (Fig. 67C, Fig. 68). Crater depth is 141 μm that is somewhat lower than the other plasma sprayed W coatings with a copper substrate. This sample has isotropic coated grains and very low porosity compared to PSW on Cu samples. The lower porosity results in higher diffusivity and explaining the smaller crater depths. However, the low porosity results in less thermal shock resistance due to residual deformability causing crack formation. As a conclusion the behavior of this material is less favourable compared to sintered W; droplets and pores were formed also for the plasma sprayed W on graphite sample surfaces, and showed more intense particle emission compared with pure sintered W.

The properties of plasma sprayed coatings differ drastically with spraying and conditions such as spraying atmosphere, size and velocity of the coating powder, spraying

distance, and substrate surface preparation before deposition. This is the reason why systematic experiments with different porosity and spraying parameters are necessary.

4.2.3.2 VDE tests

The surface (observed by SEM) and cross section images of these samples after VDE tests are shown in Fig. 70-Fig. 79. Characterization of the WC sample was not possible because the sample was broken into pieces after the VDE shots.

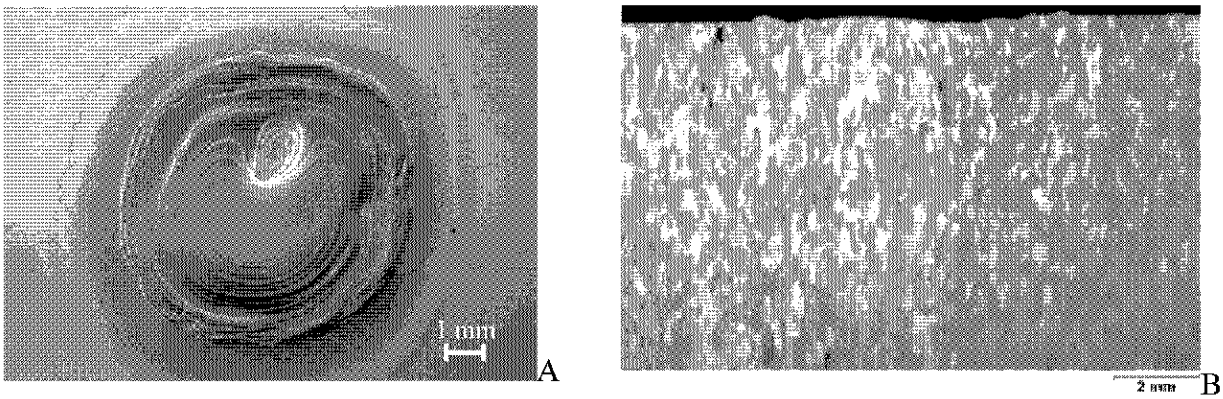

Fig. 70 SEM (A) and cross section (B) images of pure W.
(M168_6, I_{inc} = 320 mA, P_{abs} = 593 MWm^{-2}, Δt = 89 ms).

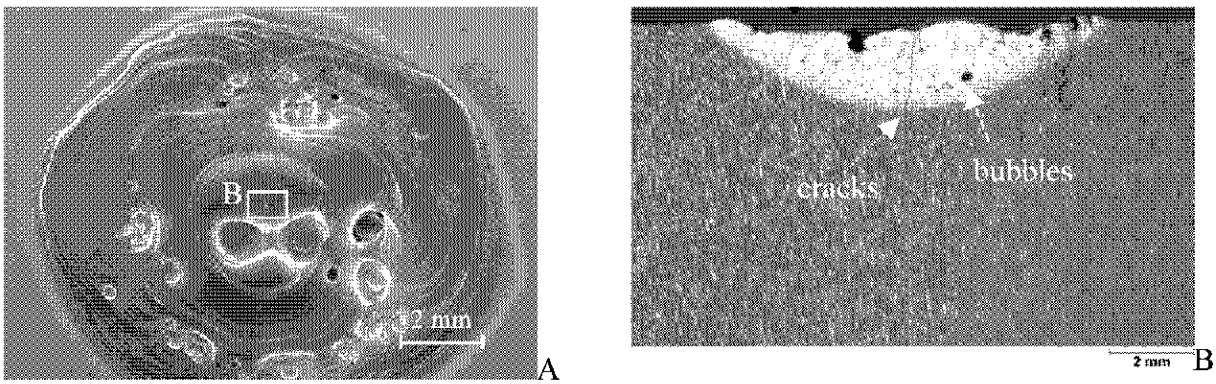

Fig. 71 SEM (A) and cross section (B) images of Mo (M20_123, I_{inc} = 320 mA, P_{abs} = 736 MWm^{-2}, Δt = 88 ms).

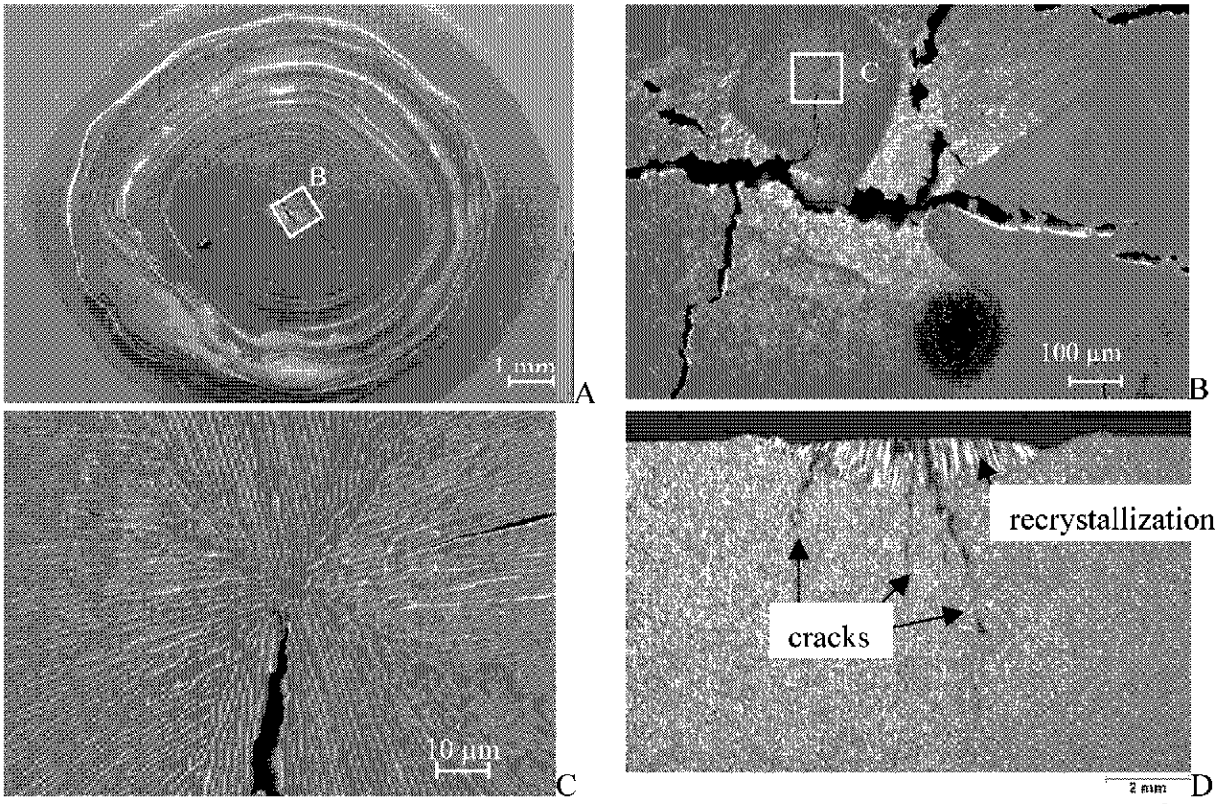

Fig. 72 SEM (A-C) and cross section (D) images of W-26%Re (M39_50, I_{inc} = 320 mA, P_{abs} = 609 MWm^{-2}, Δt = 89 ms). A: overview, B: crack formation at the center of the crater, C: microstructure of the center of the crater

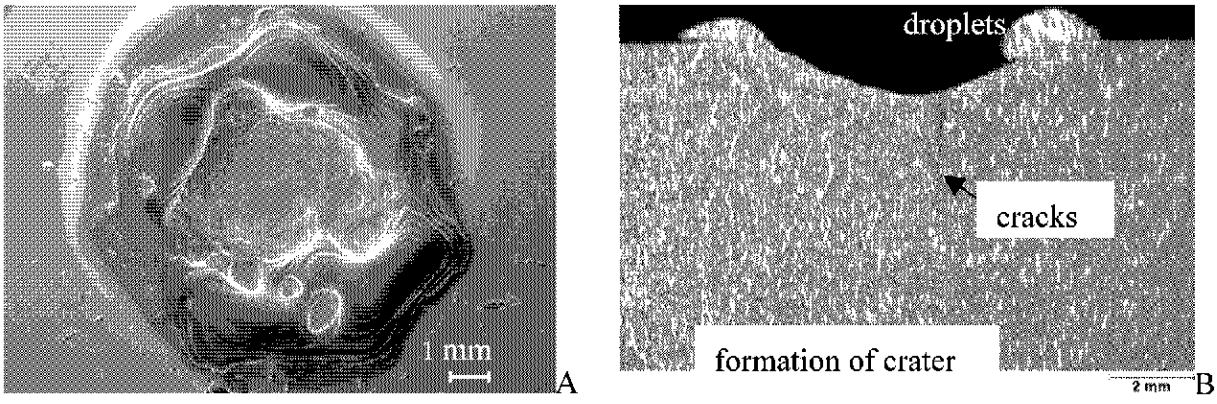

Fig. 73 SEM (A) and cross section (B) images of W-1% La_2O_3 (M129_2, I_{inc} = 320 mA, P_{abs} = 583 MWm^{-2}, Δt = 89 ms).

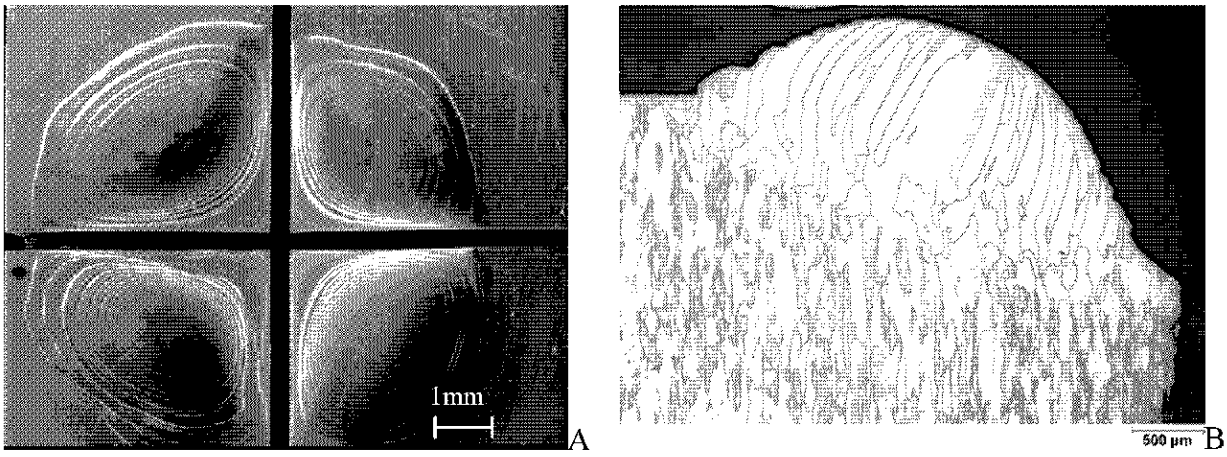

Fig. 74 SEM (A) and cross section (B) images of W-1% La_2O_3
(M171_4d, I_{inc} = 320 mA, P_{abs} = 622 MWm^{-2}, Δt = 90 ms).

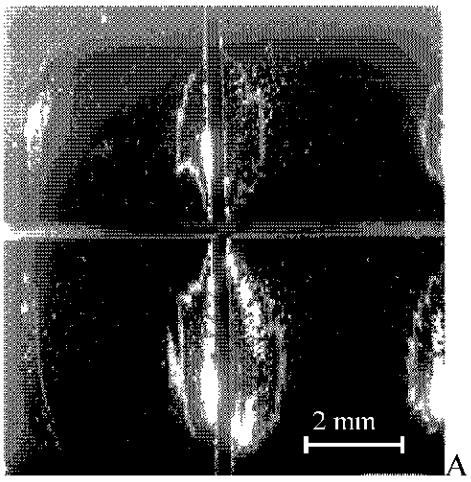

Fig. 75 SEM (A) image of W-1% La_2O_3
(M171_5d, I_{inc} = 320 mA, P_{abs}=206 MWm^{-2}, Δt = 300 ms).

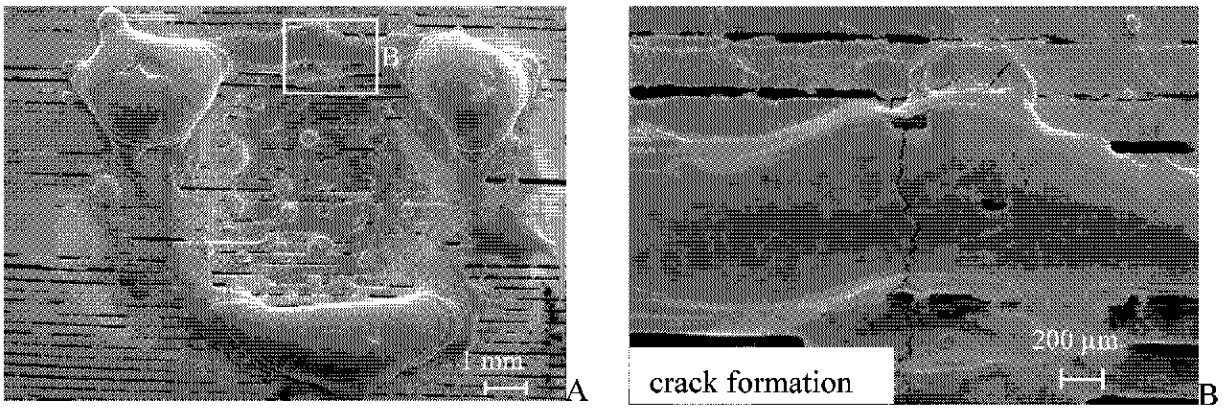

Fig. 76 SEM images of W lamellae with a thickness of 0.2 mm module (cut from an actively cooled divertor module, FT84_1a). I_{inc} = 320 mA, P_{abs} = 658 MWm^{-2}, Δt = 89 ms
A: overview, B: top of the crater

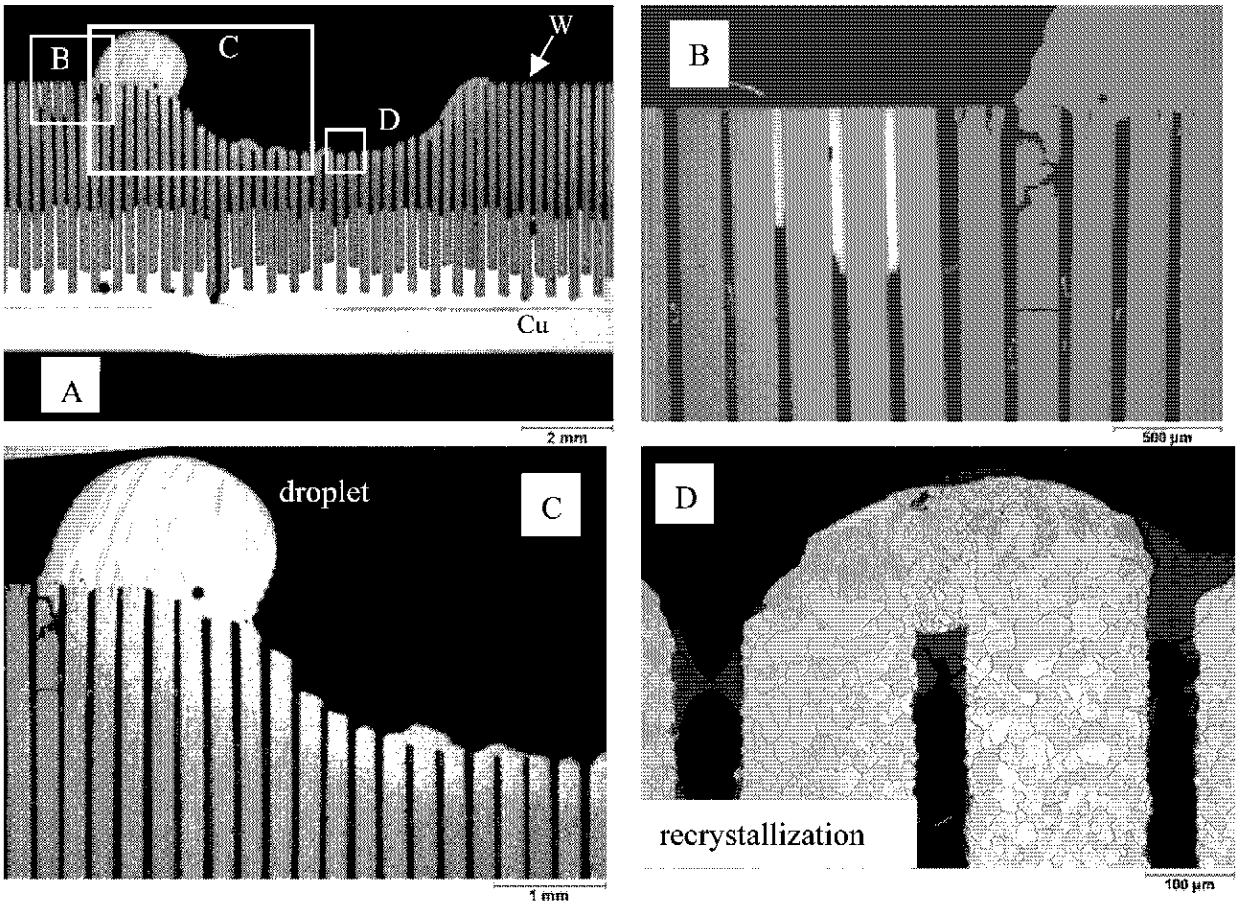

Fig. 77 Cross section of W lamellae with a thickness of 0.2 mm (part of an actively cooled divertor module) (FT84_1a, I_{inc} = 320 mA, P_{abs} = 658 MWm^{-2}, Δt = 89 ms, loaded area = 29 mm^2).

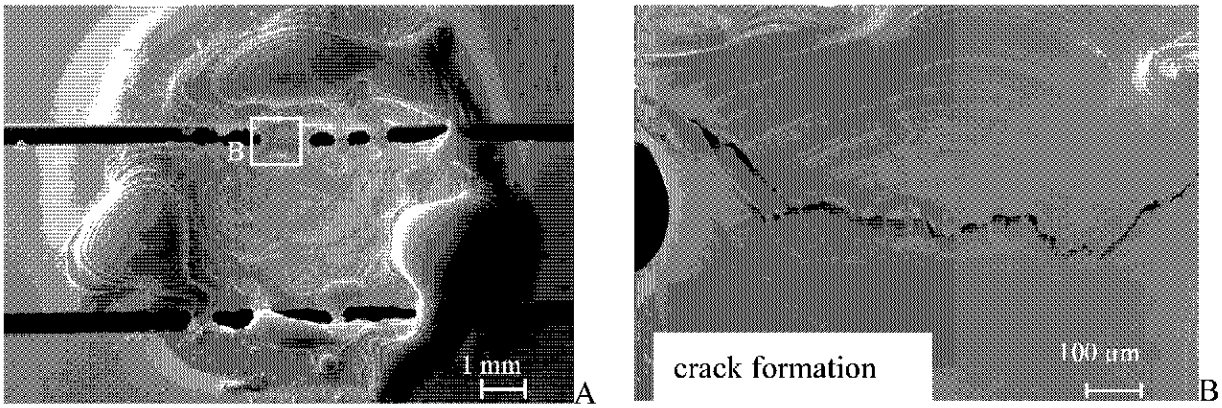

Fig. 78 SEM images of W1%La_2O_3 lamellae with a thickness of 4 mm (cut from an actively cooled divertor module, FT89_3a). I_{inc} = 320 mA, P_{abs} = 723 MWm^{-2}, Δt = 88 ms
A: overview, B: melted part between the lamellae

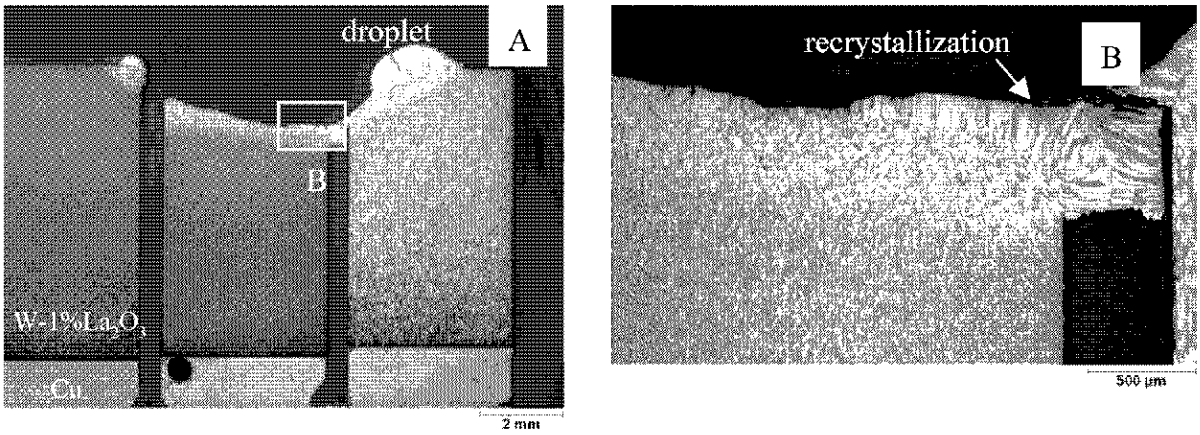

Fig. 79 Cross section of W-1%La_2O_3 lamellae with a thickness of 4 mm (cut from an actively cooled module). (FT89_3a, I_{inc} = 320 mA, P_{abs} = 723 MWm^{-2}, Δt = 88 ms, loaded area = 29 mm^2).

The variation of melt layer thickness and the max. crack lengths in different high Z materials after the VDE tests is shown in Fig. 80. After VDE tests, W and W-alloy at E_{abs} of 60-70 MJm^{-2} for 90 ms caused melt layer thickness of 1.2-1.5 mm except W 1% La_2O_3 (Fig. 80, Fig. 73). The W-La alloy and W-lamella structure ejected the melting part and formed a crater with a depth of 1.2-1.5 mm.

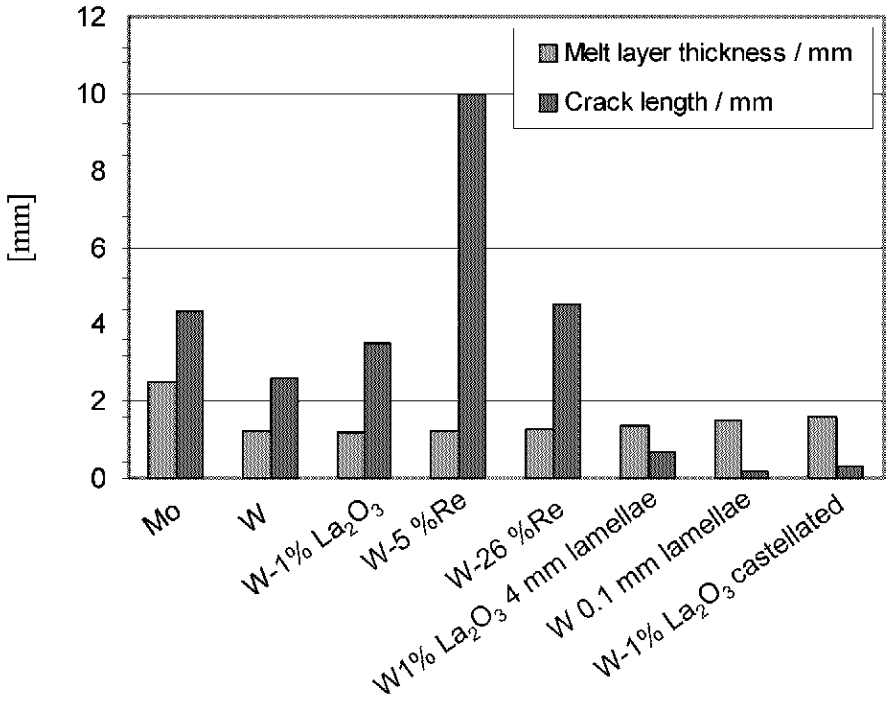

Fig. 80 Variation of maximum crack depths and melt layer thickness after VDE tests.
*d_{melt} = the sum of residual melt layer thickness and a crater depth
I_{inc} = 320 mA, loaded area = 29 mm^2, E_{abs}= 52-65 MJm^{-2} Δt = 90 ms

Pure W showed the smallest crack formation compared to other bulk materials, the residual melt layer thickness was about 1.25 mm (see Fig. 70, Fig. 80). Mo also showed melt layers with approx. 2.2 mm depth, crack formation with up to 4.4 mm depth and bubble formation after the VDE tests (Fig. 71).

After the VDE tests as well as after the plasma disruption tests, W-Re alloys tend to form cracks crossing diagonally right in the center of the loaded area (Fig. 72). The crack length was decreased as the concentration of Re became high from 5 % to 26 % because the material with higher Re concentration is more ductile (Fig. 80). Nevertheless, the melt layer of pure W is thinner compared to the W-Re alloys because the thermal conductivity of W-Re alloys is lower than the pure W.

The W-La alloy tends to form cracks both in the center and outside the beam exposed area (Fig. 73 B). Some test samples showed cracks propagated to the middle of the bulk material. But these cracks are less critical because they are oriented perpendicular to the surface and the substrate rarely ablates.

Generally craters are formed when the effect of impinged energy is higher than the cooling speed by heat conduction, and the evaporation is increased. La_2O_3 was evaporated in the heating phase. This can be proven by the sudden drop of the absorbed current. The escaping vapor exerts a large recoil force and the molten metal is expelled from the cavity. Melt ejection also takes place when the vapor recoil force exceeds the surface tension force at the periphery of the sample [122].

Castellated W-1%La_2O_3 sample in Fig. 74 shows also melting and crater formation after VDE loading as well as the bulk sample in Fig. 73. However, there was no droplet formation in the castellated sample, whereas a clear droplet formation was observed in the bulk W-1%La_2O_3 sample at almost identical heat fluxes in Fig. 73. The castellated samples are supposed to be smaller in the vapor recoil force to produce melt splashing. The produced vapor might escape through castellation and the resulting vapor recoil pressure reduces.

During the VDE tests with P_{abs}=206 MWm^{-2}, for longer beam pulses Δt = 300 ms, the recrystallization proceeded and the melt layer resolidified in its original position (Fig. 75). Obviously, the applied heat flux did not generate high surface tension in the molten layer and vapor recoil pressure was not sufficient to initiate the melt ejection process.

Two different thicknesses of lamellae were chosen for a comparison of the material behavior. The melt ejection was clearly visible on the surface of both lamellae types after the VDE tests. Both lamellae showed similar surface morphologies with melting, formation of a rim around the crater, and of droplets (Fig. 76, Fig. 78). The 0.2 mm thick lamellae showed relatively short cracks and a crater with a depth of 1.5 mm (Fig. 80, Fig. 76, Fig. 77). These micro cracks in the 0.2 mm lamellae were already formed after the thermal fatigue test [9,10] and did not show any crack growth during the VDE tests. After identical VDE tests, the 4 mm lamellae showed a crater with a depth of 1.38 mm and cracks in the left and middle lamellae (Fig. 80, Fig. 78 B, Fig. 79), which is far longer compared to the 0.2 mm lamellae. An interesting behavior is that molten metals covered some of the in-between area of the lamellae with columnar structure, and separated by perpendicular cracks (Fig. 76B, Fig. 78B). Moreover, there are relatively bigger grains in the whole right lamella (Fig. 79A). Such crack formation and grain growth are might have already occurred during thermal fatigue testing. Thus the lamellae structure showed longer melt layer thickness than the bulk material, but for these lamellae, it was a rather effective method to reduce the formation of cracks. It is caused by dispersion of the thermal stresses not only onto the surface but also onto the side of the lamellae. However, the lamellae structure showed crater and droplets formation, which is less favorable for PFMs.

4.2.3.3 Effect of samples preheating

Fig. 81 shows surface morphologies, digital camera image, current and surface temperature plot, and cross section image of the samples preheated to 200 - 460 °C under plasma disruption conditions with P_{abs} = 1.3 GWm^{-2} for Δt = 4.4 ms. The cross section image showed melting, bubble formation, micro cracks less than 50 µm deep, and long cracks up to 500 µm depth outside the melt layer (Fig. 81E). The distance between the long cracks and the melt layer decreases with increasing preheating temperature. The sample preheated at 200 °C showed long cracks with 1 mm away from the melt layer, while the sample preheated at 400 °C showed long cracks in the vicinity of the melt layer. Long and micro cracks might be associated with brittleness and fast cooling of the surface temperature. For preheated samples, crater formation, micro cracks inside the crater and longer cracks (approx. 1 mm) outside the crater. Some bubbles were also present in the resolidified melt layer which has the columnar structure of the melt layers. In contrast, non-preheated samples showed only crack formation inside and/or outside the loaded area and formation of a crater. Obviously, the preheated samples are faster to reach their melting point and boiling point. Moreover, preheated samples showed a decrease of absorbed current I_{abs} (Fig. 81D), while non-preheating sample only showed oscillation of I_{abs} (Fig. 85B). The time until I_{abs} starts to decrease was earlier for the samples preheated at higher temperature. It is 1 ms for the sample preheated at 300 °C compared to 0.5 ms for 460 °C.

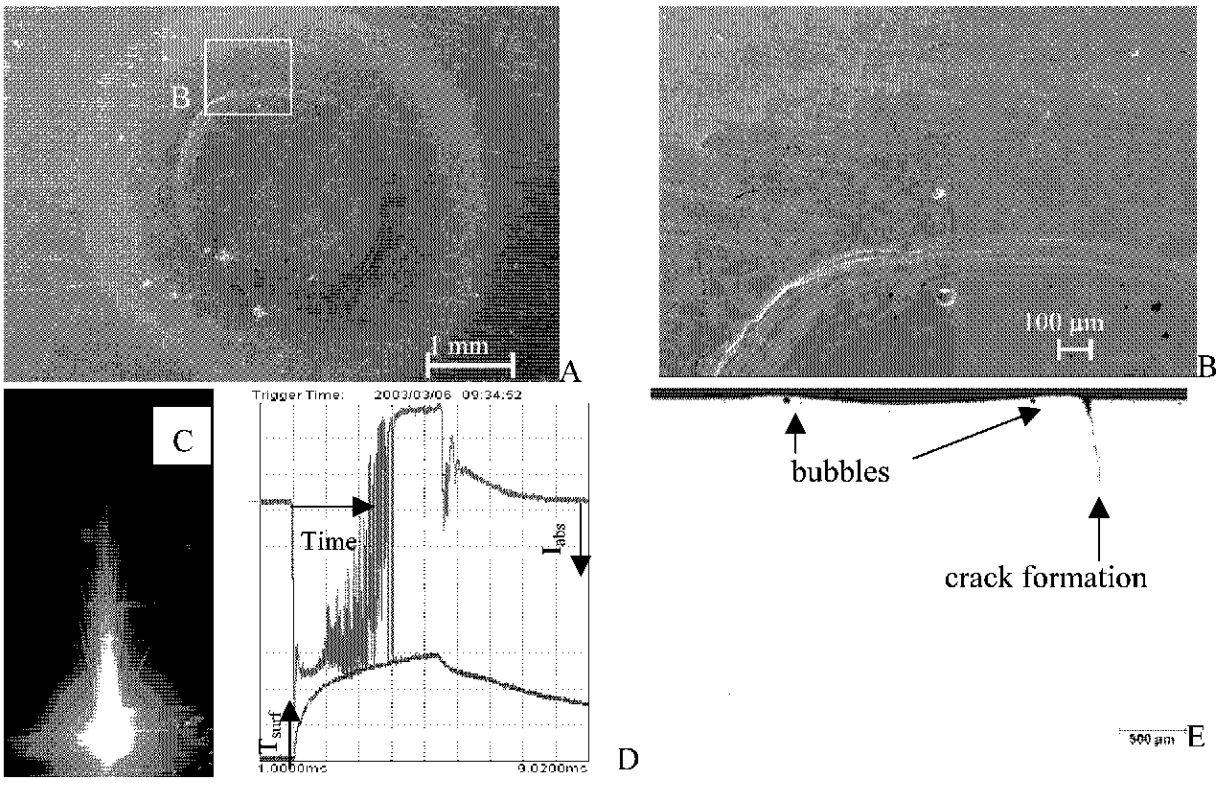

Fig. 81 SEM (A-B), particle emission (C), current (D), and cross section (E) images of pure W preheated at 400 °C (M168_29). P_{abs} = 1.5 GWm^{-2}, Δt = 4.4 ms
The I_{abs} even decreased into a negative value, which indicates thermoionic emission.

Fig. 82 shows the weight loss vs. preheating temperature for sintered tungsten. In such case erosion became higher compared to RT. The curve shows a maximum at 300 °C and slightly decreases by 0.02 to 0.04 mg for samples preheated at 400 and 460 °C. This decrease

of the weight loss for preheating over 400 °C was also reported by V.N. Litunovsky et.al [56]. The reason for the highest weight loss for the sample preheated at 300 °C is not clear yet. Maybe the increased evaporation at higher preheating temperature raised the density of the vapor cloud, and suppressed further weight loss. As an average, the weight loss for preheated samples was increased in the range of 30 to 180 μg compared to samples at RT identical heat fluxes.

Under VDE conditions, the crack formation of sintered W samples was observed up to 400 °C and at 500 °C there was no crack formation. VDEs have longer pulses 90 – 300 ms compared to plasma disruptions (1-5 ms) and the surrounding area can be heated up above DBTT and became ductile.

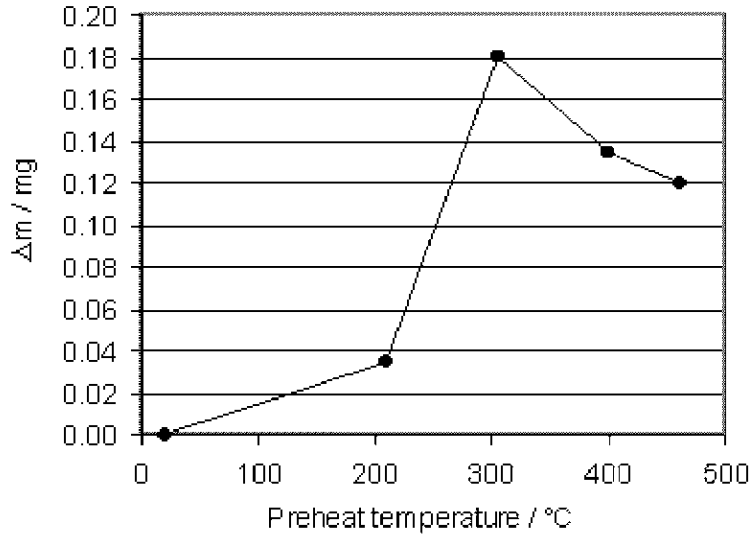

Fig. 82 Weight loss (Δm) of W samples loaded at P_{abs} = 1.4-1.5 GWm^{-2} for 4.4-4.5 ms without and with preheating up to 460 °C.

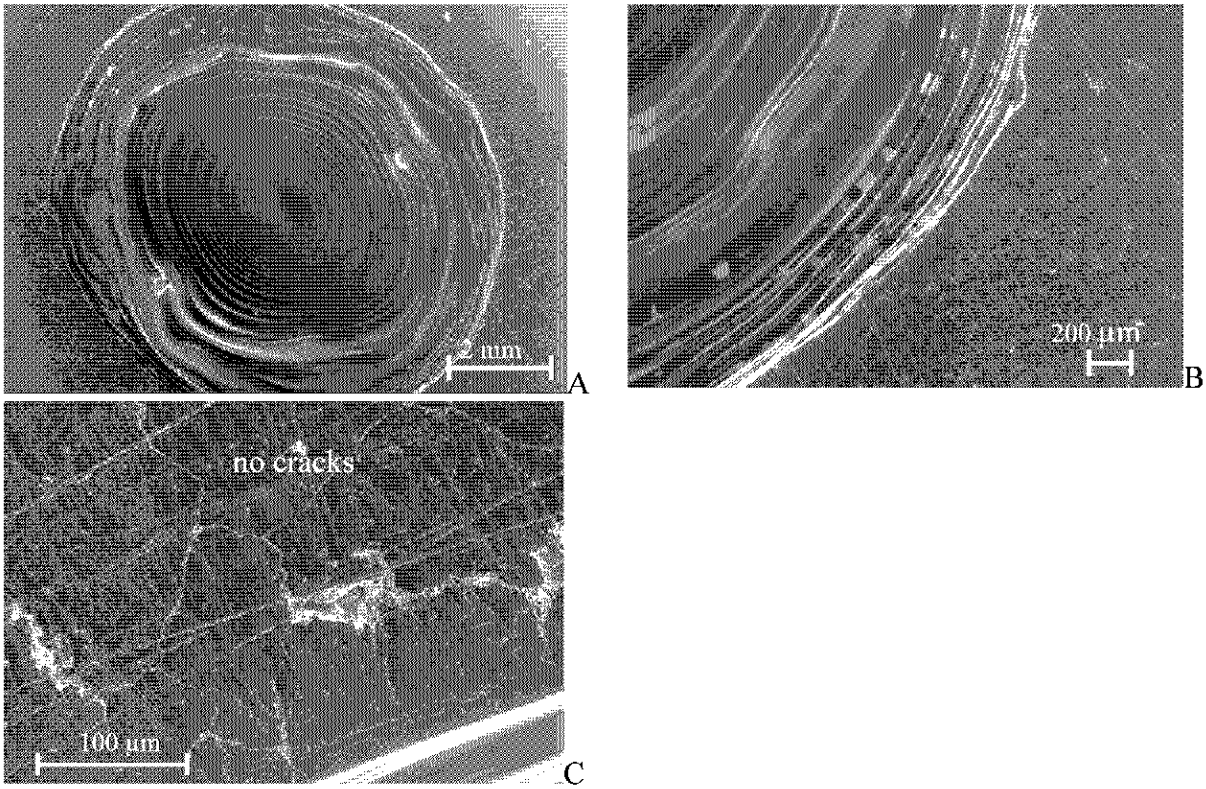

Fig. 83 SEM images of pure W preheated at 500 °C (M168_63). P_{abs} = 660 MWm^{-2} , Δt = 90 ms

4.2.3.4 Influence of the loaded area

Fig. 49 and Fig. 55 show results for identical heat fluxes and pulse duration. However, the sample in Fig. 55 with smaller loaded area clearly shows recrystallization layers and a visible crater with 50 µm depth, whereas another sample with identical composites in Fig. 49 with larger loaded area exhibits no melting. The different conditions between these two samples were incident currents and loaded areas. In Fig. 84, the variation of crater depth as a function of P_{abs} at different loaded areas is plotted.

The plots prove that the size of loaded areas has an influence on the crater depths. For example, a sample loaded at E_{abs} = 10 MJm^{-2} with a loaded area of $(3.5)^2$ mm^2 showed almost no crater (–6 µm). In contrast, another sample with identical heat flux but a reduced loading area of $(2.7)^2$ mm^2 showed a crater depth of 31 µm. Thus a reduction in loading areas tends to result in larger erosion depths at identical heat fluxes. This may be due to vapor shielding. Sample with the larger loaded area has a dense cloud compared with the small loaded area, which enhances a vapor shielding, and finally becomes lower erosion. The detail of vapor shielding effect is discussed in Chap. 4.2.3.5. Another assumption is that for smaller loading area, vapor forms faster in the center, and the vapor recoil pressure causes more melting, which are ejected from the loaded area. The overview of a sample loaded with larger loading area (3.4·3.4 mm^2) at P_{abs} = 1.3 GWm^{-2} for 5 ms, did not show a visible melting but only cracks inside and outside the loaded area (Fig. 49). The loaded surface had tensile stress during thermal loading but the surface was still brittle with larger loading areas, forming cracks inside the loaded area (Fig. 49).

Therefore, the size of the loaded area has to be taken into account for the evaluation of erosion data and extrapolation to ITER application.

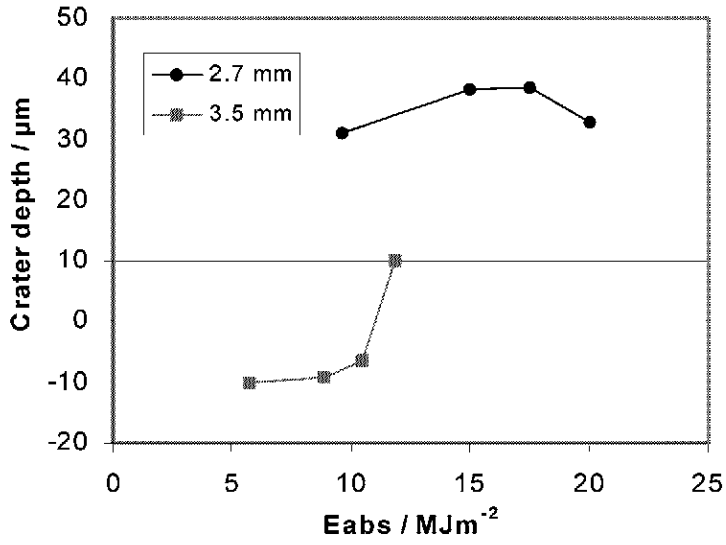

Fig. 84 Loaded area effect of W samples for pulse duration of 5 ms.
*2.7 mm : loaded area of 2.7×2.7 mm^2, 3.5 mm: loaded area of 3.5×3.5 mm^2.
Negative values mean the formation of convex shape.

4.2.3.5 Vapor shielding effect

Fig. 85 shows the surface morphologies after testing and the respective released particles which were monitored by a digital camera for absorbed power densities of 0.64, 1.2, 1.6, and 2.1 GWm^{-2} (corresponding to I_{inc} = 80, 160, 200, and 280 mA). For I_{inc} < 80 mA, there is only negligible particle emission. Above this level, clear emission of particles was observed. The intensity and the brightness of the particle trajectories increased with the beam current. Evidence of a clear melt crater was found at an incident beam current of 160 mA, i.e. well above the onset of the particle emission process. Hence, tungsten surfaces exposed to 5 ms beam pulses below the melting threshold are a source for hot or molten W-dust particles. The particle release might be associated with a brittle destruction process in analogy to CBMs. The release of particles is correlated with spikes in the current plot. At P_{abs} of 1.6 GWm^{-2}, the time interval of spikes is about 0.6 ms (Table 17). This kind of spikes in the range of particle emission was only observed in W samples (Fig. 85).

The major fraction of the particle trajectories which are emitted for $I_{inc} \geq 240$ mA consists of two separate segments: the first a faint thin line with decreasing intensity, and the second a line which is associated with a strong increase in the particle brightness after traveling with a distance of approx. 5 to 20 cm. This effect was also observed for W-1% La_2O_3 and plasma sprayed W. Fig. 86 shows the existence of La_2O_3 vapor over the loaded area (green color) and intermittent lines of emission. Other materials such as CBMs and other metals with lower melting points always showed continuous light emission.

Up to now there is no clear explanation for the existence of two separate intensities of the trajectories. A phase change from liquid to solid in the particle surface is one possible explanation. The existence of a dense, absorbing a vapor cloud could be the second cause.

After a dense vapor cloud is formed, the cloud excites the particles again. The third assumption is that reflected electrons (47% of the incident electrons of W) ionize the ablation vapor, exciting the ejected particles.

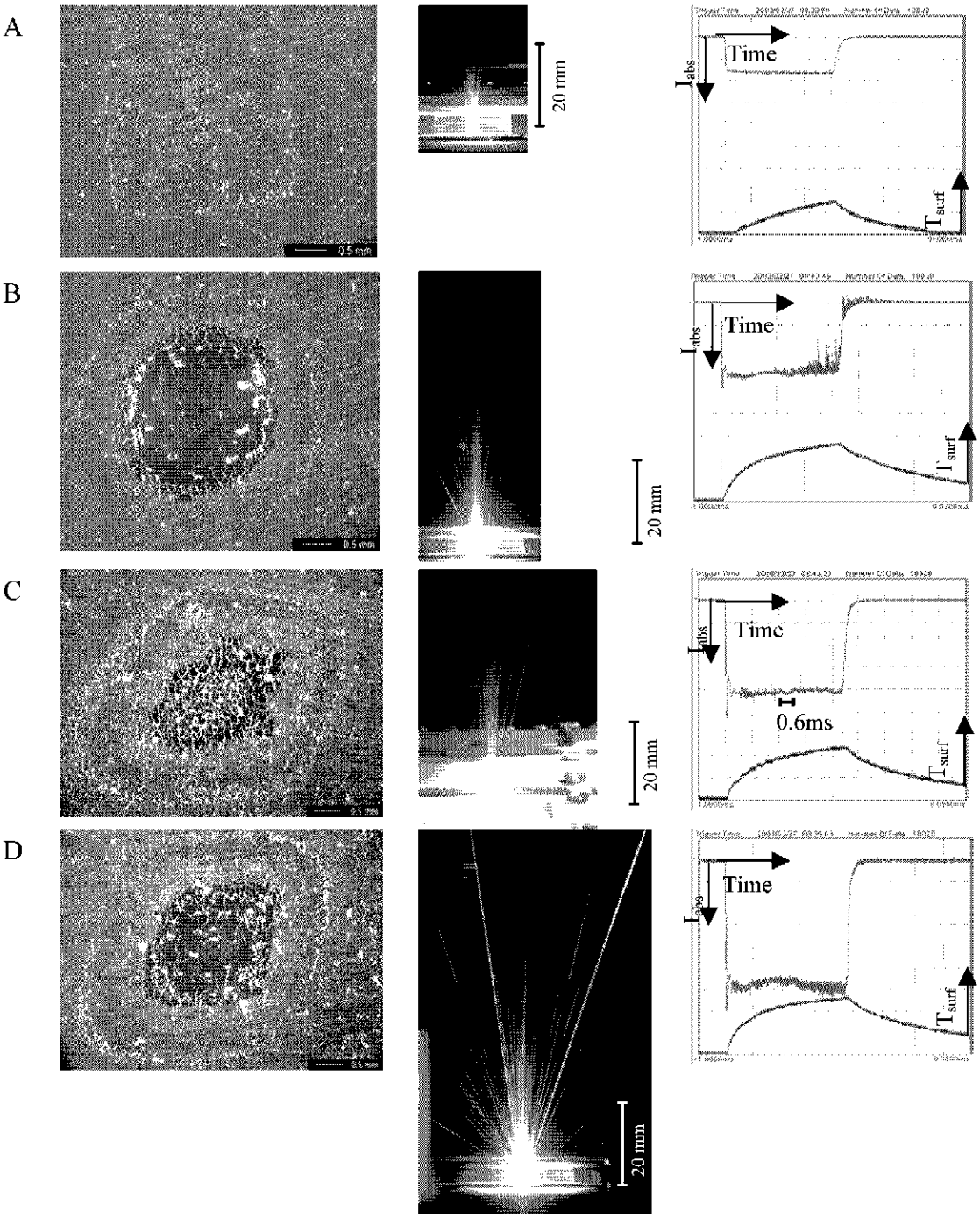

Fig. 85 Optical macrographs, digital images and current and surface temperature profiles of pure W (loaded area = 2.7·2.7 mm^2, see Table 17).
A (M168_43_2): I_{inc} = 80 mA, P_{abs} = 0.64 GWm^{-2}, Δt = 4.1 ms
B ((M168_43_4): I_{inc} = 160 mA, P_{abs} = 1.2 GWm^{-2}, Δt = 4.4 ms
C ((M168_43_6): I_{inc} = 200 mA, P_{abs} = 1.6 GWm^{-2}, Δt = 4.4 ms
D ((M168_43_9): I_{inc} = 280 mA, P_{abs} = 2.1 GWm^{-2}, Δt = 4.5 ms

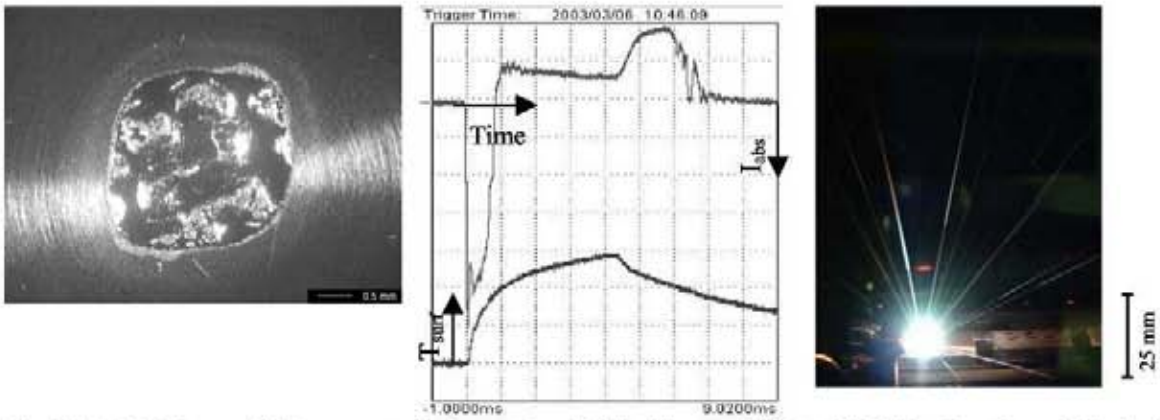

Fig. 86 Optical image (left), current plot (center), and digital image (right) of W-1%La_2O_3 at I_{inc} = 160 mA, Δt = 4.9 ms preheated at 400 °C (M129_1_5).

For medium energy densities (e.g. P_{abs} = 1.2 GWm^{-2}, Fig. 55, Fig. 84C) there is only negligible ejection of the liquid melt layer from the heated area. Nevertheless, a clear erosion crater is formed due to the high vapor pressure which tends to eject the melt outside the loaded area. At high heat flux, more splashing and material degradation take place (Fig. 87).

With increasing beam current, an additional process, namely intense boiling of the melt layer, has been observed (P_{abs} = 2.1 GWm^{-2}, Fig. 88). Obviously, some local spots were overheated exceeding the boiling temperature of tungsten. In addition intense convection of the melt occurs [122, 142 - 144]. These processes might be the source for an additional release of liquid W particles. Some cracks penetrating the boiling pores (Fig. 88B) were formed after bubble formation. This might be correspondent to the local overheating during loading with beam scanning.

The distances from the edge of the melt to the crack formed are in the range from 0.63 to 1.38 mm at absorbed power densities P_{abs} of 1 to 2.3 GWm^{-2} for pulse duration of 4 to 4.5 ms. The distance between the crack and the heat affected zone increases with power density.

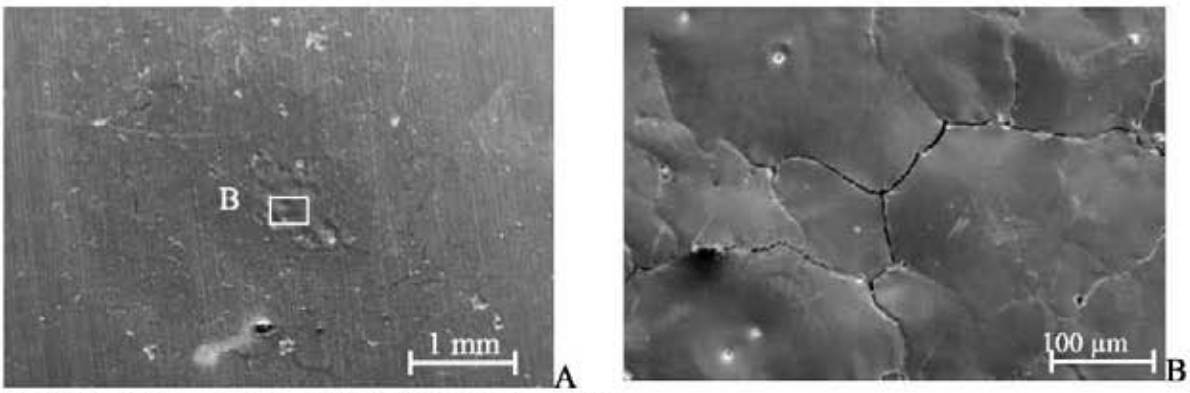

Fig. 87 SEM images of pure W (M168_43_6, Fig. 85C). P_{abs} = 1.6 GWm^{-2}, Δt = 4.4 ms, loaded area = 7.23 mm^2

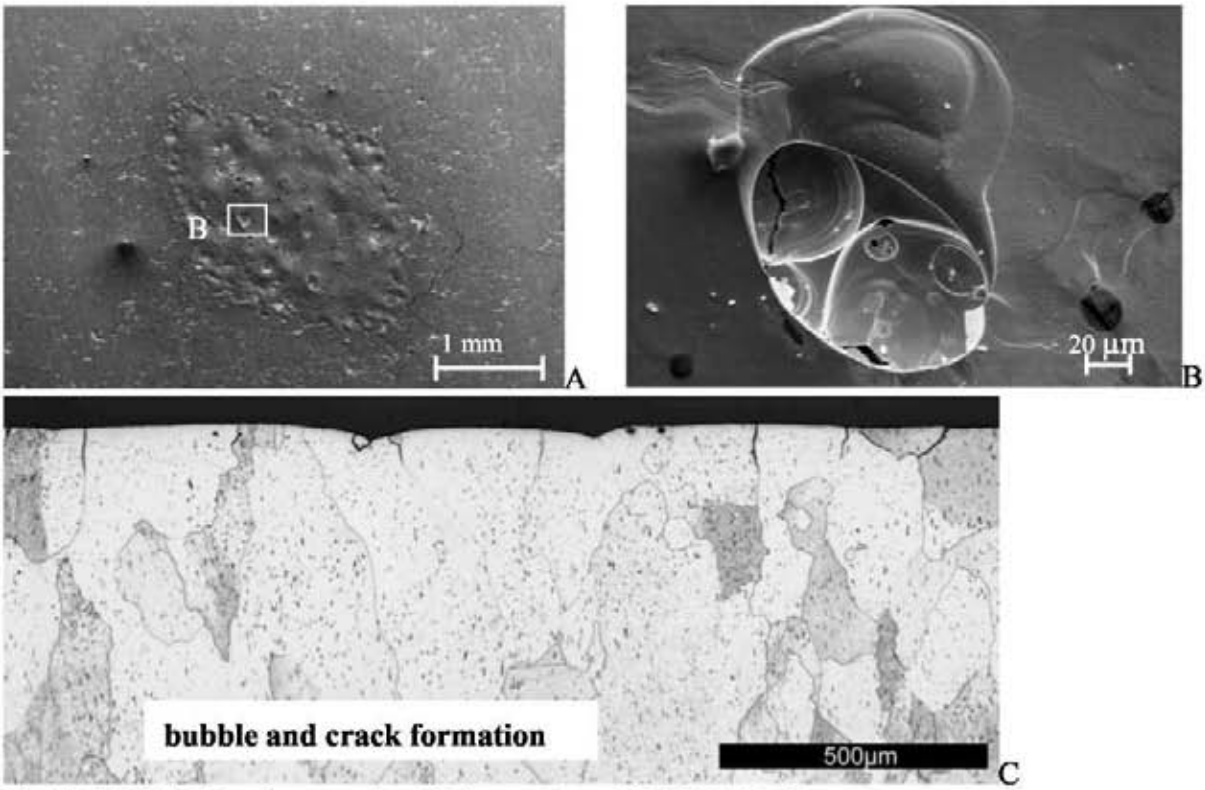

Fig. 88 SEM (A, B) and cross section (C) images of pure W (M168_43_9).
P_{abs} = 2.1 GWm^{-2} , Δt = 4.5 ms, loaded area = 7.23 mm^2

Erosion depths also indicate a shielding effect. A variation of the erosion depth with absorbed power density for pure W and plasma sprayed W (Fig. 89) showed 2 peaks at P_{abs} = 1.2, 1.9 GWm^{-2} with increasing absorbed power density. As the heat flux increases the surface started to melt and showed a convex shape with a negative erosion depth at P_{abs} of 0.8 GWm^{-2}. Between P_{abs} of 0.8 GWm^{-2} and 1.2 GWm^{-2}, the erosion depths increased. The erosion depths show a slight decrease in the range between P_{abs} = 1.2 ~ 1.6 GWm^{-2} and again an increase between P_{abs} = 1.6 ~ 1.8 GWm^{-2}. At P_{abs} of 1.6 GWm^{-2} (I_{inc} = 180 mA), the extent of particle emission also slightly decreased (Fig. 85). For example, the crater depth of plasma sprayed W on graphite at P_{abs} of 1.2 GWm^{-2} for 4.5 ms was found to be 140 µm and only 20 µm at P_{abs} of 1.5 GWm^{-2}.

The collected W particles also indicate the formation of a vapor cloud. W particles were collected with the set up (Ref. Fig. 93) and observed by SEM and TEM. The loading condition was P_{abs} = 1.2 GWm^{-2} for Δt = 4.4 ms. After 5 shots, there has not been single W particle detected on the collecting nets. However, W was determined by EDX on the stainless steel foil set around the sample, although there was no clear evidence for the particle. Increasing the number of repeated shots (n = 30), particles with 20-50 nm in diameter were detected by TEM on the TEM grids (Fig. 90). These globular objects were found to be arranged primarily separated from each other, and agglomerates of a few particles have been observed on the nets. These objects are supposed to originate an agglomeration of the W film or the condensation in the vapor phase.

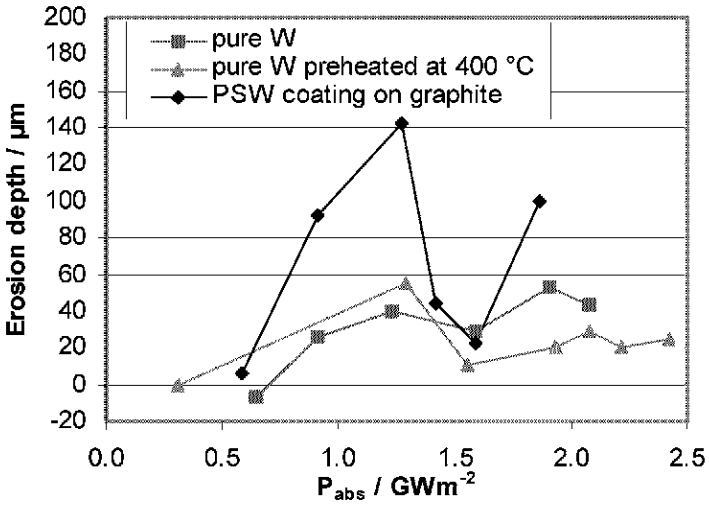

Fig. 89 Variation of erosion depth with absorbed power density for pure W, pure W preheated at 400 °C and plasma sprayed W on graphite. Δt= 4.2 to 4.5 ms

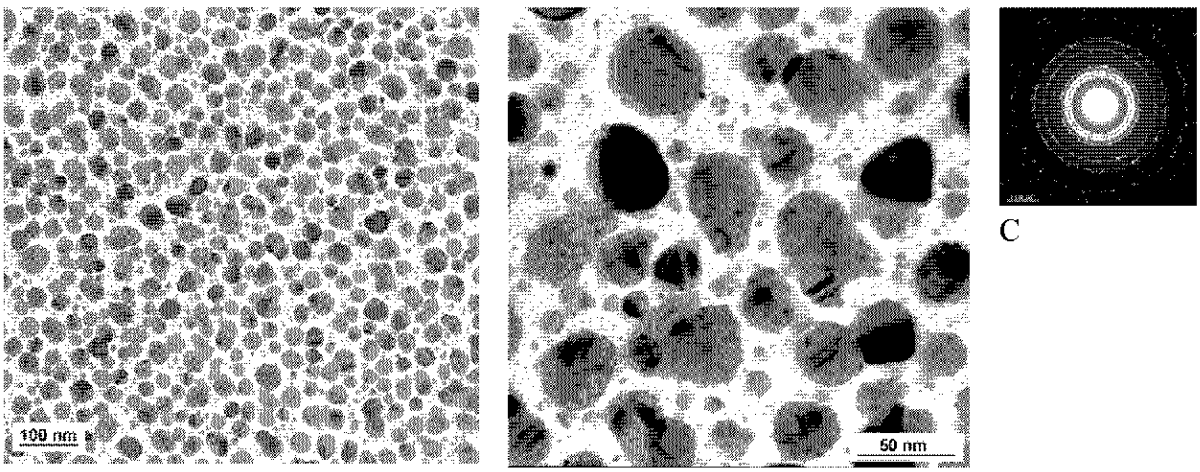

A B C

Fig. 90 TEM image of collected W particle ejected from the sample surface.
A: overview of the collected particles on the nets, B: higher magnification of A,
C: electron diffraction pattern of B

The erosion process of pure W under plasma disruptions can be explained as follows.

1. Cracks were formed inside, as tensile stresses developed during cooling down into the brittle regime after thermal loading. Cracks were also formed outside the loaded area where the temperatures remained almost constant, as the contraction on the border of the loaded area occurred after thermal loading.
2. The surface started to melt and an increase of volume going to form a convex surface. Outside the loaded area, the material was below DBTT, while the free surface of the molten layer was the only space to move.
3. A deformation of the melt layer occurred. When the surface of melt layer reached the boiling point, the convection of melt layer and the vapor recoil pressure initiated molten material to flow outside the loading area and to create a visible crater or a rippled surface.

4. Vapor shielding took place. As more material evaporated over the surface with increasing heat flux, a vapor cloud is formed over the loaded area and protected from further melting.

4.2.3.6 Results of ELMs simulation]

As the electron beam widths have been determined by calibration tests (Ref. 3.5), thermal loading under ELMs conditions could be performed by a static electron beam mode without scanning.

Secondary electron images, digital camera images and current plots of tungsten sample loaded att E_{abs} = 1.25 MJm^{-2} for 0.5 ms are shown in Fig. 91. After a single shot, cracks appeared perpendicular to the surface up to a depth of 50 to 200 µm and cracks also grew in horizontal to the surface. Moreover some W-grains in the sample surface are missing. After hundred cycles, the trajectories of emitted particles are no longer detectable and a convex melting formation with a few bubbles was found in the recrystallized material and several cracks around the crater with a depth up to approx. 500 µm (Fig. 92). The cracks around the crater became wider compared to the first shot. Some grains on the surface were ejected from the substrate, which might have occurred due to the coalescence of horizontal cracks and cracks perpendicular to the surface. This crack growth is not preferable for long-lasting PFMs. For a higher energy density (E_{abs}:of 2.7 MJm^{-2} for 0.6 ms), the cracks formed at the edge of the melt layer after 100 cycles. Obviously the cracks at the edge of the melt play a role to disconnect from the adjacent substrate and to accelerate local heating and evaporation of the melted area. The crater depth of W after a single or after 100 shots did not show a big difference.

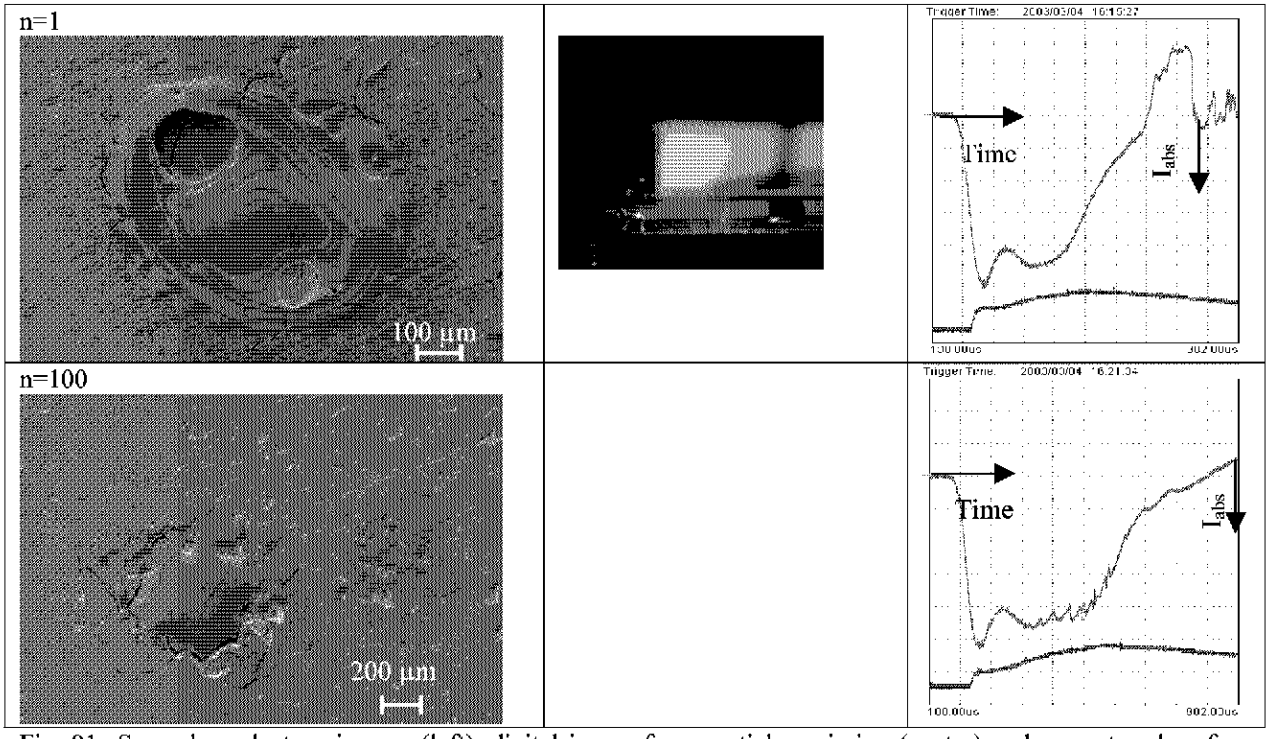

Fig. 91 Secondary electron images (left), digital image from particle emission (center) and current and surface temperature plots (right) of W at the following loading conditions; I_{inc} = 150 mA, V = 120 keV, Δt = 0.52 ms, max. P_{abs} = 2.3 GWm^{-2}, max. E_{abs} = 1.2 MJm^{-2}, n = 100. Max. erosion = 38.9 µm (n=1), 27 µm (n=100)

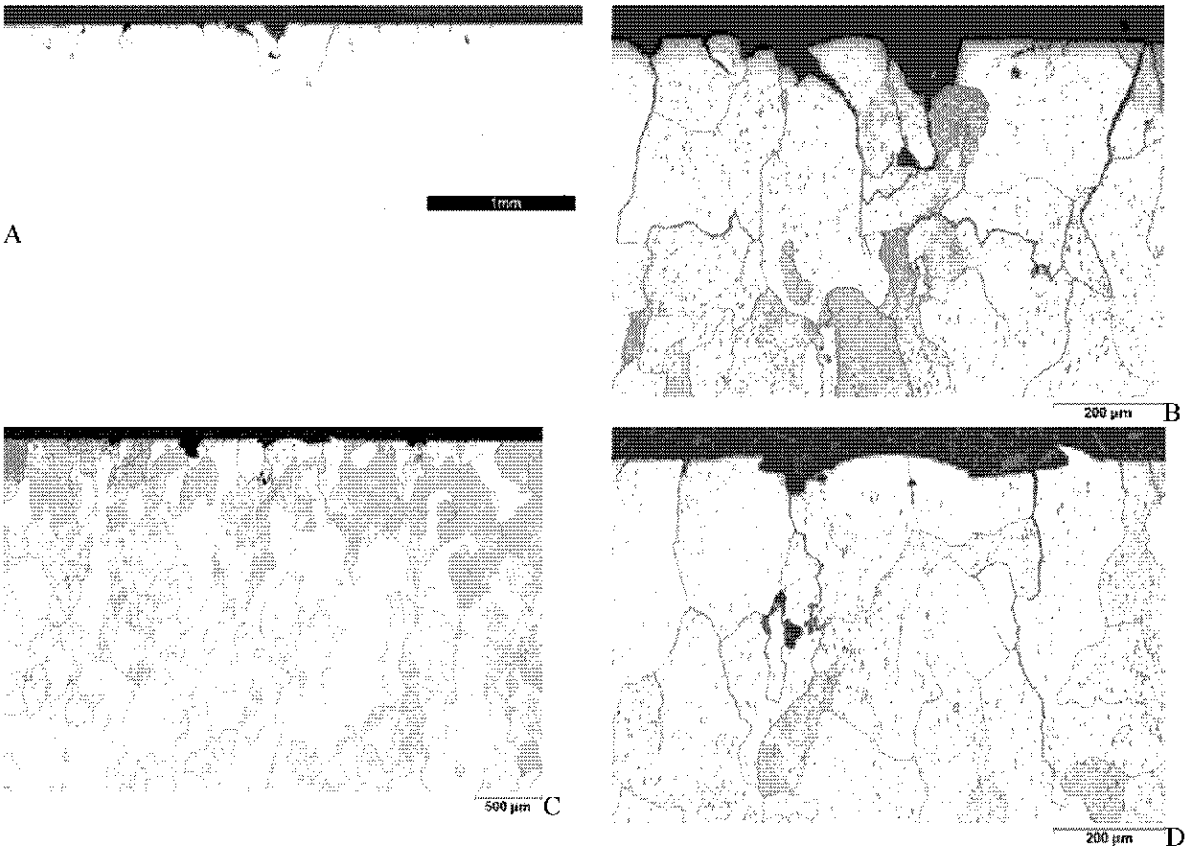

Fig. 92 Cross section images of W loaded at max. P_{abs} = 2.3 GWm^{-2}, Δt = 0.52 ms, max. E_{abs} = 1.2 MJm^{-2} n = 1 (A, B) and n = 100 (C, D).

4.2.4 Conclusion

After single disruption tests of pure sintered W and W alloys showed weight loss of about 10 µg and formed craters in the range of 50~100 µm. PSW showed dramatic damage. The coatings showed weight loss about 1~2 mg, which corresponds to a crater depth of about 200~250 µm. After single VDE test W and W alloys had a residual melt layer with a thickness of 1.2~1.5 mm. The typical material behavior under VDEs is the recrystallization and the melt layer redeposition in its original position.

Pure W and Ta are the highest resistance against intense energy deposition. W showed a relatively small weight loss and a low crater depth of about 50 µm, and several cracks with a max. depth of about 1.2 mm vertical to the surface after plasma disruption tests with P_{abs} = 1.2 - 1.4 GWm^{-2} for 4.4 ms. This crack formation in this direction is not critical for the operation. Ta showed also small weight loss and no crack formation after disruption tests for pulse duration of 5 ms. However, Ta is less favorable for PFMs in Tokamak devices because it has high affinity with hydrogen.

Single crystal W and W-Re has high cost, but did not show a significant improvement in material erosion compared to pure W. These materials are not favorable for the PFMs. W-25%Re alloy with a DBTT close to RT, still forms cracks right in the center of the loaded area.

The W-1% La_2O_3 alloy showed melt ejection, droplet and bubble formation. Moreover, these cracks propagating to the middle of the bulk after single disruption test. The generated vapor La_2O_3 deformed the molten area causing convection and ejection of the melt layer, and became rough surface.

The crack formation in this direction is not so critical and the W-1% La_2O_3 has advantages such as easy machining at RT and lower cost. However, the deformation of the surface is not desirable for the PFMs. If thermal response of this material is improved by the other approaches (i.e. castellation), this material might be suitable for PFMs.

Mo is less favorable for divertor applications because it formed bubbles, but no crater and it showed only a negligible weight loss after disruption tests.

Plasma sprayed (PS) W and tungsten carbide experienced the most severe damage such as the highest weight loss, crater depths, droplets, and crack formation after plasma disruption tests. PS W on Cu showed ablation of W layer coatings induced by crack formation both parallel and vertical to the surface between the individual splats. This cracks develop the subsequent detachment from adjacent layers, which lead to the generation of tungsten dust particles and reduce thermal conductivity.

However, these PS W samples can be improved by optimizing the spraying parameters from systematic experiments. The three plasma sprayed W samples investigated in this study showed different surface morphologies. A test sample with a PSW with a thickness of 1 mm showed droplets, while the other with a PSW with a thickness of 5 mm showed no droplets but many pores. The differences in surface morphology might be attributed to the different thermal properties caused by porosity, or by the partial detachment of W and Cu (1 mm PSW on Cu), or by inhomogeneous grains with un-molten particles in the 5 mm PSW. PS W on graphite showed some improvement in thermal behavior compared to PS W on Cu. However, this coating has not a sufficient resistance against thermal shock in comparison with bulk W because there were bubble formation. The erosion is 3 times bigger than for bulk W.

The crack formation of tungsten carbide propagated both in horizontal and vertical directions to the surface, resulted in catastrophic failure. In addition, the surface of WC transformed into α-W_2C due to evaporation of carbon induced by energy deposrition during thermal shock loading.

Castellated W-1%La_2O_3 sample shows better thermal response than the monolithic W. The castellated W-1%La_2O_3 samples showed no droplet formation, whereas the monolithic sample showed a lots of droplets outside the loaded area. The castellated samples might have a lower vapor recoil force to generate melt splashing. The produced vapor might escape through castellations and the resulting vapor recoil pressure is reduced. During VDE tests with P_{abs}=206 MWm^{-2} and longer beam pulses (Δt = 300 ms), the recrystallization proceeded but the melt layer redeposited in its original position. Under these conditions, the applied heat flux does not generate high surface tension in the molten layer or vapor recoil pressure to initiate the melt ejection process.

Lamellae modules with a lamella thickness of 4 mm showed less damage (1.38 mm of crater depth, a few cracks formed outside the loaded area) compared to lamellae with a thickness of 0.2 mm (1.5 mm crater depth; micro cracks parallel and vertical to the surface). It is assumed that the cracks which were observed in lamellae with 0.2 mm and 4 mm thickness were already formed during the thermal fatigue test, which have been applied prior to the thermal shock loading. The lamellae structure reduced the crack growth compared to monolithic tungsten. However, the lamella-structure showed crater and droplets, while pure sintered monolithic W showed melting on the surface but did not form a crater. This may be due to the barrier effect of the gaps between lamellae, resulting in the lower effective thermal conductivity of the samples.

When samples are heated up before thermal loading in the range from 300 to 500 °C, which is supposed to be ITER condition, the sample is still not ductile and showed increase of material erosion under plasma disruption conditions, such as bubble formation, cracks outside the crater and micro cracks inside the crater. Moreover, the preheating sample increased the weight loss in the range of 30~180 μg. In contrast, samples without preheating showed no bubbles and cracks outside the crater. An improved thermal response was observed for W samples preheated at 500 °C (T>DBTT) after the VDE tests. The sample did not form cracks. VDE pulses (90 ms) are longer monolithic compared to plasma disruptions (Δt = 1-5 ms) and the surrounding area can have a larger heat affected zones, reach above DBTT, and become ductile.

The size of the loaded area has to be taken into account for the comparison of erosion data obtained in different test facilities. A smaller loaded area has a slight lower threshold heat flux for the melting and crater formation compared with larger loaded area. This may be due to vapor shielding. Sample with the larger loaded area has a dense cloud compared with the small loaded area, which enhances a vapor shielding, and finally becomes lower erosion.

Erosion mechanisms of W with increase of heat flux were elucidated.

1. Cracks were formed inside, as tensile forces developed during cooling down into the brittle regime after thermal loading. Cracks were also formed outside the loaded area where the temperatures remained almost constant, as the contraction on the border of the loaded area occurred after thermal loading.
2. The surface started to melt and an increase of volume going to form a convex surface. Outside the loaded area, the material was below DBTT, while the free surface of the molten layer was the only space to move.
3. A deformation of the melt layer occurred. When the surface of melt layer reached the boiling point, the convection of melt layer and the vapor recoil pressure initiated molten material to flow outside the loading area and to create a visible crater or a rippled surface.
4. Vapor shielding took place. As more material evaporated over the surface with increasing heat flux, a vapor cloud is formed over the loaded area and protected from further melting.

Erosion depths measurements on electron beam simulated plasma disruptions with power densities of about 1.6 GWm^{-2} for 4.2~4.5 ms indicate a shielding effect. It might be correlated to the formation of vapor cloud from evaporation or reflected electrons, or a condensation in the vapor phase.

A simulation of ELMs has been performed for the first time in JUDITH. After 100 cycles of ELMs conditions the trajectories of emitted particles are no longer detectable and a concave melt layer has been formed; the metallography shows a few bubbles in the recrystallized material and several cracks around the crater with a depth up to approx. 500 μm. There was no remarkable difference in the erosion depth of W after single and 100 shots.

4.3 Brittle destruction in carbon based materials

4.3.1 Introduction

Carbon based materials (CBMs), namely graphite and CFCs are candidates for divertor strike points armour in present design of fusion devices and, in particular, for ITER. The advantages are its superior properties such as low activation, no melting, high thermal shock resistance, high mechanical strength. When off-normal events such as plasma disruptions or VDEs occur, the extremely high heat fluxes are dumped onto the divertor parts. The same applies to the so-called type I ELMs for the future Tokamak devices. During these events, CBMs might be damaged by crack formation, sublimation, and so-called brittle destruction. Brittle destruction is associated with emission of solid particles of CBMs acting in combination with sublimation caused by transient thermal loads [109, 112, 145, 146]. When the ejected dust particles are formed, they have a high affinity for redeposition with tritium to form hydrocarbons in remote areas of the vacuum vessel [45, 55, 77, 78, 147 - 155]. This tritium contaminated carbon dust will be deposited. Hence, the accumulation of tritium is rather critical from a safety point of view. Tritium in redeposited carbon layers will also have a significant influence on the total tritium inventory. Thus it is essential to characterize and quantify the erosion of the surface and the formation of dust to estimate the lifetime of the components and to quantify the tritium inventory.

In this chapter, the onset of brittle destruction and the erosion mechanisms of different CBMs (graphite, CFCs, Si-doped CFC) are being studied with respect to material erosion in different particle emission regimes [156], characterization of ejected particles, and behavior of preheated samples. Si-doped CFC is used as a reference material. Silicon doping helps to reduce the effect of chemical erosion [154]. Furthermore, the experimental data is compared with 3-D numerical simulations for the onset of brittle destruction.

4.3.2 Experimental

Thermal load experiments were performed in the electron beam test facility JUDITH. The pulse duration was varied from 0.5 ms to 90 ms, and the incident current from 50 to 350 mA at an acceleration voltage of 120 keV resulting in an absorbed power density in the range of 0.14 to 7.7 GWm^{-2}. The loaded area was 2×2 mm^2 for pulse duration of 1 to 3.5 ms, 3×3 mm^2 or 4×4 mm^2 for 4.5 ms, and 6×6 mm^2 for 90 ms, respectively. Tests have also been performed on specimens preheated at 500 and 800 °C.

For diagnostics, pulse duration and absorbed current measurements, and the surface temperature were monitored (Ref. Chap.3.2). The particles emission was observed by a CCD camera. Preheating of the samples was carried out by electron beam currents below 3 mA just before the transient heat load pulse was applied. The loading condition in the experiment corresponded to ELMs with the maximum energy density E_{abs} of 2.5 MJm^{-2} (I_{inc} = 150 mA, V = 120 kV) for pulse duration of 0.54 ms assuming a Gaussian distribution of the incident electron beam with FWHM = 1.84 mm (Ref. Chap. 3.5.3).

The set up for the collection of emitted particles is shown in Fig. 93. The test sample was placed on the specimen holder to study the morphology and size of the emitted particles. A stainless foil surrounds the specimen is stabilized by an aluminum ring from outside. A

brass plate with an aperture of 5 mm in diameter is placed on the top of the foil to avoid the escape of carbon particles. TEM grids (3 mm in diameter) with a thin carbon film for the collection of nano-particles were fixed inside the stainless steel foil. The collected particles were characterized by transmission electron microscopy.

After the transient heat load tests, the weight loss, and erosion depths were measured (Ref. Chap. 3.3). The microstructure of the surface and ceramography were also investigated.

The test materials are fine grain graphite (R6650), 3 directional (3D) CFC (NB31) and Si-doped 3-D CFC (NS31). The samples have a dimension of 12×12×5 or 25×25×10 mm^3. Before the testing, the samples were cleared from adherent dust particles in an ultrasonic baths in ethanol for ten minutes and baked at 170 °C for 4 hours.

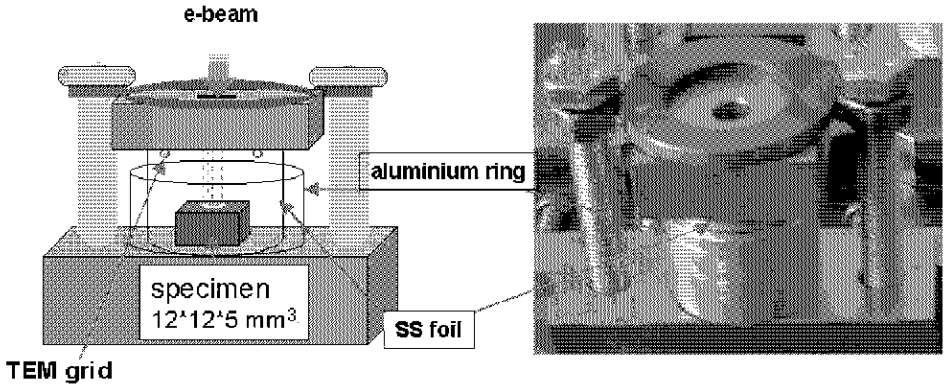

Fig. 93 Schematic diagram (left) and picture (right) of a set up for particle collection

4.3.3 Onset of particle emission

The threshold loading condition for the onset of particle emission under the conditions of ELMs, plasma disruption and VDEs, the incident power density was determined by increasing stepwise (increment 5 to 10%). For power densities below P_{abs} =144 MWm^{-2} no particles release was visible for pulse duration of Δt = 90 ms (Fig. 94A). With increasing power densities, the emission of small and medium particles became evident (Fig. 94 B, C). A further increase of the beam power (i.e. P_{abs} =1.9 GWm^{-2}, Δt = 4.4 ms) finally resulted in the emission of large objects (grains and grain clusters, Fig. 94D). In the current plots of small particle emission and big particle emission, the absorbed current suddenly decreases and remains constant at a low value seen in the center column of Fig. 94 B,C. This sudden decrease of current seems to be correspondent to the emission of particles. It's supposed that the brittle destruction process initiated at the same instant when the experimentally measured absorbed current I_{abs} suddenly decreases.

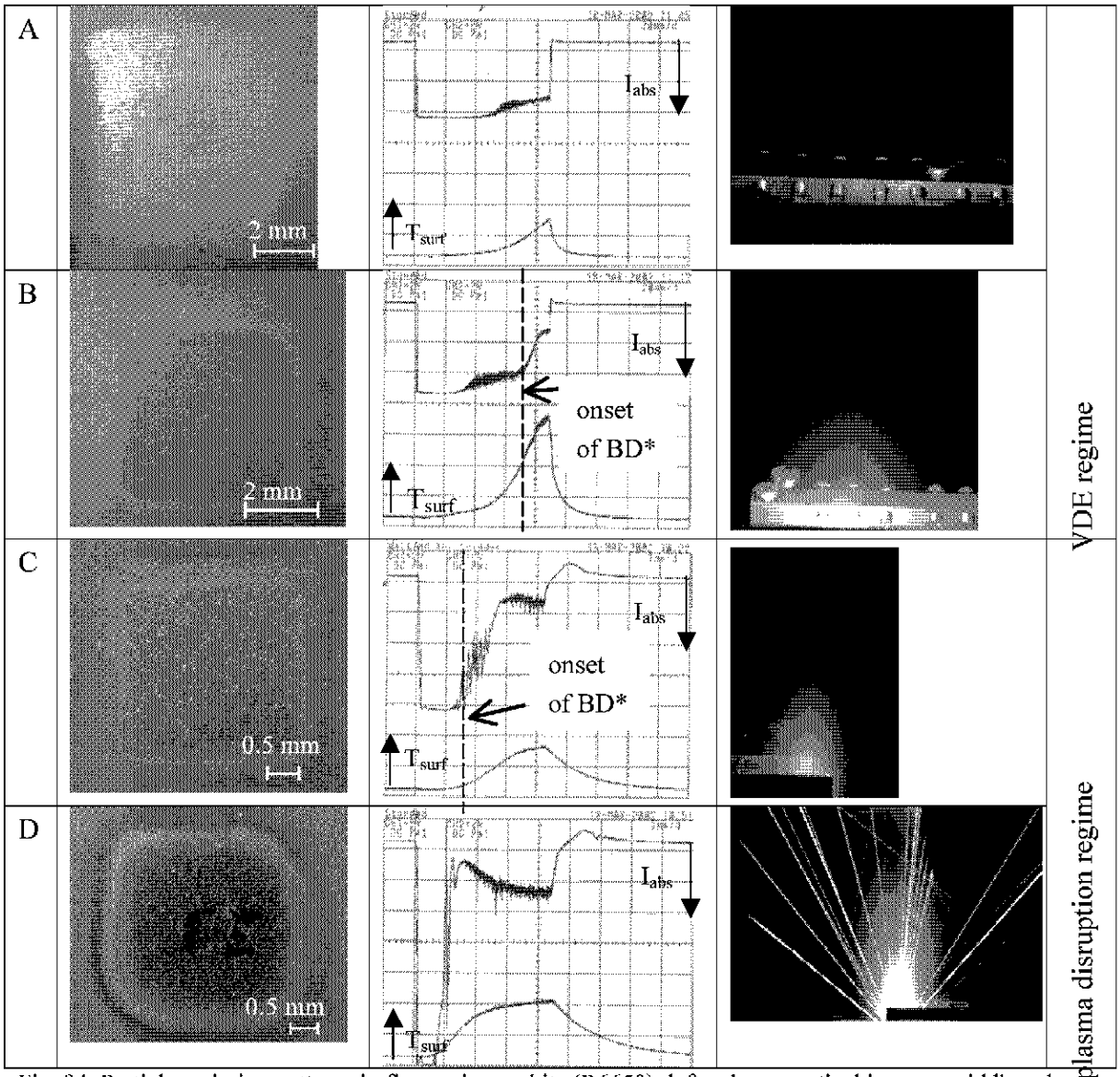

Fig. 94 Particle emission patterns in fine grain graphite (R6650); left column: optical images, middle column: current and temperature plot, right column: digital imaging by CCD camera
A: no particle emission (221_40B) P_{abs} = 144 MWm^{-2}, Δt = 90 ms
B: onset of small particle emission (221_38C) P_{abs} = 175 MWm^{-2}, Δt = 90 ms
C: small particle emission (221_34B) P_{abs} = 1.1 GWm^{-2}, Δt = 4.4 ms
D: big particle emission (221_37I) P_{abs} = 1.9 GWm^{-2}, Δt = 4.4 ms

In the following, the fine trajectories of light emission will be called "small particle emission" (Fig. 94 B,C) and the emission of strong and intense lines "big particle emission" (Fig. 94 D). The small particle emission regime is characterized by the break of bonds between grains. In the big particle emission regime macroscopic erosion occurs with the ejection of set free isolated grains or clusters. These "small" and "big" particle emission regimes can be correlated to the pore sizes of the eroded surface; the max. ratio of pore size was Ø 2-3 µm for small particle emission regime, and Ø 14 µm for big particle emission regime (Fig. 95, Fig. 96). This grain size range is consistent with the data from M. I. Guseva and W. J. Carmack in which the dust particles in the wall of Tokamaks were from sub µm to a few µm and the particle agglomerations were 10-40 µm [81, 151, 157, 158]. The particles in

nm size are also the peak in the size distribution of the pores on the surface which are much smaller than the mean particle size (7 μm) of fine grain graphite (Fig. 96B). These scale particles were also collected on TEM grids in the big particle emission regime [Ref. Chapter 4.3.6]. These nm-sized particles are supposed to be the binder phase in the graphite material associated with crack formation [156, 159], or part of the graphite particle ablated due to the high thermal shock induced stresses.

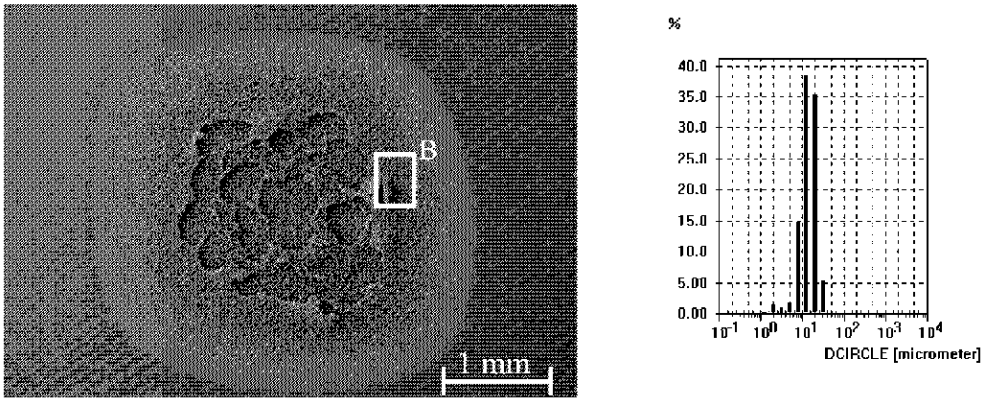

A B

Fig. 95 SEM image (A) and the size distribution of pores in area B of graphite preheated at 500 °C (221_14). I_{inc} = 150 mA, Δt = 4.4 ms, P_{abs} = 2.4 GWm^{-2}

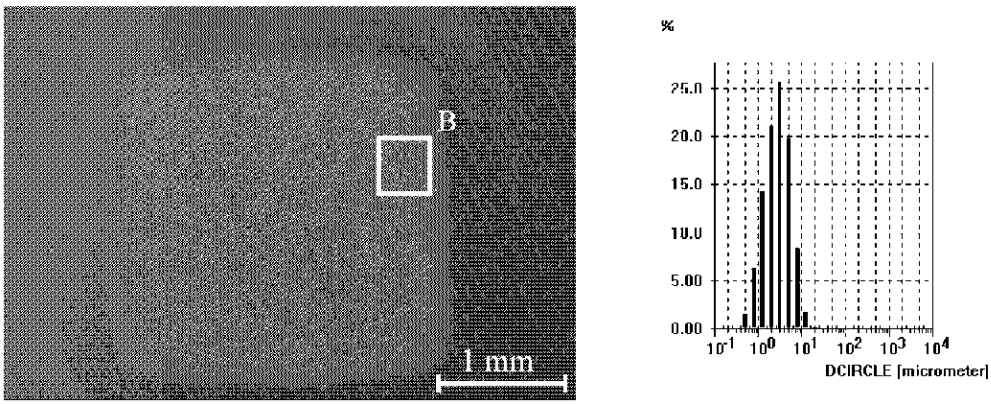

A B

Fig. 96 SEM image (A) and the size distribution of pores in area B of graphite preheated at 500 °C (221_12). I_{inc} = 80 mA, Δt = 4.3 ms, P_{abs} = 1.3 GWm^{-2}

As a conclusion the threshold for the onset of particle emission with the two emission regimes has been determined for graphite with pulse duration from 1 to 90 ms (Fig. 97). Off-normal events are in the regime above the threshold and cause catastrophic damage even after single electron beam pulses. In contrast, the expected loading conditions for ELMs are well below the threshold curve. The threshold decreases from > 4 GWm^{-2} for Δt = 1 ms to < 200 MWm^{-2} for 100 ms pulses. Increasing of the incident heat load beyond these threshold values results in the emission of particles. For the longer pulse duration (e.g. 100 ms) small/medium particles are ejected. While for disruption specific pulse lengths of a few milliseconds, the generation of large particles is becoming essential. For the very short pulse duration of 1 ms, only big particles were emitted. Under plasma disruption conditions for 1 ms, a complicated erosion scenario has been observed: up to absorbed power densities of 4 GWm^{-2} no brittle destruction has been detected. Above this value the formation of a limited number of large

particles was detected. A further increase of the incident power density revealed a second regime where no particle emission (P_{inc} = 6 to 7 GWm^{-2}) could be seen; above this level intense emission of large carbon particles was observed.

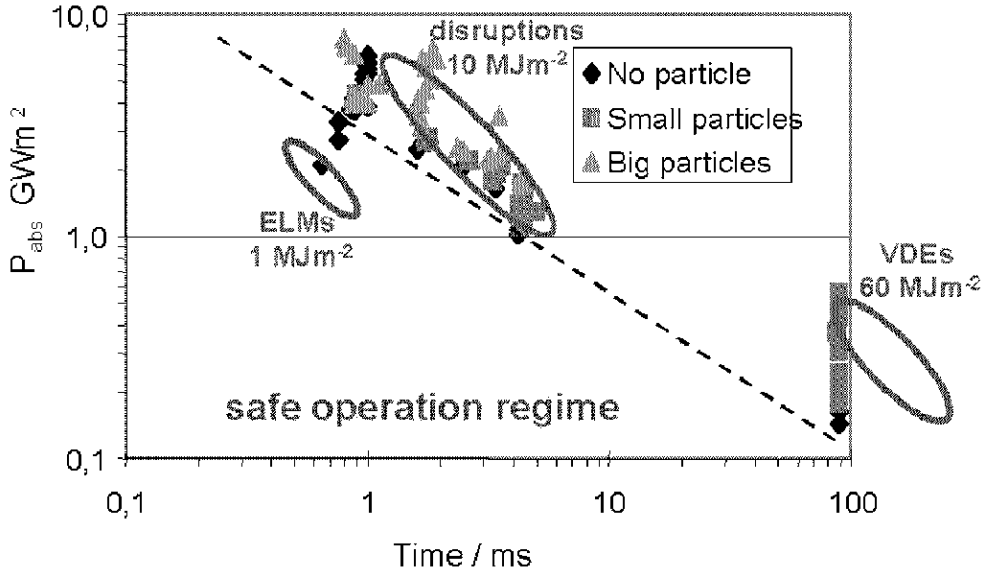

Fig. 97 Threshold heat flux for the onset of particle emission from fine grain graphite.

In order to confirm the experimentally determined brittle destruction onset, three-dimensional systematic numerical simulations were carried out using a semi-empirical approach based on the threshold value for the specific enthalpy of 10 kJ/g [89, 160]. The Monte-Carlo simulation is applied for the calculation of energy deposition of 120 keV electrons inside the graphite. In the calculations, graphite is assumed to be destroyed as soon as the specific enthalpy of the heated volume exceeds the brittle destruction threshold.

In this simulation, temperature dependent thermo-physical properties of the material, heat of vaporization, radiation, volumetric heating, and scanning of the electron beam with 1 mm diameter were taken into account. [88, Ref. Chapter 2.4]. The spatial distribution of the average heat flux at P_{abs} = 2.5 GWm^{-2} for Δt = 2.5 ms in Fig. 98 A showed rather homogeneous loaded area. The resulting erosion was calculated to be about 50 μm (Fig. 98B).

The heat flux for the onset of brittle destruction as a function of pulse duration is plotted in Fig. 99 for graphite and for CFC [88]. The thermal conductivity of CFC evaluated by S.E. Pestchanyi was applied for the calculation [161]. These properties consider the decrease of the thermal conductivity due to crack growth in the material in correlation to temperature. The numerical results for the brittle destruction onset for graphite and CFC are in rather good agreement with experimental results below power density of 1.25 GWm^{-2}. Above the absorbed power density of 1.25 GWm^{-2} small deviations were observed for CFCs (NB31 and NS31 in Fig. 99B). The time to reach the threshold value in numerical simulations is equal to the time when the current starts to drop (τ_{bd}). It confirms that the brittle destruction initiated at the time τ_{bd}.

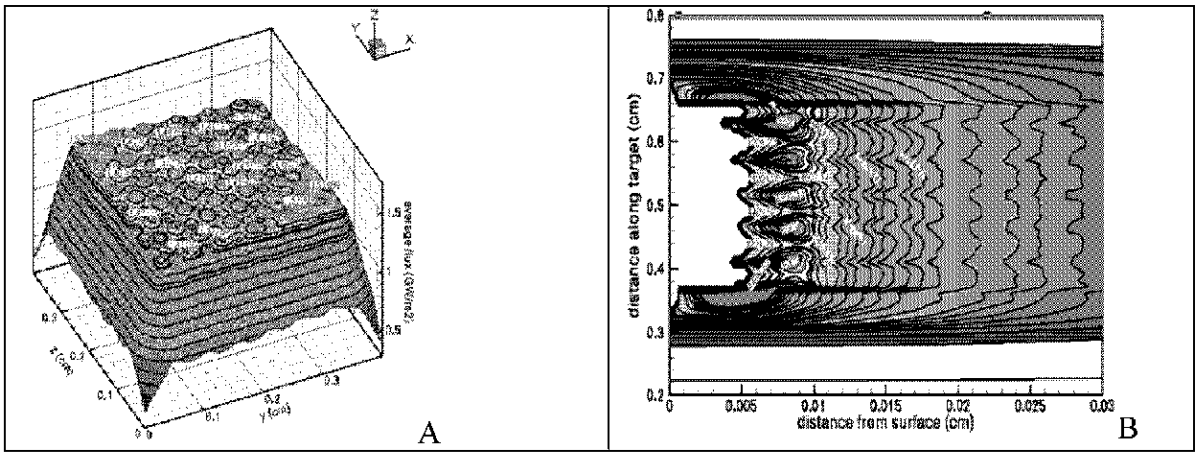

Fig. 98 Spatial distributions of the average heat flux (A) and temperature contour lines (B) of graphite sample (P_{abs} of 1.4 GW/m^2, Δt=2.5 ms) [Ref. B. Bazylev 106].

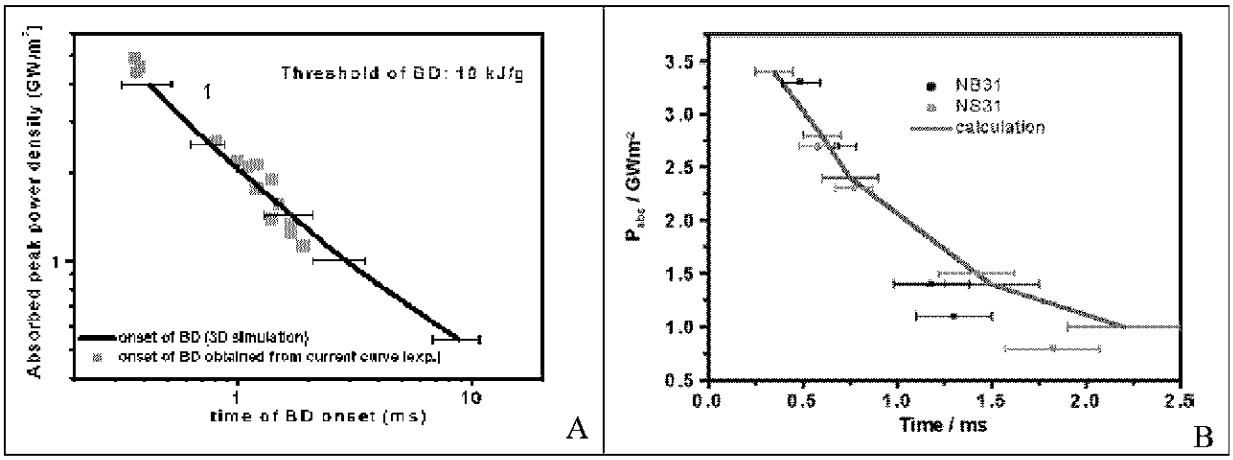

Fig. 99 Comparison of experimental and numerical results for the onset of brittle destruction in fine grain graphite (R6650, A) and 3 D CFC (NB31, NS31, B) [Ref. B. Bazylev 88].
*time of onset in graphite (R6650), NB31 and NS31 = the time where absorbed current suddenly decreased [Ref. B. Bazylev 88].

4.3.4 Particle emission pattern

Graphite and CFC samples revealed different particle emission patterns. Fig. 100 shows the morphology of the respective surfaces and the particle emission at absorbed power density P_{abs} of 1.6 GWm^{-2} for pulse duration of 4.4 ms. The graphite sample shows a homogeneous emission of fine particles with a broad angular distribution, whereas the un-doped CFC released particles with a preferred orientation perpendicular to the surface. In contrast, curved particle trajectories as well as straight lines were observed for Si-doped CFC.

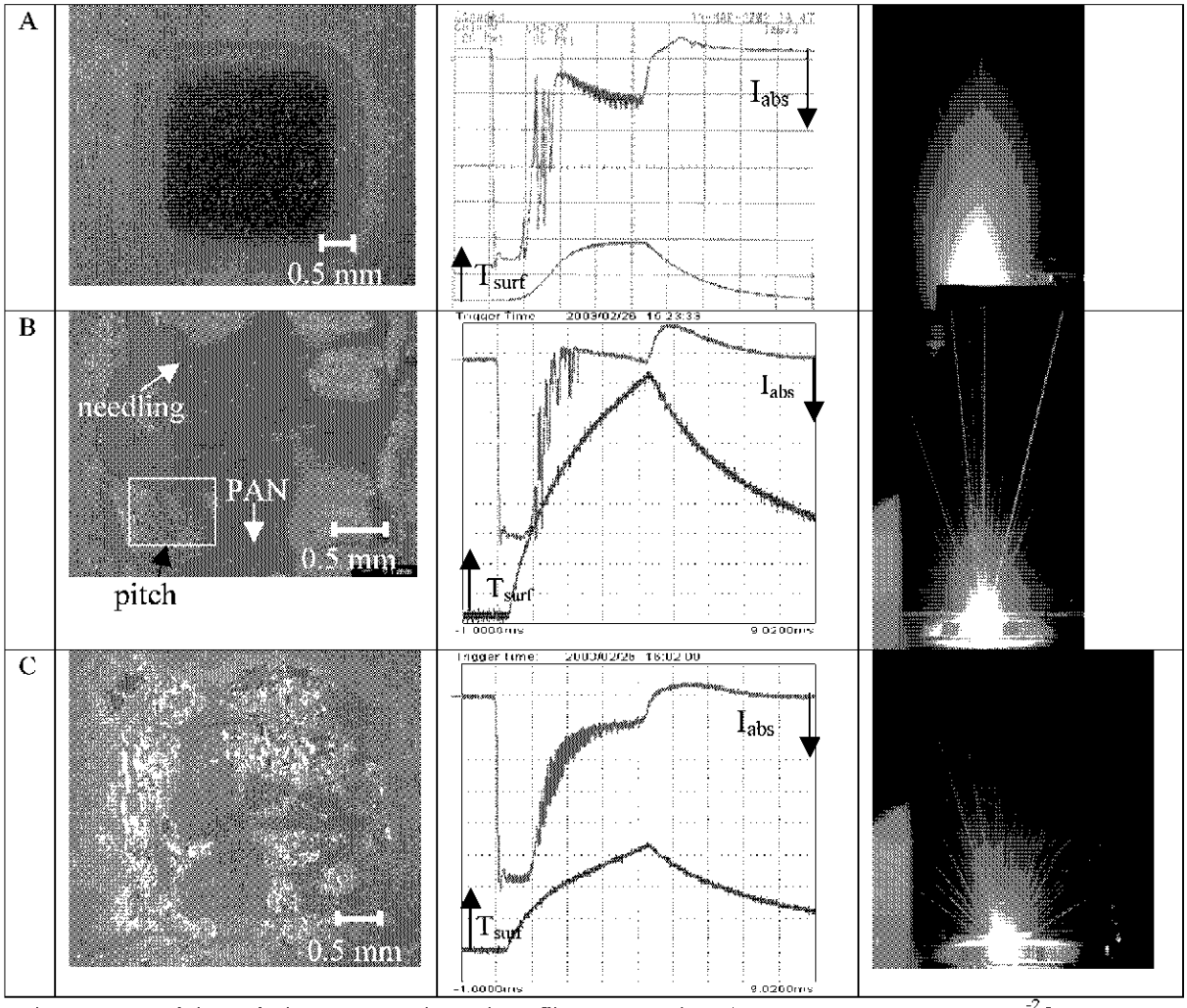

Fig. 100 Particle emission patterns in carbon fiber composites (CFCs) at P_{abs} = 1.6 GWm^{-2} for 4.4 ms; A: graphite (221_37F), B: CFCs (219_43_11), C: Si-doped CFCs (220_43_4).

4.3.5 Characterization of materials The differences in the emission pattern might come from the different structures of the materials; the graphite R6650 consists of isotropic fine grains with a mean diameter of 7 μm, whereas the CFCs are composed of fibers in a carbon matrix. The ex-pitch fibers were oriented perpendicular to the sample surface, while the PAN fibers bundles were aligned parallel to the surface. The third directional fiber, namely "needling" consists of PAN fiber and oriented perpendicular to PAN and pitch fiber bundles. The erosion crater in graphite clearly shows homogeneous erosion within the square pattern of the incident electron beam. The CFCs are characterized by a preferred erosion of the PAN fibers. The Si-doped CFCs showed segregation of Si or SiC along eroded PAN fibers.

The 2-D surface profiles of graphite and CFCs after loading (P_{abs} = 1.5 GWm^{-2} for Δt = 4.5 ms) measured by laser profilometry are shown in Fig. 101. The original surface is shown in green color, the erosion in yellow and red colors, and redeposition in blue color. In Fig. 101B the blue color also represents broken vertical fibers.

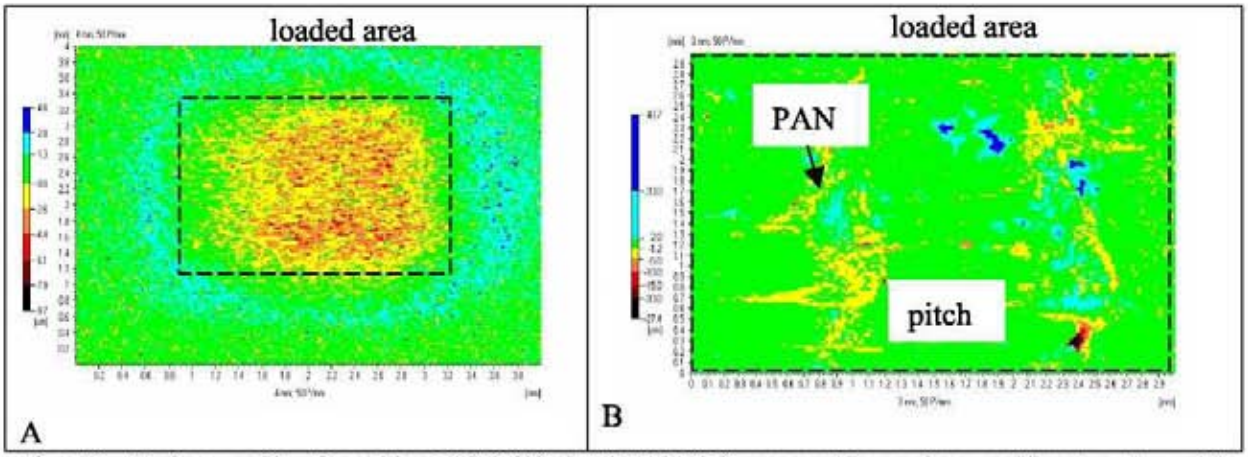

Fig. 101 Surface profile of graphite R6650 (A), CFC NB31 (B) measured by surface profilometry. P_{abs} = 1.5 GWm^{-2} for pulse duration of 4.4 ms

In graphite crater depths depend on the regime of particle emission in graphite. The variation of the crater depth with pulse duration for graphite is shown in Fig. 102. The crater depth is in the range of zero to a few μm for a loading condition below the particle emission threshold, 2 - 12 μm for small particle emission (under disruption conditions), and 10 - 80 μm for big particle emission. In the big particle emission regime, ejection of some grains or clusters is tremendous, which results in catastrophic damage of the sample surface. For VDE conditions, no big particle emission was observed. However, even small particle emission can cause crater depths from a few μm to 100 μm. VDE conditions imply rather low heat flux (< 1 GWm^{-2}) but the erosion continuously occurs up to pulse duration of 90 ms and thus results in high erosion depths.

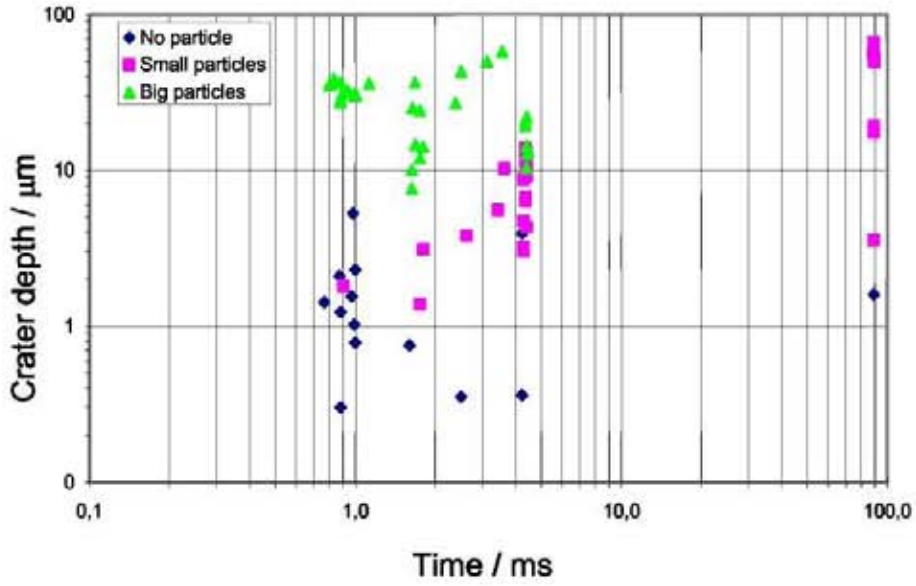

Fig. 102 Variation of crater depth with pulse duration for graphite.

CFCs and Si-doped CFCs showed a different surface morphology. CFCs do not form a crater even above the threshold of particle emission, but only some slight damage of PAN

fiber oriented parallel to the sample surface. They mainly break or ablate. At the onset of particle emission for CFCs, ablation occurred along the PAN fibers while the pitch fiber area showed no damage (Fig. 103 on the left, e.g. P_{abs} = 3.0 GWm^{-2}, Δt = 1.7 ms). When the heat flux increases, the intersection of PAN and needling fibers started to erode. The pitch fibers exhibited a detectable erosion only within the big particle regime (Fig. 103 on the right, e.g. P_{abs} >3.9 GWm^{-2}, Δt = 1.7 ms). The cross section images of CFC clearly show the breaking and ablation of PAN fiber bundles (Fig. 104 A-C), and the very slight degradation of pitch fiber strands (Fig. 104 D).

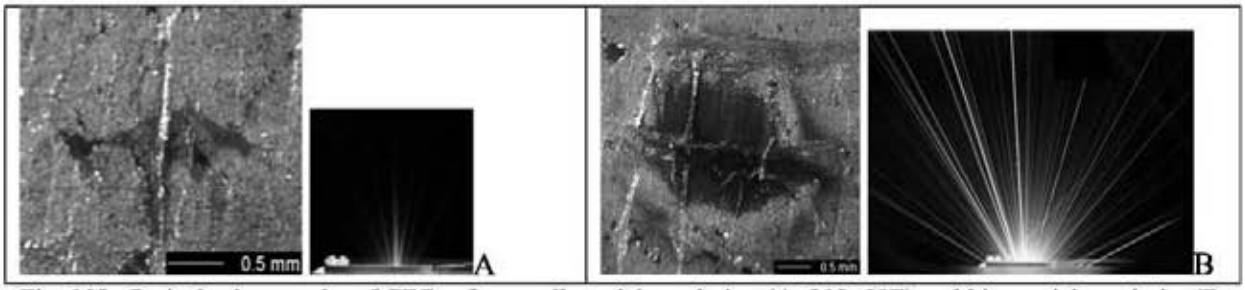

Fig. 103 Optical micrographs of CFCs after small particle emission (A, 219_58E) and big particle emission(B, 219_58J). A: P_{abs} =3.0 GWm^{-2}, Δt = 1.7 ms, B: P_{abs} =5.1 GWm^{-2}, Δt = 1.7 ms

For Δt = 1.7 ms, the CFCs have erosion depths (measured in the deepest point) in the range between 0 and 20 µm for the small particle emission between60 and 100 µm for the big particle emission regime. For pulse duration Δt = 4.5 ms the max. erosion depth was in the range of 2 to 40 µm for the small particle emission regime and of 20 to 60 µm for the big particle emission regime.

Similar to the un-doped CFCs, the Si-doped CFCs also showed a very localized degradation. However, the erosion depths in Si-doped CFCs were bigger compared to the un-doped CFCs. This is due to the fact that silicon has a low melting point ending in early melting and evaporation. For Δt = 1.7 ms, Si-doped CFCs have reached the max. erosion depth in the range up to 60 µm for a small particle emission regime and 60 and 120 µm for a big particle emission regime. For Δt = 4.5 ms, this material has erosion depths in the range from 40 to 70 µm for a small particle emission regime and from 90 to 140 µm for a big particle emission regime. There was a clear evidence for the existence of silicon in the PAN fiber area due to segregation and redeposition outside after melting. In the small particle emission regime, only in the PAN fibers was eroded similar to un-doped CFCs.

The depletion and redeposition of silicon will play an important role during plasma-wall interactions in a sense that silicon helps to reduce chemical erosion on the surface after intense energy deposition during VDEs or disruptions [49, 50].

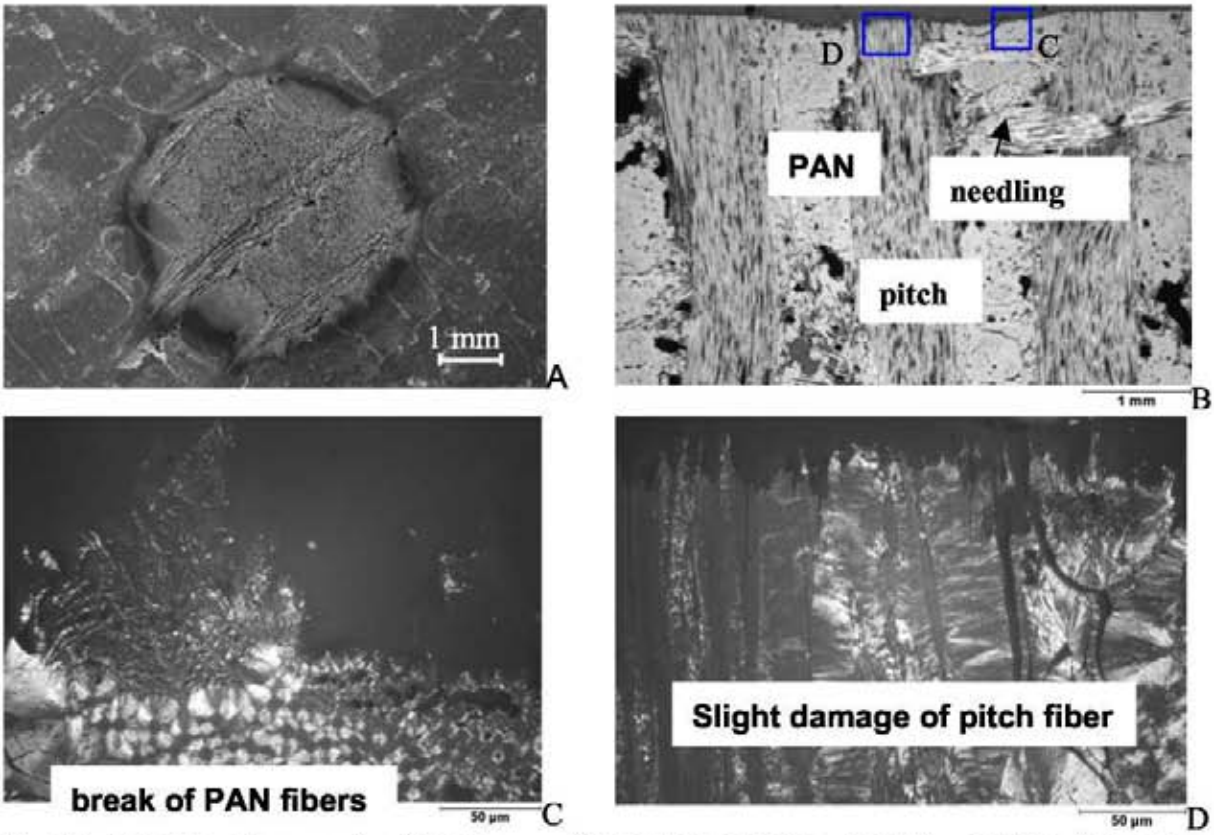

Fig. 104 SEM (A) and cross section (B-D) images of CFC (NB31, 219_5) loaded at P_{abs}= 2.0 GWm^{-2} Δt =1.5 ms with aperture Ø 5 mm of graphite.
A: SEM image, B: overview of the cross section, C: higher magnification of eroded PAN fiber with polarized light, D: higher magnification of eroded pitch fiber with polarized light,

To quantify the thermal shock induced material erosion, weight loss measurements have been performed. The variation of weight loss over absorbed power density for pulse duration of 4.5 ms is plotted in Fig. 105. For the isotropic fine grain graphite the material erosion remains negligible up to 1.5 GWm^{-2}; i.e. in the "small particle" regime the weight loss does not exceed the sensitivity range of the microbalance. Above this level, the weight loss is remarkable up to 0.5 mg. This is mainly due to the emission of large grains and grain clusters. The un-doped CFC material (NB31) does not show any significant weight loss less than 0.1 mg (6.2 $\mu g/mm^2$) even in the big particle emission regime up to P_{abs} = 2.2 GWm^{-2} (Fig. 105) [156]. The silicon doped CFC (NS31) on the other hand, shows a remarkable weight loss. Despite identical loading conditions, 'medium sized' objects have been detected with the CCD camera. Due to the high temperatures in the electron beam exposed surface region, some of silicon may be ejected from the sample surface in liquid form and will form islands of pure Si in the vicinity of the erosion crater. Besides, a significant fraction of the observed particles may consist of Si droplets. These droplets can contribute to the weight loss. The fact that the weight loss does not further increase with increasing heat flux above 2 GWm^{-2} can be attributed to the vapor shielding effect, discussed in detail in Chap. 4.2.3.5.

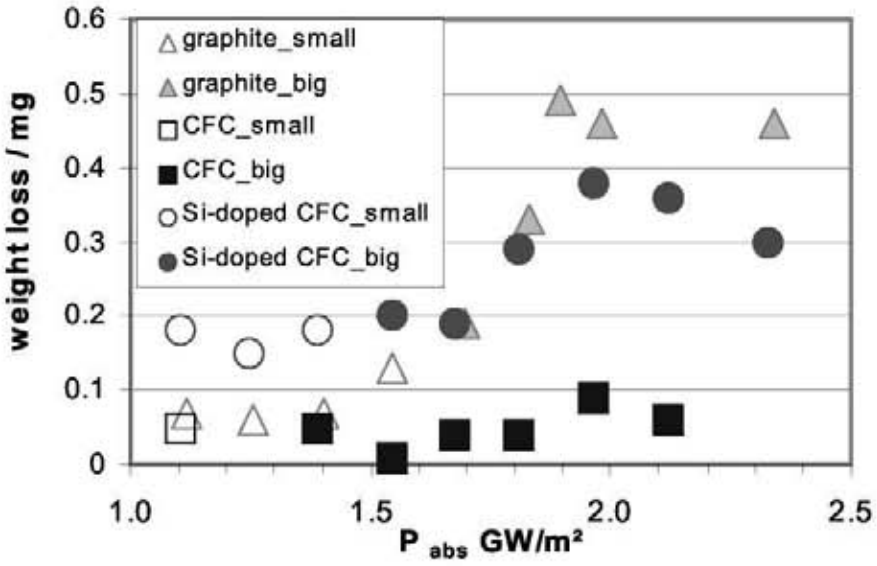

Fig. 105 Variation of weight loss of graphite (R6650), CFC (NB31) and Si-doped CFC (NS31) with P_{abs} for pulse duration of 4.5 ms.

4.3.6 Particle collection

J: Linke et.al [93] collected ejected particles under quasi-stationary heat loads (P_{abs} = 0.6 MWm^{-2}, Δt = 200 ms) on a glass collector and made investigations by SEM and TEM. In Tokamaks the majority of dust collected after long operational periods had an amorphous structure. It is originated from the disintegration of flakes [148]. To analyze the emitted particles from the surface of the samples under disruption conditions, the particles were collected with the set-up described in Fig. 93 and then characterized by TEM. Big particle emission regimes of CBMs were taken for loading conditions; 5 electron beam pulses with identical energy density have been applied to accumulate a detectable amount of emitted particles.

The particles ejected from fine grain graphite and collected on TEM grids are composed of amorphous carbon and have an elliptical shape with a cross section of ca. (50·90) nm^2 (Fig. 106A). There were no crystalline fragments collected on the TEM grids.

The fragments of CFCs were agglomeration of spherical objects with preferred crystallographic orientations (Fig. 106). Large particles or clusters were not collected on TEM grids because these particles did not adhere to the grids.

The globular particle with 1.1 μm in diameter (Fig. 107) ejected from a Si-doped CFC sample consisted of 83 % Si and 17% C. The electron diffraction pattern from a selected spot with a diameter of about 62 nm shows a crystalline structure, which indicates either Si, SiC, or a combination of both. It is too small to determine the phase by XRD. During manufacturing, silicon was infiltrated by a CVI process into the porosity of the PAN fiber area; the silicon reacted with the adjacent carbon matrix and transformed into β-SiC. Other fragments with an amorphous and elliptical shape were also observed; e.g. a large particle with a dimension of ca. 13·4 μm^2, which predominantly consisted of 97% C and 3 % Si. It assumes that the silicon was ejected in a liquid or vapor phase with carbon fiber bundles.

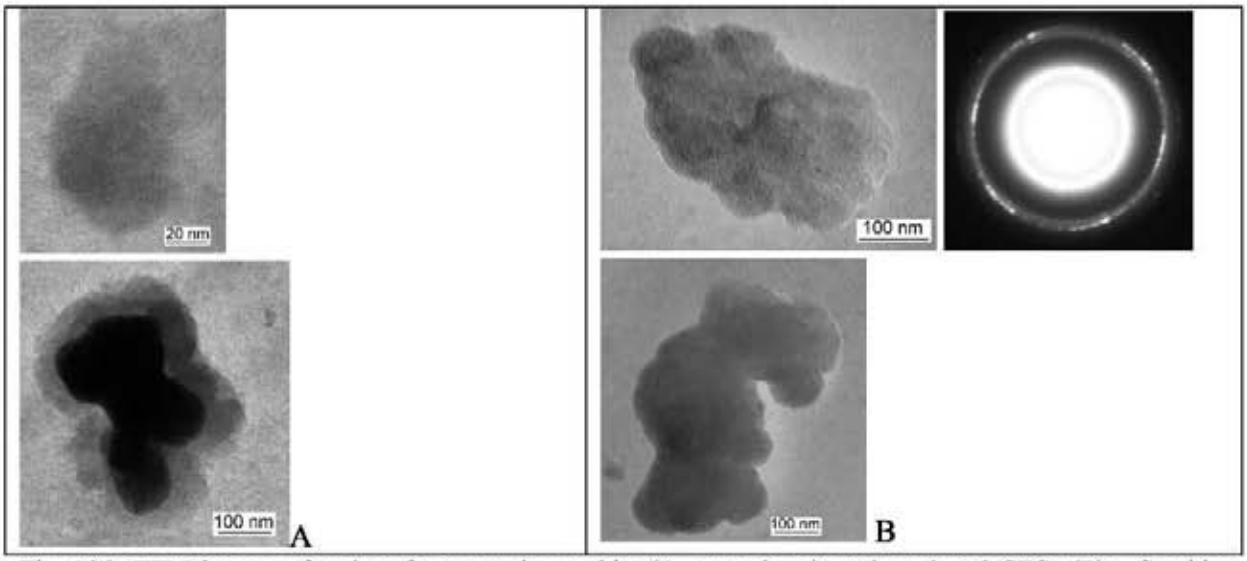

Fig. 106 TEM images of carbon fragments in graphite (A, amorphous), and un-doped CFCs (B); Graphite (R6650): P_{abs}= 2.0 GWm^{-2}, Δt = 4.3 ms n=5, CFC: P_{abs} = 4.0 GWm^{-2}, Δt = 1.7 ms n=5

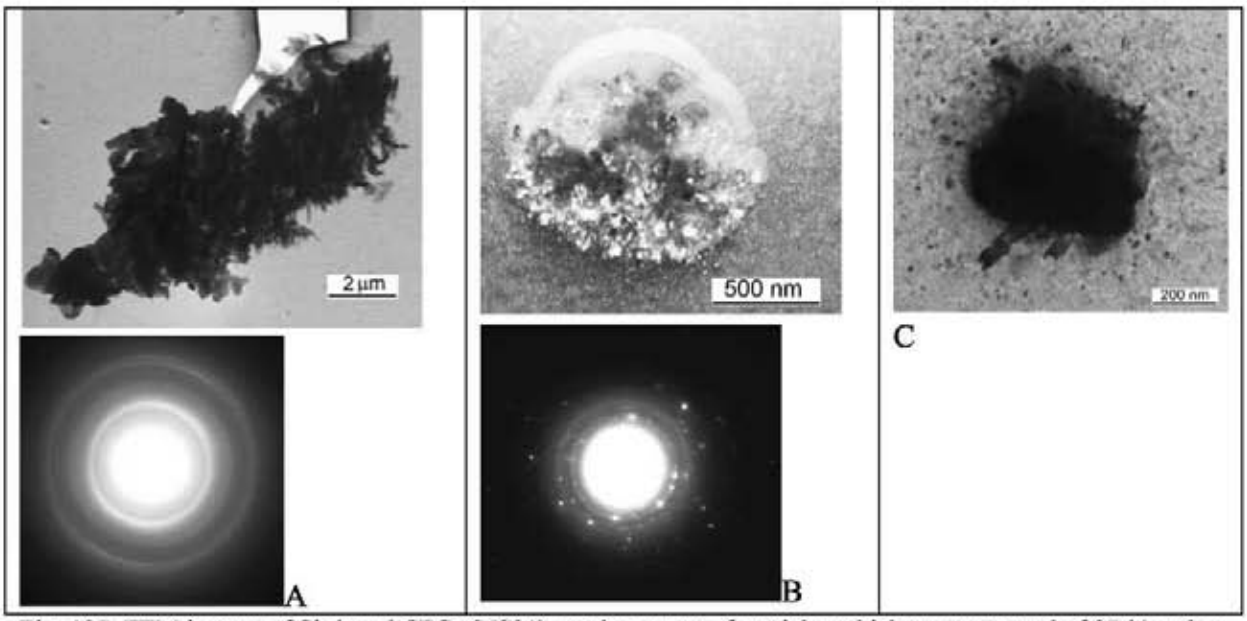

Fig. 107 TEM images of Si-doped CFCs (NS31); agglomerates of particles which are composed of 97 % carbon and 3% Si (A), a C and Si particle which consists of 83 % Si and 17 % C (B), and fine carbon particle shown in black (C). P_{abs}= 6.7 GWm^{-2}, Δt = 1.8 ms n=5

4.3.7 Effect of multiple shot

Thermal load tests on CBMs with multiple electron beam pulses were performed to study the effect on brittle destruction. The erosion depth (the deepest point) per shot as a function of absorbed power density is shown in Fig. 108. The first shot exhibited the most severe damage, decreasing from the shot to shot (pulse duration of 1 and 4.5 ms). For 90 ms, the first shot produced no crater and no particle emission, but after 10^{th} shot a 100 micrometer in crater depth emerged. This phenomenon has not been able to be explained. For short pulse duration (1 to 4.5 ms), the erosion per shot became smaller with number of shots and the surface is likely to withstand several disruption events.

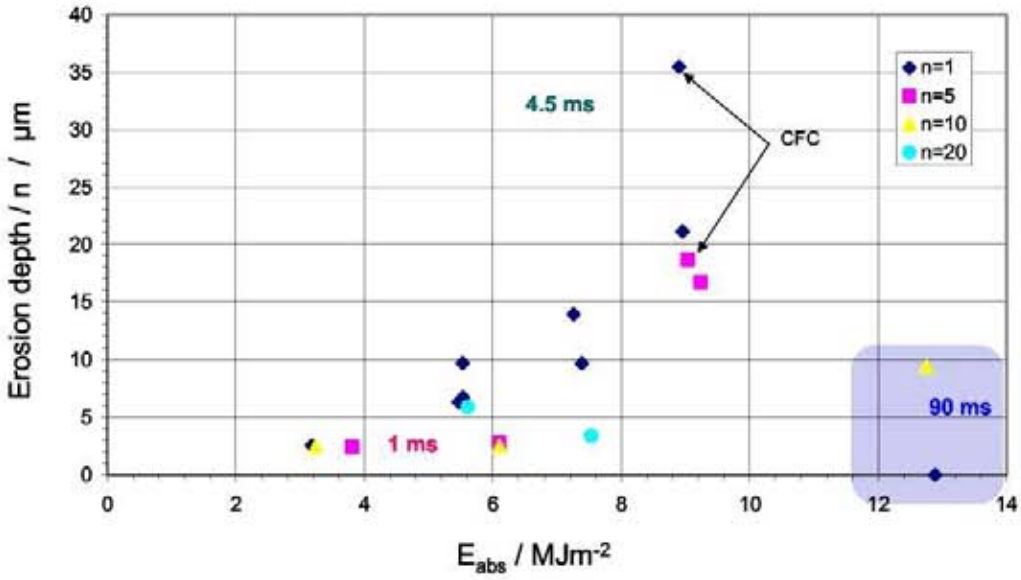

Fig. 108 Erosion depth per shot (n) as a function of absorbed energy E_{abs} of graphite and CFC (indicated in the figure) with multiple shots.

4.3.8 Effect of sample preheating

Samples were heated up to 500 °C and 800 °C. to see the influence of preheating compared to the samples loaded at RT. The preheated temperature was raised to 500 °C where chemical erosion will mainly take place and 800 °C where chemical erosion will not take place [37 - 50]. In ITER the surface temperature of the divertor will be in this range. After reaching homogeneous temperature the transient heat load was applied

The current plots showed no significant differences between samples loaded at RT and elevated temperatures. The sudden current drop which is typical for CMBs occurred at the same time in samples with and without preheating (e.g. at t = 0.3 ms for P_{abs} = 1.9 GWm^{-2}, Δt = 4.5 ms).

The SEM image of Si-doped CFCs loaded at power density P_{abs} of 3.0 GWm^{-2} for pulse duration of 4.5 ms at 500 °C showed a breaking of PAN fiber bundles and redeposition of melted Si and SiC outside the loaded area (Fig. 109). The surface morphology represents no difference for Si-doped CFCs loaded at RT in the big particle emission regime. The deposited melt layer was analysed by EDX (Fig. 109B). The gray parts in redeposited area are mainly SiC. Some white spots were composed of O, Mg, Al, Si, Ca, Fe, Mo or of Si only. These elements other than Si or C were only detected in Si-doped CFCs. NS31 contains these elements already prior to testing, which were analyzed by ICP-MS (Ref. appendix). It indicates that the impurities might contain during CVI of silicon.

Cross section images were taken after the ceramographic preparation. They show the influence of preheating on Si-doped CFCs (Fig. 110). The silicon, which was initially distributed homogeneously started to melt, has almost disappeared from the surface after loading. In the center of the loaded area, the silicon was completely removed up to a depth of 80 µm while some carbon fibers remain. These carbon fibers lost contact with the rest of the material and some parts were broken, and ready to ablate.

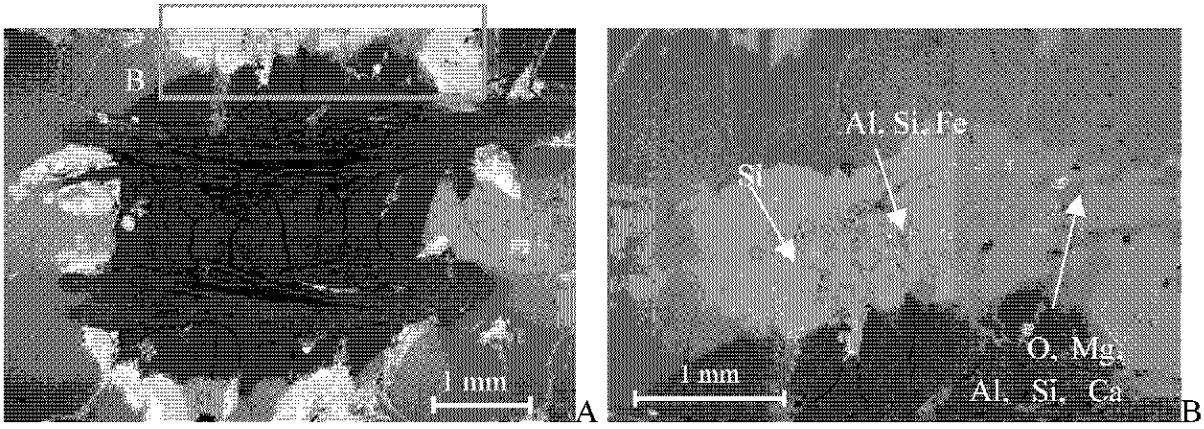

Fig. 109 Back scattered electron images of Si-doped CFC (NS31) preheated at 500 °C (220_36). I_{inc} = 200 mA, Δt = 4.5 ms, P_{abs} = 3.0 GWm^{-2} (surface view)

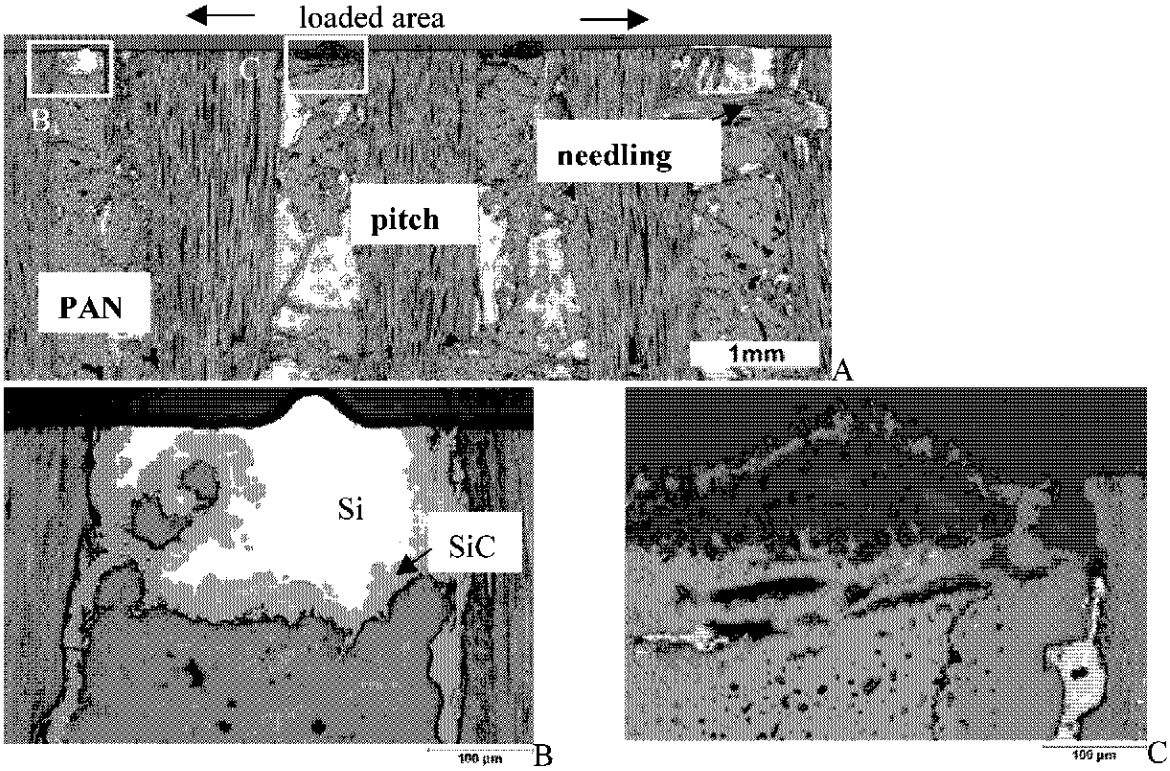

Fig. 110 Cross section images of Si-doped CFC (NS31) preheated at 500 °C (220_36).
A: overview, B: higher magnification of the part outside (B) and inside (C) the loaded area
I_{inc} = 200 mA, Δt = 4.5 ms, P_{abs} = 3.0 GWm^{-2}

The resulting weight loss of the preheated samples of all three materials was 2 to 4 times higher compared to the samples loaded at RT (Fig. 111). Sublimation might have increased the material erosion at elevated temperatures because the preheated samples reach the sublimation temperature faster compared to the samples without preheating.

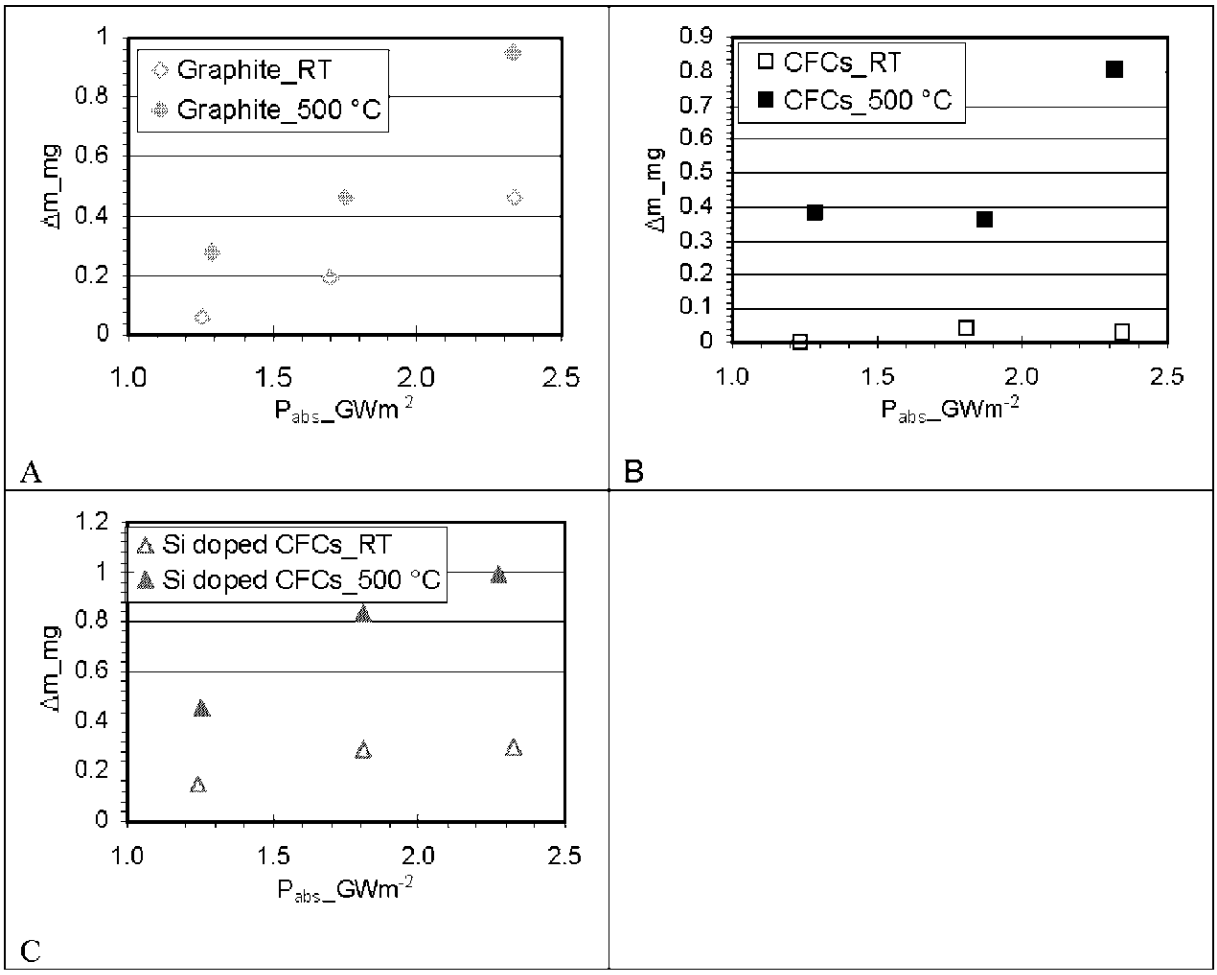

Fig. 111 Weight loss in graphite (R6650, A), CFCs (NB31, B)), and Si-doped CFCs (NS31, C) without preheating (RT), and with preheating at 500 °C as a function of absorbed power density P_{abs}. Δt = 4.5 ms

4.3.9 Sub-millisecond heat flux test

ELMs are considered to have energy density of 1 - 2 MJm^{-2} for pulse duration of 0.5 ms. Regarding the previous results (Fig. 97), each individual ELM is below the threshold of BD onset. To investigate ELM induced material damage in an electron beam facility, a static beam without scanning was applied because thermal load under ELMs conditions for pulse duration of 0.5 ms (Ref. Chap. 4.2.3.6).

Graphite sample after a single shot and after multiple shot experiments (n = 200) at the maximum energy density E_{abs} of 2.5 MJm^{-2} for pulse duration of 0.54 ms are shown in Fig. 112.

During the loading a slight emission of small particles has been detected. The erosion depth was 2.3 µm after a single shot and 54.7 µm after 200 shots. The crater formation occurred due to sublimation in the center of the beam. The erosion for 200 shots resulted in 0.27 µm per shot. Hence, the erosion per shot was decreased by a factor of 8 after 200 shots. It indicates that the first shot had the strongest influence on the surface of the material and the erosion per shot became less after multiple shots. The crater depths per shot remain in the regime of no particle emission regime in Fig. 102, which can help to estimate the lifetime of the components.

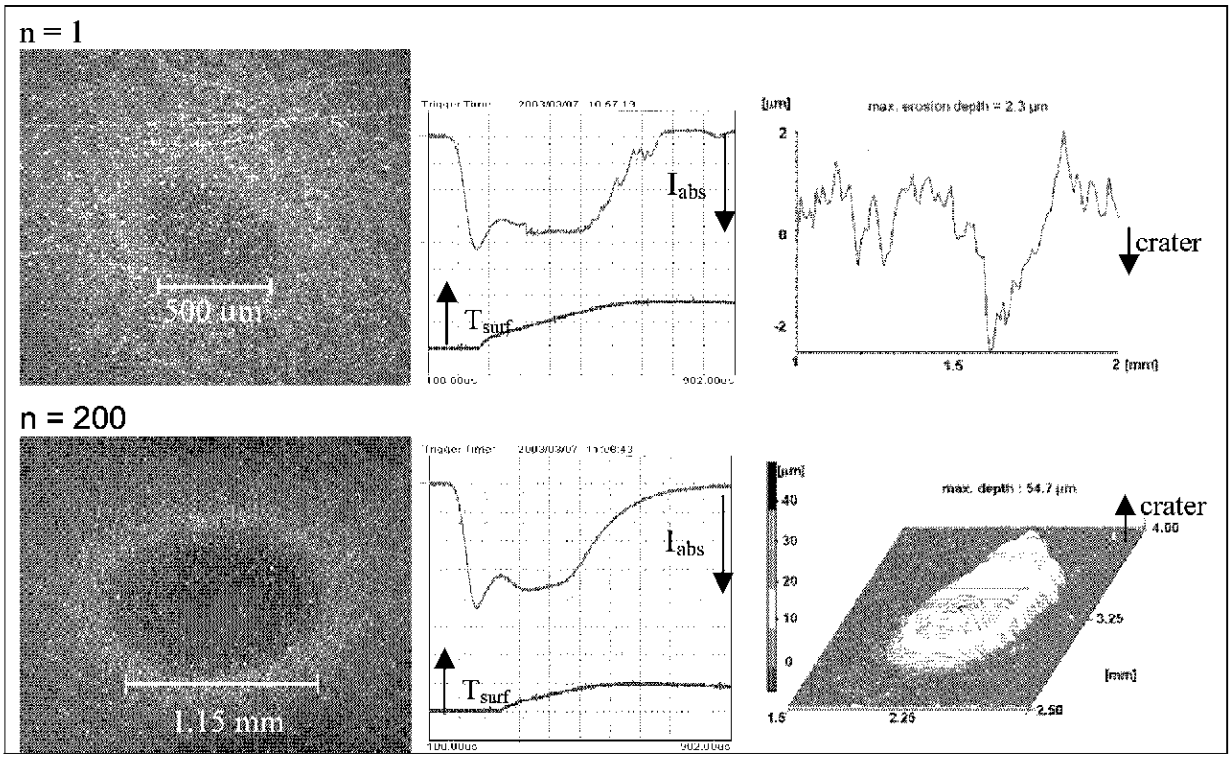

Fig. 112 Simulation of sub millisecond pulses (ELMs) on graphite R6650 using an electron beam without scanning. I_{inc} = 150 mA, V_{acc} = 120 keV, pulse duration Δt = 0.54 ms, max. E_{abs} = 2.5 MJm^{-2}, FWHM = (1.84 mm) of e-beam at focus 1 = 320 mA, focus 2 = 633 mA

4.3.10 Conclusion

The threshold values for the onset of brittle destruction of different carbon based materials have been determined in electron beam load tests for pulse duration between 1 and 90 ms as summarized in the following table.

Table 18 Threshold heat flux values for the onset of brittle destruction.

	"Small particle" emission [GWm^{-2}]	"Big particle" emission [GWm^{-2}]
1 ms	-	4.0-4.8, 6.6-7.7
1.8 ms	2.3	3.0
2.4 ms	2.2	2.4
3.3 ms	1.8	2.2
4.4 ms	1.1	1.7
90 ms	0.180	-

It was shown that off-normal events such as plasma disruption and VDEs are in the regime above the threshold and cause catastrophic damage called brittle destruction. Brittle destruction already appears after a single electron beam pulse. The expected loading conditions for each individual ELM are well below the threshold curve for both graphite and CFCs.

Depending on pulse duration and incident power density two different regimes of particle generation were detected for carbon based materials, namely "small particle regime" which is characterized by the break of bonds between grains and "big particle regime" which consists of the ejection of both isolated grains and clusters.

For graphite the resulting erosion depth was dependent on the emitted particles. For no particle emission it was in the range of 0 to 3 μm, 2 - 12 μm for small particle emission, and 10 - 80 μm for big particle emission (P_{abs} = 0.1~8 GWm^{-2}, Δt = 1-5 ms). Ejected particles with a diameter of several tens of nanometers have been detected, consisting of amorphous carbon. For 90 ms pulses and in small particle emission regime, the craters show a homogeneous erosion of about 80 μm.

The erosion of CFCs did not form homogeneous craters but started at some points in the PAN fiber. Depending on the applied loads, CFCs undergo three steps for material erosion; detachment of PAN fiber bundles, ablation of PAN fiber bundles, and finally erosion of pitch fiber bundles. Especially the intersection of PAN fibers and the needling structure is easily eroded to a depth of up to 140 μm for 4.4 ms at P_{abs} of 2.5 GWm^{-2}. There was no visible roughness in the pitch fiber area at the onset of brittle destruction. In the range of big particle emission, the whole loaded area was affected and the pitch fibers started to ablate. Particles emitted from CFCs consist of agglomerated sub μm sized agglomerated carbon fragments with preferred crystallographic orientation.

Si-doped CFCs show local degradation of Si as well as the PAN fiber area. At the onset of small particle emission both un- and Si-doped CFCs showed damage of PAN fibers, but the material erosion in terms of erosion depth and weight loss became larger at Si-doped CFCs. The reason is the melting of silicon and ejection of Si droplets. The resulting erosion depths were 5-70 μm for small particle emission and 60-140 μm for big particle emission (Δt = 4.4 ms). One globular particle with 1.1 μm in diameter was detected from Si-doped CFCs, consisting of 83 % Si and 17% C. The electron diffraction pattern from the spots with a diameter of about 62 nm indicates a crystalline structure which is supposed to be either Si, SiC, or the combination of both. The erosion of Si-doped CFC was significantly increased by preheating. The melting of Si from Si-doped CFC was accelerated by preheating and the silicon has almost disappeared from the surface in the loaded area. Several metal elements like Al and Mo were also detected as well as Si in the redeposition. From the present results, regarding weight loss, erosion depth, and early melting one can conclude that the use of Si-doped CFC is not preferable for PFMs in ITER. However the Si-doped CFC still can be included as an alternative for PFCs until it is clear if the surface with depleted or redeposited silicon still helps to reduce chemical erosion.

Preheating of the sample does not influence the time of BD onset (τ_{bd}) for all CBMs. However, the resulting weight loss of the preheated samples was 2 to 4 times higher compared to the samples loaded at RT. The interesting feature is that preheating graphite samples showed almost the same performance as CFCs under ITER relevant conditions. But here only weight loss with limited sample number is considered. Further studies are necessary.

The sub-millisecond (ELMs) simulation test at a deposited energy density of E_{abs} = 2.5 MJm^{-2} (Δt = 0.54 ms) for a relatively low cycle number (n = 200) showed that the first shot had the strongest influence on the surface of the material with respect to crater formation. The maximum crater depth was 2.3 μm after single shot and 55 μm after 200 shots. The erosion per shot was decreased by a factor of 8 after 200 shots.

5 Summary

In fusion devices based on the Tokamak principle, intense transient heat loads, known as edge localized modes (ELMs), plasma disruptions and vertical displacement events (VDEs) take place. During these events, the plasma facing materials of the divertor strongly suffer from this highly concentrated energy input, and irreversible damage may occur. Typical damages of metals are melting and re-crystallization, crack and droplet formation. In carbon based materials, crack formation, sublimation and solid particle emission tend to occur.

Beam characteristics

In order to evaluate the degradation of the plasma facing components under these conditions, simulation experiments using the electron beam facilities JUDITH and JEBIS have been performed. Both test facilities are characterized by specific beam modes and loading parameters. A comparison between the two facilities showed that the material erosion rate was higher in JEBIS (static beam, 52 – 65 kV) compared to JUDITH (scanned beam, 120 kV) for identical thermal loads. Three major factors were identified as basic cause for this effect. First, the static beam mode which were applied in JEBIS does not generate a homogeneous energy input throughout the full beam pulse. In fact the distribution is supposed to be Gaussian which means that the maximal heat flux was absorbed in the center while the impact on the surrounding areas was lower. In addition, due to self-focusing of the beam the local power density distribution changes during the pulses. These effects result in a high temperature gradient and thus high stresses between center and border of loaded area. In the case of a more homogeneously distributed heat flux, these stresses are only generated on the edge of the loaded area. When the surface melts, the surface tension of the melt layer in JEBIS becomes higher than in JUDITH, and ejection of melt layer occurs earlier. Melting of the center and ejection of liquid metals or solid particles continuously occur, resulting in higher material erosion. The second important factor is the scanning mode used in JUDITH. As the beam is diverted with high frequencies both in x and y direction over the loaded area a continuous highly localized alternation among melting, convection of melt layer, boiling, and re-solidification take place. The molten and re-solidified materials remain within the loading area, which leads to a rippling of the exposed surface loaded in JUDITH. Third the penetration of the electron beam in JUDITH is more than twice as deep as the beam in JEBIS. The effect of volumetric heating becomes higher for JUDITH samples, resulting in lower degradation of the materials.

On the basis of a well analyzed and calibrated experimental set-up it became possible to investigate the performance of different candidate plasma facing materials designated for integration in future fusion devices. Within these candidates two main groups of material candidates are distinguished, high Z materials and carbon based materials.

Performance of the high Z materials

The behavior of the different high Z materials W, Ta, Mo, WC, W-alloys (W-La, -Re), and plasma sprayed (PS) W has been compared under plasma disruption conditions (P_{abs} = 1.2-1.6 GWm^{-2}, Δt = 4~ 4.5 ms) in JUDITH.

From tests on different high Z materials, pure W and Ta were found to show the highest resistance against thermal shock under plasma disruption conditions. With respect to melt layer loss and crack formation, tungsten showed only a relatively small weight loss and a low crater depth of about 50 μm. Some cracks with the maximum depth of 1.2 mm were produced vertical to the surface. Ta showed a relatively small weight loss as well and no crack formation. A comparable performance has been established for Ta as a reference material. However, Ta is less favorable for PFMs in Tokamak devices because it has high affinity with hydrogen.

W-1% La_2O_3 has been considered as an alternative to pure W due to its easier machinability at room temperature, higher re-crystallization temperature, and higher strength after re-crystallization textured material. During the experiments in JUDITH it showed melt ejection, deep crack, droplet and bubble formation. It was found that the early evaporation of La_2O_3 was responsible for the less favorable performance and the non-desirable roughening of the surface morphology under transient heat load compared to pure W.

Plasma sprayed (PS) W is considered as an attractive coating technique because of the high deposition rate, and technically feasible coating thickness up to several mm. However, the thermal shock behavior, and the thermal and mechanical properties of PS W turned out to be inferior to those of sintered W. To be precise PS-W experienced the highest weight loss, crater depths, droplets and crack formation of all tested materials. The crack formation both parallel and vertical to the surface between the individual splats develops the subsequent detachment from adjacent layers. This leads to the generation of tungsten dust particles and reduce thermal conductivity.

To increase the performance of pure tungsten and to overcome the drawbacks of a high DBTT, different configurations of the PFMs were considered. Castellated samples showed a better thermal response than the bulk samples. The crack growth could be significantly reduced by using a lamellae structure. However, the lamellae structure showed deeper craters and a distinct tendency to form droplets. As a conclusion, castellated components showed to be the most favorable configuration to reduce thermal stresses and to avoid significant damage not only during thermal fatigue loading but also during intense transient heat loads.

The obtained results were further used to describe the damage mechanisms of high Z materials. Four thermal responses are observed with increasing the heat flux.

1. Cracks were formed inside, as tensile forces developed during cooling down into the brittle regime after thermal loading. Cracks were also formed outside the loaded area where the temperatures remained almost constant, as the contraction on the edge of the loaded area occurred after thermal loading.
2. The surface starts to melt and an increase of volume going to form a convex surface after loading. Outside the loaded area, the material is approximately at RT, while the free surface of the molten layer is the only space to move.
3. A deformation of the melt layer occurs. When the surface of melt layer reaches the boiling point, the convection of melt layer and the vapor recoil pressure initiate molten material to flow outside the loading area and to create a visible crater or a rippled surface.

4. Vapor shielding takes place. As more material evaporates over the surface with increasing heat flux, a vapor cloud is formed over the loaded area and protected from further melting.

In future Tokamak devices, this vapor shielding (4) which protects the divertor from further melting will have a significant impact on the lifetime of the high heat flux components.

Performance of carbon based materials

Three carbon-based materials (CBMs), isotropic graphite, CFC and Si doped CFC, were investigated. It was found that besides evaporation, particle emission has to be considered as major contribution to the total erosion of CBMs. This phenomenon is also known "brittle destruction". The reasons for the particle emission were correlated to breaking of the bonds among grains, and fibers of the materials, initiated by high thermally induced stresses due to the anisotropy of these materials on a macroscopic scale.

A criterion was found to define the onset of brittle destruction in the electron beam experiment for both graphite and CFC. Thus threshold values for short (1~5 ms) and medium (90 ms) pulse duration were experimentally determined and a curve quoting a safe loading regime over heat flux and pulse duration was introduced. The typical off-normal events, plasma disruptions and VDEs were in the regime above this threshold for all three candidates, which in consequence has to be considered in future devices such as ITER: The expected loading inputs during individual ELM are well below the threshold curve.

The catastrophic damage due to brittle destruction even after single electron beam pulses is characterized by two different regimes of particle generation, namely a "small particle regime" and a "big particle regime". The first one was characterized by breaking of the bonds among grains, releasing small particles of a few microns in size, whereas during the second regime macroscopic erosion occurred with the ejection of isolated grains and clusters (approx. 10 microns in size). In CFC materials, also fragments of individual fiber and fiber clusters were emitted.

Out of three CBMs, un-doped CFC has demonstrated the best resistance against disruption specific thermal shock experiments. The weight loss was in each case below 0.1 mg, while graphite and Si-doped CFCs lost up to 0.5 mg at P_{abs} = 1~2.3 GWm^{-2} for 4.2~4.5 ms. Also the change of the surface morphology was smallest for the CFC. No visible erosion was observed in the pitch fiber area up to the regime for onset of brittle destruction. The pitch fibers which mainly account for the superior thermal conductivity and the high mechanical strength of CFCs, oriented perpendicular to the sample surface. However, loading in the range of big particle emission, affected the whole loaded area and the PAN fibers with an orientation parallel to the heat affected surface started to ablate. Isotropic graphite showed homogeneous craters in the loading area. For the Si-doped CFCs the local degradation and early evaporation of Si was found to cause the higher erosion depth and weight loss compared to un-doped CFC. From the present results Si-doped CFCs are less favorable for PFMs in terms of thermal shock resistance. However, Si or re-deposited Si helps to reduce chemical erosion during plasma exposure. On the basis of the present results a final conclusion about the use of Si-doped CFC can therefore not be made.

The ejection of carbon particles has much higher intensity compared to metals and can be a serious concern for long-term operation in fusion reactors. In JEBIS it was not possible

to prolong the pulse duration beyond 1.7 ms for CBMs maybe because of an arcing effect in the plasma source, or the faster velocity of ejected particles or droplets of CBMs compared to metals to reach the plasma source. The emission for metallic droplets did not obstruct the performance of the plasma-type electron beam source for thermal loads up to 5 ms, although the weight loss of metals was higher than that of CBMs at identical heat flux.
Indication of vapor shielding in JUDITH was also observed for CBMs similar to W. It obviously suppressed brittle destruction for P_{abs} =5-6 GWm^{-2} and short beam pulses in the 1 ms-range.

Influence of further loading parameters

For a reliable prediction of the material performance in real applications the influence of other possible factors must be known, or experimentally investigated. In the case of ITER the main differences between experiments and applications, concerning thermal loading, are based on the higher operational temperature of the components, larger loaded areas and repeated transient thermal loads.

At higher initial temperatures in the range from 300 to 500 °C for W and from 500 to 800 °C for CBMs, the resulting weight loss was increased in comparison to testing at room temperature for both CBMs and W. The W samples have not yet achieved a ductile condition and a progressive material erosion took place. Bubble formation, cracks outside the crater, and micro cracks in the crater were observed. For CBMs, especially Si-doped CFCs showed a significant increase of the depletion and evaporation of Si.

Multiple shots [ELMsand disruption conditions]

The defocused beam profiles were calibrated and a simulation of ELMs has been performed for the first time in JUDITH. There was no remarkable difference in the material degradation for W with respect to the maximum erosion depth after single and 100 ELMs conditions because only a light melting occurred during the shots followed by a subsequent re-crystallization. However, after 100 shots, microstructure images showed a few bubbles in the convex melt layer and several cracks around the crater with a depth up to approx. 500 μm. In contrast, progressive erosion of graphite occurred under ELMs with deposited energy density of E_{abs} = 2.5 MJm^{-2} for pulse duration Δt = 0.54 ms. An interesting feature is the fact that the first shot had the strongest influence on the surface of the material with respect to crater formation. The maximum erosion depth per shot decreased by a factor 8 after 200 shots. This erosion occurs below the threshold for brittle destruction. Therefore the driving force for the process is supposed to be thermal sublimation. A similar behavior was also seen under plasma disruption conditions. The max. erosion per shot decreased with the shots number for E_{abs} = 3~9 MJm^{-2} (P_{abs} >1GWm^{-2}) at short pulse duration from 1 to 4.5 ms.

Differences in performance between W and un-doped CFC

The weight loss of un-doped CFC loaded with P_{abs} = 1.2 GWm^{-2} for Δt = 4.4 ms were negligible both for pure W and un-doped CFC. In un-doped CFC, no crack formation, nor any erosion in the pitch fiber area, but a 28 μm of maximum erosion depth in the PAN fiber area has been detected. W showed 50 μm in maximum erosion depth and1.2~1.6 mm deep cracks. With initially elevated temperatures (500 °C), the weight loss became 0.4 mg for CFC, but only 0.16 mg for W under simulation of plasma disruptions. Under VDE conditions (E_{abs}

= 50 MJm^{-2}, Δt = 90 ms), pure W developed cracks and a melt layer with 1.2 mm thickness, but did not form a visible crater. Because these materials did not eject the melt layer but re-solidified in its original position.

The higher weight loss of CFCs is associated with the ejection of solid particles. The dust formation above the surface was much higher compared to refractory metals and can be a serious concern for fusion reactors. From the present results pure W showed to be the most favorable as a plasma facing material among the investigated materials.

Symbols

A ..... area [m^2]
a ..... thermal diffusivity [m^2s^{-1}]
α ..... surface tension coefficient
b.p. ..... boiling point [K or °C]
α ..... coefficient of thermal expansion [10^{-6} K^{-1}]
C_p ..... specific heat [$Jkg^{-1}K^{-1}$]
ΔH_m ..... enthalpy of melting [Jkg^{-1}]
ΔH_v ..... enthalpy of vapor [Jkg^{-1}]
Δt ..... pulse duration [ms]
dz ..... depth step [m]
E ..... elastic module [GPa]
ε ..... emissivity
ε_{abs} ..... absorbtion coefficient
E_{abs} ..... absorbed energy density [Jm^{-2}]
f_x ..... frequency in x direction [kHz]
f_y ..... frequency in y direction [kHz]
h ..... height of the melt layer [m]
I_{abs} ..... absorbed current [A]
I_{inc} ..... incident current [A]
$\vec{j}$ ..... surface density of heat flux [Wm^{-2}]
λ ..... thermal conductivity [$Wm^{-1}K^{-1}$]
μ ..... viscosity of melt [Pa s]
n ..... outward drawn normal
m.p. ..... melting point [K or °C]
ρ ..... density [$kg \cdot m^{-3}$]
P_{abs} ..... absorbed power density [Wm^{-2}]
P_v ..... volumetric heat flux density [Wm^{-3}]
$Q(x,y,z)$ ..... sum of the volumetric heating [J]
Γ ..... position of the boundary surface
R_m ..... penetration depth [m]
σ ..... Stefan-Boltzmann constant, $5.67 \cdot 10^{-8}$ [$Wm^{-2}K^{-4}$]
T ..... temperature [K]
T_{inp} ..... nominal pulse length [ms]
u_v ..... velocity of the evaporated particles [ms^{-1}]
V_m ..... velocity of melt [m s^{-1}]
V, U_B ..... acceleration voltage [V]

Abbreviation

AMC® ..... Active Metal Casting®
BD ..... Brittle Destruction
CBMs ..... Carbon Based Materials
CFCs ..... Carbon Fiber Composites
CVI ..... Chemical Vapor Infiltration
CTE ..... Coefficient of Thermal Expansion [10^{-6} K^{-1}]
DBTT ..... Ductile to Brittle Transient Temperature
dpa ..... dose per atom
EB ..... Electron Beam
EDX ..... Electron Disperse X-ray analysis
ELMs ..... Edge Localized Modes
FEM ..... Finite Element Method
FGM ..... Functionally Graded Material
FWHM ..... Full Width at Half Maximum intensity
HIP ..... Hot Isostatic Pressing
JEBIS ..... JAERI Electron Beam Irradiation Stand
JUDITH ..... Juelicher Divertor Testanlage in den Heißen Zellen
PAN ..... Poly AcryloNitoril
PFCs ..... Plasma Facing Components
PFMs ..... Plasma Facing Materials
PM ..... Powder Metallurgy
PS ..... Plasma Sprayed
RES ..... Radiation Enhanced Sublimation
RT ..... Room Temperature
SEM ..... Secondary Electron Microscopy
TEM ..... Transmission Electron Microscopy
VDEs ..... Vertical Displacement Events
XRD ..... X-Ray Diffractometry

Appendix

Chemical composition of stainless steel (1.4571).

	Al	Si	Cr	Mn	Fe	Ni	Mo
Conc. %	1.0	0.5	16.0	0.9	69.6	10.6	1.4

Results of LA-ICP-MS-Analysis of Si-doped 3D CFC (NS31).

Element	Concentration in µg g^{-1}	Element	Concentration in µg g^{-1}
Li	< 30	Cs	< 9.6
Na	833	Ba	< 16
Mg	150	La	< 10
Al	1535	Ce	< 8.1
Sc	< 118	Pr	< 6.8
Ti	226	Nd	< 20
V	< 56	Sm	< 22
Cr	< 135	Eu	< 7.0
Mn	153	Gd	< 25
Fe	7200	Tb	< 5.7
Co	< 21	Dy	< 17
Ni	256	Ho	< 4.3
Cu	550	Er	< 20
Zn	110	Tm	< 5.2
Ga	< 40	Yb	< 26
Ge	< 30	Lu	< 4.4
As	< 16	Hf	< 15
Sr	15	Ta	< 22
Y	< 8.9	W	< 36
Zr	101	Re	< 11
Nb	< 9.3	Os	< 10
Mo	25	Ir	< 11
Ru	< 42	Pt	< 16
Rh	< 9.8	Au	< 12
Ag	< 5.8	Hg	< 40
Cd	< 33	Tl	< 9.4
In	< 15	Pb	< 19
Sn	< 30	Bi	< 6.9
Sb	< 2.9	Th	< 4.0
Te	< 13	U	< 4.1

Loading conditions and results of stainless steel samples (Ref. Chap. 4.1.4)

Sample ID	Focus 1 mA	Focus 2 mA	I_{inc} mA	I_{abs} mA	Δt ms	area mm^2	P_{abs} GW/m^2	E_{abs} MJ/m^2	Erosion µm	Comments
M139_5_1	320	633	30	20.4	3.93	7.6	0.32	1.3	22.7	static beam
M139_5_2	320	633	50	34.1	4.31	7.6	0.54	2.3	92.8	static beam
M139_5_3	320	633	75	51.3	4.45	7.6	0.80	3.6	137	static beam
M139_5_4	320	633	100	74.2	4.58	7.6	1.2	5.3	207.4	static beam
M139_5_5	260	630	75	53.3	4.57	4.3	1.5	6.8	80.9	static beam
M139_5_6	260	630	100	71.2	4.66	4.3	2.0	9.3	133	static beam
M139_5_7	320	633	120	91.7	4.62	7.6	1.4	6.6	199	static beam
M139_5_8	290	613	50	35.4	4.28	4.4	1.0	4.2	136	static beam
M139_75	290	613	340	235	5	17.4	1.6	8.1	238	scanning beam
M139_78	320	633	100	64.6	4.62	7.6	1.0	4.7	148	static beam, Ø 5 mm aperture
M139_77	320	633	100	58.8	4.59	7.6	0.92	4.2	80.0	static beam, Ø 3 mm aperture

loaded area of static beam = $\pi \times (\sigma)^2$

Loading conditions and results for preheating samples of carbon based materials.

Sample ID	Preheat °C	I_{inc} mA	I_{abs} mA	Δt ms	Area mm	P_{abs} GWm^{-2}	E_{abs} MJm^{-2}	
221_19	483	180	175	4.42	4.0	1.3	5.7	0.275
221_20	500	240	238	4.49	4.0	1.8	7.9	0.46
221_97	480	350	317	4.57	4.0	2.3	10.7	0.51
219_39	490	180	175	4.42	4.0	1.3	5.7	0.38
219_40	470	260	254	4.49	4.0	1.9	8.4	0.36
219_41	483	350	315	4.61	4.0	2.3	10.7	0.805
220_40	485	180	171	4.42	4.0	1.3	5.6	0.455
220_41	560	260	246	4.53	4.0	1.8	8.2	0.83
220_42	525	350	308	4.61	4.0	2.3	10.5	0.99

Loading conditions and results for carbon based materials

shot No.	Name AREA	Sample ID	n	Area mm	T_{impact} ms	Δt ms	I_{beam} mA	I_{abs} mA	P_{abs} GW/m²	E_{abs} MJ/m²		Comment Current curve - Data files
	A	221/28	1	3.0	5	5	100	93	1.27	6.37	9.23	fine particle emission
11/12	B		1	3.0	5	4.4	120	116	1.60	7.03	12.94	fine particle emission, file number 2212813 i,t x,y
13	C		1	3.0	5	4.4	140	136	1.86	8.10	20.41	big particle emission
14	D		1	3.0	5	4.4	140	136	1.87	8.22	22.06	big particle emission
15	E		1	3.0	5	4.4	120	116	1.60	7.02	17.26	fine particle emission
16	F		1	3.0	5	4.4	130	126	1.72	7.50	19.23	big particle emission, threshold between 120 and 130 mA
17	A	221/29	1	3.0	5	4.4	110	106	1.45	6.31	11.53	fine particle emission
18	B		1	3.0	5	4.4	100	96	1.31	5.71	9.07	fine particle emission
19	C		1	3.0	5	4.2	90	86	1.18	4.98	3.92	no particle emission
20	A	221/30	1	3.0	5	4.3	95	89	1.22	5.26		fine particle emission, threshold between 90 and 95 mA, file number 2213020 i, t
21	B		1/n°1	3.0	5	4.4	130	126	1.72	7.55		8 big particles
22	B		1/n°2	3.0	5	4.3	130	126	1.72	7.45		20 ~ 30 smaller particles
23	B		1/n°3	3.0	5	4.3	130	126	1.72	7.40		medium particles
24	B		1/n°4	3.0	5	4.4	130	126	1.72	7.50		medium particles
25	B		1/n°5	3.0	5	4.5	130	126	1.72	7.71		small particles
	B		4	3.0	5	5.0	130	126	1.73	8.63		
26	B		1/n°10	3.0	5	4.4	130	126	1.72	7.50		medium particles
	B		9	3.0	5	5.0	130	126	1.72	8.62		
27	B		1/n°20	3.0	5	4.4	130	125	1.71	7.53	67.66	small particles
28	C		1	10	4500 s	3880	10	9	0.01	42.74		no particle emission
29	D		1	10	4500 s	3880	20	19	0.02	86.14		
30	A	221/31	1	10	45 00s	3880	30	27	0.03	124.78		visible crater
31	B		1	10	4500 s	3880	40	37	0.04	170.88	174.7	visible crater

shot No.	Name AREA	Sample ID	n	Area mm	T_{impur} ms	Af ms	I_{beam} mA	I_{abs} mA	P_{abs} GW/m²	E_{abs} MJ/m²		Comment Current curve - Data files
32	A		1	3.0	5	4.3	100	94	1.29	5.53	7.63	particles due to dust from previous test on samples?
33	B		1/n°1	3.0	5	4.4	100	94	1.29	5.61	117.78	
34	B		1/n°2	3.0	5	4.3	100	94	1.29	5.53		
35	B		1/n°3	3.0	5	4.4	100	94	1.29	5.61		
36	B		1/n°4	3.0	5	4.4	100	94	1.29	5.66		no record
37	B		1/n°5	3.0	5	4.4	100	94	1.29	5.67		
38	B	**221/32**	1/n°6	3.0	5	4.4	100	94	1.29	5.67		
	B		3	3.0	5	4.4	100	94	1.29	5.67		
39	B		1/n°10	3.0	5	4.4	100	94	1.29	5.67		no record
	B		4	3.0	5	4.4	100	94	1.29	5.67		
40	B		1/n°15	3.0	5	4.4	100	94	1.29	5.67		
	B		4	3.0	5	4.4	100	94	1.29	5.67		
41	B		1/n°20	3.0	5	4.4	100	94	1.29	5.61		
1	**A**		1	3.0	5	4.23	80	74	1.02	4.31	0.36	Nothing
2	**B**		1	3.0	5	4.29	90	82	1.13	4.84	4.72	Small particles, threshold at 80 ~ 90 mA
3	**C**		1	3.0	5	4.29	85	80	1.10	4.70	3.23	Small particles & 1 medium
4	**D**	**221/34**	1	3.0	5	4.35	100	93	1.27	5.53	6.75	Small particles
5	**E**		1	3.0	5	4.41	110	102	1.40	6.18	9.23	Small particles & 3 medium
6	**F**		1	3.0	5	4.41	120	112	1.54	6.79	12.11	Small particles & 2 medium
7	**G**		1	3.0	5	4.35	130	122	1.67	7.26	13.93	Small particles & medium
8	**H**		1	3.0	5	4.4	140	131	1.80	7.91	10.37	Big particles, threshold at 130 ~ 140 mA
9	**I**		1	3.0	5	4.4	150	134	1.84	8.08	14.37	Big particles

shot No.	Name AREA	Sample ID	n	Area mm	T_{impur} ms	Δt ms	I_{beam} mA	I_{abs} mA	P_{abs} GW/m²	E_{abs} MJ/m²		Comment Current curve - Data files
10	**A**		1	3.0	5	4.23	80	74	1.01	4.26		Very few small particles
11	**B**		1	3.0	5	4.29	85	82	1.13	4.84	3.03	Small particles
12	**C**	**221/37**	1	3.0	5	4.41	90	87	1.19	5.26	4.33	Small particles
13	**D**		1	3.0	5	4.35	100	92	1.26	5.47	6.34	Small particles
14	**E**		1	3.0	5	4.29	110	102	1.40	6.02	8.74	Small particles
15	**F**		1	3.0	5	4.41	120	112	1.53	6.75	10.28	Small particles
16	**G**		1	3.0	5	4.47	130	121	1.65	7.38	9.71	Small particles
17	**H**	**221/37**	1	3.0	5	4.41	140	130	1.78	7.85	13.27	Big particles
18	**I**		1	3.0	5	4.47	150	140	1.92	8.57	12.77	Big particles
19	**A**		1	6.1	99	88.94	80	74	0.24	21.61	17.53	Small particles
20	**B**	**221/38**	1	6.1	99	88.94	70	63	0.21	18.34	19.18	Small particles
21	**C**		1	6.1	99	88.94	60	54	0.175	15.60	3.55	Beginning of Small particles
22	**D**		1	6.1	99	88.94	55	49	0.16	14.23	1.59	Nothing, threshold at 55 ~ 60 mA
23	**A**		1	6.1	99	88.94	100	93	0.30	27.09	65.88	Small particles
24	**B**	**221/39**	1	6.1	99	88.23	120	112	0.37	32.34	56.47	Small particles
25	**C**		1	6.1	99	88.94	140	131	0.43	38.08	51.76	Small particles
26	**D**		1	6.1	99	89.4	160	149	0.49	43.79	49.40	Small particles
27	**A**		1	6.1	99	89.4	180	168	0.55	49.15	52.94	Small particles
28	**B**	**221/40**	1	6.1	99	88.94	50	44	0.14	12.89		Nothing
29	**C**		1/n°2	6.1	99	88.9	50	44	0.15	12.89		
30	**C**		8/n°10	6.1	99	88.23	50	44	0.14	12.76	94.50	

shot No.	Name AREA	Sample ID	n	Area mm	T_{input} ms	Δt ms	I_{beam}	I_{abs} mA	P_{abs}	F_{abs} MJ/m²		Comment Current curve - Data files
1	A	221/21	1	2.0	1	0.65	80	72	2.11	1.37		Nothing
2	B		1	2.0	1	0.76	100	92	2.70	2.05		Nothing
3	C		1	2.0	1	0.765	120	111	3.27	2.50	1.42	Nothing
4	D		1	2.0	1	0.87	140	129	3.80	3.30	2.09	Nothing
5	E		1	2.0	1	0.87	160	144	4.24	3.69	36.28	Big particles
6	F		1	2.0	1	0.88	160	144	4.24	3.73	28.14	7 Big particles
7	G		1	2.0	1	0.88	150	135	3.98	3.50	36.37	9 Big particles, 1 Medium, 1 Small
8	H		1	2.0	1	0.88	140	125	3.68	3.23	1.23	Nothing
9	I		1	2.0	1	0.88	145	129	3.79	3.34	0.3	Nothing
10	A	221/22	1	2.0	1	0.85	145	129	3.79	3.22		Nothing
11	B		1	2.0	1	1	180	165	4.84	4.84	31.1	6 Big particles, 2 Medium, 2 Small
12	C		1	2.0	1	1	200	185	5.45	5.45	-1.21	Nothing
13	D		1	2.0	1	0.982	200	185	5.45	5.35		Nothing
14	E		1	2.0	1	0.976	220	206	6.06	5.91	-0.88	Nothing
15	F		1	2.0	1	1	220	206	6.06	6.06	-0.79	Nothing
16	G	221/22	1	2.0	1	0.88	240	225	6.62	5.82	27.47	3 Big particles, 1 Medium
17	H		1	2.0	1	0.82	260	244	7.18	5.89	36.26	Big particles
18	I		1	2.0	1	0.8	280	263	7.74	6.19	35.34	Big particles
19	A	221/41	1	2.0	1	1	145	135	3.97	3.97	30.22	3 Big particles
20	B		1	2.0	1	1	140	130	3.83	3.83		Nothing
21	A	221/42	1	2.0	1	0.98	180	163	4.80	4.70	5.285	Nothing
22	B		1	2.0	1	0.89	160	144	4.24	3.77	30.7	Big particles
23	C		1	2.0	1	0.98	200	185	5.45	5.34		Nothing
24	D		1	2.0	1	0.97	220	206	6.06	5.87	1.55	Nothing
25	E		1	2.0	1	1	240	225	6.62	6.62	2.29	Nothing
	F		1	2.0	1	1	260	243	7.13	6.78		
26	G		1	2.0	1	0.83	260	243	7.13	5.92	38.73	Big particles
27	H		1	2.0	1	0.94	150	135	3.98	3.74	32.26	3 Big particles
28	I		1	2.0	1	1.125	170	154	4.54	5.11	36.11	Big particles, Small particles

shot No.	Name AREA	Sample ID	n	Area mm	T_{impact} ms	Δt ms	I_{beam} mA	I_{abs} mA	P_{abs} GW/m²	E_{abs} MJ/m²		Comment Current curve - Data files
29	**A**		1	2.0	1	0.835	145	129	3.81	3.18	2.56	Nothing
30	B		5	2.0	1	1	145	129	3.81	3.81	12.08	Nothing
31	C		10	2.0	1	1	145	129	3.81	3.23	24.79	1 Big particle, Small particles
32	D		1	2.0	1	0.95	220	207	6.10	5.79	-1.39	Nothing
33	E	**221/23**	2 / n°2	2.0	1	1	220	207	6.10	6.10	17.03	Nothing
34	E		1/n°3	2.0	1	1	220	209	6.14	6.14		
35	E		2/n°5	2.0	1	1	220	207	6.10	6.10		
36	E		1/n°6	2.0	1	1	220	207	6.10	6.10		
37	F		10	2.0	1	1	220	207	6.10	6.10	25.5	Small particles
shot No.	**Name AREA**	**Sample ID**	**n**	**Area Mm**	**T_{impact} ms**	**Δt ms**	**I_{beam} mA**	**I_{abs} mA**	**P_{abs} GW/m²**	**E_{abs} MJ/m²**		**Comment Current curve - Data files**
1	**A**		1	2.0	1	0.82	145	141	4.15	3.41	1.81	Small Particles beginning
2	**B**		1	2.0	2	1.63	145	141	4.15	6.76	7.64	Big Particles
3	**C**		1	2.0	1	0.99	220	215	6.31	6.25	1.02	Nothing
4	**D**		1	2.0	2	1.68	220	215	6.31	10.61	14.59	Big Particles
5	**E**	**221/45**	1	2.0	1	1	200	196	5.76	5.76	0.78	Nothing
6	**F**		1	2.0	2	1.75	200	194	5.71	9.98	24.14	Big Particles
7	**G**		1	2.0	2	1.8	180	174	5.10	9.18	14.08	Big Particles
8	**H**		1	2.0	2	1.75	160	156	4.58	8.02	12	Big Particles
9	**I**		1	2.0	2	1.63	140	135	3.98	6.49	10.03	Big Particles
10	**A**		1	2.0	2	1.64	120	118	3.46	5.67	25.04	Big Particles
11	**B**		1	2.0	2	1.67	100	94	2.77	4.62	3.11	Small Particles
12	**C**	**221/46**	1	2.0	2	1.6	90	84	2.47	3.96	0.75	Nothing
13	**D**		1	2.0	2	1.76	95	85	2.51	4.42	-0.1	Nothing
14	**E**		1	2.0	2	1.56	95	90	2.65	4.13	1.38	Small Particles
15	**F**		1	2.0	2	1.647	110	106	3.11	5.12	36.58	Big Particles

shot No.	Name AREA	Sample ID	n	Area Mm	T_{input} ms	Δt ms	I_{beam} mA	I_{abs} mA	P_{abs} GW/m²	E_{abs} MJ/m²		Comment Current curve - Data files
16	G		1	2.0	3	2.38	90	85	2.51	5.97	27.04	6 Big Particles
17	H	221/46	1	2.0	3	2.5	80	75	2.21	5.51	3.78	Small Particles
18	I		1	2.0	3	2.35	75	71	2.08	4.88	0.35	Nothing
19	A		1	2.0	3	2.38	85	82	2.42	5.77	43.18	Big Particles
20	B		1	2.0	4	3.38	75	71	2.08	7.02	10.24	Small Particles
21	C		1	2.0	4	3.29	70	65	1.90	6.26	5.54	Small Particles
22	D	221/47	1	2.0	4	3.18	65	61	1.78	5.67		Small Particles
23	E		1	2.0	4	3.235	60	56	1.64	5.32		Nothing
24	F		1	2.0	4	3.26	85	79	2.34	7.61	58.03	Big Particles
25	G		1	2.0	4	3.13	80	74	2.16	6.77	50.03	Big Particles
26	A	221/49	1	2.0	4	3.24	80	76	2.25	7.29		Big Particles
27	B		1	2.0	2	1.82	220	219	6.44	11.72		Big Particles
28	H	221/47	1	2.0	2	1.94	220	215	6.31	12.25	84.3	Big Particles
29	A	221/50	1	2.0	2	1.85	220	218	6.40	11.84		Big Particles
30	B		1	2.0	4	3.53	120	118	3.46	12.21		Big Particles
shot No.	Name	Sample ID	n	Area Mm	T_{input} ms	Δt ms	I_{beam} mA	I_{abs} mA	P_{abs} GW/m²	E_{abs} MJ/m²		Comment Current curve - Data files
31	A		1	2.0	2	1.62	100	93	2.732	4.43		Medium Particles
32	B		1	2.0	2	1.56	100	93	2.723	4.25		2 big + medium Particles
33	C		1	2.0	2	1.68	100	94	2.767	4.65		1 big + medium Particles
34	D		1	2.0	2	1.62	110	103	3.03	4.90		Medium Particles
35	E		1	2.0	2	1.62	110	103	3.03	4.90	50.2	
36	F	219/58	1	2.0	2	1.76	120	113	3.33	5.86		Big Particles
37	G		1	2.0	2	1.73	140	134	3.93	6.81		Big Particles
38	H		1	2.0	2	1.61	160	154	4.54	7.31		Big Particles
39	I		1	2.0	2	1.8	180	174	5.10	9.18		Big Particles
40	J		1	2.0	2	1.72	180	172	5.06	8.70		
41	K		1	2.0	2	1.67	200	193	5.66	9.46		

shot No.	Name AREA	Sample ID	n	Area mm	T_{input} ms	Δt ms	I_{beam} mA	I_{abs} mA	P_{abs} GW/m^2	E_{abs} MJ/m^2		Comment Current curve - Data files
42	**L**		1	2.0	2	1.74	220	212	6.23	10.84		Big Particles
43	**A**	**219/59**	1	2.0	2	1.76	240	229	6.75	11.87	68.84	Big Particles
44	**B**		1	2.0	2	1.74	260	250	7.35	12.79	84.51	Big Particles
45	**C**		1	2.0	2	1.75	280	268	7.87	13.77	86.85	Small Particles and Medium
46	**D**		1	2.0	2	1.8	300	285	8.39	15.10	87.4	Big Particles
47	**E**		1	2.0	2	1.8	320	297	8.74	15.73	100.63	
48	**F**		1	2.0	2	1.8	340	312	9.17	16.51	61.87	Big Particles

shot No.	Name AREA	Sample ID	n	Area mm	T_{input} ms	Δt ms	I_{beam} mA	I_{abs} mA	P_{abs} GW/m^2	E_{abs} MJ/m^2		Comment Current curve - Data files
49	**A**	**220/58**	1	2.0	2	1.6	100	91	2.68	4.29	39.71	Small Particles
50	**B**		1	2.0	2	1.66	100	91	2.68	4.45	29.48	1 big + medium particles
51	**C**		1	2.0	2	1.58	110	103	3.03	4.78	56.85	Medium particles
52	**D**		1	2.0	2	1.64	120	112	3.29	5.39	52.68	1 big + medium particles
53	**E**		1	2.0	2	1.67	140	129	3.81	6.36	39.7	Small and Big Particles(bright)
54	**F**		1	2.0	2	1.78	160	153	4.50	8.00	49.53	Medium particles
55	**G**		1	2.0	2	1.73	180	172	5.06	8.76	49.65	Medium particles
56	**H**		1	2.0	2	1.77	200	190	5.58	9.87	66.08	Small & 2 Big Particles
57	**I**		1	2.0	2	1.76	220	206	6.06	10.66	86.01	small Particles
58	**A**	**220/59**	1	2.0	2	1.8	240	226	6.66	11.99	86.86	8 Big Particles
59	**B**		1	2.0	2	1.8	260	244	7.18	12.92	82.98	Small Particles
60	**C**		1	2.0	2	1.8	280	262	7.70	13.86	92.34	3 Big +small Particles
61	**D**		1	2.0	2	1.8	300	274	8.04	14.48	117.37	Small Particles
62	**E**		1	2.0	2	1.8	320	294	8.65	15.57	66.39	Big Particles
63	**F**		1	2.0	2	1.8	340	304	8.95	16.11	63.25	Big Particles
64	**G**		1	2.0	2	1.6	90	82	2.42	3.87	4.67	Small Particles
65	**H**		1	2.0	2	1.63	85	76	2.25	3.67	5.65	Small particles

shot No.	Sample ID	n	Area mm	T_{input} ms	Δt ms	I_{beam} mA	I_{abs} mA	P_{abs} GW/m²	E_{abs} MJ/m²			Comment Current curve - Data files
1	**221/1**	1	4	5	5.0	160	149	1.12	5.58	0.07	9.71	small and 1 big (perhaps dust)
2	**221/2**	1	4	5	4.4	180	168	1.26	5.53	0.06	10.82	small particles
3	**221/3**	1	4	5	4.5	200	187	1.40	6.30	0.07	8.16	beginnning of big particles
4	**221/4**	1	4	5	4.4	220	206	1.54	6.79	0.13	8.84	more small, no big
5	**221/5**	1	4	5	4.5	240	226	1.70	7.59	0.19	12.12	2 big
6	**221/6**	1	4	5	4.5	260	244	1.83	8.24	0.33	16.5	nothing is visible (reflectivity of the shield)
7	**221/7**	n1	4	5	4.5	150	138	1.037	4.66	0.46		some particles
8		n2	4	5	4.5	280	264	1.98	8.95		21.14	nothing (because of the relf. or another limit)
9	**221/8**	n1	4	5	4.4	140	129	0.97	4.27	0.46		small
10		n2	4	5	4.6	350	312	2.34	10.73		21.59	small?
11	**221/9**	n1	4	5	4.4	130	118	0.88	3.88	0.49		Nothing (limit)
12		n2	2.96	5	4.5	150	138	1.89	8.46		27.5	big particles
shot No.	**Sample ID**	**n**	**Area mm**	**T_{input} ms**	**Δt ms**	**I_{beam} mA**	**I_{abs} mA**	**P_{abs} GW/m²**	**E_{abs} MJ/m²**			**Comment Current curve - Data files**
13	**219-23**	1	4	5	4.4	160	147	1.103	4.80	0.05	27.5	medium
14	**219-24**	1	4	5	4.4	180	165	1.235	5.41	-0.06	36.89	medium
15	**219-25**	1	4	5	4.5	200	185	1.39	6.21	0.05	47.9	2 big+medium
16	**219-26**	1	4	5	4.4	220	206	1.54	6.81	0.01	57.53	1big + medium
17	**219-27**	1	4	5	4.4	240	224	1.68	7.39	0.04	58.11	big particles
18	**219-28**	1	4	5	4.5	260	241	1.81	8.09	0.04	38.55	big particles
19	**219-29**	1	4	5	4.5	280	262	1.96	8.89	0.09	35.47	big particles
20	**219-30**	1	4	5	4.5	300	282	2.12	9.59	0.06	27.5	idem
21	**219-31**	n1	4	5	4.4	170	159	1.19	5.25	0.03		2 big+medium particles
22		n2	4	5	4.6	350	313	2.35	10.78		62.18	medium particles

shot No.	Sample ID	n	Area mm	T_{laser} ms	Δt ms	I_{beam} mA	I_{abs} mA	P_{abs} GW/m²	E_{abs} MJ/m²			Comment Current curve - Data files
23	**220/23**	1	4.0	5	4.5	160	147	1.103	4.93	0.18	49	medium particles
24	**220/24**	1	4.0	5	4.4	140	127	0.950	4.16	0.14		2 big and small
25	**220/25**	1	4.0	5	4.5	180	166	1.247	5.57	0.15	73.83	small
26	**220/26**	1	4.0	5	4.4	200	185	1.390	6.13	0.18		medium particles
27	**220/27**	1	4.0	5	4.4	220	206	1.544	6.81	0.2	139.3	1 big +medium particles
28	**220/28**	1	4.0	5	4.5	240	224	1.676	7.49	0.19	63.2	small and medium
29	**220/29**	1	4.0	5	4.5	260	241	1.809	8.09	0.29		idem but particles a little bit bigger
30	**220/30**	1	4.0	5	4.6	280	262	1.964	9.01	0.38	58.4	idem but medium
31	**220/31**	n1	4.0	5	4.4	130	115	0.860	3.79			some big
32		n2	4.0	5	4.5	300	282	2.118	9.59	0.36	92.62	3 big+medium
33	**220/32**	n1	4.0	5	4.4	120	106	0.794	3.45			1 big+small
34		n2	4.0	5	4.6	350	310	2.327	10.68	0.3	98.0	1 big and medium bright
shot No.	**Sample ID**	n	Area Mm	T_{laser} ms	Δt ms	I_{beam} mA	I_{abs} mA	P_{abs} GW/m²	E_{abs} MJ/m²			**Comment Current curve - Data files**
35		n1	4.0		4.5		266	2.00	8.92	1.9	83.6	
36		n2	4.0		4.6		268	2.01	9.21			
37	**221/10**	n3	4.0	5	4.6	280	268	2.01	9.21			the emission of particles rises
38		n4	4.0		4.6		268	2.01	9.21			
39		n5	4.0		4.6		268	2.01	9.21			
40		n1	4.0		4.5		268	2.007	8.97	0.29	93.4	
41		n2	4.0		4.6		268	2.01	9.33			some particles
42	**219/32**	n3	4.0	5	4.6	280	268	2.01	9.21			
43		n4	4.0		4.5		268	2.01	9.09			some big particles
44		n5	4.0		4.5		268	2.01	8.97			big particles (more than in n4)

Reference

1. K. Niu, *Nuclear fusion*, Cambridge university press (1989).
2. J. Ongena and G. van Oost, *Controlled thermonuclear fusion*, EURATOM association (1999).
3. R. A. Gross, *Fusion energy*, John wily & sons (1984).
4. J. Raeder, *Controlled nuclear fusion*, Chichester New York (1986).
5. G. Vieider *et.al*, "European development of prototypes for ITER high heat flux components", Fus. Eng. Des., 49-50, pp135-143 (2000).
6. V. Barabash *et.al*, "Selection, development and characterization of plasma facing materials for ITER, J. Nucl. Mater., 233-237, pp718-723 (1996).
7. F. Elio *et.al*, "Engineering design of the ITER blanket and relevant research and development results", Fus. Eng. Des., 46 pp159-175 (1999).
8. R. R. Parker, "Design of in-vessel components for ITER", Fus. Eng. Des., 36, pp33-48 (1997).
9. A. Cardella *et.al*, "Design of ITER EDA plasma facing components", Fus. Eng. Des., 39-40, pp377-384 (1998).
10. T. Hino and M. Akiba, "Japanese developments of fusion reactor plasma facing components", Fus. Eng. Des., 49-50, pp97-105 (2000).
11. M. Rödig *et.al*, "Testing of actively cooled high heat flux mock-ups", J. Nucl. Mater., 258-263, pp967-971 (1998).
12. I. Smid *et.al*, " Lifetime of Be-, CFC-, W-armoured ITER divertor plants", J. Nucl. Mater., 233-237, pp701-707 (1996).
13. C. Ibbott *et.al*, "Advanced solutions for beryllium and tungsten plasma-facing components", Fus. Eng. Des. 39-40, pp409-417 (1998).
14. C. B. Baxi and C. P. C. Wong, "Review of helium cooling for fusion reactor applications", Fus. Eng. Des., 51-52, pp319-324 (2000).
15. H. Haas, Chr. Day, A. Mack and D. K. Murdoch, "Performance tests of the ITER model pump", Fus. Eng. Des., Vol 69, pp91-95 (2003).
16. ITER-FEAT Outline Design Report, ITER meeting, Tokyo, January 2000.
17. ITER, Materials assessment report, G74 MA 9 00-10 W 0.1.
18. K. Ehrlich, E.E.Bloom and T. Kondo, "International strategy for fusion material development", J. Nucl. Mater., 283-287, pp79-88 (2000).
19. T. Tanabe, "Chemistry of excited states:Its impact on plasma wall interactions in fusion devices", J. Nucl. Mater., 248, pp418-427 (1997).

20. C. H. Wu *et.al*, "Progress of European R&D on plasma-wall interactions, neutron effects and tritium removal in ITER plasma facing materials", Fus. Eng. Des, 56-57, pp179-187 (2001).

21. M. Merola *et.al*, "European achievements for ITER high heat flux components", Fus. Eng. Des., 56-57, pp173-178 (2001).

22. G. Federici *et.al*, "Erosion of plasma-facing components in ITER", Fus. Eng. Des., 61-62, pp81-94 (2002).

23. A. W. Leonard *et.al*, "The impact of ELMs on the ITER divertor", J. Nucl. Mater., 266-269, pp109-117 (1999).

24. D. N. Hill, "A review of ELMs in divertor tokamaks", J. Nucl. Mater., 241-243, pp182-198 (1997).

25. G. Janeschits, ITER JCT and HTs, "Section1. Reviews Plasma-wall interaction issues in ITER", J. Nucl. Mater., 290-293, pp1-11 (2001).

26. ITER Design Description Document, Physics, Disruption (July 1998).

27. C. D. Croessmann, G.L. Kulcinski, and J.B. Whitley, "Study of the vapor produced by intense energy deposition", J. Nucl. Mater., 145-147, pp429-439 (1987).

28. V.G. Belan *et.al*, "Features of dynamics and structure of the shielding layer of the interaction of plasma flow with target", J. Nucl. Mater., 233-237, pp763-766 (1996).

29. B. E. Gatewood, "Thermal stresses", McGRAW-HILL Book company inc (1957).

30. A. Gervash *et.al*, "Disruption simulations on tungsten specimens in plasma accelerator", Fusion Technology 1996. Proceedings of the 19th Symposium on Fusion Technology pp499-502 (1997).

31. M. Merola *et.al*, "Behavior of plasma facing materials under VDE", J. Nucl. Mater., 258-263, pp653-657 (1998).

32. M. Rödig *et.al*, "Investigation of tungsten alloys as plasma facing materials for the ITER divertor", Fus. Eng. Desi., 61-62, pp135-140 (2002).

33. T. Tanabe *et.al*, "Material mixing on W/C twin limiter in TEXTOR-94", Fus. Eng. and Des., 49-50, pp355-362 (2000).

34. D. Ciric *et.al*, "Light emission from graphite surfaces during beam bombardment, observation and consequences for use of graphite in divertors", Fusion technology, pp391-394 (1995).

35. A. Hassanein *et.al*, "Modeling and simulation of melt-layer erosion during a plasma disruption", J. Nucl. Mater., 241-243, pp288-293 (1997).

36. J. Linke *et.al*, "Performance of beryllium, carbon, and tungsten under intense thermal fluxes", J. Nucl. Mater., 241-243, pp1210-1216 (1997).

37. J. W. Davis and A. A. Haasz, "Impurity release from low-Z materials under light particle bombardment", J. Nucl. Mater., 241-243, pp37-51 (1997).

38. W. Eckstein, V. Phillips, Physical Processes of the Interaction of Fusion Plasmas with Solids – Physical sputtering and radiation enhanced sublimation, Academic Press (1996)

39. E. Gauthier et al, "Physical sputtering of low Z materials", J. Nucl. Mater.,, 176-177, pp438-444 (1990).

40. R. Behrisch, "Sputtering by particle bombardment I Physical sputtering of single-element solids", Springer-Verlag (1981).

41. E. Salonen *et.al*, "Swift chemical sputtering of amorphous hydrogenated carbon", Physical review B, 63, pp195415 (2001).

42. E. Salonen *et.al*, "Chemical sputtering of amorphous silicon carbide under hydrogen bombardment", Applied surface science, 184, pp387-390 (2001).

43. V. Rohde *et.al*, "Carbon layers in the divertor of ASDEX Upgrade", J. Nucl. Mater., 290-293, pp317-320 (2001).

44. H. Maier *et.al*, "Detection of sputtered and evaporated carbon aggregates: relative and absolute electron ionization fragmentation yields", J. Nucl. Mater., 290-293, pp291-294 (2001).

45. E. Grote *et.al*, "Chemical sputtering yields of carbon based materials at high ion flux densities", J. Nucl. Mater., 266-269, pp1059-1064 (1999).

46. T. Zecho *et.al*, "Hydrogen-induced chemical erosion of a-C:H thin films: Product distribution and temperature dependence", J. Phys. Chem. B, 105, pp6194-6200 (2001).

47. M. Balden *et.al*, "Chemical erosion of carbon doped with different fine-grain carbides", J. Nucl. Mater., 290-293, pp52-56 (2001).

48. M. Nishikawa, "High flux dependence of erosion and retention in beam experiments and its significance to fusion systems", Fus. Eng. Des., 41, pp47-53 (1998).

49. Z. K. Shang *et.al*, "Plasma surface engineering in first wall of tokamak", Surface and coating technology, 131, pp109-115 (2000).

50. C. Garcia-Rosales *et.al*, "First results on the development of improved doped carbon materials for fusion applications", Physica Scripta, T91, pp130-133 (2001).

51. P. Frenzen *et.al*, "Line-of-sight measurements of the radiation-enhanced sublimation of graphite", J. Appl. Phys., 78(2), pp817-827 (1995).

52. M. Balden, "Overview on the effects of dopants on chemical erosion and RES of carbon-based materials", Physica Scripta, T81, pp64-69 (1999).

53. V. Philipps *et.al*, "Radiation enhanced sublimation of carbon and carbon related materials", J. Nucl. Mater., 179-181, pp25-33 (1991).

54. M. Mayer *et.al*, "Transport and redeposition of eroded material in JET", Physica Scripta, T81, pp13-18 (1999).

55. A. von Keudell, T. Schwarz-Selinger, W. Jacob and A. Stevens, "Surface reactions for hydrocarbon radicals suppression of the re-deposition in fusion experiments via a divertor liner" J. Nucl. Mater, 290-293, pp231-237 (2001).

56. V. N. Litunovsky *et.al*, "Study of material response in disruption simulation experiments with variable irradiation duration", Fus. Eng. Des., 39-40, pp303-308 (1998).

57. S. Ishiyama, M. Akiba and M. Eto, "Irradiation damage analysis on the flat plate type target plate of the divertor for fusion experimental reactors", J. Nucl. Mater., 228, pp275-283 (1996).

58. S. Sato *et.al*, " Neutron irradiation effects on thermal shock resistance and fracture toughness of graphites as plasma-facing first wall components for fusion reactor devices", Carbon, Vol. 27 No. 4, pp507-516 (1989).

59. C. H. Wu, J. P. Bonal and B. Kryger, "The effect of high-dose neutron irradiation on the properties of graphite and silicon carbide", J. Nucl. Mater., 208, pp1-7 (1994).

60. T. D. Burchell, "Radiation damage in carbon-carbon composites:structure and property effects", Physica scripta, T64, pp17-25 (1996).

61. V. Barabash *et.al*, "Neutron irradiation effects on plasma facing materials", J. Nucl. Mater., 283-287, pp138-146 (2000).

62. M. Rödig *et.al*, "Reference testing of actively cooled mock-ups for the neutron-irradiation experiments PARIDE3 and 4", Fus. Eng. Des., 56-57, pp417-420 (2001).

63. J.P. Bonal and C.H. Wu, "Neutron irradiation effects on carbon based materials annealing at 350 °C and 800 °C", J. Nucl. Mater., 277, pp351-359 (2000).

64. M. Rödig *et.al*, "Post Irradiation Testing of Samples from the Irraddiation Experiments PARIDE 3 and PARIDE" to be published.

65. W. Wang *et.al*, "Blister formation of tungsten due to ion bombardment", J. Nucl. Mater., 208, pp124-131 (2001).

66. H. O. Pierson, *Handbook of Carbon, Graphite, Diamonds and Fullerenes,* Noyes Publications (1993).

67. D. D. L. Chung, "Review Graphite", J. of Materials science, 37, pp1475-14898 (2002).

68. H. O. Pierson, "HANDBOOK OF CARBON; GRAPHITE; DIAMOND AND FULLERENES Properties, Processing and Applications", Noyes Publications (1993).

69. G. Savage, *Carbon – Carbon Composites,* University Press, Cambridge (1993).

70. A. Makhankov *et.al*, "Performance of the different tungsten grades under fusion relevant power loads", J. Nucl. Mater., 290-293, pp1117-1122 (2001).

71. M. Uda *et al.*, "Thermal shock test of neutron irradiated carbon fiber reinforced carbon composites with OHBIS", Physica Scripta, T81, pp98-100 (1999).

72. T. Tanabe *et.al*, "Examination of material performance of W exposed to high heat load: Postmortem analysis of W exposed to TEXTOR plasma and E-beam test stand", J. Nucl. Mater., 241-243, pp1164-1169 (1997).

73. S. Mukherjee *et.al*, "High-intensity non-brazed heat shield for safe steady-state operation", Fus. Eng. Des., 56-57, pp303-307 (2001).

74. J. G. Van der Laan and H. T. Klippel, "Simulation and analysis of the response of carbon materials to off-normal heat loads accompanying plasma disruptions", J. Nucl. Mater., 179-181, pp184-188 (1991).

75. A. Benz *et.al*, "Therma shock behavior of various first-wall materials under simulation load tests by laser beam irradiation", J. Nucl. Mater., 212-215, pp1318-1322 (1994).

76. J. P. Qian *et.al*, "Thermal shock resistance of graphite and carbon/carbon composites in plasma disruption simulation tests", J. Nucl. Mater., 212-215, pp1183-1188 (1994).

77. Ph. Chappuis *et.al*, "Dust characterization and analysis in Tore-Supra", J. Nucl. Mater.,, 290-293, pp245-249 (2001).

78. A. T. Peacock *et.al*, "Dust and flakes in the JET MKIIa Divertor, analysis and results", J. Nucl. Mater.,, 266-269, pp423-428 (1999).

79. J. Linke *et.al*, "Erosion of metals and carbon based materials during disruptions-simulation experiments in plasma accelerators", J. Nucl. Mater., 212-215, pp1195-1200 (1994).

80. V. N. Litunovsky *et.al*, "Material response due to simulated plasma disruption loads", *Fus. Eng. Des.*, 49-50, pp249-253 (2000).

81. V. Safronov *et.al*, "Material erosion and erosion products under plasma heat loads typical for ITER hard disruptions", J. Nucl. Mater., 290-293, pp1052-1058 (2001).

82. N. I. Arkhipov *et.al*, "Material erosion and erosion products in disruption simulation experiments at MK-200 UG facility", Fus. Eng. and Des., 49-50, pp151-156 (2000).

83. W. Würz *et.al*, "Erosion of ITER-FEAT vertical targets during off-normal events", Fus. Eng. and Des., 56-57, pp349-354 (2001).

84. S. Shiller *et al.*, "Electron beam technology", John wily & sons (1982).

85. G. D. Archard, "Back scattering of electrons", *J. app.phy.*, 32, No. 8, pp1505-1509 (1961).

86. T. E. Everhart, "Simple theory concerning the reflection of electrons from solids", J. Appl. phys., 31 No. 8, 1483-1490 (1960).

87. S. Kakaç and Y. Yener, *Heat conduction,* Hemisphere Pub. Corp (1985).

88. B. Bazylev *et.al*, "Energy threshold of brittle destruction for carbon based materials", Physica Scripta T, to be published.

89. B. Bazylev and H. Würz, "Melt layer erosion of metallic armour targets during off-normal events in tokamaks", J. Nucl. Mater., 307-311, pp69-73 (2002).

90. A. Cardella *et.al*, "Effects of plasma disruption events on ITER first wall materials, J. Nucl. Mater,, 283-287, pp1105-1110 (2000).

91. A. R. Raffray and G. Federici, "RACLETTE: a model for evaluating the thermal response of plasma facing components to slow high power plasma transients. Part I: Theory and description of model capabilities", J. Nucl. Mater., 244, pp85-100 (1997).

92. C. H. Wu *et.al*, "The impact of larger clusters formation C_5, C_6, C_7, C_8, C_9, and C_{10} on the rates of carbon sublimation at elevated temperatures", J. Nucl. Mater., 782-786, pp258-263 (1998).

93. J. Linke *et.al*, "High heat flux simulation experiments with improved electron beam diagnostics", J. Nucl. Mater., 283-287, pp1152-1156 (2000).

94. J. F. Shackelford ; W. Alexander, "CRC materials science and engineering handbook" , CRC press (2000).

95. H. E. Boyer, "Metals handbook ",American Society for Metals (1985).

96. Y. S. Touloukian and D. P. DeWitt, "Thermophysical properties of matter", Y. S. Touloukian and D. P. DeWitt, IFI/PLENUM (1970).

97. J. P. Bonal, "Thermal properties of NB31 and NS31 carbon fiber composites", CEA Rapport DMN/SEMI/LM2E/RT/01-003 (2001).

98. C. H. Wu *et.al*, "EU results on neutron effects on PFC materials", Fus. Eng. Des., 39-40, pp263-273 (1998).

99. N. Yoshida, "Review of recent works in development and evaluation of high-Z plasma facing materials", J. Nucl. Mater., 266-269, pp197-206 (1999).

100. M. U. Valdes *et.al*, "High heat load testing of plasma sprayed W coatings", in 12th PSI conference, 1996.

101. R. Kingswell, D.S. Rickerby, S. J.Bull. and K. T. Scott, "Erosive wear of thermally sprayed tungsten coatings", Thin solid films, 198, pp139-148 (1991).

102. W. Gocht, "Handbuch der Metall märkte", Springer-Verlag (1974).

103. M. D. Crapper et al, "The measurement of the intensity profile of an electron gun using modulation techniques", Vacuum, 46 No. 1, pp23-25 (1995).

104. S. Wojcicki and G. Mladenov, "A new method of experimental investigation of high-power electron beam", Vacuum, 58, pp523-530 (2000).

105. G. Rigon, P. Moretto and F. Brossa, "Experimental simulation of plasma disruption with an electron beam", Fus. Eng. Des., 5, pp299-315 (1987).

106. B. Bazylev and H. Würz, *private communication* (2002).

107. J. Linke *et al.*, "Material degradation and particle formation under transient thermal loads", 290-293, pp1102-1106 (2001).

108. M. Fujitsuka *et.al*, "High heat load test on tungsten and tungsten containing alloys", J. Nucl. Mater., 233-237, pp638-644 (1996).

109. H. Bolt, J. Linke, H. J. Penkallla and E. Tarret, "Emission of solid particles from carbon materials under pulsed surface heat loads", Physica Scripta, T81, pp94-97 (1999).

110. E. de la Cal and E. Gauthier, "Chemical sputtering measurements in Tore Supra by aftershot mass spectrometry outgassing studies", J. Vac. Sci. Technol. A,15(5), pp2597-2604 (1997).

111. C. Mair *et.al*, "Detection of sputtered and evaporated carbon aggregates: relative and absolute electron ionization fragmentation yields", J. Nucl. Mater., 290-293, pp291-294 (2001).

112. J. Linke *et al.*, "Brittle destruction of carbon based materials under severe thermal loads", Fus. Eng. Des., 49-50, pp235-242 (2000).

113. K. Nakamura *et.al*, "Disruption erosions of various kinds of tungsten", *Fus. Eng. Des.*, 39-40, pp295-301 (1998).

114. J. Linke *et.al*, "Material damage to beryllium, carbon and tungsten under severe thermal shocks", J. Nucl. Mater., 258-263, pp634-639 (1998).

115. M. Rödig *et.al*, "Comparison of electron beam test facilities for testing of high heat flux components", Fus. Eng. Des., 51-52, pp715-722 (2000).

116. J. F. Crawford, J. M. Gahl, and J.M. McDonald, "Simulated disruption testing of candidate PFC materials:beryllium, graphite, and other metals", J. Nucl. Mater., 203, pp280-284 (1993).

117. M. Fujioka *et.al*, "Thermal shock experiments for carbon materials by electron beams", J. Nucl. Mater., 179-181, pp189-192 (1991).

118. T. R. Anthony and H. E. Cline, "Surface rippling induced by surface-tension gradients during laser surface melting and alloying", J. Appl. Phys., Vol. 48 No. 9, pp3888-3894 (1977).

119. R. W. Cahn and A. S. Argon, *Physical metallurgy*, North Holland (1996).

120. T. DebRoy and S. A. Cavul, "Physical processes in fusion welding", Rev. Moder. Phys., Vol. 67 No. 1, pp85-112 (1995).

121. S. Schiller et al, *Electron beam technology*, pp289-290, (1982).

122. G. Tsotridis and L. Goded, "The influence of impurities on the molten depths in simulated plasma disruptions", Fusion technology, 26, pp7-16 (1994).

123. V. I. Tereshin *et.al*, "Influence of plasma pressure gradient on melt layer macroscopic erosion of metal targets in disruption simulation experiments", J. Nucl. Mater., 313-316, pp685-689 (2003).

124. V. Semak and A. Matsunawa, "The role of recoil pressure in energy balance during laser materials processing", J. Phys. D: Appl. Phys., 30, pp2541-2552 (1997).

125. Gmelin handbook, Springer (1991).

126. B. N. Singh *et.al*, "Effects of neutron irradiation on microstructure and deformation behaviour of mono-and polycrystalline molybdenum and its alloys", J. Nucl. Mater., 258-263, pp865-872 (1998).

127. A. Hassanein and I. Konkashbaev, "Comprehensive modeling of ELMs and their effect on plasma-facing surfaces during normal tokamak operation", J. Nucl. Mater. 313-316, pp664-669 (2003).

128. B. Bazylev, G. Janeschitz, I. Landman, and S. Pestchanyi, "Erosion of divertor tungsten armor after man ELMs", EPS conference in St. Petersburg, 2003.

129. C. H. Wu, private communication 2002.

130. K. Ohya *et.al*, "Particle emission from a tungsten test limiter in TEXTOR-94: a comparison between experimental and Monte Carlo simulated results", J. Nucl. Mater., 266-269, pp629-634 (1999).

131. T. Tanabe *et.al*, "Application of tungsten for plasma limiters in TEXTOR". J. nucl. Mater., 283-287, pp1128-1133 (2000).

132. K. Krieger, H. Maier, R. Neu, ASDEX Upgrade Team, "Conclusions about the use of tungsten in the divertor of ASDEX Upgrade", J. Nucl. Mater., 266-269, pp207-216 (1999).

133. J. Gilligan, D. Hahn, and R. Mohanti, "Vapor shielding of surface subjected to high heat fluxes during plasma disruption", J. Nucl. Mater., 162-164, pp957-963 (1998).

134. A. Hassanein and I. Konkashbaev, "Macroscopic erosion of plasma facing and nearby components during plasma instabilities: the droplet shielding phenomenon", J. Nucl. Mater., 290-293, pp1074-1078 (2001).

135. A. Hassanein *et.al*, "Material effects and design implications of disruptions and off-normal events in ITER", Fus. Eng. Des. 39-40, pp201-210 (1998).

136. R. Eck *et.al*, "Behaviour of tungsten, molybdenum, and alloys under unusual heating conditions", *High temperatures-high pressures*, 21, pp497-505 (1989).

137. T. Venhaus *et.al*, "Behavior of tungsten exposed to high fluences of low energy hydrogen isotopes", J. Nucl. Mater., 290-293, pp505-508 (2001).

138. F. C. Sze, R.P. Doerner, S. Luckhardt, "Investigation of plasma exposed W-1% La_2O_3 tungsten in a high ion flux, low ion energy, low carbon impurity plasma environment for the International Thermonuclear Experimental Reactor", J. Nucl. Mater, 264, pp89-98 (1999).

139. M. Rödig, "Reference Testing of Actively Cooled mock-ups for the Neutron-Irradiation experiments PARIDE3 and 4", Fus. Eng. Des., 56-57, pp417-420 (2001).

140. C. Garcia-Rosales *et.al*, "High-heat-flux loading of tungsten coatings on graphite deposited by plasma spray and physical vapor deposition", Fusion technology, 32, pp263-276 (1997).

141. S. Deschka *et.al*, "Manufacturing and high heat flux loading of tungsten coatings on fine grain graphite for the ASDEX-Upgrade divertor", J. Nucl. Mater., 233-237, pp645-649 (1996).

142. A. Hassanein, "Prediction of material erosion and lifetime during major plasma instabilities in tokamak devices", Fus. Eng. Des., 60, pp527-546 (2002)

143. G. Tsotridis and H. Rothar, "The role of surface-tension-driven convective flows on the molten depths in simulated plasma disruptions", Fusion technology, 27, pp389-400 (1995).

144. G. Tsotridis, "The melting of tungsten during plasma disruptions", J. Nucl. Mater., 233-237, pp758-762 (1996).

145. T. Burtseva, A. Hassanein, I. Ovchinnikov, V. Titov, "Study of brittle destruction and erosion mechanisms of carbon-based materials during plasma instabilities", J. Nucl. Mater., 290-293, pp1059-1063 (2001).

146. J. Linke *et.al*, "Carbon particles emission, brittle destruction and co-deposit formation: experience from electron beam experiments and controlled fusion devices", Physica Scripta, T91, pp36-42 (2001).

147. J. Winter and G. Gebauer, "Dust in magnetic confinement fusion devices and its impact on plasma operation", J. Nucl. Mater., 266-269, pp228-233 (1999).

148. M. Rubel *et al.*, "Dust particles in controlled fusion devices: morphology, observation in the plasma and influence on the plasma performance", Nuclear Fusion, Vol. 41 No. 8, pp1087-1099 (2001).

149. J. P. Coad *et al.*, "Erosion/deposition in JET during the period 1999–2001", J. Nucl. Mater., 313-316, pp419-423 (2003).

150. J. P. Sharpe, D. A. Petti, and H. W. Bartels, "A review of dust in fusion devices: Implications for safety and operational performance", Fus. Eng. Desi., 63-64, pp153-163 (2002).

151. W. J. Carmack *et.al*, "Collection and analysis of particulate from the DIII-D Tokamak", Fus. Eng. Des., 39-40, pp477-483 (1998).

152. A. Cambe, E. Gauthier, J. Hogan and J. M. Layet, "Chemical sputtering of carbon in Tore-Supra outboard pump limiter", J. Nucl. Mater., 313-316, pp364-369 (2003).

153. K. Nakamura *et al.*, "Disruption and sputtering erosions on SiC doped CFC", J. Nucl. Mater., 258-263, part 1, pp828-832 (1998).

154. C. H. Wu *et al.*, "Overview of EU CFCs development for plasma facing materials", J. Nucl. Mater., 258-263, pp833-838 (1998).

155. M. F. Stamp *et.al*, "Spectroscopy of hydrocarbon fluxes in the JET divertor", Physica Scripta, T91, pp13-17, 2001.

156. J. Linke *et al.*, "Brittle destruction of carbon based materials in transient heat load tests", Fus. Eng. Des., 66-68, pp395-399 (2003).

157. M. I. Guseva *et.al*, "Erosion products of ITER plasma facing materials under plasma disruption simulation", Fus. Eng. Des., 66-68, pp389-394 (2003).

158. M. I. Guseva et. al, "Selfsputtering of beryllium and sputtering and erosion of C-C composite in the experiments on plasma disruption simulation", J. Nucl. Mater., 220-222, pp957-960 (1995).

159. H. Bolt, T. Kuroda, A. Miyahara, H. Nickel, "Behavior of candidate materials for fusion applications under high surface heat loads", Juli Bericht 2214, pp78-79 (1988).

160. V.T. Astrelin *et.al*, "Hot electron target interaction experiments at the GOL-3 facility", Nuclear fusion, 37, pp1541-1558 (1997).

161. S. E. Pestchanyi and I. S. Landman, "Effective thermal conductivity of graphite materials with cracks", Physica Scripta to be published.

Acknowledgement

The author would like to acknowledge Prof. Dr.-Ing. L. Singheiser for giving an opportunity to work at the institute in Forschungszentrum supervising during the study. The author really appreciates that Prof. Dr. rer. nat. F. Schubert has supported and suggested for the dissertation.

For Dr. J. Linke's effort to improve the whole work through advices, fruitful discussion, and suggestions I am sincerely grateful. For the assistance of high heat flux testing by electron beam facility I would like to acknowledge Dr. M. Rödig, Mr. Kühnlein and Mr. Münstermann. In experimental and characterization of the results, Mr. E. Lehmann, Ms. S. Amouroux, and Mr. E. Berthe helped me and contributed for the evaluation of the results. From the theoretical point of view, Dr. B. Bazylev helped me through the useful discussion and suggestions and contributed in the simulation, which support the experimental results.

I would like to thank Ms. G. Gutzeit and Mr. G. Böling for their help and supports in the experimental set up, the sample preparation and the surface analysis. For the surface analyses by SEM, I would like to acknowledge Dr. E. Wessel. For Mr. V. Gutzeit's help in preparation and observation of cross section (ceramography and metallography) of the samples I would like to express special thanks. I appreciate Mr. P. Joecken for his technical support for the network and PC. My special thanks are extended to Dr. O. Ogorodnikova, Dr. P. Majerus, and Dr. K. Verfondern for making corrections of my thesis and the useful discussion.

For their help to solve technical problems I would like to acknowledge my office mates: Dr. D. Danciu, Ms. A. Kapoustina, Ms. L. Mikulova, and Mr. G. Pintsuk. I would like to extend my thanks to my colleagues and friends for sharing pleasant and wonderful time that brought me an invaluable life in Germany.

Finally I would like to thank my family and my best friend Mr. L. Koldert for their constant support.

Forschungszentrum Jülich
in der Helmholtz-Gemeinschaft

Jül-4137
Juni 2004
ISSN 0944-2952